# INVESTIGATION AND COMPUTER MODELLING OF THE PORE STRUCTURE OF PAPER AND OF CONSOLIDATED PIGMENT COATINGS

by

## JOHN. KETTLE

A thesis submitted to the University of Plymouth

in partial fulfilment for the degree of

## DOCTOR OF PHILOSOPHY

Department of Environmental Sciences

Faculty of Science

In collaboration with

ECC International plc.

· 1996

# Investigation and computer modelling of the pore structure of paper and of consolidated pigmented coatings

by

**John Kettle**

## ABSTRACT

The aim of this project was to enhance the current state of knowledge of the void structure of paper, and pigments used to coat paper. The porosities and pore size distributions of consolidated pigments were measured using mercury porosimetry. Prior to this work, mercury porosimetry was rarely used in this field due to problems associated with the conventional interpretation of mercury porosimetry data. These problems were examined and two limitations of mercury porosimetry were addressed. Firstly, the shrinkage of compressible samples causes an apparent increase in void volume and secondly, large void spaces shielded by smaller ones are not intruded until anomalously high applied pressures of mercury are reached. The first limitation was overcome by means of a new correction procedure which, uniquely, also allows the measurement of the bulk modulus of the continuous solid phase of a porous sample. Shielding effects have been taken into account by means of a software package known as Pore-Cor, which generates a three dimensional structure which has both a mercury intrusion curve and porosity in close agreement with experiment. It has also been possible to calculate the permeabilities and tortuosity of the simulated structure and this provides realistic and useful values, which may not be measured experimentally.

Mercury porosimetry and a range of specialised absorption techniques, including liquid porosimetry, were used to characterise the porous structures of a highly filled paper which had been calendered using a range of different conditions. A unique feature of this work is that for the first time it has been shown that two porosimetric techniques which measure overlapping pore size distributions may be combined to give a better indication of the total pore size distribution.

# LIST OF CONTENTS

# LIST OF FIGURES

# LIST OF TABLES

# LIST OF PLATES

# DEDICATION

To Sarah and our children, Sean, Laura and Jack

# ACKNOWLEDGEMENTS

I must express my sincere gratitude to my supervisor, Dr Peter Matthews, Principal Lecturer in Physical Chemistry at the University of Plymouth for his support, inspiration and guidance throughout the course of this work. I am also indebted to Professor Barry Jennings, Research Director of ECCI and Dr John Adams, Research Manager of ECCI for allowing me to pursue one of my goals.

Dr P. McGenity, Dr L. Gate and Dr P. Gane are also thanked for their valuable cooperation and suggestions during the work and preparation of the manuscripts. Dr G. Drage is thanked for her excellent criticism of the draft version of this document. Thanks are also due to Dr Lars Wagberg, SCA Research, Sweden who has provided the ESEM micrographs and the liquid porosimetry data, but most importantly has shared in my joy in advancing the world-wide understanding of the porous nature of fibre systems.

I should also like to thank my colleagues at ECCI, especially those in the Paper Research group, and fellow students at the University of Plymouth for their stimulating discussions and inspiring company. I must especially thank Miss Cathy Ridgway, a fellow PhD student working with Pore-Cor, for her computing expertise and her sense of humour.

Last but certainly not least I wish to express my sincere thanks to my wife, Sarah, who has endured my thesis writing as well as a third pregnancy during one of the hottest of summers. Without her support over a number of years this work would not have been possible.

# AUTHOR'S DECLARATION

At no time during the registration for the degree of Doctor of Philosophy has the author been registered for any other University award.

This study was financed by, and carried out in collaboration with ECC International Ltd. SCA Research AB are acknowledged as the source of the ESEM images and the liquid porosimetry measurements.

Relevant scientific seminars and conferences were attended regularly at which work was presented; external research centres and institutions were visited for consultation purposes and several papers prepared for publication.

**Publications:**

**Computer modelling of the pore structure and permeability of pigmented coatings.**

Kettle, J.P., Matthews, G.P., Tappi Coating Fundamentals Conference 1993

Published in Conference Proceedings, 121-126

**Void space structure of compressible polymer spheres and consolidated calcium carbonate paper-coating formulations.**

Gane, P.A.C., Kettle, J.P., Matthews, G.P., Ridgway, C.J.

Published in Industrial Chemical and Engineering Research Journal, **(35)**, pages 1753-1764, No. 5 , May, 1996.

**Performance of LWC grade papers in a pilot - scale calendering study.**

Kettle, J.P., PITA Annual Coating Conference, Leicester, March 1995

Published in Conference Proceedings.

**Pore structure characterisation and modelling of paper using novel porosimetric and absorption techniques: application to super and soft nip calendering.**

P.A.C., Kettle, J.P., Matthews, G.P., Ridgway, C.J., Wagberg, L.,

Abstract accepted by FRC in Cambridge for presentation in 1997.

**Planned publications:**

Techniques to evaluate the pore structure of paper.

Kettle, J.P., Matthews, G.P., Ridgway, C.J., Wagberg, L.

To be submitted to Journal of Measurement Science and Technology.

Response to calendering of filled sheets and the characterisation of filler pigment alignment and pore structure within the sheet.

Kettle, J.P., Matthews, G.P., Ridgway, C.J.

To be submitted to Journal of Materials Science.

**Presentations and International Conferences attended:**

Tappi Coating Fundamentals Conference, Minneapolis, USA, April 1993 (attended)

Institute of Physics, London, December 1993 (presented paper)

STFi Conference, Stockholm, Sweden, March, 1994 (attended)

PITA Annual Coating Conference, Leicester, March 1995 (presented paper)

**Within ECCI:**

Paper, Packaging and Printing Working Group of Institute of Physics, December 1993 (presented paper)

Regional Technical Managers Training, January, 1994 (presented paper)

International Paper, USA, May, 1994 (presented paper)

SCA Research AB, Sundsvall, Sweden, September, 1994 (presentation at SCA / ECCI / STFi symposium)

Valmet Paper Machinery Oy, Jarvenpaa, Finland, November 1994 (presentation at Valmet ECCI / Valmet Symposium)

**External Contacts:**

Dr Lars Wagberg, Research Director, SCA Research AB, Sundsvall, Sweden.

Dr Bob Groves, Research Director, Doverstrand Ltd., Essex, England.

CHAPTER 1

# 1. INTRODUCTION

## 1.1 *Background of the project*

In modern life, paper has many uses and one of the most important uses is as a medium for information transfer. To transfer information successfully, paper has to be printed with an image of the required information and the print has to be distinct from its background and sufficiently durable to prevent loss of quality by handling. For a high quality printed image to be achieved, the paper should be smooth to allow good ink transferance, opaque to prevent image "showthrough" and have sufficient capillarity to allow the ink film to set within the timescale of a modern printing press. These important parameters of paper quality are key issues within the paper and printing industries. The smoothness of papers can be improved by coating and calendering. (The term "coating" within the paper industry refers to the application of an aqueous pigment / binder suspension to the surface of the paper followed by drying; and the term "calendering" refers to the thermal and physical compression of the paper to smoothen and densify it). The opacity of paper can be improved by the addition of a filler of higher refractive index than cellulose, to improve the light scatter of the sheet structure. The ink uptake of paper is determined by its pore structure and its surface chemistry at the paper / ink interface.

The pore structures of coated papers are very complex and this project has focused upon these complexities. With the use of advanced experimental techniques which generate data to input into a 3D computer modelling program, progress has been made to ascertain some of scientific facts behind the unexplained anecdotal tales about print performance supplied by paper mills and printers.

The extent of these complexities is exemplified by a *basepaper*. The term basepaper refers to paper that has been made on a paper machine using an aqueous suspension of cellulose fibres, fine mineral pigment and sufficient chemicals to keep the whole matrix together. Although this is a simple system in paper industry terms, the void space of the structure is determined by a series of complicated variables, namely fibre type, fibre size distribution and fibre orientation, as well as pigment filler type and filler distribution across the thickness of the paper sheet. Even in this simple case, the qualities of basepaper can usually improved by coating and / or calendering, which adds another level of complexity to the investigation of its pore level structure.

Finished paper is even more complicated, because there is usually at least one coating layer on the base paper. The pore space of this coating layer is determined by the particle packing of the coating pigment, and the interactions of pigment particles with binders and with the paper substrate whilst the coating is dried and consolidated.

## *1.2    Experimental design of the project*

It is clear that even the simplest usable paper structure is too complicated to act as a starting point for this project, so to simplify the initial analysis, the experimental work commenced with *model systems* such as solid spherical plastic pigments, and only later approached real usable paper systems. The philosophy of this approach is shown in Figure 1. In line with other workers, initial studies concentrated on the evaluation of structures formed by spheres coated onto substrates which are smooth, flat, impermeable and incompressible. Such systems are referred to as model systems in this work. The aim of the model systems was firstly to develop an experimental procedure to evaluate

consolidated coatings of sub-micrometre particles and secondly to gain experience using the mercury porosimeter and its related software (right hand side of Figure 1).



**Figure 1: Outline of this project**
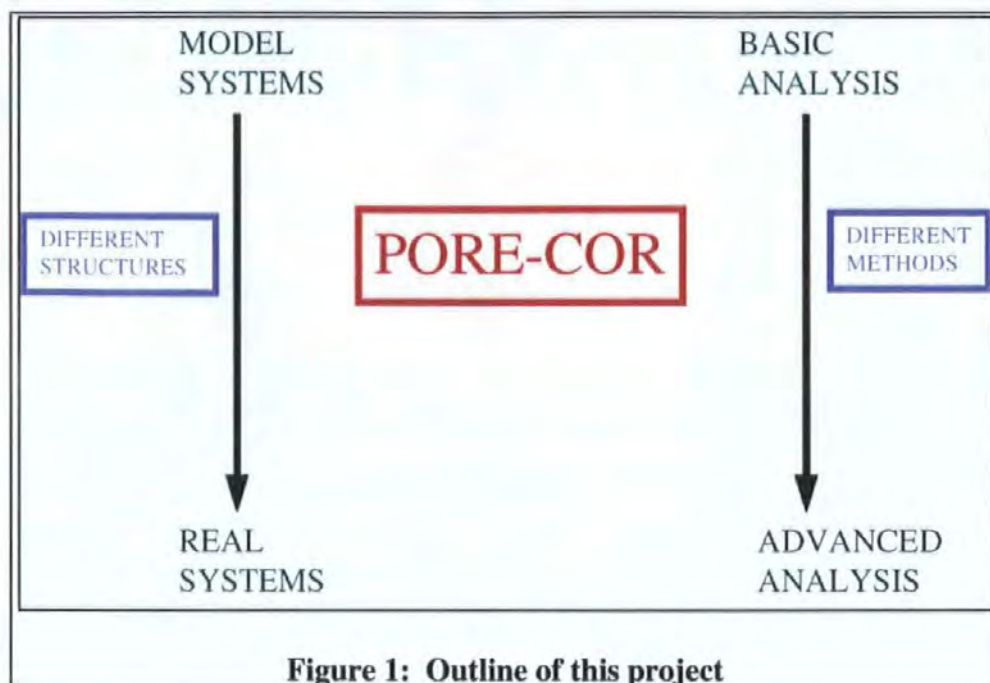
Samples of different particle sizes were obtained and consolidated by air drying, at ambient temperature, a thin layer of plastic pigment suspension on to an impervious substrate. The consolidated samples were analysed using mercury porosimetry (Section 3.7). Building upon this initial work, blends of these plastic pigments were prepared, dried in the same way and the pore structures characterised as before.

Taking one step nearer to reality, that is one step further down the left hand side of Figure 1, a selection of calcium carbonate mineral pigments was evaluated. Electron microscopy studies of process ground calcite have indicated that it forms "blocky" (low aspect ratio) particles. The pore structures of consolidated films of calcites of differing particle size were characterised by mercury porosimetry. In order to attempt to mimic the structures of a pigmented calcite coating applied to paper, consolidated films of a calcite with a selection of different latex binders were prepared and characterised. The other

major mineral type used for paper coating is kaolin. The particle shape of kaolin is traditionally defined as "platey" (high aspect ratio) and its shape further complicates the particle packing. In this work, consolidated structures of kaolins with differing particle size distributions, different latex binder types were characterised. A set of simple commercially produced papers was also examined. Samples of paper containing a kaolin filler were calendered using a variety of conditions.

The different methods on the right-hand side of Figure 1 include porosimetry and permeatry, microscopy, and surface and optical measurements. Pore-Cor is a new software package, developed by the University of Plymouth, for modelling the pore-level properties of porous solids. Figure 2 shows the project structure in more detail. Particle size analysis of the pigments used in this work were made by Sedigraph or Zetasizer. The pore structures of the consolidated pigment samples were probed using mercury porosimetry. Conventional analysis of mercury porosimetric data was proven to be inadequate for our needs to take into account sample compression effects. In this work new equations have been developed which have made it possible to extend the existing theory to incorporate a calculation of the bulk modulus of the solid phase. The surface and bulk structures of the paper samples were investigated using mercury porosimetry as well as Gurley permeability, low pressure liquid porosimetry and surface air leakage techniques. The new technique of *liquid porosimetry* was used to evaluate the porosity and pore size distribution of paper samples (mimimum 6μm diameter). A unique feature of this work is that for the first time it has been shown that two porosimetric techniques which measure overlapping pore size distributions may be combined to give a better indication of the total pore size distribution.

The consolidated pigment structures were viewed using SEM and an ESEM was used to view the paper samples. The z-direction thicknesses (calipers) of the papers were measured using optical microscopy and image analysis software (Section 3.3.3). The conventional physical, optical and printing properties of all of the papers prepared in this study were tested according to standard test procedures (TAPPI).

Mercury porosimetry data and liquid porosimetry data were entered into the Pore-Cor modelling program for simulations of the various pore structures examined. The Pore-Cor program (developed by the Fluid Interactions Research Group at University of Plymouth) is beginning to be accepted within the world of Geo-Petroleum research, and external interest in our application of this technique to paper coating structures has now been expressed by SCA Research AB, Sweden. The Pore-Cor program generates a three dimensional structure which matches the experimentally determined porosity and pore size distribution of the sample under test. The simulated network requires values for pore and throat size distribution, connectivity, pore size : throat diameter ratio, and contact angle. The absence of entirely arbitrary parameters allows the same network to be used for the simulation of other properties such as permeability and tortuosity, which in some cases can be compared to actual measurements of these parameters on the samples in question. This feature also allows the causes of discrepancies from experiment to be identified. The approach represents a major advance on many other experimentally related network simulations (Section 6.4), which often are derived simply from the first derivative of the mercury intrusion curve.

In order to maintain a logical sequence of presentation, this dissertation has been written so that the sample descriptions are given in Chapter 2. It is necessary to provide the reader with an understanding of the wide ranging experimental techniques used (Chapter 3), and

to note the theories of particle packing for different systems (Chapter 4). The porosimetric techniques have been advanced and this discussion forms Chapter 5. The computer model, Pore-Cor, is described in Chapter 6. A description of the experimental results is given in Chapter 7 and comparisons made with simulated properties in Chapter 8. Finally, future important links and conclusions are summarised in Chapter 9. The research areas of paper science and porous media are extensively documented and to avoid lack of focus in the introduction, the literature review is spread between Chapters 2 - 6. Examples of the author's published papers are given in Appendix 4.

**Model System**

Cross-check, particle packing and consolidation mechanisms  `4`

**Basic Analysis**

**Fundamental Properties**

**Sample Types**  `2`  `3`

**PORE COR**

**Fundamental Properties**

Particle size analysis
Stokes / Sedigraph
Zeta sizer

(Oil Absorption)

Pore and surface structure
Gurley Permeability
Mercury Porosimetry
Liquid Porosimetry
Surface air leakage

Microscopy
SEM
ESEM
Optical Microscopy / Profilometry

Direct surface & optical measurement
Profilometry
Paper gloss
Light scatter / Light absorption

Printing properties
Ink gloss / density
Ink Tack force

**Plastic pigments**

Monosized hollow

Wide particle size distribution

**Calcite**

Different particle size distributions
Different latex types

**Kaolin**

Different particle size distributions
Different formulation types

**Paper**
Fibre

Uncalendered

Supercalendered

Hot soft nip calendered

`6`
**Simulated Properties**

Interpret to give increased understanding of structures

Future important links  `9`

**Comparison**  `8`

**Direct comparison**  `7`

**Advanced analysis**

Calibration for compression effects
Combination of data from mercury and liquid porosimetry  `5`

**Real System**

Key: Boxed numbers are Chapter numbers

**Paper Quality as perceived by customer**

**Figure 2:   Overall thesis plan**

## 2. SAMPLE TYPES

Most of the samples used in this study are commercially available, and the producers of these samples are listed in Appendix 1.

### 2.1 Plastic pigments

In line with other workers (Leskinen (1987), Lee (1970)), initial studies concentrated on the evaluation of structures formed by packed spheres, coated onto substrates which are smooth, flat, impermeable and incompressible. In general, plastic pigments are emulsions of polystyrene spheres which are characterised in terms of their spherical diameters whilst in suspension. In this study two pigments, Lytron 2301 and Lytron 2601, which were commercially designed to enhance paper coating gloss comprise aqueous emulsions of solid spheres made from polystyrene. Lytron 2301, has a quoted mean particle diameter of 0.3 $\mu$m, and Lytron 2601 has a quoted mean particle diameter of 0.6 $\mu$m. The mean diameters of these plastic pigments were measured as 0.32 $\mu$m and 0.61 $\mu$m respectively by photon correlation spectroscopy. The pH's of these pigments are in the range of 8.7 - 9.3 and they have glass transition temperatures ($T_g$) of greater than 60°C.

Another plastic pigment, Ropaque HP91, has been developed by Rhom and Haas to impart both gloss and opacity to paper coatings. In aqueous emulsion it comprises water-filled styrene-acrylic copolymer spheres which dehydrate to form a dry, consolidated coating of hollow spheres with a quoted mean diameter of 1 $\mu$m. The mean diameter was measured as 1.01 $\mu$m by photon correlation spectroscopy, and HP91 was shown to be essentially monosized by scanning electron microscopy. The $T_g$ of Ropaque HP91 is quoted as being

greater than 95$^o$C, its pH of suspension as 9.5, wet density as 1.03 g cm$^{-3}$, and dry density as 0.55 g cm$^{-3}$.

The samples for porosimetry were prepared by taking 10 g samples of each of these pigments emulsions and leaving them to air dry, on an aluminium dish, in a dessicator. The drying process took about 48 hours to complete. It was possible to remove intact lumps of these consolidated coatings from the aluminium. Approximately 0.2 g of each consolidated sample was removed and used for mercury porosimetry.

## 2.2    *Calcium carbonates*

The calcium carbonate samples used in this study were produced by ECC International (Europe), and have the trade names Carbital 90, Carbital 60 and LX 60. Carbital 90 is a fine paper coating grade of calcium carbonate made from ground marble and has 90 % by weight of its particles finer than 2 μm. In Carbital 60, 60 % of the particles are finer than 2 μm. LX 60 is made from limestone and has 60 % finer than 2 μm, but also has been engineered to have fewer fine (less than 0.5 μm) particles than a conventional carbonate pigment, i.e it has a steeper particle size distribution. Figure 3 shows the different particle size distributions for these three calcium carbonates, as measured  by a Micromeritics Sedigraph.
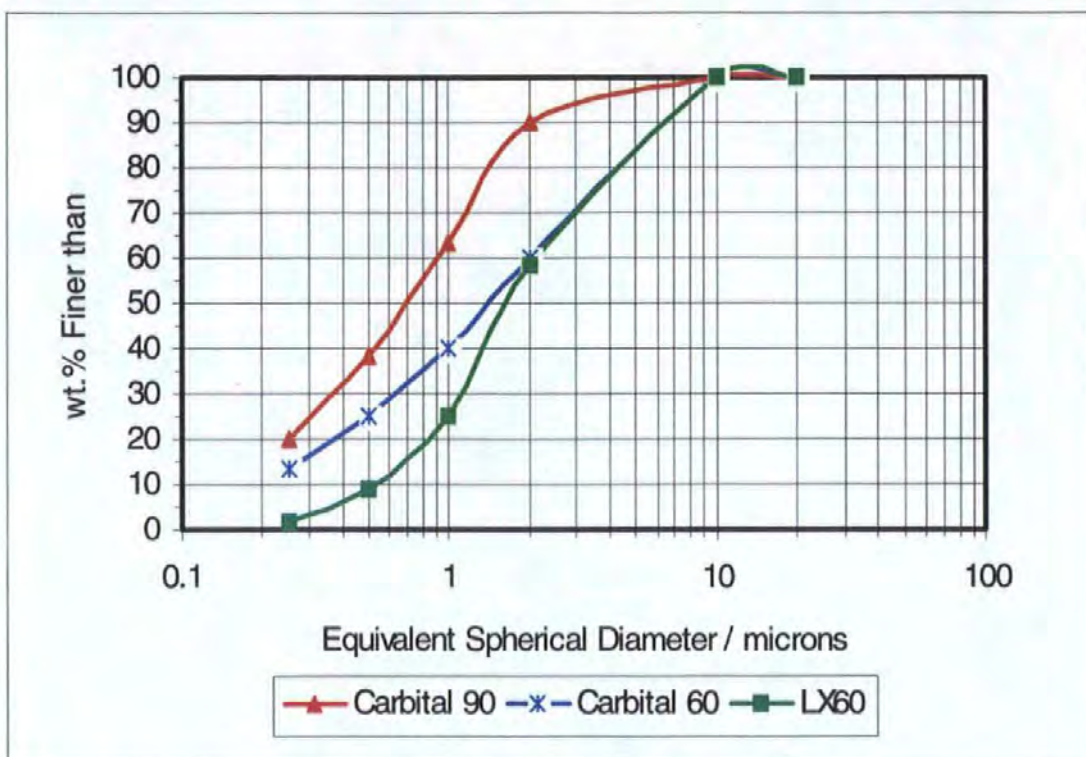
**Figure 3: Particle size distribution of calcium carbonates**

A study has also been made of Carbital 90 mixed with 12 parts per hundred (pph) by weight, relative to 100 parts of dry pigment, of three different latex binders. The first was an Acronal styrene-acrylic copolymer latex (S801), with a glass transition temperature ($T_g$ ) in the manufacturer's quoted range 26 - 44 $^{\circ}$C, and a pH of 8 to 8.5. The second binder was a Revinex styrene-butadiene latex (95L10), with a $T_g$ around 5 $^{\circ}$C. The third, DL 950, was a carboxylated styrene-butadiene copolymer, with a $T_g$ of 8 $^{\circ}$C, and pH of 5.5.

The calcium carbonate samples Carbital 90, Carbital 60 and LX 60 were supplied in a fully dispersed slurry form at 75 wt.% solids by weight. Each slurry was stirred to ensure that it was homogeneous. Approximately 5-10 g of each slurry was coated onto aluminium foil and dried at room temperature in order to form a consolidated slab of pigmented coating. Approximately 1 g of each consolidated sample was then cleaved from the slab to produce a lump that was the full depth of the dried slab, which was then placed in the penetrometer.

The preparation of the coating colour involved pouring the Carbital 90 slurry, at 75 wt% solids by weight, into a high speed mixer, adding 12 parts per hundred (pph) by weight of the latex, and adjusting to pH 9 with sodium hydroxide. The colour was then passed through a 53 µm screen, coated onto aluminium and oven dried at 100 °C. Since this temperature is much higher than any of the glass transition temperatures, it might be expected that the latex would film-form after the coating colour reaches the First Critical Concentration (Section 4.2), and we have confirmed this by electron microscopy.

## 2.3    Kaolins

Two types of kaolin from ECC International's portfolio have been used in this study, an ultrafine U.S. No1 high brightness coating clay (Alphafine) and an English coating clay (SPS). In order to study the effect of particle size distribution upon pore structures the Alphafine clay was dispersed at high solids (75 wt%) and the resulting slurry divided into three. One sample was retained as the control, the other samples were diluted to a density of less than 1.1 g.cm$^{-3}$ and centrifuged using a Broadbent Centrifuge for 9 minutes at maximum speed. The coarse fractions were redispersed separately and their particle size distributions were much steeper (fines - deficient) than the particle size distribution of the starting material, Figure 4. The fine fractions were not used for any further work in this study.
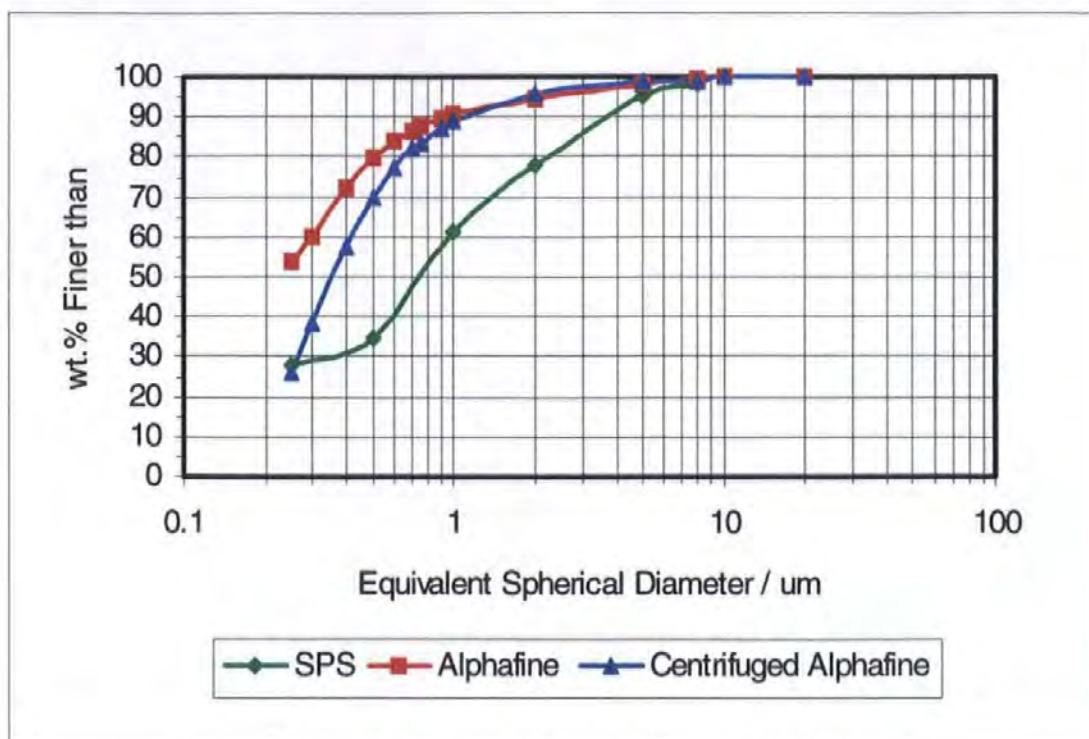
**Figure 4: Particle size distributions of kaolins**

Coating colours were prepared from the Alphafine slurry and the centrifuged slurry, referred to as Centrifuged Alphafine, at an addition level of 14 pph Dow 950 latex. The target solids level for the coating colours was 60 wt% at pH 9. The coating colours were applied to a coarse carbonate precoated LWC basepaper using hand-draw-down bars. In addition, colours which contained 14 pph latex were coated using the same technique onto Synteape (a synthetic, impermeable paper).

The English coating clay, SPS, was used in two significantly different formulations. The first formulation consisted of SPS with 15 wt% latex (a hard styrene-butadiene latex containing 25 % butadiene), and the second formulation consisted of SPS with 4 wt% starch (Nylgum A55, a phosphate ester of a potato starch). The SPS slurry was blended with either the latex or starch to form coating colours which were then dried under ambient conditions and in an oven at 110 °C.

For simplicity, all the samples in this study were homogeneous lumps of dried coating material. Although such lumps are never encountered in commercial paper making or coating, their study provides a basis for understanding the properties of paper coating constituents; Alince and Lepoutre, for example, have studied the porosity and opacity of clay coated onto a transparent polyester film (1980a), and of a coating made solely from plastic pigments (1980b) neither of which are met in commercial practice. We have examined typical lump samples by electron microscopy, which shows the expected void size range and film-forming characteristics.

## 2.4    Paper

A kaolin filled commercial paper was used for a pilot-scale calendering study. The paper was analysed and found to contain 18 % chemical pulp and 82 % mechanical pulp. The terms *chemical pulp* and *mechanical pulp* refer to the pulping treatment (chemical or mechanical defibrilation) that the wood fibres have undergone to form the two different pulp types. The paper had a relatively high filler content of 30 wt%. This paper was calendered using two different types of calender, a supercalender and a soft nip calender. The supercalender consists of a vertical stack of alternating steel and cotton rolls which are at elevated temperature. These rolls are forced into contact to form a nip and rotate at a preset speed. The paper is threaded through the stack and calendered using conditions set by the operator. The soft nip calender consists of two sets of two rolls (steel and cotton). These rolls have larger diameters than the rolls of a supercalender, can be driven faster, and therefore can be operated at higher speeds. The larger roll diameters form longer nips between the rolls, with the result that paper can be calendered more per nip on a soft calender than on a supercalender. The calenderability of paper (i.e. the response of paper to calendering) can be improved by calendering the paper when it has a high moisture

13

content and is warm. This can be achieved by locating steam showers to spray the paper before it passes through the calender nip. Reviews of calendering technologies and processes have been given by Crotogino (1982), Hilden and Sawley (1987), Keller (1992, 1994), Kettle (1995), Millington (1995), Peel (1990, 1993) and Santkuyl (1995).

A pilot calendering study comprises a matrix of calender speeds, applied pressures and temperatures. For this project, nine samples were selected; the uncalendered basepaper, a paper supercalendered at 800 m.min$^{-1}$, with and without steam pretreatment, and soft nip calendered papers calendered at 400 m.min$^{-1}$, 800 m.min$^{-1}$ and 1800 m.min$^{-1}$, with and without steam pretreatment. These papers were tested for their standard paper properties, rotogravure printability (Chapter 7) and pore structure. The pore structures were evaluated using mercury porosimetry (for the fine pore structure) and liquid porosimetry (for the larger pore structure). These data were combined (Chapter 5) and successfully modelled using Pore-Cor (Chapter 8).

## 3. CONVENTIONAL EXPERIMENTAL TECHNIQUES

This chapter describes the experimental testing procedures that have been employed in this study.

### *3.1 Conventional Paper Testing*

The techniques used in this study are listed below, and were all carried out according to the TAPPI procedures stated. A collection of these test procedures have been listed by TAPPI in a publication entitled *TAPPI Test Methods (Volumes 1 and 2).*

### 3.1.1 Gloss

Gloss is related to the ratio of specularly reflected light to incident light. For optically smooth surfaces, gloss varies with refractive index and angle of incidence according to Fresnel's law, (Lepoutre, 1989). Gloss is also a function of roughness and can be used to characterise surface roughness. Specular gloss of paper is measured at 75 degrees (15 degrees from the plane of the paper) and a full description of this test methodology is described as TAPPI standard test T 480 om-85.

### 3.1.2 Brightness (Spectral reflectance / transmittance)

The spectral reflectance factor and transmittance are determined by means of a spectrophotometer in which the specimen is illuminated with heterogeneous light of known spectral power distribution. The instrument incorporates the CIE (Commission

Internationale de l'Eclairage) integrating sphere geometry for the measurement of normal-diffuse reflectance and transmittance, and the CIE 45 ° - 0 ° geometry for the measurement of reflectance factor (opacity) and regular transmittance. The optical properties of the samples in this study were measured using a Datacolour 2000 instrument which measures in accordance with the description above. Full details of this test procedure are described in T 442 om-88.

### 3.1.3 Smoothness

Surface smoothness has an important influence on the printing quality, as uniform ink coverage of the paper can be achieved only when the ink film on the printing plate reaches the bottoms of the deepest depressions of the paper surface under impression. Smoothness also affects properties such as the coefficient of friction, gloss and coating absorption. The smoothness of a paper is usually characterised by an air flow / leakage technique. Essentially this is a measure of the air flow between the paper and two pressurised, concentric annular rings which are impressed into the sample from the top side. The rate of air flow between the rings and the surface of the paper is related to the surface smoothness of the paper. In the Parker Printsurf (Parker, 1981), the paper is backed by a rubber disc of similar hardness to the rubber rollers used in offset litho printing processes. A full description of this method is quoted in T 538 om-88.

### 3.1.4 Gurley Permeability

This method is used to measure the air resistance of paper when a pressure difference is applied across the boundaries of the specimen. It is evaluated by obtaining the time taken for a given volume of air to flow through a specimen of given dimensions under standard conditions of pressure, pressure difference, temperature and relative humidity.

The absolute permeability 'k' of a porous solid may be defined in terms of Darcy's Law. With reference to a cell of the solid of unit volume, this may be written as:

$$\frac{dV}{dt_{cell}} = \frac{-kA_{cell}}{\mu} \frac{\delta P_{cell}}{l_{cell}} \qquad (1)$$

where $\mu$ is the viscosity of the fluid, $(dV/dt)_{cell}$ is the volumetric flow rate across the cell, $\delta P_{cell}/l_{cell}$ is the pressure gradient across the length, $l_{cell}$, of the cell, $A_{cell}$ is the cross - sectional area of the cell and $k$ is the permeability. The permeability units are microDarcies, where $1\ \mu D = 9.87 \times 10^{-13}\ m^2$. A full description of this technique is given in T 460 om-88.

## 3.2    Conventional Print Testing

### 3.2.1   Ink gloss / density

In the rotogravure process the printing image is engraved or etched into the surface of a "gravure cylinder" in the form of a regular pattern of cells. The cells are then filled by rotating the cylinder in a trough of ink, the excess ink being removed from the surface of the cylinder with a "doctor blade". Printing is achieved by passing the paper between the gravure cylinder and an impression roller under pressure, so that the ink in the cells is directly transferred to the paper. High quality rotogravure printing demands intimate contact between the paper and the ink in the cells in order to achieve good transfer of the ink. The factors which determine printability are those which influence the absorbency, smoothness, compressibility and flexibility of the paper. The gloss and density of the printed image are measured using a paper gloss meter and a Macbeth print densometer respectively in the solid black region of the print forme.

### 3.2.2 Ink tack test

This technique was developed recently within ECC Central R&D by Gane and Seyler. The development of tackiness of commercial offset inks on paper is dependent upon the pore structure and the wettability of the coating layer. Imbibition of the fluid phase of the ink controls the cohesive build within the ink layer. The complexity of ink transfer to paper and subsequent ink film separation is not dependent solely on ink cohesion with the paper surface. Full descriptions of ink transference have been made by Zang (1993), Bery and Loel (1992), and Aspler and Lepoutre (1991). Improved computer control systems for data aquisition and processing on the tack tester enables detailed analysis of ink setting with time. The initial rate of ink tack force development is related to the rapidity of imbibition by the uncoated or coated paper surface on initial contact with the ink. The micro-porosity and wettability of the coating are major contributing factors to rapid rise in ink tack force. A plateau in tack force values often develops at maximum observed tack force. This plateau is a combined measure defined predominantly by the adhesivity of the immobilised ink layer in contact with the coating surface and the cohesivity within the ink contained in the surface voidage of the coating as a function of bulk cohesion of the ink layer. The ink tack decay is dependent upon the drying of the ink at longer time scales and is seen as an increase in affinity of the ink surface for the paper surface. The time taken for this decay to occur is dependent on the total "available" pore volume for the uptake of ink fluid. A full description of this method has been given by Gane and Seyler (1994).

### *3.3    Microscopy*

### 3.3.1   Scanning Electron Microscopy (SEM)

A Jeol JSM - 840A Scanning Electron Microscope was used for this work. This instrument was used to provide a means of photographing the particles of the pigment samples in order to give some visual indication of their respective sizes. The basics of

electron microscopy have been fully documented by others, e.g. Edington (1990). An electron microscope uses a series of magnetic lenses to focus an electron beam which is accelerated, by a high potential, through the specimen in vacuo. The main features of a modern microscope are given in Appendix 2. Micrographs of the various pigments are included at relevant points in this dissertation.

### 3.3.2 Environmental Scanning Electron Microscopy (ESEM)

This instrument is very similar to a conventional SEM, but it allows samples to be examined in gaseous environments at pressures up to 2.7 Kpa (20 Torr). This is made possible by a combination of a differentially pumped vacuum system, small travel distances for the electron beam, and a biased specimen current detector known as a gaseous detector device (GSD). Resolution in ESEM is near that for a conventional SEM, i.e. about 5 nm. Exterior surfaces of hydrated samples can be examined without freezing, fracturing or metal coating (Sheehan and Scriven, 1991). This type of instrument was used to generate images of the selected paper samples. These photomicrographs were kindly prepared by the staff at SCA Graphic Research.

### 3.3.3 Optical microscopy - measurement of coating thickness

The thickness of a base sheet is not uniform, and as expected the coating layer of a coated paper will also vary in thickness. The overall sheet thickness (basepaper plus coating layer) is traditionally measured to reasonable accuracy using a bench-top caliper instrument with a measuring anvil area of circa 1 $cm^2$. The roughness of the paper surface is, however, on a smaller scale than the scale of the measuring anvil and hence it preferentially measures the maximum thickness of the sheet, and does not take into account the variations in thickness. In this study we need to know accurately the mean paper thickness. Recently, a technique for measuring $z$-direction thickness variation of samples has been developed by the Paper Science Research Group at ECC International. This new

technique, devised by Gane, Hooper and Baumeister (1991), involves the use of optical microscopy and image analysis. A Polyvar Met Optical Microscope has been used to examine the cross sections of these paper samples. The image quality obtained from the optical microscope depends critically on the optimised adjustment of the microscope, the optical properties of the specimen and the method and quality of specimen preparation. Image quality is most important for detection of features by the image analysis software. At ECCI, a Quantimet image analysis system is installed and is used for this work. The aim is to achieve a high contrast, high resolution image when viewed with incident bright field illumination. The samples to be examined in this way must first be embedded in a suitable support medium and then sectioned using a microtome. Epoxy resin was found to be the most suitable for this work. The microtomed samples are sputtered with a thin layer of gold to assist optical contrast. The cross sectional image is digitised and the profiles of the basepaper are measured and stored for each field of view. 30 fields of view are measured for each sample, that is 3840 measurements spaced at 2 $\mu$m intervals covering a distance of approximately 7.5 mm. The data for each of the paper samples selected from the calendering trial were plotted as the frequency of occurrence of base paper thickness against basepaper thickness size (Chapter 7).

### 3.4    *Particle size measurement*

### 3.4.1    Micromeritics Sedigraph

The particle size distributions of the calcium carbonate slurries and the kaolin slurries were evaluated using a Micromeritics Sedigraph. This X - ray sedimentation technique uses the X - ray density as a proportional measure of the weight of pigment particles in the beam. Stokes' Law is used to estimate the *equivalent spherical diameters* of particles which are in the beam at any moment in time. The technique is considered valid for particles smaller

than 10 μm diameter, but larger than 0.25 μm diameter. The results are plotted out as a cumulative curve of the weight of particles finer than a particular equivalent spherical diameter. A full review of this technique is given in the Micromeritics Sedigraph Users Manual and in Allen (1989).

### 3.4.2 Malvern Zetasizer

The Zetasizer (Model 4) can measure the size of particles with diameters in the range from 5 nm to 5000 nm, using the method of photon correlation spectroscopy (PCS). Particles in this size range are often called *colloids* and one of their characteristics is that they are in constant random thermal (Brownian) motion. This motion causes the intensity of light scattered from the particles to vary with time. Large particles move more slowly than small particles, so that the rate of variation in intensity of light scattered from them is slower. Photon correlation spectroscopy uses the rate of change of these light fluctuations to determine the size distribution of the particles scattering light. This technique was used to measure accurately the particle size of the plastic pigments used in this study because the Sedigraph was unable to determine the size of these spheres that had densities similar to that of water. A full description of the Operational procedure the Zetasizer is given in the Malvern Instruments Zetasizer 4 Users Manual.

### *3.5 X- ray diffraction*

The orientation of kaolin pigment particles in the paper samples has been studied using X-ray diffraction. A full description of this technique is given in Appendix 3.

Diffraction data were collected using a Philips PW 1825 X-ray generator with a copper anode long fine focus X-ray tube and a PW 1050 vertical goniometer, in which the paper samples were mounted. The collimating geometry consisted of a 1° divergence slit and a

0.3 mm receiving slit. Intensities were measured using a diffracted beam graphite monochromator and proportional counter. X-ray tube power was set to 40 kV at 45 mA.

For the (001) peak, scans were made over the angle range $11.00° < 2\theta < 13.26°$ in 0.02° steps with a counting time of 20 s per step. For the less intense (020) peak, a much longer counting time of 200 s per step was used with scans made over the range $19.00° < 2\theta < 20.50°$. Total measurement time for each sample amounted to around 5 hours. Samples with an irradiated area of 2 cm² were spun in the plane of the paper during data collection to eliminate any influence of directionality.

Single measurements were made on each of the paper samples and the peak areas for the 001 and 020 reflections were measured. The larger the A(020) / A(001) ratio, the greater the degree of randomness. The 020 lattice planes are inclined at about 88° to the basal 001 planes. The relative error in the degree of orientation due to counting statistics is about 3% - 4 %. The X-ray results are discussed in Chapter 7.

### 3.6    Oil absorption test

The oil absorption test was used by Gate and Windle (1973) to determine the porosity of thin porous samples. This test relies upon the principle that when a low viscosity oil is placed on the surface of a coating it will penetrate the pore space which is connected to the external surface of the sample. In the test, droplets of oil were placed onto the surface of a coating and allowed to spread to form a continuous film. The oil was left on the surface of the coating for 5 minutes. After this time, the excess oil was removed by gentle wiping. Removal of the oil reduced the "wet" gloss of the surface until a point at which the gloss decrease plateaued. At this point the weight of the sample remained constant. Knowing the weight of sample before and after application of the oil, it was possible to calculate the

weight of oil that had been imbibed into the coating. The density of the oil being known, permitted the volume of the imbibed oil to be calculated. This volume was taken to be equal to the void volume of the coating that was accessible to the oil, of known viscosity, by capillary uptake. This oil-accessible void volume may be converted into a percentage porosity if the volume of the solid phase of the porous structure into which the oil has penetrated can be calculated. The oil absorption results are discussed in Chapter 7.

## 3.7 Mercury Porosimetry

Washburn (1921a,b) proposed that mercury injection into a porous material could be used to measure pore size distributions. This idea was first developed by Ritter and Drake (1945) when they developed a pressure porosimeter for the determination of complete macro-pore size distributions. As is normal in this field, the Washburn (or Laplace) equation is used in the present work to relate throat size to mercury pressure:

$$d = -\frac{4\gamma \cos\theta}{P} \qquad (2)$$

where $\gamma$ is the interfacial tension at the mercury surface, $P$ the applied pressure, $\theta$ the contact angle and $d$ the throat diameter.

Garboczi (1991) has suggested that the two main limitations of using a percolation algorithm based on the Washburn equation are, (i) that the throats are all considered to be cylindical, and (ii) that the mapping of the effective network derived from the mercury porosimetry curve is not the same as the real network. In a bulletin, the manufacturers of the porosimeter used in this work (Micromeritics), recommended that "the true value of the contact angle should be employed when it is to be known to be other than $130^{\circ}$ ". In an earlier study (Gate and Lyne, 1971) the advancing mercury / pigment surface contact angle was measured from profiles of sessile drops using a microscope fitted with a

goniophotometer eyepiece. These results indicated that a contact angle of $140^{\circ}$ would be appropriate for mineral coatings and this contact angle has been used throughout this work, but the measurement of contact angles on flat, external surfaces may be an inappropriate estimate for contact angles experienced by mercury in the pore space. It is also true that the contact angles may be different for paper (cellulose), pigment (clay or calcium carbonate), and binder (starch or latex).

The inter-facial tension, $\gamma$, at the mercury / mineral / nominal air interface was assumed to be 0.48 $Nm^{-1}$. Uncertainties in this value have been limited by the use of instrument grade mercury, the impurities in which were thought to be sufficiently dilute not to diffuse to the surface at an appreciable rate. If gaseous impurities are released by desorption from the solid phase of the sample then this would be seen as a prolonged time for outgassing the sample. This was not observed for any of the samples tested in this study. In 1949 Tolman reported that for micropores, there may be a depression in surface tension when the radius of curvature is very small (the Tolman effect). The Tolman effect is hard to estimate, but it has been suggested that it will only be significant at the smallest pore diameters, e.g. pore diameters corresponding to five mercury atom diameters (atomic diameter of mercury is 0.31 nm, Brown 1981). Therefore, the effect is only significant for pore diameters smaller than 1.55 nm, and this is smaller than the minimum pore diameter that can be sampled using the porosimeter described in this work.

It is widely accepted that the pore walls within "real" consolidated mineral pigment structures will not be perfectly smooth and will probably be rougher than the surface. The contact angle of mercury, $\theta$, on a rough porous surface is generally greater than that on a microscopically smooth surface. A review of some roughness theories is given by Good and Mikhail (1981).

Assuming a contact angle of 140°, and an inter-facial tension of 0.48 Nm$^{-1}$, as described above, equation (2) predicts that mercury will intrude voids with throat entries of 0.0072 μm at the upper experimental pressure limit of 207 MPa.

The mercury intrusion curve of a porous sample comprises measurements of the volume of mercury intruded against applied mercury pressure, $P$. The volume of mercury intruded is often converted to a percentage of the total void volume ( = 100% x volume intruded at pressure $P$ / volume intruded at highest attainable pressure), and the applied mercury pressure converted to a throat diameter via equation (2).

A Micromeritics 9320 porosimeter was used for the mercury porosimetry experiments reported in this study, Figure 5.
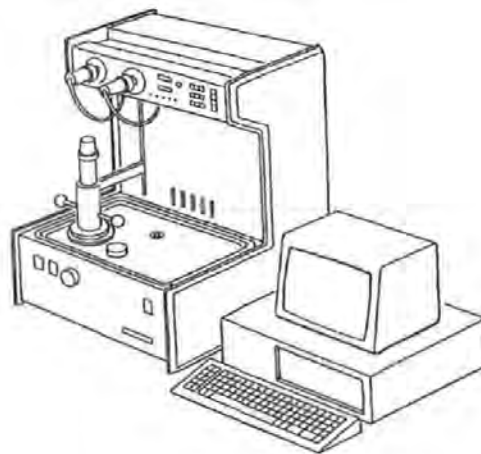


**Figure 5: Micromeritics 9320 mercury porosimeter**

A mercury porosimetry experiment entails the addition of a weighed amount of sample to a clean glass penetrometer. The penetrometer, Figure 6, is then sealed using Apezion grease, and installed in the low pressure port of the porosimeter.

**Figure 6: Glass penetrometer**

The vacuum system evacuates the porous sample to remove trapped gases, after which the sample is surrounded with mercury. The amount of mercury displaced by the sample allows calculation of the sample's bulk volume, $V_{bulk}$. Pressure is then applied to the mercury so that it intrudes into the sample through pores connected to the external surface up to a pressure equal to that of the atmosphere. The penetrometer is then removed from the low pressure port, weighed and inserted into a high pressure port. In the high pressure port the penetrometer is surrounded with silicone oil. This port is closed and trapped gases in the surrounding oil are bled from the system. The porosimeter is then set to increase the pressure step-wise to the maximum possible, using preset periods of equilibration time. In order to obtain results of sufficient accuracy for the present work, it was necessary to impose two important restrictions on the operating conditions of this instrument, which are also relevant when using other porosimeters. Firstly, it was found that if the mercury pressure was increased too quickly, equilibrium was not achieved at each step. As a consequence, when the applied pressure was decreased from its maximum value to measure the hysteresis curve,

the intruded volume initially continued to increase. To avoid this, the pressure had to be held for at least one minute at each pressure setting. Therefore, to be certain of complete equilibrium, the porosimeter was in fact held at each applied pressure for four minutes before measuring the intruded volume and changing the pressure. Secondly, it was found that the expansion characteristics of the glass porosimeters could change between runs, and therefore it was impossible to provide a totally reliable value of the blank volume, $\delta V_{blank}$, appertaining to a particular experimental run. Lee and Maskell (1973) reported problems with blank runs on a Micromeritics 903-1 porosimeter, and overcame them by means of a consideration of the precise geometry of the penetrometer, and the subsequent matching of empirical factors to experiment. In practice, sufficient accuracy was obtained by using sample weights large enough such that $\delta V_{blank}$ was less than 10% of the intruded volume at the highest pressure, and by remeasuring, $\delta V_{blank}$ for a particular penetrometer after every few runs. A full discussion of the necessary corrections to the mercury porosimetry data is given in Chapter 5. The fully corrected data were then input to the Pore-Cor computer program so that pore level properties such as air permeability and tortuosity could be calculated for the 3D-structures which had the same porosity and pore size distribution as the experimental data.

## 3.8    Liquid Porosimetry

Liquid porosimetry is another technique for determining the pore volume distribution within a macroporous solid. It is similar to mercury porosimetry in its use of the Washburn equation. The technique of liquid porosimetry was first described by Miller and Tyomkin (1986, 1994) and may be used with a variety of probe liquids (e.g. wetting and non-wetting). It may also be used to predict the absorption and retention characteristics of the sample material. According to the Washburn equation (equation 2), if there is a change in

the external pressure on a non-wetting fluid surrounding a porous solid, then filling or emptying of the pore space will start with the largest pore and proceed to the smallest pores. The technique of liquid porosimetry was used in an extrusion mode for the paper samples in this study, i.e., liquid is forced out of the saturated porous network rather than into it. The working values of contact angle and surface tension of hexadecane on paper (cellulose) were quoted as $\theta = 0$ and $\gamma = 32$ mN.m$^{-1}$. The basic arrangement for extrusion porosimetry is illustrated in Figure 7.
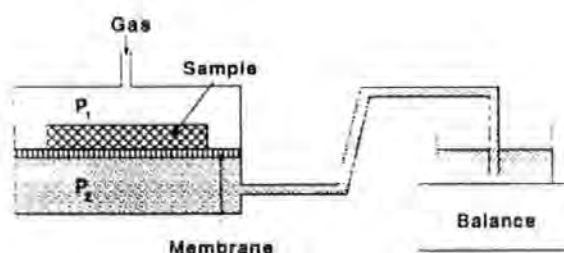


**Figure 7: Basic arrangement for the liquid porosimeter**

A presaturated paper specimen is placed on a microporous membrane upon a rigid porous plate. The gas pressure in the sample chamber is increased in steps, causing liquid to flow out of the sample through the largest pores first. A thermocouple sensor is installed in the sample chamber to monitor temperature changes. Even small temperature fluctuations can produce changes in density of the liquid which would cause error in the evaluation of the pore volume. The weight of liquid removed is monitored by a top-loading recording balance. In this way, each level of applied pressure (which determines the largest effective pore size that remains filled) is related to an increment of liquid mass. The readout of the thermocouple is fed to the computer and the recorded liquid mass changes are automatically corrected for any observed temperature drift.

To drain the pores in this step-wise manner requires very small increases in pressure over a narrow range which is slightly above atmospheric pressure. To achieve this, the chamber is pressurised by means of a computer controlled, reversible motor driven piston / cylinder arrangement which can produce the required changes in pressure to cover a pore diameter range from 6 μm to 1000 μm. The pressure is monitored by one of two transducers (a pair are used to maintain sufficient accuracy at both low and high pressures): the signal is fed to the computer which, through feedback logic, adjusts the piston position to set the target pressure almost instantly. The complete assembly is shown in Figure 8.
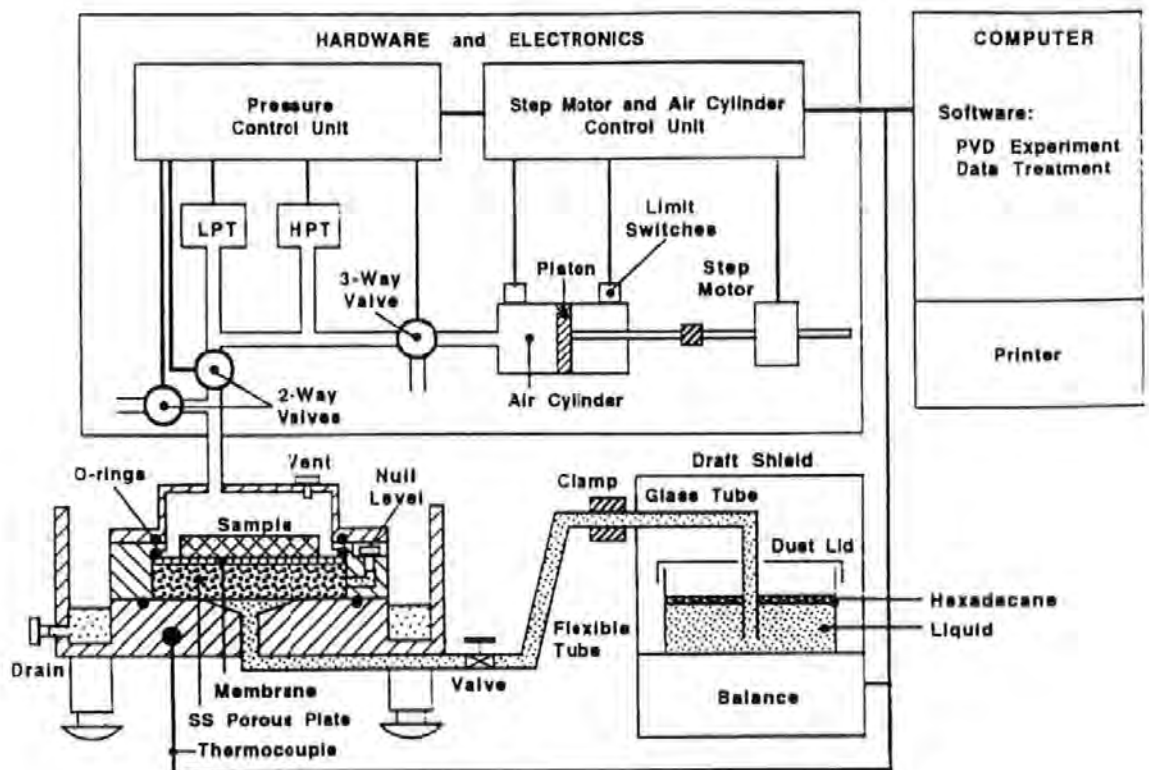


**Figure 8: The TRI Autoporosimeter for determining pore volume distribution**

By monitoring the balance output the computer that ensures equilibrium is reached prior to further pressurisation. This process is repeated for the whole pressure range. Although not used for this work, it is possible that when the highest applied pressure has been achieved, the program can act in reverse to perform a set of stepwise intrusions. Also if required,

multiple drainage / uptake cycles can be programmed to run automatically on the same sample. One of the important goals of this work was to minimise the problems associated with both types of porosimetry. These involved a range of experimental considerations for mercury porosimetry, and the minimisation of edge effects for both mercury and liquid porosimetry. For the liquid porosimetry it was found that the use of only a few sheets resulted in very small volumes of liquid extruded, whereas the use of many sheets resulted in liquid trapped between the inter-sheet spaces. Therefore the maximum precision and minimum edge effects involved choice of an intermediate number of sheets. The optimisation procedure and generation of a unique data set from the combination of both porosimetry data sets are discussed in Section 5.6 and the results are discussed in Section 7.4.

CHAPTER 4

## 4. THEORETICAL ASPECTS OF POROUS NETWORKS

### 4.1 Packing arrangements of spheres

The simplest packing arrangements are those for mono-sized spheres. There are three main

packing types of interest with monosized spheres; ordered, random loose and random

dense. An ordered packing has periodic structure that repeats over a specific small

distance. Random loose packing is represented by particles placed in a container without

agitation. In contrast, random dense packings are attained by agitating or vibrating a

random loose packing to achieve the maximum density. Random packings of hard spheres

have been the subject of considerable attention for many years, mainly due to their role in

understanding the structure of amorphous, porous and random materials. Mason (1971)

described random sphere packing in terms of "tetrahedral subunits". This approach gave

results which agreed with properties of randomly packed spheres and some capillary

properties to be estimated. A full review of sphere particle packing was made by German

(1989).

Leskinen (1987) has reviewed the theory of particle packing and porosity of bimodal

systems of spherical particles. Nolan and Kavanagh (1992) have described a computer

simulation which can pack hard spheres randomly and this work has been (1993) for

computer simulations of log-normal distributions of spheres. Recently (1994), they have

investigated the size distributions of interstices in random packings of spheres of log-

normal size distributions. Even more recently (1995), they have investigated random

packing of nonspherical particles by computer simulation. They claim to have found

31

excellent agreement between their simulation results and experimental values of the packing density for random close packing.

## 4.2    Packing of mineral pigments in coating formulations.

Coating formulations have evolved and developed in response to ever more stringent requirements with respect to both paper coating and the handling properties of the coating. Coating colours are aqueous dispersions containing two basic ingredients, pigments and binders. They range from 50 wt.% to more than 70 wt.% in total solids. Kaolin is the most common pigment, but other pigments include calcium carbonate and plastic pigments. The plastic pigments (polystyrene) are used in combination with other pigments to provide high gloss. The purpose of the binder (or adhesive) is to cement the pigment particles firmly to the paper surface and each other. The final dried coating is not a continuous film but a porous structure of pigment particles cemented together at their points of contact. If too much binder is used, the voids begin to fill and some light scattering ability is lost.

The drying of clay-latex coatings has been studied by Watanabe and Lepoutre (1982). In the first phase of the process, water evaporates or is drawn from a dispersion in which clay and latex particles can move freely. At the First Critical Concentration, free motion ceases and a bulky and deformable three dimensional network forms. The wet coating then shrinks under the increasing capillary forces until, at the Second Critical Concentration, all structural changes stop. From this time on, capillaries empty until drying is completed. Thus the dried coating is not a continuous film, but a porous structure of pigment particles bound together at their points of contact. The particle diameters of the mineral pigments in the coating range from  around 0.01 μm to 10 μm ($10^{-8}$ - $10^{-5}$ m), and the synthetic pigments, and latex particles prior to film formation, are in the 0.1 μm to 1 μm diameter range. The voids within the dried paper coating are therefore in a similar size range. The

structure, size and inter-connectivity of these voids affects both the optical properties of the paper (Alince and Lepoutre (1980a), Climpson and Taylor (1976), Lepoutre and Rezanowich (1977), Stanislawska and Lepoutre (1995)) and the way in which ink sets on the paper during the very short time period allowed in modern high-speed printing presses (Gane and Seyler 1994). The void structure of the surface has been studied directly by profilometry of the surface and electron microscopy of vertical sections through resin-embedded samples, Kent, Climpson, Gane, Coggon and Hooper (1986). Other studies have involved the measurement of the change in reflectance of an imbibed ink drop with time, Larrondo and St-Amour (1992, 1995), Ranger (1976). Hamlen and Scriven (1991), have developed regular and irregular pore models of fibre sheets and used them in the study of the variation of permeability on compression. Pan, Davis and Scriven (1995) have also developed a six-coordinated interconnected network for the modelling of moisture and binder migration in drying paper coatings.

## 4.3    Packing of paper fibres with pigment fillers to form paper.

Paper is formed on a fine screen from an aqueous suspension of cellulose fibres (pulp) and fillers known as *mineral pigments*. The mineral pigments are usually made from high brightness calcite (ground marble or limestone) or china clay (kaolin) which has undergone various grinding and separation processes. To improve gloss, shade, opacity and printing characteristics, paper is often coated with a *coating colour* (Section 4.2).

## 4.4    Pore volume distribution and hysteresis in mercury porosimetry

The mercury intrusion curve of a porous sample comprises measurements of the volume of mercury intruded, $V$, against applied pressure. The applied pressure may be converted to a

throat diameter and this intrusion curve is typically sigmoid in shape and traditionally it has been assumed that the distribution of throat sizes (not distinguished from pore sizes) can be equated to the first derivative of an intrusion curve $dV / dd$. This results in a distribution which has a peak at the point on the intrusion curve which has the highest gradient i.e. the point of inflection. The Washburn-derived throat diameter at this point is often described as the characteristic throat diameter. However, the use of the first derivative is only valid for a porous solid which comprises a bundle of non-interconnecting capillary tubes, which can be tortuous, but which must be of constant diameter along their length. Porosimeter control software usually incorporates the first derivative assumption and such software sometimes extends this assumption to derive a particle size distribution for the solid. The Pore-Cor model does not use this capillary bundle assumption, but as stated earlier uses a percolation algorithm. The advantage of a percolation algorithm is that it takes into account of the fact that a large pore may be "shielded" from mercury intrusion at the pressure predicted by the Washburn equation by small surrounding throats.

At a sufficiently high applied pressure, mercury intrudes all of the accessible pore space within a sample. However, if the applied pressure is then decreased, more mercury stays in the sample at any particular pressure than the amount specified by the intrusion curve, and there is a residual amount of mercury trapped even at the lowest possible applied pressure. These effects are referred to as hysteresis. There are various causes of the hysteresis between intrusion and extrusion curves in mercury porosimetry, which are now discussed.

### 4.4.1   Structural hysteresis in individual pore and throat chains

On intrusion of non-wetting phase, such as mercury, the throat radius controls the pressure at which that throat is intruded. However, secondary imbibition, the emptying of mercury from pores, is controlled by the pore size. This can be explained by considering Figure 9, which shows a series of cylindrical pores and throats in a single chain.
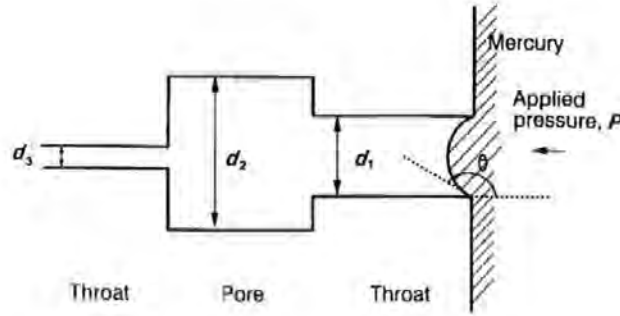


**Figure 9: One-dimensional pore and throat network**

The network is exposed to mercury, to which a pressure $P$ is applied. For simplicity in this explanation, we assume that equation (2) may be simplified to:

$$d = \frac{1470}{P} \qquad (3)$$

in which $d$ is in micrometres and $P$ is in kiloPascals.   The pressure is increased until it exceeds $1470/d_1$, whereupon it overcomes the capillary forces within the throat of diameter $d_1$. It then fills this throat, and also the pore of diameter $d_2$ in which the capillary resistance is less. After a further increase in applied pressure to greater than $1470/d_3$, the throat of diameter $d_3$ will fill.

Subsequent decrease of the applied pressure $P$ causes withdrawal of the mercury and imbibition of the nominal wetting phase. As the pressure decreases below $1470/d_3$, the throat of diameter $d_3$ will empty back into the pore, and an equivalent amount will extrude to the outer surface. Next to empty is the pore of diameter $d_2$. This empties when $P$

becomes less than $1470/d_2$, whereas it fills at the higher pressure of $1470/d_1$; hence hysteresis occurs.

### 4.4.2 Snap-off

There is another complication which occurs during withdrawal of the mercury. If $d_2$ is very much larger than $d_1$, it is difficult for the mercury to re-adjust its shape to extrude from the large pore through the narrow throat. Wardlaw and McKellar (1981) have photographed this effect in glass micro-models of pore and throat chains, with trapping occurring for values of the pore size : throat diameter ratio $R = d_2/d_1 > 6$.

The reasons for this $R$ dependent trapping effect are given a possible explanation by Dawe, (1978). When an interface travels though an irregularly shaped channel, the shape of its meniscus has to adopt non-equilibrium shapes. However the meniscus is always trying to achieve its minimum energy configuration, which can be achieved by a sudden change in shape. The liquid therefore does not flow uniformly but moves between pores in jumps known as Haines jumps. For a certain value of $R$ this attainment of minimum energy may result in 'snap-off' of the mercury column. Wetting phase, compressed and trapped in surface undulations or micro-pores during imbibition, can re-expand and act as the seed of such snap-off. Li and Wardlaw (1986a, 1986b) have also studied other pore and throat arrangements of various shapes using glass micro-models, explaining the observed effects in terms of theories involving geometry and wetting behaviour.

Snap-off, and consequent trapping, can also occur because of the structure of an interconnected network. For non-wetting phase to empty there must be a continuous

unbroken line of non-wetting phase to the outside surface. Consider the two-dimensional network shown in Figure 10:
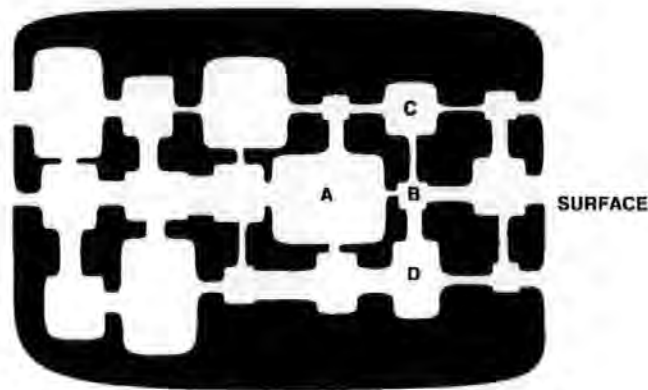


**Figure 10: A two-dimensional pore and throat network**

By the time the pressure has dropped for pore A to empty, its neighbouring pores (B, C and D), will have already emptied as they are smaller. Therefore there is no inter-connected route for mercury to escape from A to the surface, and it will remain trapped. In three-dimensional networks, as presented in this work, the routes available for escape are more complicated, and the trapping effects more subtle than those shown in Figure 10.

### 4.4.3 Correlation of pore and throat sizes

It is evident from the preceding discussion that the relative sizes of adjacent pores and throats affect intrusion and withdrawal. Therefore if these sizes are correlated - i.e. there are regions of large pores and throats together, or small pores and throats together, either as clusters or bands - there is likely to be a consequent effect on intrusion and hysteresis. Payatakes and Constantinindes (1989) have found that pore size : throat diameter correlation, with no pore size : pore size correlation in the sense of local clustering of pores of similar size, has a weak effect on the mercury intrusion. They find that pore size clustering together with pore size : throat diameter correlation has a strong effect on the curves, spreading them over a wider range of pressures. Li *et al.* (1986) and Li and

Wardlaw (1990) and Wardlaw (1990) demonstrate analytically, for the case of a linear throat size distribution, how correlation effects reduce shielding, thus causing intrusion at lower pressure and a reduction of entrapment during secondary imbibition. Wardlaw (1990), also shows this effect in multiple intrusion / extrusion scanning loops.

### 4.4.4 Dead-end pores

Structural hysteresis is also caused by dead-end or 'ink bottle' pores, which are pores with only one throat. Indeed, in many fields, dead-end pores are considered to be the only cause of hysteresis. During intrusion, the dead-end pores fill with non-wetting phase. During imbibition of the wetting phase, a situation arises where wetting phase has reached the throat of a dead-end pore. However, it can only enter the dead-end pore by surface flow down the walls of the throat accompanied by withdrawal of the non-wetting phase through the middle of the throat. This process does not usually occur, and therefore dead-end pores cause trapping of the non-wetting phase. The percentage of dead-end pores increases as the coordination number decreases, and hence the relative effect of dead-end pores rises with decreasing connectivity.

### 4.4.5 Contact angle hysteresis

There is much evidence in the literature for contact angle hysteresis, i.e. a difference in contact angle dependent on whether the mercury is advancing during intrusion, or receding during wetting phase imbibition, Bell, van Brakel and Heerjtes (1981), Kloubek (1981). The angle commonly used in the analysis of mercury porosimetry curves is 140 ° for both the advancing and receding angle. However, the magnitude of the contact angle has a substantial effect in the analysis of mercury intrusion and extrusion by means of the Washburn equation. Van Brakel, Modry and Svata (1981) have shown in principle that

irreversible penetration of mercury may be caused solely by contact angle hysteresis. A possible explanation of contact angle hysteresis is given by Wardlaw and Taylor (1976). The mercury intruded into an advancing mercury meniscus tends to clean the meniscus because of its expanding surface. On withdrawal, impurities can gather at the meniscus because of its contraction. It is well known from laboratory experiments using the tilting plate method for contact angle measurement, Shaw, (1986) that hysteresis is caused by impurities in the liquid, or roughness of the surface which the liquid is advancing or receding over.

There are many different estimates in the literature of the magnitude of contact angles, which have been summarised by Good and Mikhail (1981). Advancing angles of 180 $^o$ have been quoted for mercury in sandstones, whereas Dunmore and Schols (1979) and Kloubek (1981) found an advancing angle of 138.4 $^o$ and a receding angle of 127.4 $^o$ on smooth quartz.

# CHAPTER 5

## 5. NEWLY ADVANCED OR DEVELOPED EXPERIMENTAL TECHNIQUES

### 5.1 Overview

In this work we describe the use of mercury porosimetry for the characterisation of the pore structure of papers and of consolidated pigment coatings, i.e. the measurement of the volume of mercury injected and withdrawn from a sample at a range of increasing and then decreasing applied pressures. Mercury porosimetry has been little used for the study of paper coatings, and in this work we overcome two limitations of the method. The first is that some of our samples are compressible. The compressibility may be related to mineral particle inter- and/or intra-compaction, the compression of the latex binder, or, in the case of the synthetic pigments, to the compression or collapse of the polystyrene spheres. A new method for compensating for these effects is presented, which also provides an important new method of measuring the compressibility of just the solid phase of a porous sample rather than of the porous matrix as a whole. The second limitation is that the traditional interpretation of mercury porosimetry measurements is based on a bundle of tortuous capillary tubes (Yamazaki and Munakata (1993)), and does not allow for the fact that small void spaces, or *throats*, can shield larger void spaces, *pores*, from injection by mercury within a three-dimensional interconnected network. In this project measurements have been interpreted by means of a computer modelling package known as 'Pore-Cor' (Pore-level properties Correlator). Pore-Cor does take shielding effects into account.

A new technique of Liquid Porosimetry was used to evaluate the porosity and pore size distribution of paper samples. A unique feature of this work is that for the first time it has been shown that two porosimetric techniques which measure overlapping pore size distributions may be combined to give a better indication of the total pore size distribution.

40

## 5.2    *Correction terms for incompressible samples*

Various corrections must be applied to mercury porosimeter measurements to obtain a true measure of the increase of intruded volume with pressure. The approach which we describe in this section and in Section 5.3 is an extension of that described by Cook and Hover for concrete (1993).

The intruded mercury volume reading, $V_{obs}$, observed during a mercury porosimetry experiment is not only a measure of the volume of intrusion into the sample, $V_{int}$, but also contains significant volumes corresponding to the expansion of the porosimeter chamber or *penetrometer*, $dV_{pen}$, and the compression of the mercury $dV_{Hg}$ :

$$V_{obs} = V_{int} + dV_{pen} + dV_{Hg} \qquad (4)$$

(Any term such as the mercury compression, $dV_{Hg}$, or sample compression, which makes a positive contribution to the observed volume, $V_{obs}$, is given a positive numerical value. d denotes a small correction to a larger term.) The mercury also expands because of heat transfer from the pressurising fluid (oil), but we assume that this effect is the same for the sample experiment as for the blank experiment, described below, and therefore that the resultant effect is zero.

INTRUDED VOLUME / cm3
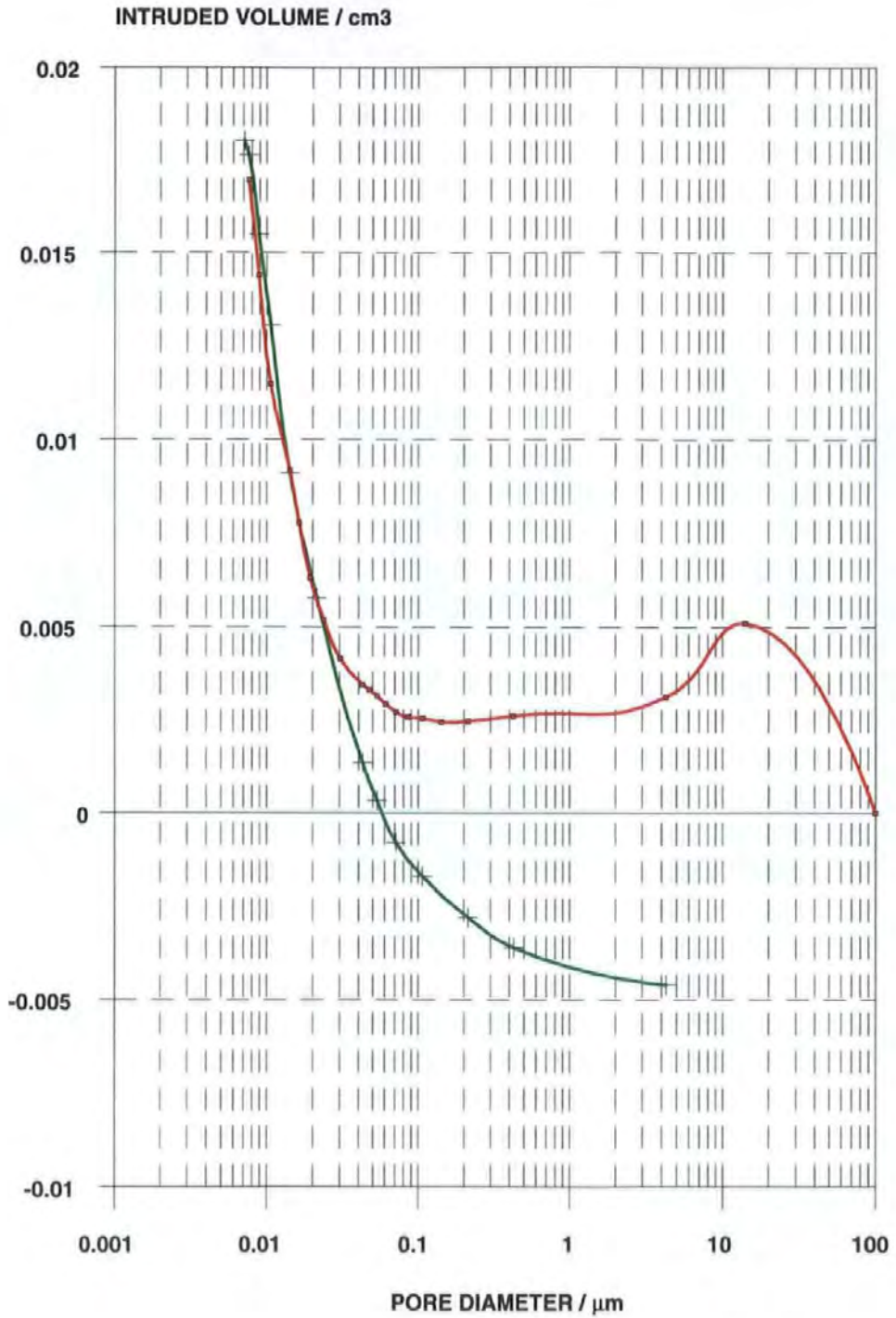


**Figure 11: Mercury porosimeter data for a typical blank run**

A *blank* experiment is one carried out under the same temperature and pressure conditions, but with no sample in the penetrometer. In Figure 11, the red line indicates the volumes measured whilst increasing the applied pressure, whilst the green line indicates the measured

volumes when the pressure was decreased. The volume, $V^1_{blank}$, of mercury used in the blank experiment is equal to the volume of the penetrometer, $V^1_{pen}$, both at one atmosphere pressure:

$$V^1_{blank} = V^1_{pen} \qquad (5)$$

(Superscripts are used to denote the value of a particular variable at a specified pressure.)

The change in the blank volume reading, $dV_{blank}$, is taken as zero at the lowest experimentally attainable applied pressure $P$. Increases in $dV_{blank}$ with pressure are caused by the compression, $dV_{Hgpen}$, of the volume of mercury needed to fill the empty penetrometer, and increases in the available volume, $dV_{pen}$, of the penetrometer due to expansion of the glass chamber:

$$dV_{blank} = dV_{Hgpen} + dV_{pen} \qquad (6)$$

When a sample is mounted in the penetrometer, it displaces a volume of mercury, $V^1_{Hgbulk}$, equal to the sample bulk volume, $V^1_{bulk}$, at 1 atmosphere pressure. The penetrometer is loaded with mercury to the same calibration mark as for the blank experiment, and thus the total volume of mercury, $V^1_{Hg}$, now used in the experiment is

$$V^1_{Hg} = V^1_{Hgpen} - V^1_{Hgbulk} \qquad (7)$$

The same relationship holds for the mercury expansion:

$$dV_{Hg} = dV_{Hgpen} - dV_{Hgbulk} \qquad (8)$$

Eqs (4), (6) and (8) can be combined to yield:

$$V_{obs} = V_{int} + dV_{blank} - dV_{Hgbulk} \qquad (9)$$

The compression, $dV_{Hgbulk}$, of the additional mercury volume in the blank experiment can be related to its volume, $V^1_{bulk}$, at atmospheric pressure by use of a form of the Tait equation (Cook and Hover (1993), Smithwick (1982)), which gives an experimentally derived expression for the compression of mercury, equivalent to a mercury compressibility of 0.40 x $10^{-10}$ $Pa^{-1}$:

$$dV_{Hgbulk} = 0.175 (V^1_{bulk}) \log_{10}(1 + P/1820) \qquad (10)$$

in which $P$ is in MPa (1820 MPa = 264,000 psi). (Note that equation (8) has the wrong asymptote as $P \rightarrow \infty$, but is correct for the smaller pressure changes, and hence small relative compressions, considered here.)

The working equation for incompressible samples may, therefore, be derived from equations (9) and (10):

$$V_{int} = V_{obs} - dV_{blank} + 0.175 (V^1_{bulk}) \log_{10}(1 + P/1820) \qquad (11)$$

An example of this correction is illustrated with reference to the mercury porosimetry data for the consolidated sample of Carbital 90 (C90), Figure 12.
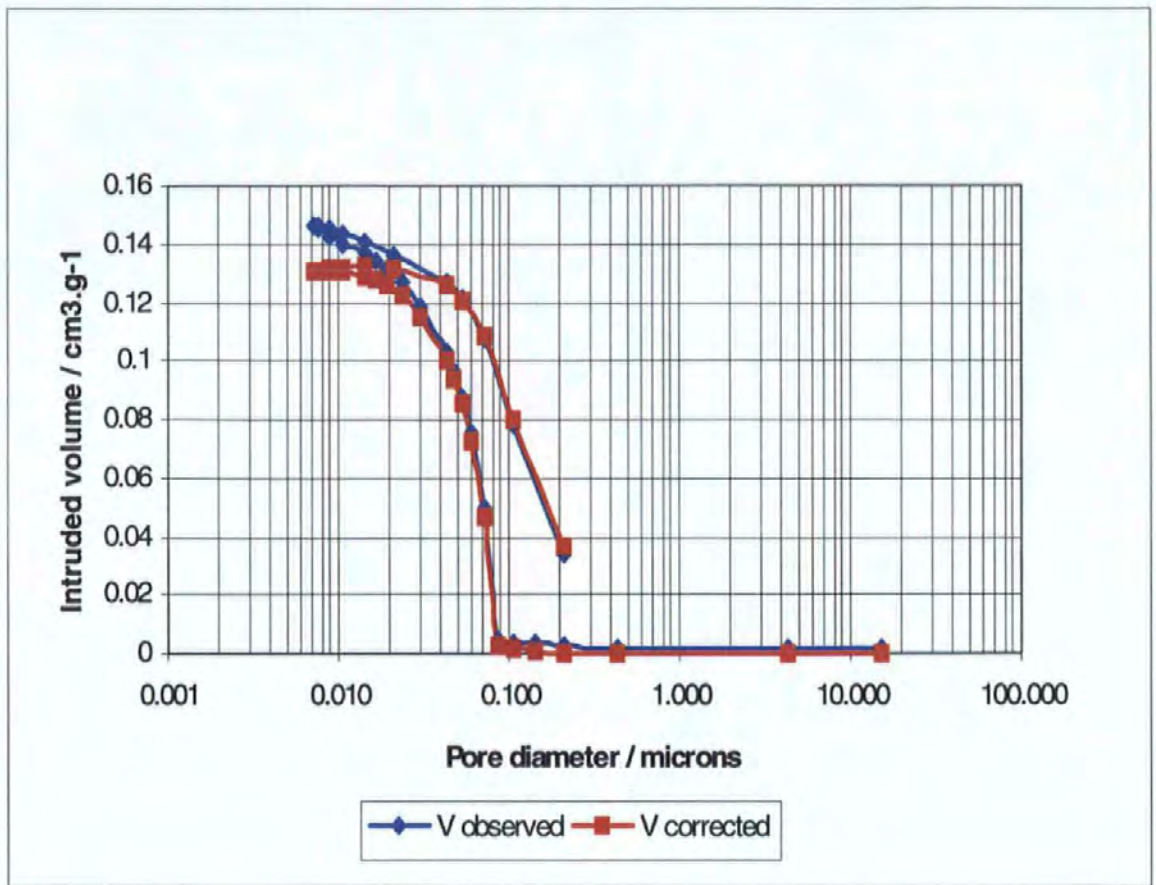
**Figure 12: Example of uncorrected and corrected data**

## 5.3    *Corrections for compressible samples*

Mercury at a high applied pressure will not only intrude a porous compressible sample, but also cause it to compress by an amount $dV_{sample}$. Compression effects typically become important above pressures of 40 MPa (at which pressure mercury penetrates throats with diameters down to 0.04 μm), and cause an increase in apparent intruded volume. For compressible samples, equation (9) becomes:

$$V_{obs} = V_{int} + dV_{blank} - dV_{Hgbulk} + dV_{sample} \qquad (12)$$

where $dV_{sample}$ is the (positive) increase in observed mercury volume caused by the compression of the sample.

The compressibility $\psi_{ss}$ of a homogeneous, continuous solid sample may be expressed in terms of its bulk modulus $M_{ss}$:

$$M_{ss} = \frac{1}{\psi_{ss}} = dP \left/ \left( \frac{-dV_{ss}}{V_{ss}} \right) \right. \tag{13}$$

(For an incompressible sample, $\psi_{ss}$ is zero, and $M_{ss}$ is infinite.) However, the compression of a porous sample by intruding mercury is more complicated. If the mercury entirely surrounds the continuous solid phase, it will compress it according to equation (13) above. This type of compression will occur above a pressure $P^z$ (the *zero void pressure*) at which all the accessible void space has been intruded by mercury, up to the maximum experimentally attainable applied pressure $P^{max}$ provided that no other changes in the sample are induced. Increasing the applied mercury pressure $P$ above $P^z$ causes the continuous solid phase of the porous sample to compress from volume $V^z_{ss}$ to a volume $(V^z_{ss} - dV_{ss})$, and the apparent volume of mercury intruded to increase by an amount $dV_{ss}$. Integrating equation (13) to find $dV_{ss}$:

$$\int_{P^z}^{P} dP = M_{ss} \int_{V^z_{ss}}^{V^z_{ss} - \delta V_{ss}} \frac{dV_{ss}}{V_{ss}} \tag{14}$$

and thus

$$\delta V_{ss} = V^z_{ss} \left( 1 - \exp\left[ \frac{(P^z - P)}{M_{ss}} \right] \right) \tag{15}$$

The zero void pressure $P^z$ may be identified from experimental curves as the point above which the corrected intrusion curve continues to indicate an increase in intruded mercury volume, but the extrusion curve, measured during subsequent pressure decrease, is identical to the intrusion curve. The coincidence of the two curves indicates an absence of mercury

trapping, and therefore demonstrates that the only cause of the corrected mercury volume increase, $dV_{sample}$, is compression of the continuous solid phase of the sample. (Incompressible samples show no increase in mercury volume above $P^z$.) Thus,

$$\text{for } P > P^z, \quad dV_{sample} = dV_{ss} \text{ , and } \frac{dV_{int}}{dP} = 0 \qquad (16)$$

However, at applied mercury pressures below $P^z$, there are unintruded voids in the sample, and the sample can undergo an additional type of compression, $dV_{su}$, because of compression into this void space (Warren and Nashner (1976)). Both this compression into the void space and the compression of the solid phase contribute to the increase, $dV_{sample}$, in the observed intruded volume of mercury, and the effects are impossible to distinguish as they proceed:

$$\text{for } P < P^z, \quad dV_{sample} = dV_{ss} + dV_{su} \qquad (17)$$

Thus we are compelled to assume that the compression of the solid into unintruded void space, $dV_{su}$, equation (17), is negligible, an approximation which is also implicit in the work of Cook and Hover (1993).

The maximum compressions of the samples in the present work are mostly less than 1% of the sample bulk volume, rising to 6% for the most compressible sample. For these small relative compressions, the compression may be related to the volume, $V^1_{ss}$, of the solid phase at atmospheric pressure $P^1$, to a level of approximation much better than the experimental uncertainty. Thus equation (14) becomes:

$$\int_{P^1}^{P} dP \approx M_{ss} \int_{V^1_{ss}}^{V^1_{ss} - \delta V_{ss}} \frac{dV_{ss}}{V_{ss}} \qquad (18)$$

Also at one atmosphere pressure the solid state volume is, to a similarly good approximation, calculable from the bulk volume and the porosity $\phi$:

$$V^1_{ss} = V^1_{bulk} \cdot (1 - \phi^1) \tag{19}$$

Applying these approximations to equation (15):

$$\delta V_{sample} = V^1_{bulk} \, (1 - \phi^1) \left( 1 - \exp\left[ \frac{(P^1 - P)}{M_{ss}} \right] \right) \tag{20}$$

The working equation for compressible samples is then derived from eqs (8), (10) and (20):

$$V_{int} = V_{obs} - dV_{blank} + \left[ 0.175(V^1_{bulk}) \, \log_{10}(1 + P/1820) \right] - V^1_{bulk} \, (1 - \phi^1) \left( 1 - \exp\left[ \frac{(P^1 - P)}{M_{ss}} \right] \right)$$

$$\tag{21}$$

$\phi^1$ can be determined as described in Section 5.5 below. Thus all the terms on the right of equation (21) can be measured, except for $M_{ss}$ which can be found by simultaneously satisfying equation (16) and equation (21).

## 5.4    Correction terms for samples with unintrudable compressible space

In this work, we measure and interpret the mercury porosimetry curves of two types of samples containing unintrudable compressible space. The first type are samples which are microcrystalline - i.e the particles contain mosaics of crystals in close proximity to each other, with imperfections and discontinuities between the crystals which are much too small to be intruded by mercury, but which nevertheless contribute to the compressibility of the

48

sample, Deer, Howie and Zussman (1980). If the sample is ground to produce finer particles, the grinding causes cleavages at these microcrystal boundaries. The smaller particles thus contain relatively fewer microcrystal boundaries, and are less compressible, Shinohara (1990).

The second type of unintrudable compressible space occurs in the centres of the hollow plastic spheres of the Ropaque plastic pigment. At a sufficently high applied mercury pressure, which is above $P^z$, the spheres collapse irreversibly.

## 5.5    *Measurement of porosity*

If no correction is made for the compressibility of a sample, its porosity $\phi$ appears to increase with pressure because more mercury is intruded than expected. Conversely, if a proper correction has been made for compressibility, the corrected porosities at 1 atmosphere pressure and at elevated pressure should be the same, and their similarity can be used as a verification of the correction procedure.

At atmospheric pressure

$$\phi^1 = (V^1_{bulk} - V^1_{solid}) / V^1_{bulk} \qquad (22)$$

where $V^1_{solid}$ is the volume of the solid phase at one atmosphere pressure, calculated from the known composition and densities of the sample constituents by means of a simple relationship which for a coating colour is:

$$V^1_{solid} = \frac{m_{sample}}{(w_{pigment} + w_{binder})} \left( \frac{w_{pigment}}{\rho_{pigment}} + \frac{w_{binder}}{\rho_{binder}} \right) \qquad (23)$$

where $m_{sample}$ is the mass of the sample, $w$ the weights of pigment and binder, and $\rho$ the densities. As mentioned previously, in the present work the weights are measured on a parts per hundred of pigment scale, i.e. $w_{binder}$ relates to $w_{pigment} = 100$.

At higher pressures, the porosity, $\phi_{uncorr}$, uncorrected for compressibility would be

$$\phi_{uncorr} = (V_{int} + dV_{sample}) / (V_{int} + dV_{sample} + V_{solid}) \qquad (24)$$

whereas the corrected porosity is simply

$$\phi_{corr} = V_{int} / (V_{int} + V_{solid}) \qquad (25)$$

## 5.6    Liquid porosimetry

Ideally, liquid porosimetry should provide an unambiguous measure of hexadecane drainage for a particular paper sample. However, various problems arise. The first is that the paper must be mounted on a support grid, which itself drains. An attempt was made to correct for this by simply assuming that the support grid behaved as a single sheet, and that its weight disappeared when sample sheets were placed on it. However, this proved to be too crude a correction, giving negative drainage values. Therefore, it was necessary to extrapolate the drainage of the multi-sheet samples to a zero-sheet drainage.
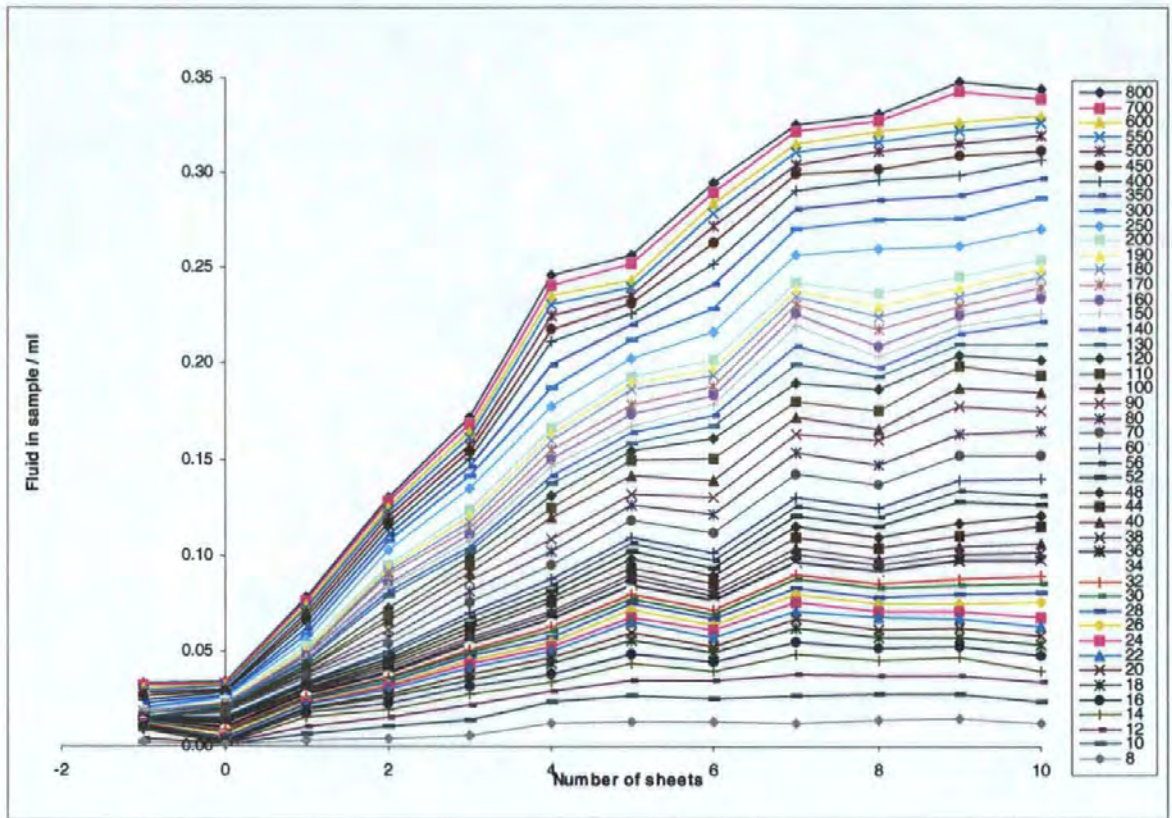
**Figure 13: Observed liquid porosimetry drainage**

This is shown in Figure 13 (moved to the left for clarity), the pressures already having being converted to Washburn throat diameters, Section 3.8. The grid is then assigned an effective sheet-weight, such that its drainage then agrees with the zero-sheet drainage, as shown in the figure. Having carried out this procedure, the support grid drainage is then subtracted  from the multi-sheet drainage curves, to give the net drainage of the paper sheets on their own , Figure 14.
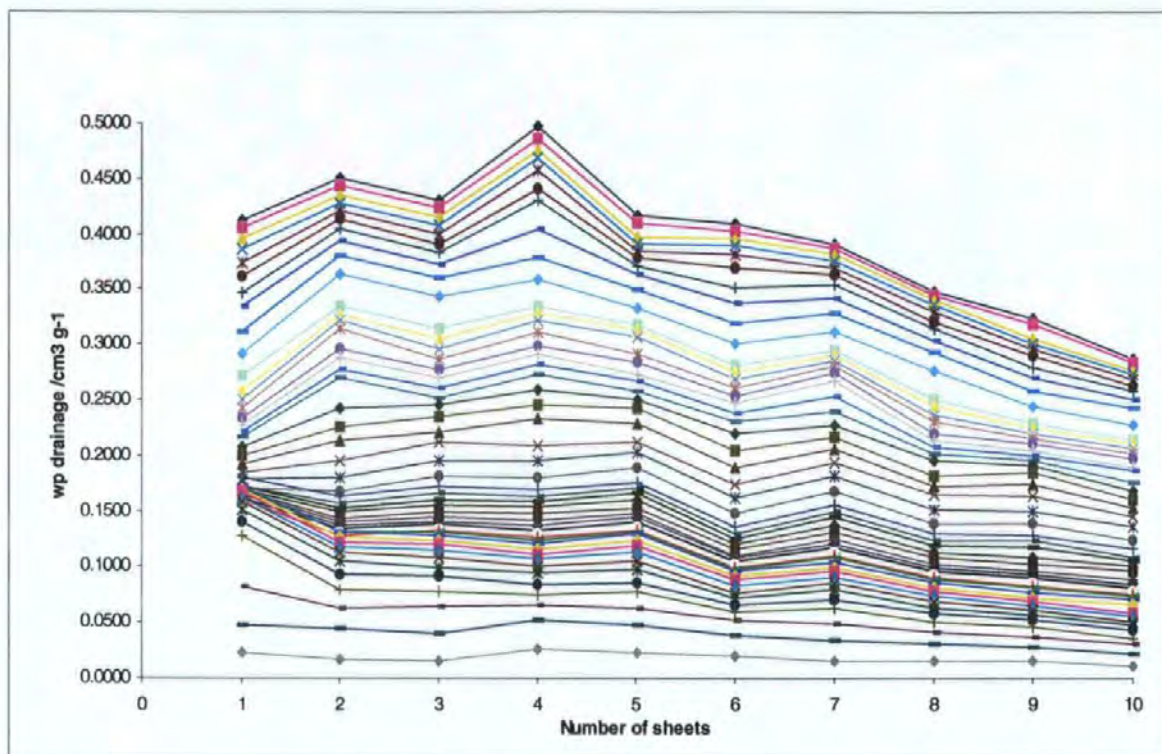
**Figure 14: Wetting phase drainage after subtraction of support grid**

In Figure 14, the drainage has been expressed normalised by sheet weight, i.e. it is expressed as ml.g $^{-1}$. One would therefore expect the drainage at each Washburn diameter to be independent of the number of sheets. However, Figure 14 shows two effects. Firstly, that many of the drainage lines diverge from one to two sheets, which is attributed to the fact that the support-grid drainage dominates the small amount of drainage from the single sheet sample. To eliminate this effect entirely, it is wise to use at least three sheets. For high numbers of sheets, the normalised drainage decreases, which is attributed to fluids being trapped in the inter-sheet spaces. Therefore, three sheets was taken to be the representative sample, as shown in the figure.

### 5.7 Combined porosimetry

Mercury porosimetry, as described in Section 3.7, determines pore structure at pressures greater than the pressure at which the penetrometer has been filled with mercury. This means that mercury may have already partially filled or "flopped in" to some of the pore

space before the measurement cycle has commenced. Mercury porosimetry curves are normally sigmoid in shape, having one main point of inflection followed by a plateau. Three-dimensional percolation theory simulations demonstrate that sigmoid curves arise from a sampling of the whole interconnected pore network. Liquid porosimetry only provides a probe of large macro-pores (> 6 micron diameter). Thus for structures containing smaller pores and throats, such as the basepaper shown in Plate 1, liquid porosimetry may not probe a fully interconnected network, and therefore a non-sigmoidal curve may result, Figure 15. In mercury intrusion experiments, the intrusion of a non-wetting phase (mercury) is measured as a function of pressure. The mercury displaces a nominal wetting phase, comprising a vacuum and sometimes residual air. By contrast, liquid porosimetry comprises the drainage of a wetting phase, which in the present study is hexadecane. (Other substances may be studied using water drainage, but water cannot be used for paper because it causes the fibres to swell.) As the wetting phase (hexadecane) drains, a non-wetting phase, in this case air, intrudes. Percolation theory models the intrusion of a non-wetting phase. Thus to combine mercury porosimetry and liquid porosimetry , the liquid porosimetry results must be expressed as air intrusion, Figure 15.
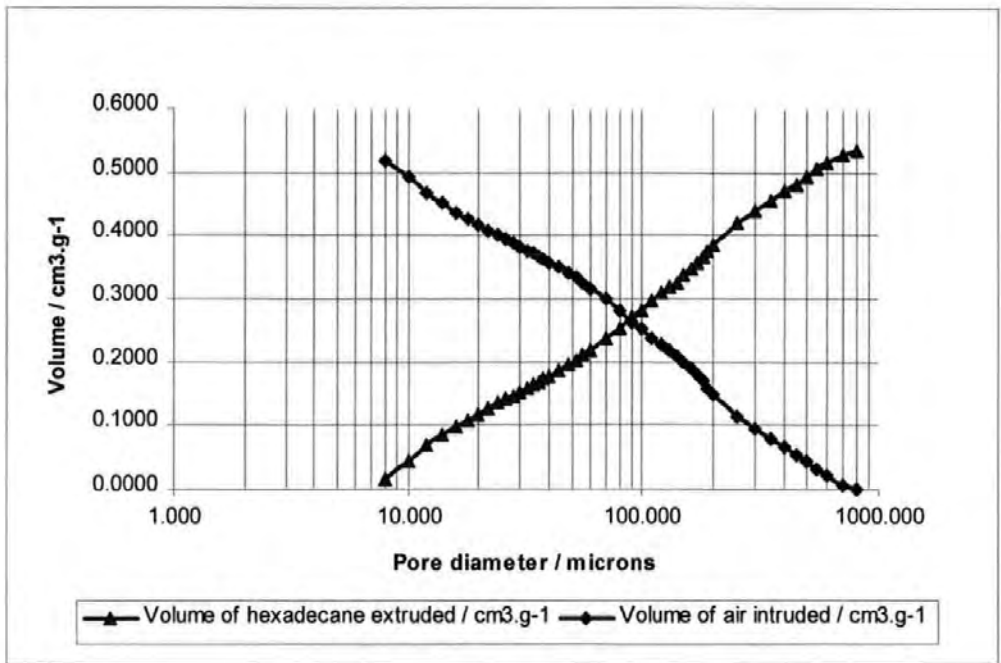
**Figure 15: Hexadecane drainage from paper sample**
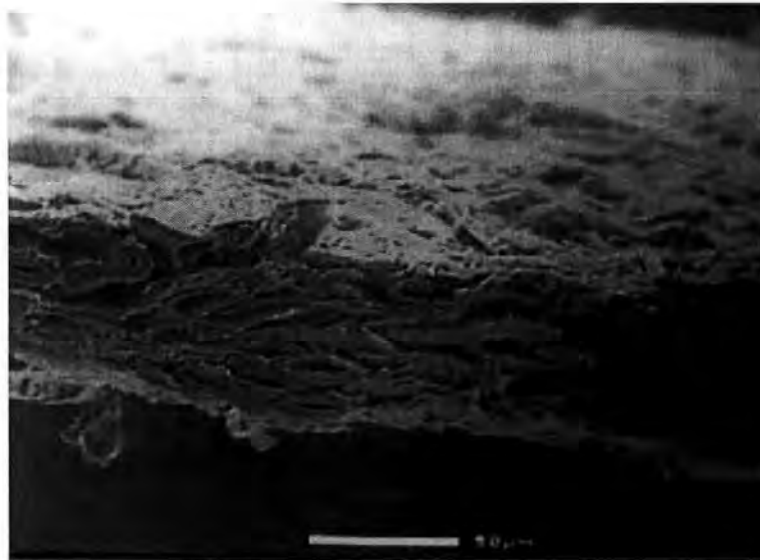


**Plate 1 : ESEM Micrograph of basepaper cross - section**

CHAPTER 6

## 6. COMPUTER MODELLING : PORE-COR

### *6.1 Development of a computer program to simulate 3- dimensional networks*

In this work the void space within a porous medium, (e.g. paper or consolidated pigmented coating) may be regarded as an array of larger voids (pores) connected by smaller voids (throats). The void space is simulated with a network of *nodes* positioned at the centre of each pore, connected by *arcs* along the line of each throat. The complete network comprises a series of identical 3-dimensional unit cells, repeating indefinitely in each Cartesian direction *x, y* and *z*. The modelling is explained in this chapter, and illustrated with some of the experimental samples. All of the Pore-Cor results are discussed in Chapter 8.

Each unit cell contains 1000 nodes in a 10 x 10 x 10 array equally spaced in the Cartesian coordinates. The void volume in the unit cell consists of up to 1000 cubic pores centred on the nodes. Each pore is connected to a maximum of six cylindrical throats which lie along the line of the arcs in the positive and negative *x, y*, and *z* directions. The number of throats connected to a particular pore is referred to as the *co-ordination number* and the arithmetic mean of this quantity over the whole unit cell is referred to as the *connectivity*. The two outermost layers of a typical unit cell (LX 60) are shown in Figure 16.

unit cell
7.20 um

z
y
x
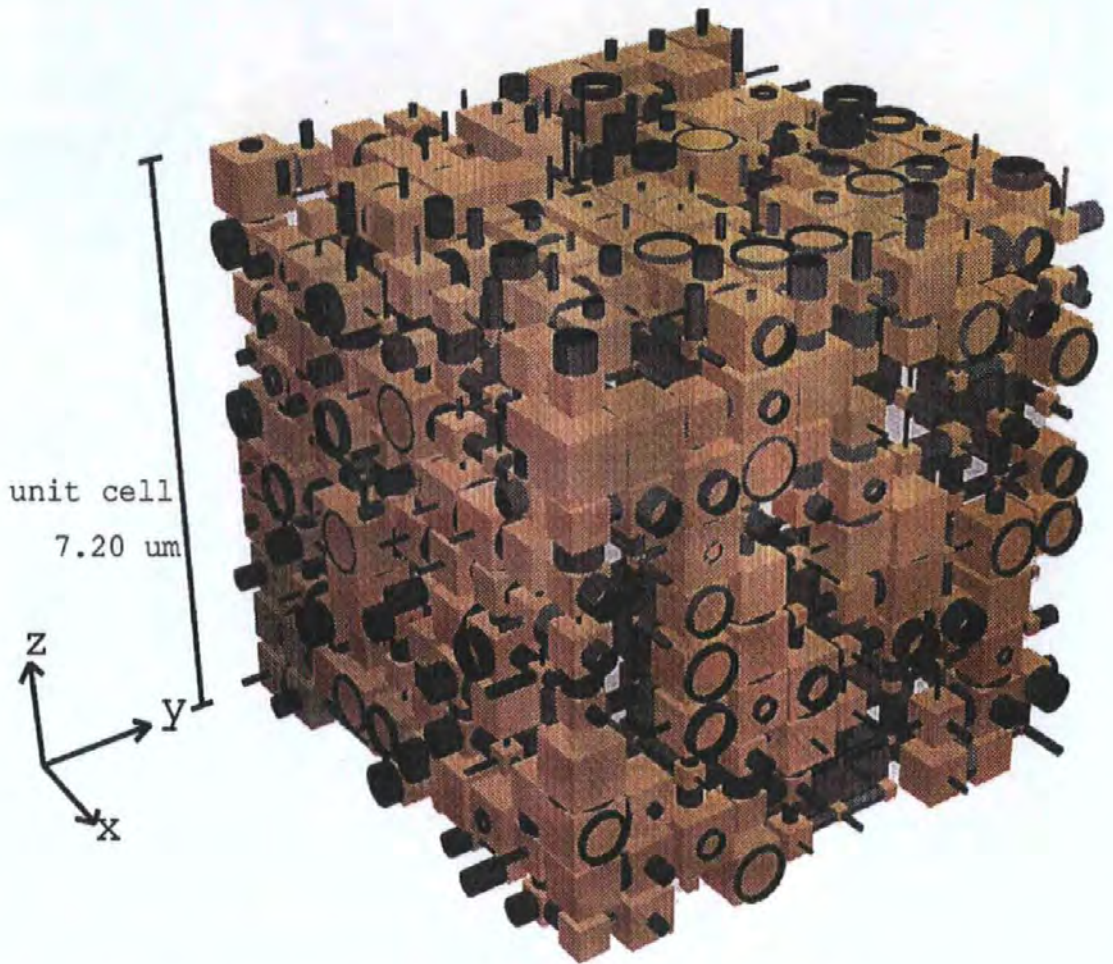
**Figure 16: The two outermost layers of the unit cell of LX 60**

It can be seen that in this case, the cell is a cube of length $l_{cell} = 7.20$ μm. For the calculation of the intrusion and extrusion of a non-wetting fluid, and the permeability to a wetting fluid, the fluid is applied at the top face ($z = l_{cell}$) in the $-z$ direction, or withdrawn in the $+z$ direction, for each repeating unit cell. Thus intrusion and permeability both apply to an infinite sheet of thickness $l_{cell}$, although in practice the permeability is the same as it would be for an infinite lump of the modelled substance.

The throat size distribution consists of 100 different sizes spread log / linearly between the minimum and maximum diameters calculated by applying the Washburn equation to the

experimental data.   The term *skew* is defined as being the percentage of throats of the smallest of these 100 diameters.
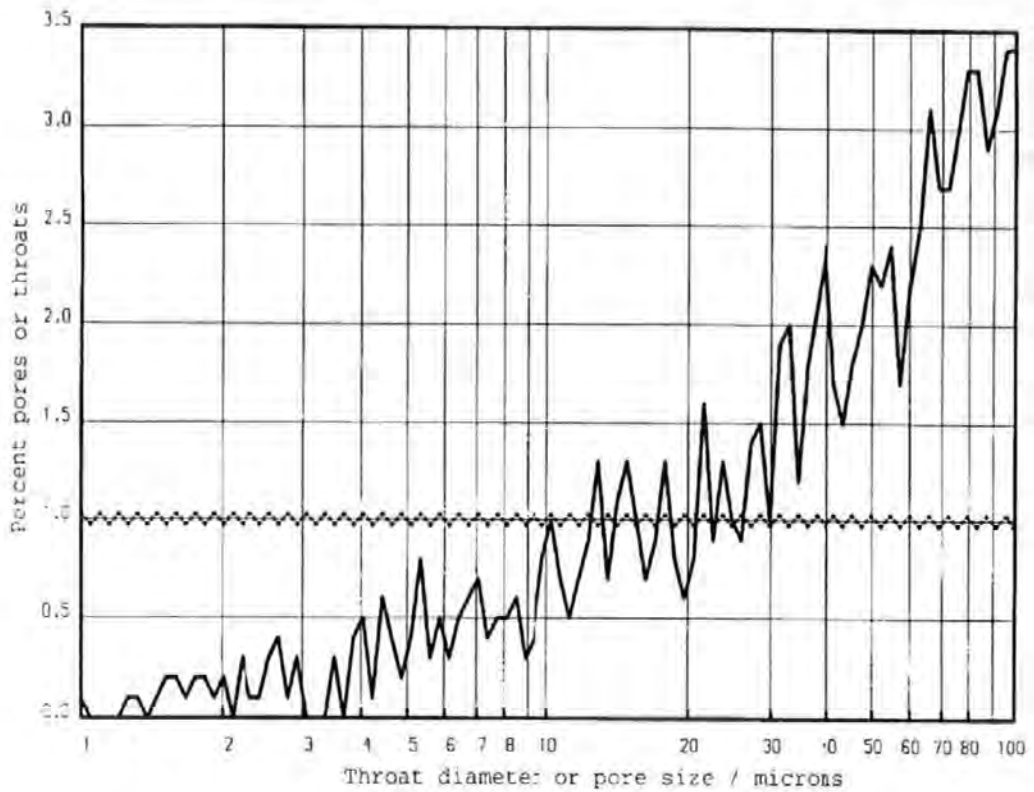


**Figure 17:  Unskewed throat diameter and pore size distribution**

In Figure 17, the skew is set to 1.00%,  i.e. 1.00% of the throats have the smallest diameter, 1 μm.  As there are 100 different diameters, it follows that there are 1.00% of each of the other diameters, to the nearest whole number of throats. Hence we term this an *unskewed* distribution. The connectivity of the distribution is 3.5, i.e. there are on average 3.5 throats per pore.  As there are always 1000 nodes in the unit cell, and each throat connects to two nodes, the number of throats in this instance is 1750.  Hence there are, to the nearest integer, 17 or 18 throats set at each of the 100 diameters, which explains the oscillation of the throat size distribution (dotted line) in Figure 17. The random positioning of the throats introduces a degree of randomness into the pore sizes, as shown. The distribution can also be skewed.

Figure 18, for example, shows a distribution over the range 0.007 μm to 0.213 μm with a skew of 0.97% (and connectivity 4.0), which is that for Alphafine clay with 14 pph latex.
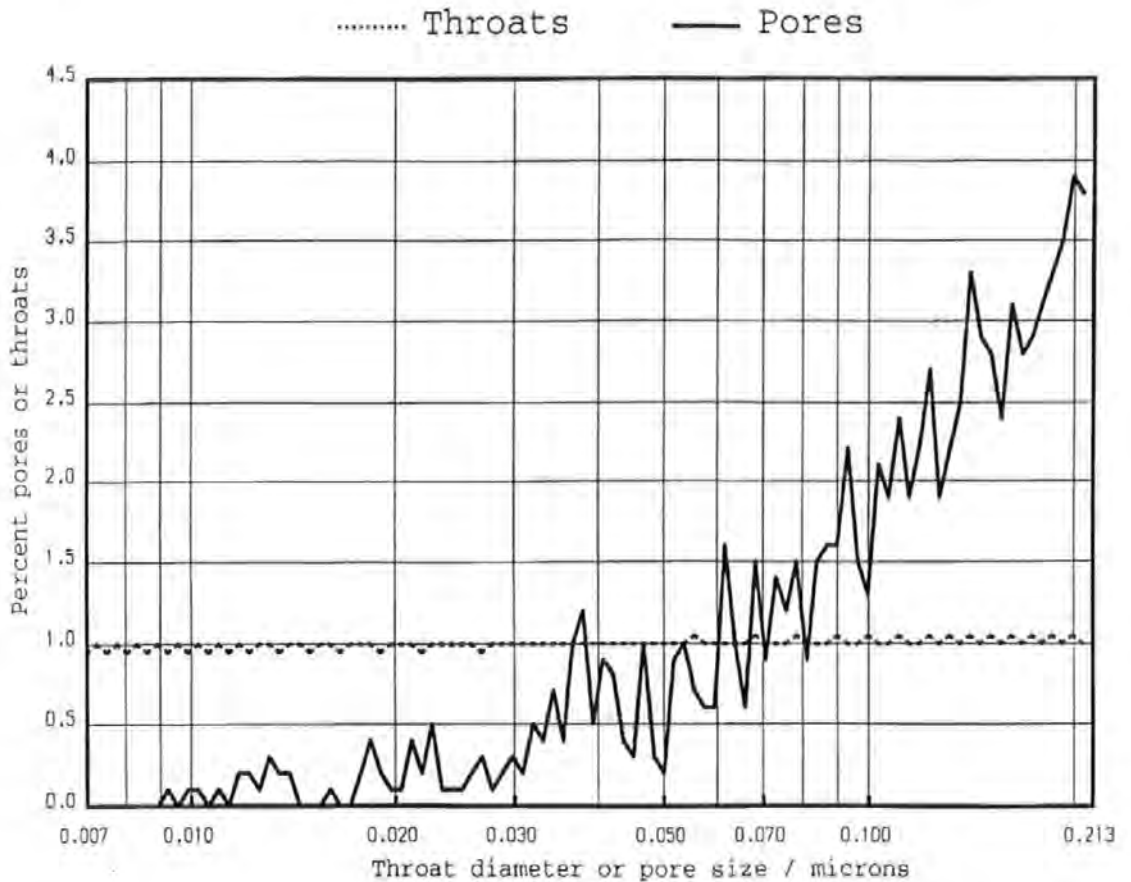


**Figure 18: Pore and throat size distribution for Alphafine with 14 pph latex**

A pore is then assigned to each node that has at least one throat connected to it, the pore being of a size equal to the diameter of the largest throat reaching that node. This pore size : throat size correlation is typical of natural (unground) sandstone but not natural limestone, Wardlaw and McKellar (1981), Spearing and Matthews (1991). However, gaining such information from paper coatings is much more complicated, Kettle and Matthews (1993). In the absence of electron microscope serial tomographic studies of pigment structures, which would reveal the relationship between pore and throat sizes, the pores are set equal to the diameter of the largest throat entering them.

Mercury intrusion is simulated by means of an invasion percolation algorithm which calculates the fraction of pore volume occupied at a series of increasing, static mercury pressures. The mercury intrusion curve was fully discussed in Section 4.4 and it was stressed that traditionally it has been assumed that the distribution of throat sizes (not distinguished from pore sizes) can be equated to the first derivative of an intrusion curve $dV / dd$. This results in a distribution which has a peak at the point on the intrusion curve which has the highest gradient i.e. the point of inflection. The Washburn-derived throat diameter at this point is often described as the characteristic throat diameter. However, the use of the first derivative is only valid for a porous solid which comprises a bundle of non-interconnecting capillary tubes, which can be tortuous, but which must be of constant diameter along their length. Porosimeter control software usually incorporates the first derivative assumption and such software sometimes extends this assumption to derive a particle size distribution for the solid. The Pore-Cor model does not use this capillary bundle assumption, but as stated earlier uses a percolation algorithm. The advantage of a percolation algorithm is that it takes account of the fact that a large pore may be "shielded" from mercury intrusion at the pressure predicted by the Washburn equation by small surrounding throats.

Once the mercury intrusion curve is simulated, it can be adjusted to fit the experimental curve by altering the skew and connectivity. Increasing the skew moves the curve to smaller pore sizes and higher values of connectivity shift the curve to larger pore sizes, and also introduces too high an upper shoulder as a consequence of increasing the gradient at the point of inflection due to the greater suddenness with which the mercury invades the network near the breakthrough pressure. Also, breakthrough occurs at a lower pressure (greater throat diameter) because of the increased number of routes available through the network. The throat size distribution and the connectivity can be adjusted iteratively until a

59

close fit to the experimental mercury porosimetry intrusion curve is attained, Matthews, Moss and Ridgway (1995a), Matthews, Ridgway and Spearing (1995b). Finally, the row spacing of the matrix is set so that the porosity of the simulated network equals that of the experimental sample. Increasing the pore row spacing lengthens the throats, increases the unit cell size and hence reduces the porosity. If the unit cell of the model was infinite, then the random positioning of the throats (and hence pores) within a given set of parameters would always produce unit cells with identical cell properties. However, in the present unit cell, with only 1000 nodes, different sets of random numbers produce unit cells with different properties. For a typical unit cell converged onto experimental data as explained below, the permeability (as described in Section 6.3) varies by a root mean square relative change of 101%, i.e. the permeability can vary by slightly more than double or half of the mean value. The obvious solution to this problem would be to increase the number of nodes in the unit cell, but this is prevented by the processing limit of the DINIC network analysis algorithm mentioned previously. Therefore the random positioning of throats uses a pseudo random number generator with the same seed for every simulated structure. Thus structures with similar parameter values, e.g. skew and connectivity, have very similar structures and properties, and the trends induced by the changes in parameter values can be isolated from the changes induced by different random number sets.

## 6.2    Characteristics of the Pore-Cor network

The Pore-Cor network model has real geometry, and the same network with precisely the same geometry is used to model other pore level properties. Essentially, the model does not use any arbitrary fitting parameters. The model needs fitting parameters, namely the skew of the throat size distribution and the connectivity, which are optimised automatically; however, the parameters are actual properties of the sample and therefore

can be checked as having realistic values. The model's real pore space geometry, in the form of a 3-dimensional unit cell, has been shown previously in Figure 15. The space-filling geometry of the network contrasts with other networks used for the simulation of porous media, which are mathematical arrays of nodes and arcs which often cannot be represented by a 3-dimensional image.

The wide range of pore level properties which have already been modelled for sandstones include the experimental mercury intrusion and extrusion curves, porosity, connectivity, pore : throat size and throat : throat size correlation, tortuosity, and gaseous diffusion through a dry sample of sandstone, Matthews *et al.* (1991, 1993, 1995a, 1995b). The surface area of the simulated void space is too smooth to match the experimentally determined surface area by up to two orders of magnitude, but this can be roughened easily to match experiment, Matthews and Spearing (1991).

### 6.2.1  Automatic convergence onto experimental intrusion data

In this section, three methods are described in which more powerful programming procedures have been applied. Instead of manual trialling of a range of skew and connectivity values, automatic procedures have been introduced to find the values which give the best fitting simulation curve. The first method fits the curve at the point of inflection by adjusting the skew and using a fixed connectivity; the other two methods run through a range of skew and connectivity values and calculate the deviation between the simulated and the experimental curves, expressed on a least-squares minimisation basis. The least-square values are stored in a file which can then be used, if required, to produce a contour plot. The minimum of this plot shows the skew and connectivity which best fits the experimental data, and the monotonicity of the descent of the contours to this minimum gives clues about the quality of the modelling and of the experimental data. For each

method, the porosity of the simulation matches the experimental porosity as close as possible.

## 6.2.2 Automatic fitting a mercury intrusion curve

The simplest method of fitting the mercury intrusion curve is to optimise only a single variable parameter. The skew is varied, with the connectivity arbitrarily fixed at 3.5. The single criterion for fit is that the deviation $\Delta_{50\%}$ between the throat diameter of the simulation and experimental curves must be within 3% of the total logarithmic range of the graph, at the point at which 50% of the available pore volume has been filled with mercury. This is called the 50% method, and the fit criterion may be expressed mathematically as:

$$\Delta_{50\%} = \mid \log d_{\text{sim}(V=50\%)} - \log d_{\text{exp}(V=50\%)} \mid < 0.03 \, (\log d_{\text{max}} - \log d_{\text{min}}) \qquad (26)$$

For the initial simulation an unskewed throat diameter distribution is used, and for the second, either a skew of 0.50% or 1.50%, whichever is expected to give the closer fit. Then, using a linear interpolation/extrapolation algorithm, a third, best-fit skew is calculated. Further iterations of the algorithm are possible, but for all the samples described in this work, the three-point convergence has proved adequate.

To improve the fit between simulation and experiment, the respective curves must be compared not only at the 50% pore volume point, but also at other positions. Thus it is necessary to calculate the horizontal difference (throat diameter difference at a particular percentage of pore volume intruded) between the simulated and experimental curves at spaced intervals along the vertical pore-volume axis. Ideally, for a valid comparison of a series of simulations with experiment, there must be the same relative weightings of the deviations over different portions of the curves, and the easiest way to achieve this is to

have the comparison points evenly spaced along the pore-volume axis. The problem is that experimental measurements from mercury porosimeters are not usually evenly spaced in this way. One could use an interpolation algorithm to produce a set of points, $V_i$, $V_{i+1}$, ..., which were precisely evenly spaced, but this would introduce inaccuracies because the functional form of the experimental curve, and hence of the interpolation algorithm, is unknown. Thus a compromise is used, which is to use experimental measurements whenever possible, but to remove or linearly interpolate points if the pore volume spacing is outside set limits. These limits are arbitrarily set at half and twice the spacing along the pore volume axis compared to the spacing that there would be if the experimental points were evenly spaced:

$$\frac{V_{tot}}{2n} < |V_i - V_{i-1}| < \frac{2V_{tot}}{n} \tag{27}$$

where $V_{tot}$ is the volume intruded at the highest experimental pressure, and $n$ is the total number of experimental points. A flow diagram for the selection and calculation of comparison points is given by Ridgway (1995).

Once obtained, the same set of comparison points is used for each simulation of a particular experimental curve. The horizontal difference between experimental and simulation i.e. the difference in Washburn throat diameter, is determined at each appropriate pore volume. Two different measures of deviation may be used; the linear deviation $\Delta_{lin}$ and logarithmic deviation $\Delta_{log}$. The minimisation of $\Delta_{lin}$ with skew and connectivity is referred to as the linear method, and the corresponding minimisation of $\Delta_{log}$ as the logarithmic method.

63

In this study the logarithmic method was used and is defined as:

$$\Delta_{log} = \frac{\sum_{i=1}^{n} (\log d_{exp(Vi)} - \log d_{sim(Vi)})^2}{n} \tag{28}$$

The linear method appears to give undue weighting to deviations at low pore volume and large throat diameter. The logarithmic method, however, corresponds to the best fit over the whole curve on a logarithmic scale, i.e. the fit that one would tend to perform visually. The reduced statistical weighting which the logarithmic method gives to the fit of large throat diameters, relative to the linear method, is also in accord with partial allowance for edge corrections. In using either the linear or logarithmic methods, two parameters are varied, namely the connectivity and the skew, in contrast to the 50% method where the connectivity was fixed. These two parameters have different effects on the simulated curves as discussed previously. In both the linear and the logarithmic methods, the 50% method is still used to find a skew value that will be a suitable centre for the range of skews to be tested. The total skew range tested is set as this central value ±0.70, at intervals of 0.10. The total connectivity tested is 2.6 to 4.0, at intervals of 0.1. In practice, the lower limit of connectivity tested is usually above 2.6, determined by the fact that connectivities are not accepted which cause the formation of isolated pore and throat systems. Currently this method involves simulating the intrusion curve for every combination of skew and connectivity in the specified ranges. This can take an appreciable length of time (10 minutes on a 25 Mips workstation) and work is in hand to incorporate a Simulated Annealing/Simplex method to speed up the process. The parameter used to assess the level of fit is the mean of the squares of the differences in actual or logarithmic throat diameters, taken at each of the comparison points which have been calculated from the experimental data.

## 6.3 Permeability simulation within Pore-Cor

Assuming Poiseuillian flow occurs across the whole cell in the -z direction, that is from the top face to the bottom face of the unit cell, then:

$$\left(\frac{dV}{dt}\right)_{cell;-z} = -\frac{\pi}{8\mu}\ \Omega\ \left(r_{tube;z}^4\right)_{cell}\ \frac{\delta P_{cell}}{l_{cell}} \tag{29}$$

$\Omega$ is an averaging operator over the whole unit cell operating on the fourth power of the individual radius $r_{tube;z}$ of all tubes lying parallel to the z axis. It is defined such that equation (29) is satisfied and generates a term which is related to the effective Poiseuillian capacity of the cell for flow in the -z direction. Since, at this stage of the calculation, all the tube lengths $l_{tube;-z}$ are identical and $l_{tube;\ z} = l_{cell}/\ \beta$ , where $\beta$ is the number of tubes in the z direction of the unit cell (in this case 10), we can include these lengths in the averaging function, so that:

$$\left(\frac{dV}{dt}\right)_{cell;-z} = -\frac{\pi}{8\mu}\ \Omega\ \left(r_{tube;z}^4\right)_{cell}\ \delta P \tag{30}$$

However, the unit cell is not a series of tubes of length $l_{tube}$, but a three dimensional interconnecting network. Flow in the +z direction is not allowed, but flow in the $\pm x$ and $\pm y$ directions is permitted.

$$\left(\frac{dV}{dt}\right)_{cell;-z} = -\frac{\pi}{8\mu}\ \Omega\ \left(r_{tube;z}^4\right)_{cell}\ \frac{\delta P}{\beta} \tag{31}$$

By considering tubes in the $\pm x$ and $\pm y$ directions as well, and comparing with the Darcy equation (1) it follows that:

$$k = \frac{\pi}{8\beta}\ \Omega \left(\frac{r_{tube}^4}{l_{tube}}\right)_{cell} \frac{l_{cell}}{A_{cell}} \qquad (32)$$

A network analysis approach to this problem supplies the term $\Omega(r_{tube}^4 / l_{tube})$ as the maximal flow capacity through the network of pores and throats. The term $(r_{tube}^4 / l_{tube})$ is modified to take into account the flow capacity through individual pore-throat-pore arcs. $\Omega$ is an averaging operator over all the arc capacities in the unit cell, Matthews *et al.*,(1993). There is an overall conservation of flow, so that the entire volume of fluid entering the top of the unit cell emerges at the bottom with no build-up through the network. However, the unit cell infinitely repeats in all horizontal ($x$ and $y$) directions and fluid can pass out sideways from one unit cell to the next. Conservation is maintained by an identical volume flowing in at the opposite face of the cell. The value obtained as the maximal flow is an average of the capacity values over only the channels found to carry flow. In this work, the fluid is taken to be an incompressible fluid with a negligible mean free path distance between molecular collisions relative to the size of the pores and throats. The capacities of the arcs, $r_{arc}^4 / l_{arc}$ provide a complete description of the network to the Operational Research Network analysis algorithm (DINIC). The algorithm calculates the maximum possible flow through each arc, allowing for shielding by neighbouring arcs of low capacity and then calculates a single capacity term $(r_{arc}^4 / l_{arc})_{cell}$. Permeability may be expressed in Darcies, the units traditionally used by geologists: 1 Darcy $= 9.87 \times 10^{-13}$ m$^2$. The calculation of permeability by use of an overall capacity term avoids the necessity of making arbitrary assumptions about intermediate pressures within the pore structure, as is necessary for the successful solution of simultaneous flow equations in analyses of the

fracture network type. Having calculated this maximal capacity, the network analysis algorithm finds a "minimum cost" solution, Whittaker (1984). This corresponds to a flow arrangement which, while maintaining the maximal throughput, minimises the distance travelled by the fluid and, for example, prevents unnecessary "swirling" within a horizontal layer.

In this study permeabilities were calculated for both liquid and air at one atmosphere pressure, by a method described previously by Matthews *et al.* (1993, 1995a). It was assumed that in a liquid, there is a negligible mean free path length between intermolecular collisions in the fluid phase, and that the mean free path length in air is the same as that of nitrogen, i.e. 0.0698 μm. Permeability is very dependent on connectivity and correlation effects, which are not well characterised for the reasons described previously. The permeability calculations are therefore the best available with the current state of knowledge, but should be used for ranking the samples rather than as absolute values.

### 6.4    Literature review of other pore space networks.

Calculations on specific shapes of pores have been carried out by Mason *et al.* (1988). Mason has also modelled the intrusion and extrusion of mercury in an array of packed spheres, Mason and Mellor (1994) by using the Haines in-sphere approximation, Haines (1927), to model the void spaces between them. The pore space of a simple granular medium (a close packing of equal spheres) has been shown to be spatially correlated, Bryant, Mason and Mellor (1996). Conner *et al.* (1988) used a range of rod-like and plate-like structures to demonstrate that there is a relationship between the shapes of pores and throats and the shapes of mercury intrusion and extrusion hysteresis curves. Yanuka and co-workers (1986) have also used different void shapes, in the form of a three dimensional network of intersecting ellipsoids, for their simulation of percolation processes, and

Kloubek (1994) uses a model of pores with conical terminations. However, Garboczi (1991) showed that a range of pores and throats of different shapes and sizes could be represented adequately by a random network of interconnecting elliptical cylinders. The elliptical cylinders can range from circular (major and minor axis equal) through to cracks (minor axis zero). In this work the mercury intrusion curve is mapped using only throat size distribution, known pore-size : throat-size correlation, and connectivity. Although pore shape is important, it is much less influential than either size or connectivity; the resulting sizes incorporate the effect of the shapes of the void spaces (Cebeci, 1980).

A survey of networks used by other workers up to 1975, ranging from bundles of capillary tubes through to 3-dimensional interconnecting networks, is given by van Brakel (1975). The networks generated by the Pore-Cor model are based on actual samples and although not based on any form of tomography (Lymberopoulos and Payatakes, 1992), it is closer to an actual representation of void volume than it is to a mathematical network. Lenormand and coworkers (1988, 1989) have used 100 x 100 x1 and 25 x 25 x 1 networks to simulate two-phase displacement effects, namely capillary viscous fingering and stable displacements. Blunt and King (1990, 1991) generated 2-dimensional and 3-dimensional networks of up to 80000 pores of equal volume, with pore coordination numbers in the range 3 to 12, and a connectivity of 6; the throat sizes follow a uniform linear distribution. Chatzis and Dullien (1985) used 33 x 33 x 1 and 18 x 18 x 12 networks formed by angular capillary tubes with angular bulges to represent pores. The pore volume network was fitted to experimental data, which deviated by up to 8% above 70% pore volume. Conner and Horowitz (1988) used a 10 x 10 x 10 matrix with all the pores of the same volume, throats of zero volume and a connectivity of 6. Mercury intrusion curves were calculated using the Washburn equation. Throat size distributions are often assumed to be the derivatives of mercury intrusion curves and these authors corrected these derivatives using a distortion

factor and a structural factor. The necessary but arbitrary choice of a connectivity of 6 in their simulation was found to be very limiting. Payatakes and co-workers (1989, 1992) have used 20 x 20 x 20 and 30 x 30 x 2 networks for the simulation of mercury intrusion and extrusion curves. They used an invasion percolation algorithm effectively the same as in this work, but include resistance effects due to pore shape (Payatakes *et al.*, 1990). Kent and Lyne (1989) have discussed the effect of the local geometry of the pore system in paper on fluid penetration.

Much work has also been carried out to determine the effect of pore and throat size correlations. Payatakes and Tsakiroglou (1992) generated 30 x 30 x 2 and 20 x 20 x 20 networks of cylindrical throats and spherical pores with shaped necks, and demonstrated that the points of inflection of the simulated mercury intrusion curves were less pronounced within pore-size:pore-size and pore-size:throat-size correlated models compared to uncorrelated structures. Pore-size : pore-size correlations result in areas of high and low porosity within the same unit cell. This may be a good representation of a paper coating which may have porosity gradients throughout the structure (Bunker and Conners, 1991) and pore-size : pore-size correlation effects can now be modelled by the Pore-cor program.

Uncorrelated networks developed by other workers range from parallel bundle models which do not take any shielding effects into account (Yamasaki and Munakata, 1994), through two dimensional models that model shielding effects and hysteresis, [Androutsopoulos *et al.* (1979, 1981), Hampton *et al.* (1993), Hirasaki (1990), Mason *et al.* (1991), Gavrilenko *et al.* (1989)] to more complicated three dimensional models, [Blunt and King (1991), Portsmouth and Gladden (1991), Zgrablich *et al.* (1991), Garboczi (1991), Koplik (1984), Bryant *et al.* (1993)].

In studies of correlation effects, other workers have generated void space networks with pore size and throat size distributions and correlation levels obeying pre-set mathematical functions. These models can be very precise in themselves but are often only loosely related to experimental samples. Li, Laidlaw and Wardlaw (1986), and Li and Wardlaw (1990) have shown how correlation effects reduce shielding and cause intrusion to occur at a lower pressure. This in turn causes a reduction of entrapment during secondary imbibition. This effect has also been shown by Wardlaw (1990) in multiple intrusion/extrusion scanning loops. Ioannidis and Chatzis (1993a, 1993b) have represented porous media by a 50 x 50 x 50 array of cubes with different grey levels representing different pore sizes, and have shown that mercury intrusion becomes slightly more gradual with increasing pressure as the structure is correlated. The retention of mercury after secondary imbibition also increases. Day *et al.* (1988), point out that a two step mercury intrusion curves would result from extreme positive and negative pore-size:pore-size correlation if such correlation produced a bimodal distribution. Jerauld and Salter (1990) have used a 20 x 20 x 20 Voronoi network to demonstrate that increasing the extent of correlation between throats increases non-wetting phase relative permeability and slightly decreases wetting phase relative permeability.

## 7. EXPERIMENTAL RESULTS OF SAMPLES RANGING FROM MODEL SYSTEMS TO REAL SYSTEMS

To simplify the initial analysis, the experimental work commenced with model systems such as solid spherical plastic pigments and only later approached real usable paper systems. This philosophy was represented in Figure 1. In line with other workers, initial studies concentrated on the evaluation of structures formed by spheres coated onto substrates which are smooth, flat, impermeable and incompressible. Such systems are referred to as model systems in this work. Taking one step nearer to reality, that is one step further down the left hand side of Figure 1, a selection of calcium carbonate mineral pigments were evaluated. Electron microscopy studies of process ground calcite have indicated that it forms "blocky" (low aspect ratio) particles. The other major mineral type used for paper coating is kaolin. The particle shape of kaolin is traditionally defined as "platey" (high aspect ratio) and its shape further complicates the particle packing. However these systems are still less complex than a *basepaper*. The term basepaper has been previously described as a paper that has been made on a paper machine using an aqueous suspension of cellulose fibres, fine mineral pigment and sufficient chemicals to keep the whole matrix together.

Figure 2, gives a representation of the detail of this project structure. The pore structures of the consolidated pigment samples were probed using mercury porosimetry. The surface and bulk structures of the paper samples were investigated using mercury porosimetry as well as Gurley permeability, low pressure liquid porosimetry and surface air leakage techniques. The consolidated pigment structures were viewed using SEM, and an ESEM was used to view the paper samples. The z-direction thicknesses (calipers) of the papers

were measured using optical microscopy and image analysis software (Section 3.3.3). The conventional physical, optical and printing properties of all of the papers prepared in this study were tested according to standard test procedures (TAPPI), described previously in Chapter 3.

## 7.1    Porosimetric measurements of model coating systems

The simplest model coating systems were comprised of spherical plastic pigment. The mercury porosimetry data is often described in terms of a "characteristic pressure" at which the 50 % pore volume intruded occurs. Using the Washburn equation the characteristic pore diameters may be calculated from the pressure value. Using  our correction calculations (page 43) it is also possible to generate values of sample compressibility and solid phase bulk modulus.   The mercury porosimetry results for these consolidated structures are summarised in Table 1 and discussed within this section.

**Table 1:  Properties of consolidated plastic pigment samples**

| Type of Sample | Characteristic Pressure, $P_{50}$ / MPa | Characteristic Diameter $d_{50}$ / $\mu$m | Porosity / % $\phi^I$, $\phi_{uncorr}$, $\phi_{corr}$ | Compressibility $\psi_{ss}$ / $10^{-10}$ Pa$^{-1}$ | Bulk Modulus $M_{ss}$ / GPa |
|---|---|---|---|---|---|
| HP 91 | 5.0 | 0.294 | 32.9, 41.1, 40.1 | 6.40 | 1.6 |
| Lytron 2601 | 9.0 | 0.163 | 27.9, 32.5, 30.0 | 0.87 | 12 |
| Lytron 2301 | 35 | 0.042 | 23.2, 30.7, 25.1 | 1.4 | 6.9 |

### 7.1.1   Monosized spheres - Rhopaque HP91 plastic pigment
The consolidated sample of this hollow monosize pigment has been viewed by SEM; the resulting micrograph is shown in Plate 2:
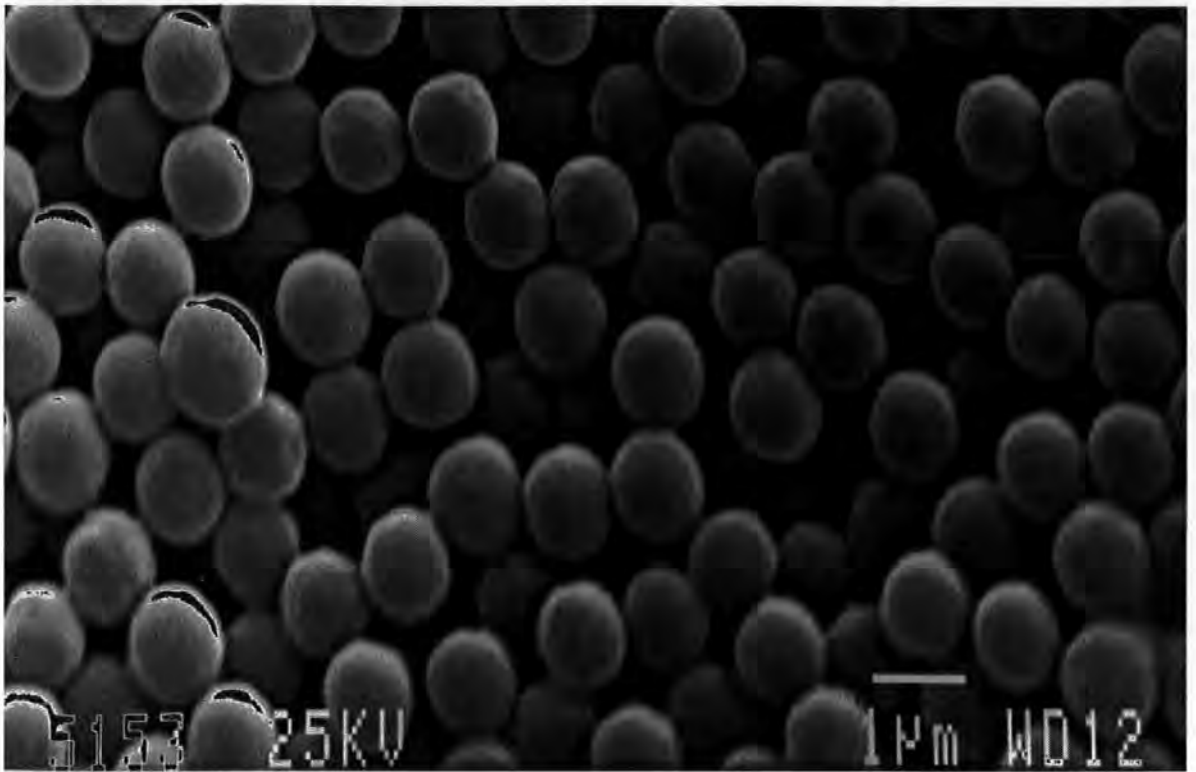
**Plate 2: Surface micrograph of consolidated HP91**

The micrograph indicates that the particle diameter is approximately 1 μm and that HP91 has a relatively monosized distribution of particles. The particle packing at the surface is random, and it is probable that there are localised areas of dense and loose packing throughout the structure.

The mercury porosimetry curve for the consolidated sample of HP91 pigment is shown in Figure 19. The intrusion curve has two points of inflection, at 5 MPa (equivalent to 0.3 μm) and 41 MPa (equivalent to 0.035 μm). The first results from intrusion of the spaces between the spheres, and the second from the compression of the hollow spheres themselves. As can be seen, the extrusion curve is nearly horizontal, demonstrating that the high pressure compression of the hollow spheres is irreversible and the spheres have collapsed.
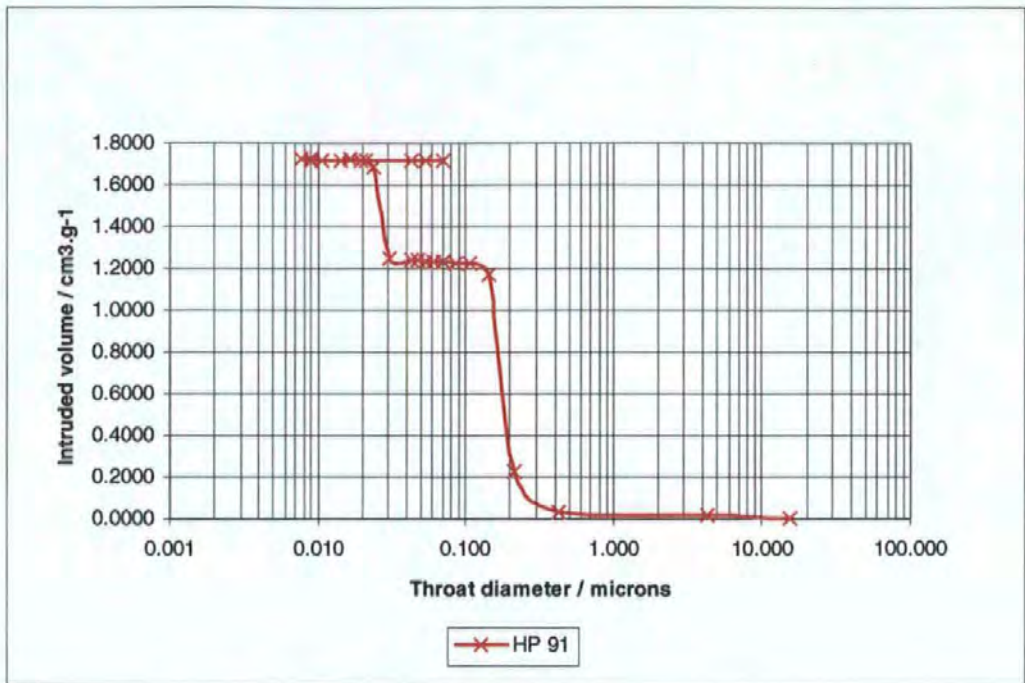
**Figure 19: Mercury porosimetry data for consolidated sample of HP91**

The porosity of the sample, $\phi^{I}_{atm}$ is approximately 33 %, which is similar to the porosity of randomly packed monosized spheres quoted by German (1989). However, there is a discrepancy between the Ropaque HP91 porosity values of $\phi^{I}_{atm} = 32.9$ % and $\phi_{corr} = 40.1$ %. A possible explanation is that the effective dry density is 0.65 g cm$^{-3}$ rather than 0.55 g cm$^{-3}$ as quoted, which would change the porosity values to 43.2 % and 44.1 % respectively, via equations (22), (23) and (25), however, these values are probably slightly too high to indicate loose random packing (normally between 30 % to 35 %).

### 7.1.2 Plastic pigments with broad particle size distributions

In this study two plastic pigments supplied by Lytron were used. These samples were labelled Lytron 2301, and Lytron 2601. The consolidated structures formed by these samples have been viewed by SEM and the micrographs are shown below.
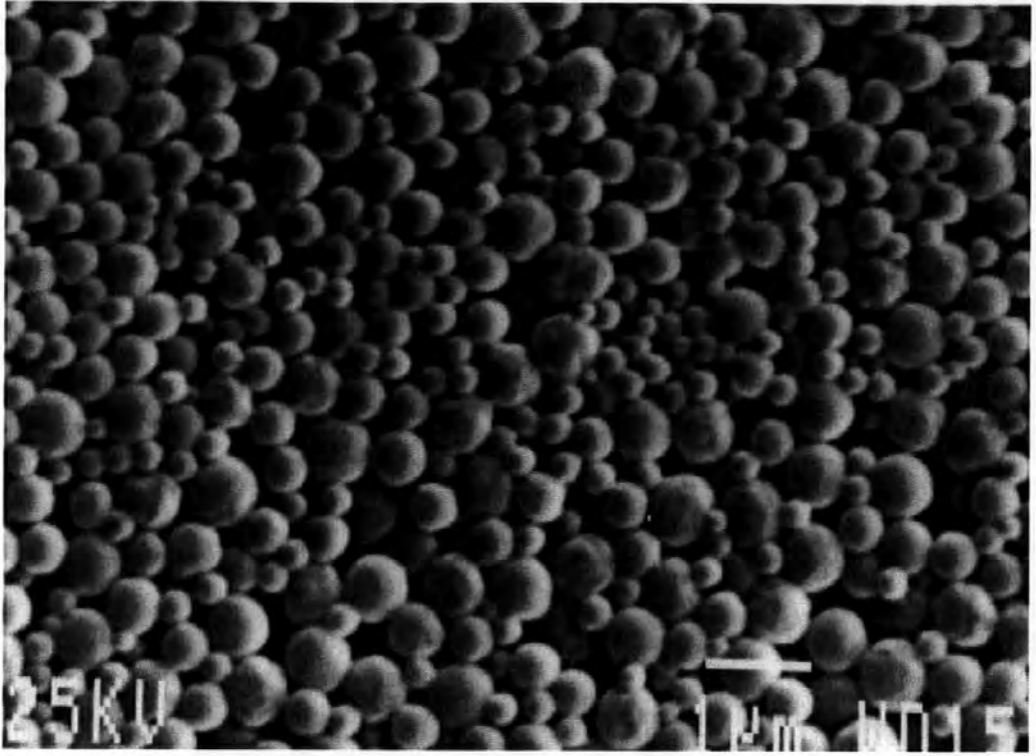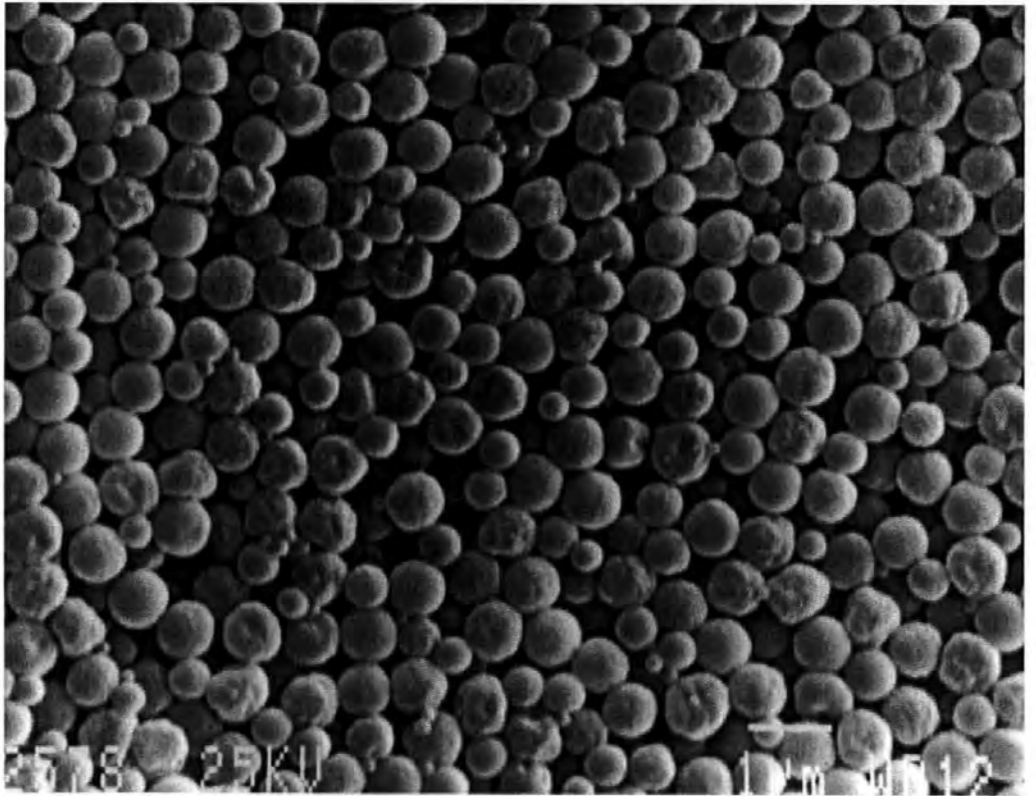
**Plate 3: Surface micrograph of Lytron 2301**



**Plate 4: Surface micrograph of Lytron 2601**

The suppliers of Lytron have indicated that although they quote a particle size for each of their products, e.g. 0.6 micron particle diameter, they are referring to a mean particle diameter and our micrographs confirm the polydispersity of the particles. The mercury porosimetry data for the consolidated Lytron samples are shown in Figure 20, and Table 1.
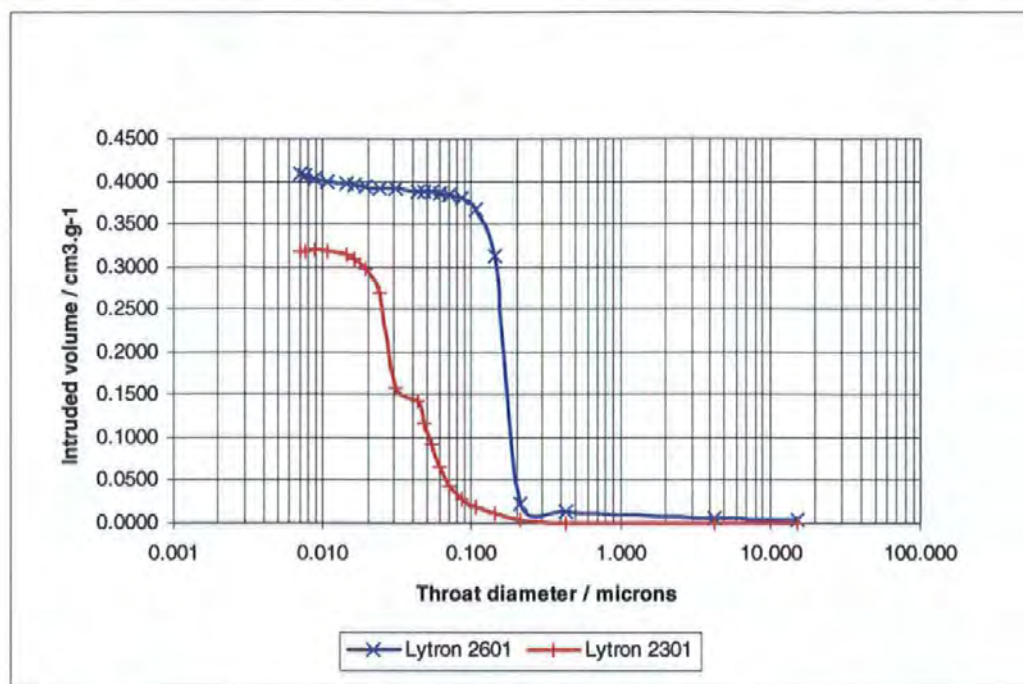


**Figure 20: Mercury porosimetry data for Lytron samples**

The characteristic intrusion pressures $P_{50}$ ($d_{50}$) for Lytron 2601 and Lytron 2301 are 9 MPa (0.163 µm) and 35 MPa (0.042 µm) respectively. The smaller particle size (and compressibility) of the Lytron 2301 affects the First Critical Concentration (Watanabe and Lepoutre, 1982), and leads to a structure in which there are smaller void spaces.

The oil absorption test was used to determine the porosity of the consolidated structure formed by sample Lytron 2601 and results were compared to those with mercury porosimetry:

| Oil absorption technique, $\phi$ | 28.8 % |
|---|---|
| Mercury porosimetry (at atmospheric pressure), $\phi^1$ | 27.9 % |
| Mercury porosimetry (at maximum applied pressure), $\phi_{corr}$ | 30.0 % |

The above porosity values are 29 ± 1 % and are considered to be accurate within experimental error. Clearly there is scope for error in the oil absorption method, firstly because the oil intrudes by means of capillary forces at ambient pressure, rather than under a positive applied pressure, and secondly because the sample has to be wiped with an absorbent lens tissue, which itself has some capillarity to suck oil out of the sample due to the tissue's own capillary forces.

The solid phase bulk moduli of the plastic pigments decrease in the order Lytron 2601, Lytron 2301, Ropaque HP91, corresponding to an increase in compressibility from medium to very compressible, Table 1. Thus the agglomeration of smaller Lytron spheres is rather more compressible than that containing the larger spheres and, as expected, the agglomeration of hollow spheres is much more compressible than that of the solid spheres. By comparison, the bulk modulus of solid nylon is around 5.3 GPa, similar to Lytron 2301 (Cook and Hover (1993)).

## 7.2 Porosimetric measurements of calcium carbonate systems

Taking one step nearer to reality (industrial practice), a selection of calcium carbonate mineral pigments were evaluated. The pore structures of consolidated films of calcites of differing particle size were characterised by mercury porosimetry. In order to mimic the structures of a pigmented calcite coating applied to paper, consolidated films of a calcite with a selection of different latex binders were prepared and characterised. The porosimetric results are summarised in Table 2.

### Table 2: Properties of consolidated calcium carbonate samples

| Type of Sample | Characteristic Pressure, $P_{50}$ / MPa | Characteristic Diameter $d_{50}$ / $\mu$m | Porosity / % $\phi^1$, $\phi_{uncorr}$, $\phi_{corr}$ | Compressibility $\psi_{ss}$ / $10^{-10}$ Pa$^{-1}$ | Bulk Modulus $M_{ss}$ / GPa |
|---|---|---|---|---|---|
| Carbital 90 | 23 | 0.64 | 26.2, 28.4, 26.1 | 0 | $\infty$ |
| Carbital 60 | 11 | 1.34 | 28.8, 29.3, 28.7 | 0.51 | 20 |
| LX 60 | 5 | 2.94 | 40.9, 42.0, 39.7 | 2.4 | 4.1 |
| C90 + 12pph Acronal S801 | 13 | 1.13 | 19.4, 24.9, 22.5 | 0 | $\infty$ |
| C90 + 12pph Revinex 95L10 | 16 | 0.92 | 19.3, 22.7, 19.2 | 0.48 | 21 |
| C90 + 12pph Dow 950 | 15 | 0.98 | 21.3, 25.2, 20.5 | 0.72 | 14 |

## 7.2.1 Effects of particle size distribution

The consolidated structures have been viewed by SEM. The resulting micrograph of Carbital 90 is shown in Plate 5. The micrograph provides an indication of the "blocky" nature of the particles in comparison to the micrographs of the plastic pigment spheres (Plates 2-4).
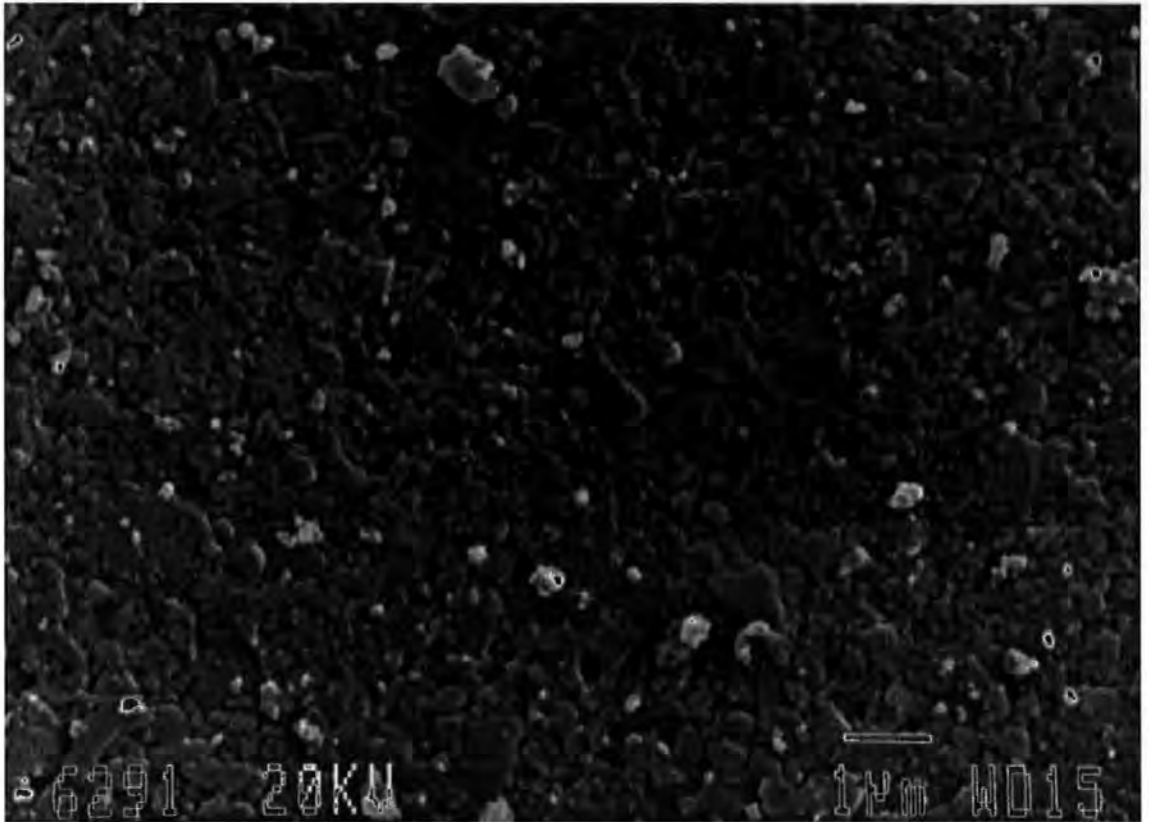


**Plate 5: Surface micrograph of Carbital 90**

The mercury porosimetry data for the consolidated calcite structures are shown in Figure 21. The characteristic intrusion pressures $P_{50}$ at which 50% of the void volume of each is intruded are shown in Table 2. ($P_{50}$ is insensitive to the exact measure of 100% pore volume intruded.) It can be seen in Table 2, and in Fig. 21, that $P_{50}$ decreases in the order C90, C60 and LX 60.
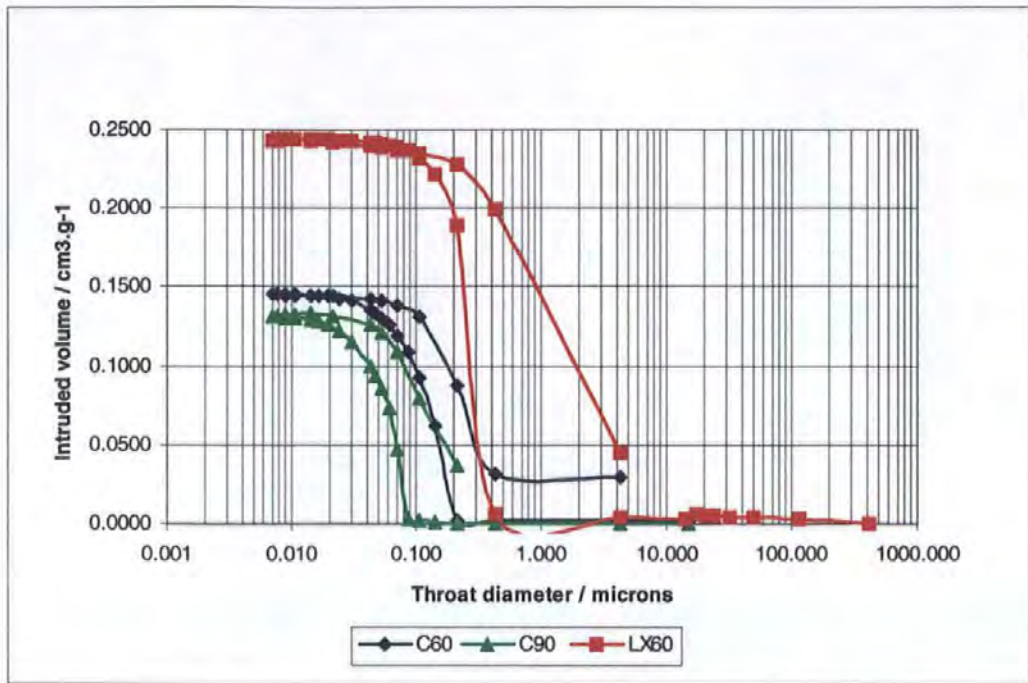
**Figure 21: Mercury porosimetry of dried calcite slurries**

For Carbital 90, the corrected extrusion curve diverges from the intrusion curve immediately the applied pressure is reduced. Carbital 90 is, therefore, assumed to be incompressible, according to the criteria discussed previously, as indicated by the values for $\psi_{ss}$ and $M_{ss}$ in Table 2. (A selection of the simulated intrusion curves are shown and discussed in Chapter 8).

Also shown in Table 2 are the Carbital 90 porosity at 1 atmosphere $\phi^1$, equation (22), and the uncorrected and corrected porosities $\phi_{uncorr}$ and $\phi_{corr}$, equations (24) and (25), determined at the maximum applied pressure. The values are 26.2%, 28.4% and 26.1% respectively, and the close agreement between $\phi^1$ and $\phi_{corr}$ brought about by application of the correction terms provides an independent validation of the correction procedure.

The corrected extrusion curve for Carbital 60 coincides with the intrusion curve, to within experimental uncertainty, at pressures above a $P^z$ value of around 130 MPa (0.025μm),

Figure 21. Also, both of the coincident curves increase with pressure above $P^z$. Thus Carbital 60 is compressible, and the intrusion and extrusion curves may be solved according to equations (16) and (21) to give a solid phase compressibility $\psi_{ss}$ of 0.51 x $10^{-10}$ Pa$^{-1}$ and a solid phase bulk modulus $M_{ss}$ of 20 GPa (2 x $10^{10}$ Nm$^{-2}$), Table 2. Correction of the intrusion and extrusion curves for compressibility via eq. (21) gives the fully corrected intrusion and extrusion curves which also satisfy equation (16).

The corresponding results for LX 60 are also shown in Figure 21 and listed in Table 2. For both Carbital 60 and LX 60, the $\phi_{corr}$ values include the correction for compressibility, and their similarity with the $\phi^1$ values confirm the derived compressibilities and bulk moduli.

For discussion purposes, the samples in the present study which have an infinite solid phase bulk modulus are refered to as incompressible, those with a bulk modulus between 10 GPa and 100 GPa as medium compressible, and those with a bulk modulus less than 10 GPa as very compressible. It can be seen from Table 2 that Carbital 90 is incompressible, Carbital 60 is medium compressible and LX 60 very compressible. Calcite in its crystalline form might be expected to be incompressible. However, as discussed previously in Chapter 5, mineral samples are seldom formed from single macro-crystals, and the medium compressibility of Carbital 60 may be attributable to compression at microcrystalline boundaries within an internal mosaic structure. It is more compressible than solid glass, which typically has a bulk modulus of around 40 GPa (Cook and Hover (1993)). LX 60, by contrast, is made from limestone, and its high compressibility can be attributed to its formation from the remains of marine organisms together with a significant organic content.

### 7.2.2  Carbital 90 samples with added latex binder

The consolidated structure of Carbital 90 with 12 pph D950 latex has been viewed by SEM and the micrograph is shown below (Plate 6) in order to make comparison with the consolidated Carbital 90 sample previously shown in Plate 5.
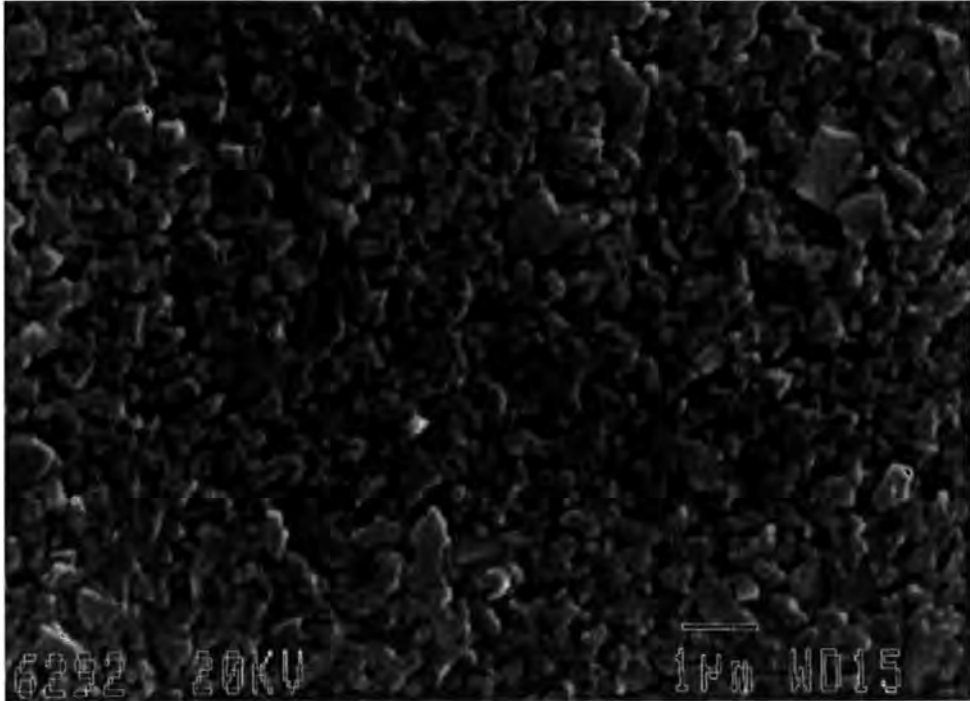


**Plate 6:  Surface micrograph of C90 with 12pph D950**

The latex emulsion has film-formed during the drying process and this has changed the appearance of the particle surfaces especially at the points of particle - particle contact.  This is shown even more clearly by Plate 7.
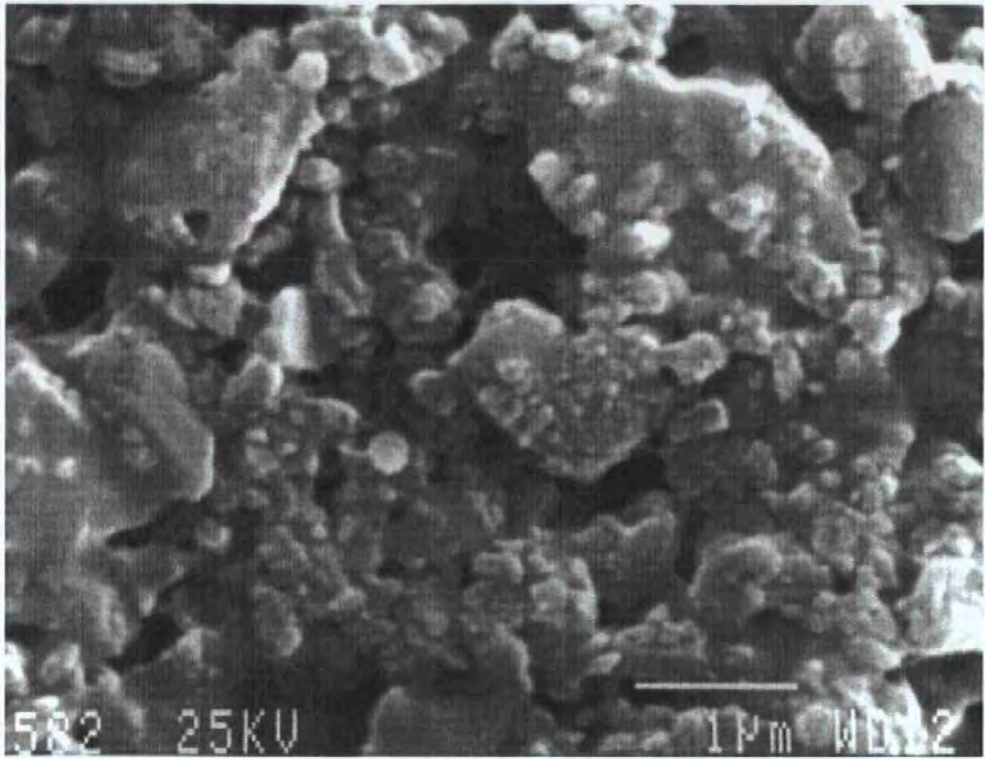
**Plate 7: Surface micrograph of C90 with D950**

The mercury porosimetry curves of the coating colours consisting of Carbital 90 with 12 pph (parts per hundred by weight) of three different latex binders are presented in Figure 22.
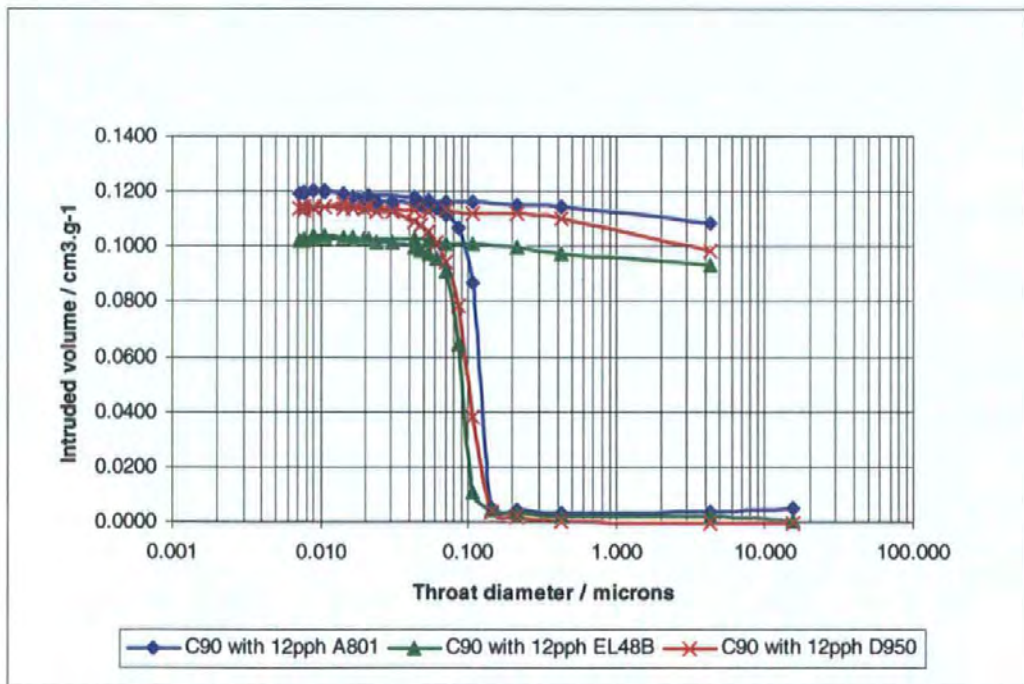


**Figure 22: Mercury porosimetry curves for Carbital 90 with different latices**

As can be seen, the characteristic intrusion pressures $P_{50}$ are similar for these three samples. The porosities $\phi^1$ are all around 20%, and once again the corrections improve the agreement between the high pressure porosity and that at one atmosphere. The major difference between the samples is that the Carbital 90 / Acronal S801 coating colour is incompressible, as indicated by its horizontal intrusion curve at high pressure, Figure 22. In contrast, the coating colours containing the latices Revinex 95L10 and DL 950 are medium compressible. A possible explanation of this is that the compressibility of the latter two samples is caused by the latex forming interstices with high surface-to-volume ratios between the calcite grain contact points as the coating colour passes through the First Critical Concentration, whereas the Acronal S801 with a higher $T_g$ does not do this. However, this cannot be proved from our electron micrographs, because the latex films mask the grain contact points.

## 7.3    Porosimetric measurements of kaolin systems

In this work, consolidated structures of kaolins with differing particle size distributions, different latex binder addition levels and different binder types were characterised using mercury porosimetry and the results summarised in Table 3.

**Table 3:  Characteristic properties of kaolin samples**

| Type of Sample | Characteristic Pressure, $P_{50}$ / MPa | Characteristic Diameter $d_{50}$ / $\mu$m | Porosity / % $\phi^I$, $\phi_{uncorr}$, $\phi_{corr}$ | Compressibility $\psi_{ss}$ / $10^{-10}$ Pa$^{-1}$ | Bulk Modulus $M_{ss}$ / GPa |
|---|---|---|---|---|---|
| Alphafine | 38.1 | 0.039 | 36.0, 34.2, 33.6 | 0.40 | 25 |
| Centrifuged Alphafine | 22.1 | 0.067 | 40.5, 38.8, 38.4 | 0.27 | 38 |
| Alphafine with 14 pph D950 | 25.8 | 0.057 | 29.2, 27.7, 27.3 | 0.31 | 31.8 |
| Centrifuged Alphafine with 14 pph D950 | 10.3 | 0.143 | 31.4, 28.9, 27.5 | 0.91 | 11.0 |
| SPS with 17 pph latex Dried at 23°C | 34.7 | 0.042 | 19.8, 19.1, 17.9 | 0.70 | 14.2 |
| Dried at 110°C | 67.8 | 0.022 | 17.2, 15.0, 13.2 | 1.00 | 9.9 |
| SPS with 5 pph starch Dried at 23°C | 10.4 | 0.141 | 37.4, 37.5, 37.2 | 0.20 | 48.9 |
| Dried at 110°C | 10.2 | 0.144 | 38.8, 39.6, 38.0 | 1.26 | 7.9 |

### 7.3.1 Kaolin - Effects of changing particle size distribution

To indicate the differences in particle shape between calcite particles and kaolin particles, the consolidated structures of Alphafine and Centrifuged Alphafine have been viewed by SEM and the resulting micrographs, Plate 8 and Plate 9 are presented below for comparison with Plate 5.
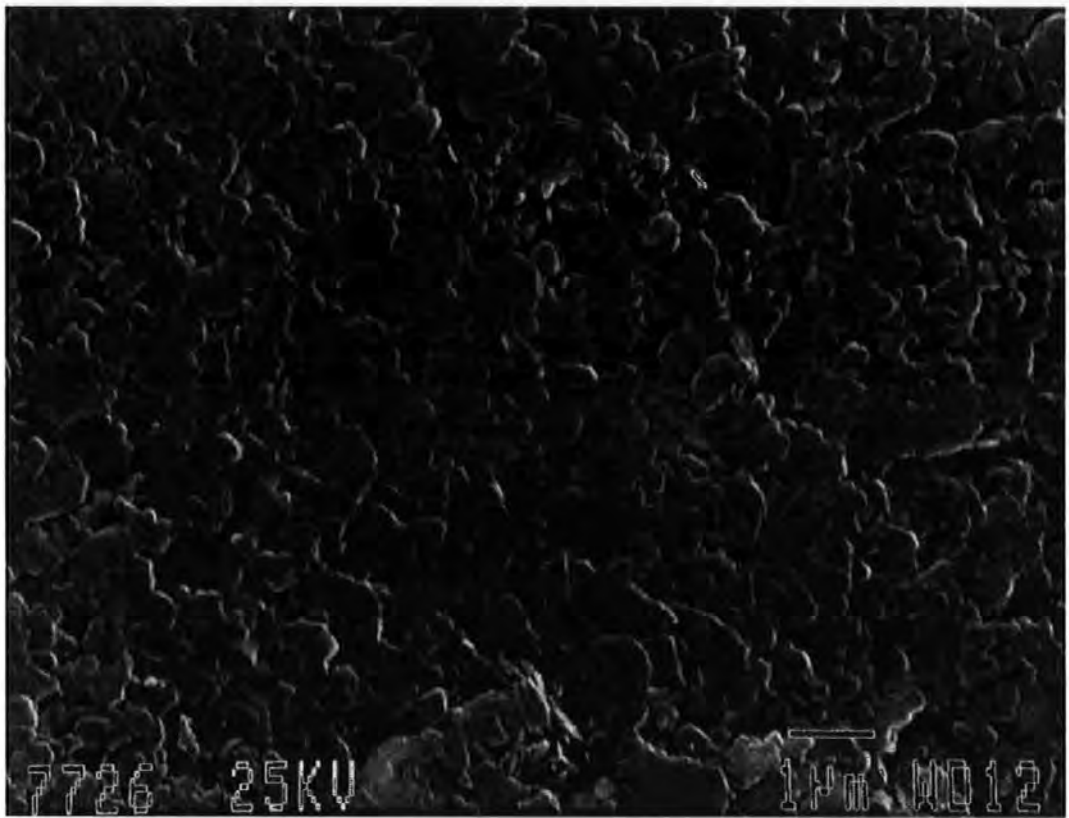


**Plate 8: Surface micrograph of Alphafine**
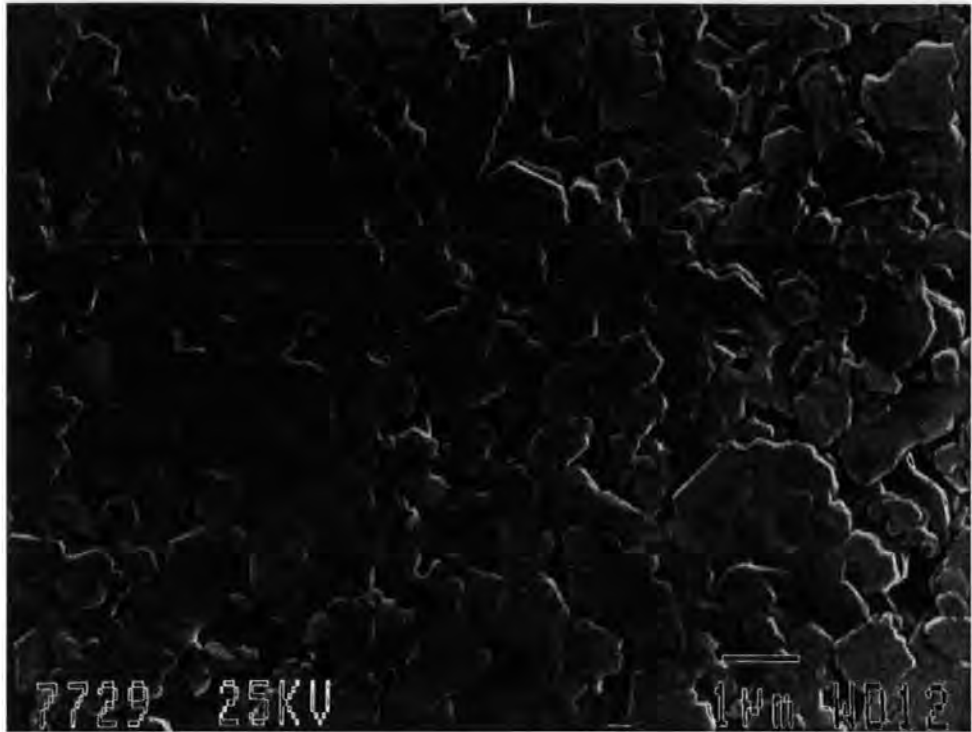
**Plate 9:  Surface micrograph of Centrifuged Alphafine**

The kaolins consist of higher aspect ratio (plate-like) particles than the calcites.  Alphafine was centrifuged to form Centrifuged Alphafine (Chapter 2) and comparison of Plate 8 and Plate 9 gives an indication of the ultrafine material removed from Centrifuged Alphafine.

The mercury porosimetry data for these consolidated samples are listed in Table 3 and shown in Figure 23.  The consolidated Centrifuged Alphafine was more porous and had a larger characteristic pore diameter than the consolidated Alphafine sample.
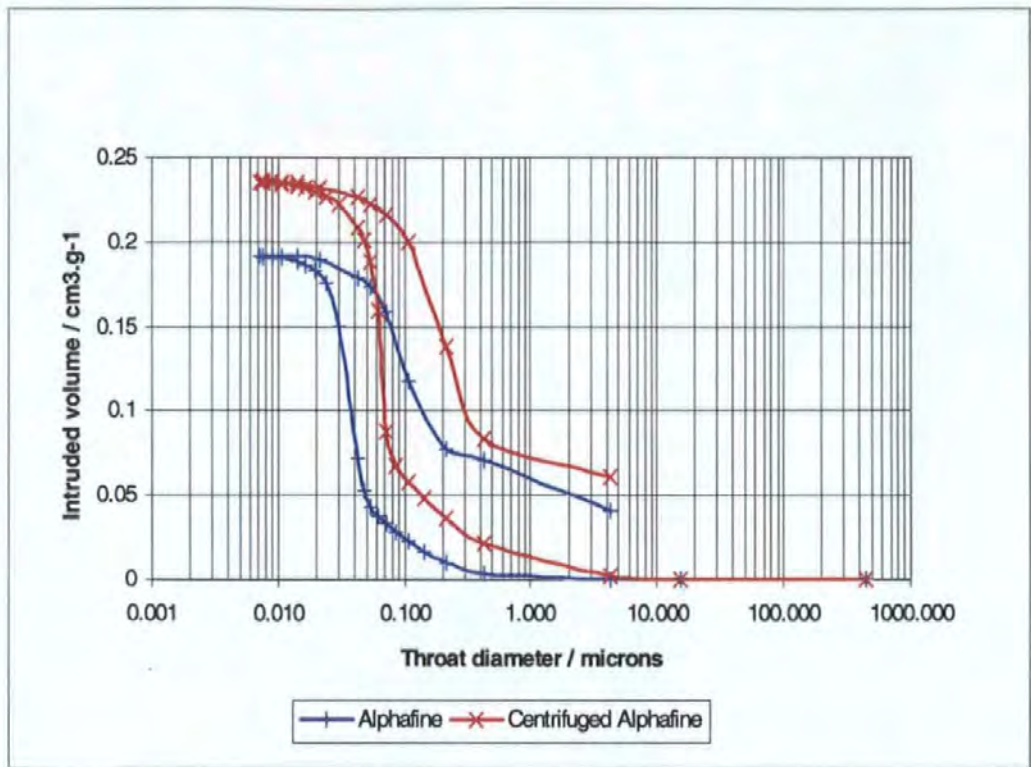
**Figure 23: Mercury porosimetry of dried slurry sample**

The hysteresis curves indicate that approximately 20 % of the intruded mercury is entrapped in the void space of the sample upon depressurisation. The structures formed by the Centrifuged Alphafine are less compressible than the Alphafine. A possible interpretation of this is that the bulk moduli are measures of the compressibilities of the "pigment-dispersant" composite and this may be partially dependent upon the surface area of the pigment. Hence the compressibility is reduced by removing fine particles from the system.

### 7.3.2 Comparison of the effect of adding 14 pph D950 latex to Alphafine and Centrifuged Alphafine

Addition of latex to the slurries produced consolidated samples which were less porous but had larger median pore sizes (Table 3). Packing of the latex spheres (approximately 0.15μm diameter) within the pigment matrix disrupts the packing of the pigment particles

88

prior to film formation and shrinkage. During consolidation, the latex film-formation within the void space may be envisaged as having formed "elastic diaphragms" which effectively mask the finer pores, Figure 24.
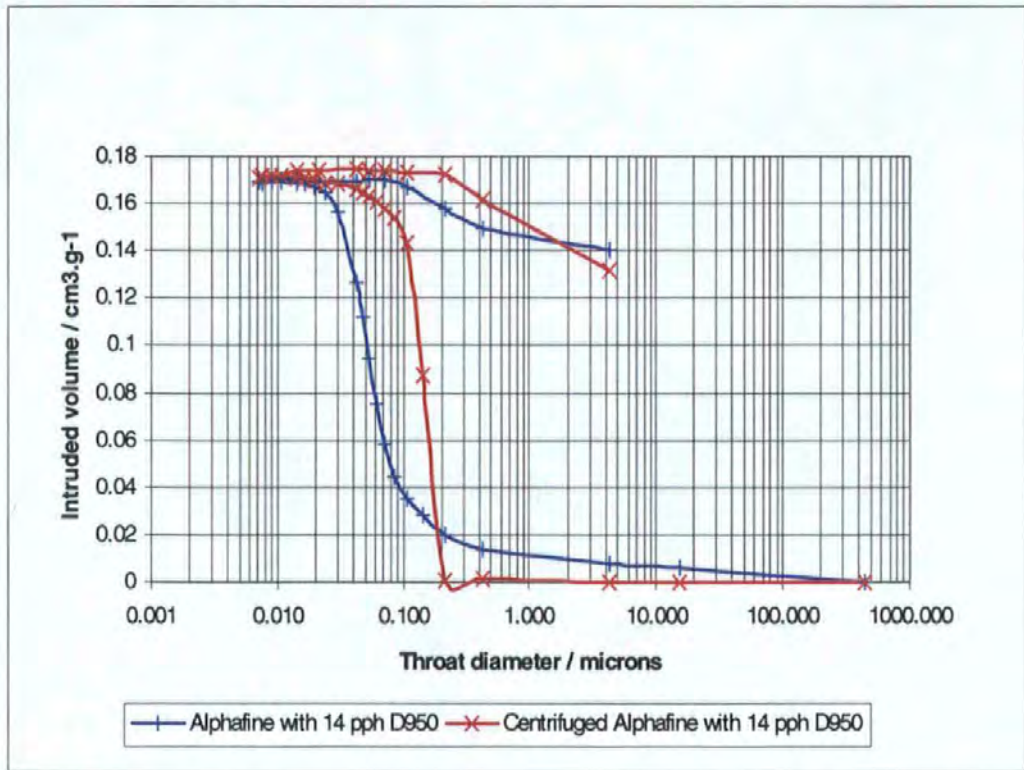


**Figure 24: Mercury porosimetry of kaolins with 14 pph D950**

The porosities at elevated pressures are lower than those measured at atmospheric pressure indicating that some of the pores are inaccessible. The hysteresis curves indicate that approximately 70% of the intruded mercury is entrapped in the sample upon depressurisation. This high level of entrapment can be related to an effective reformation of the "elastic diaphragms" which renders the pores narrower as the applied external pressure is reduced.

A Zeiss Elrepho reflectometer was used to measure the reflectances $R_O$ and $R_\infty$ (reflectance of single sheet and a stack of sheets respectively) at 550 nm of the coatings containing 14pph DL950 on a synthetic impermeable white substrate, Synteape. A program called "SK" was used to calculate the Kubelka-Munk light scattering, Gate (1974),

Robinson (1975), and Mark (1984) and light absorption coefficients from the Elrepho measurements (TAPPI T425) and these values are tabulated below:

**Table 4 : Optical properties of coatings**

| Pigment type | Light scatter / $cm^2g^{-1}$ | Light absorption / $cm^2g^{-1}$ |
|---|---|---|
| Alphafine | 1050 | 19.6 |
| Centrifuged Alphafine | 1250 | 17.7 |

The differing light-interactive pore space in these coating layers is evidenced by the changes in light scattering coefficient, Table 4. Centrifuged Alphafine has a steeper particle size distribution and its particles pack more loosely in the 0.1 μm to 0.3 μm pore diameter region to produce more intrusively porous coatings than the Alphafine sample. The pore size distributions of these samples in Figure 23 support these light scattering measurements and demonstrate that mercury porosimetry intrudes the light interactive pore space.

### 7.3.3 Paper and Printing properties of Alphafine and Centrifuged Alphafine

The ink-tack development cycle after printing with a two-phase ink on a coated paper has been measured. This technique described in Chapter 3 studies the interaction between fluid phase imbibition, as determined by the pore structure and wettability, and the adhesion between the wet ink and the coating surface. Basically the instrument measures the force required to separate a nitrile rubber printing disc contacting a setting print at known time intervals. Figure 25 illustrate the tack force generation of the Alphafine and Centrifuged Alphafine coatings (with various latex doses) coated onto a basepaper.
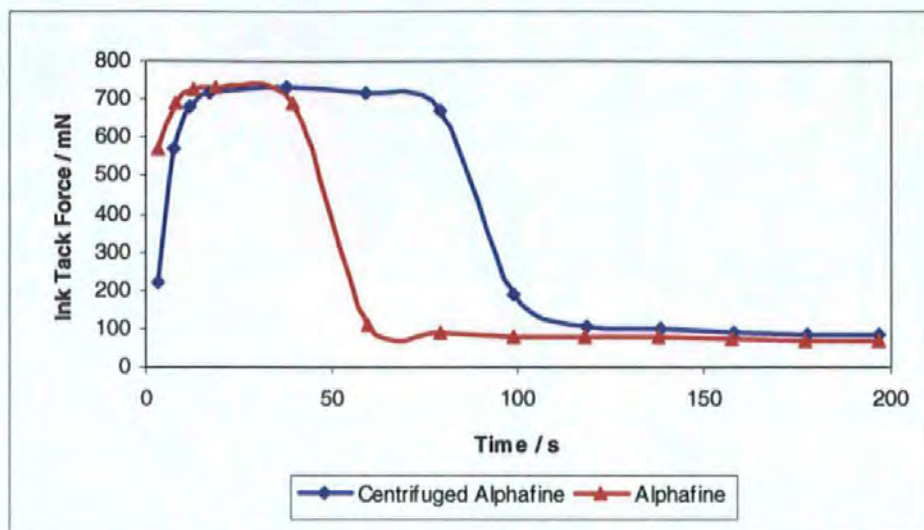
**Figure 25: Ink tack force for Alphafine coatings**

The ink tack development curves for all of the samples are basically similar in shape and each curve may be divided up into three segments: an initial rise in tack force, a plateau, followed by a decay in tack force. The initial rise in tack force is related to the rate of imbibition of ink into the coating upon initial contact. The Alphafine coating is more microporous to imbibition than the coating of Centrifuged Alphafine, as expected from the particle size distribution.

The plateau of the tack cycle curve corresponds to the maximum separation force and is related, for glossy papers, to the adhesivity of the wet immobilised ink layer to the coating.

The ink tack force decay is related to the drying of the ink at longer timescales and is a measure of the "total available" pore volume for the imbibition of ink solvent, i.e. the earlier the onset of tack decay the higher the total pore volume. The tack decay was slower for Centrifuged Alphafine than for Alphafine. This may be interpreted as relating to the presence of more "free" latex in the coatings associated with the lower surface area pigment, Centrifuged Alphafine, which more effectively masks imbibing pores. Another theory is that as the ink layer loses solvent, it starts to behave like a microporous structure

and the larger pores (e.g. Centrifuged Alphafine) can no longer win the "capillary tug of war" for solvent.

### 7.3.4 Effects of formulation type and drying rate

A different kaolin was used in this part of the project. The full details of this pigment are given in Section 2.3. The structure of consolidated SPS has been viewed by SEM and the micrograph is shown below (Plate 10). The micrograph indicates that this pigment has a very high aspect ratio, with a mean particle diameter in the region of 0.8 $\mu$m to 1 $\mu$m.
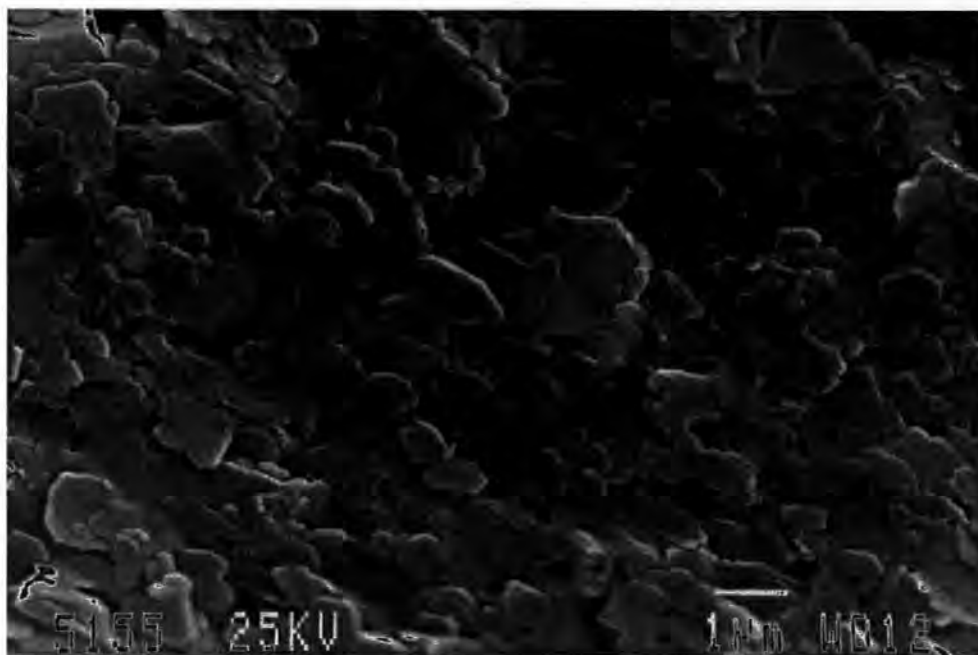


**Plate 10:  Surface micrograph of SPS coating**

Two sets of consolidated SPS structures were formed, the first set contained 17pph latex and the second set contained 5 pph starch. The mercury porosimetry curves for the latex containing samples are shown in Figure 26, and have characteristic properties listed in Table 3.
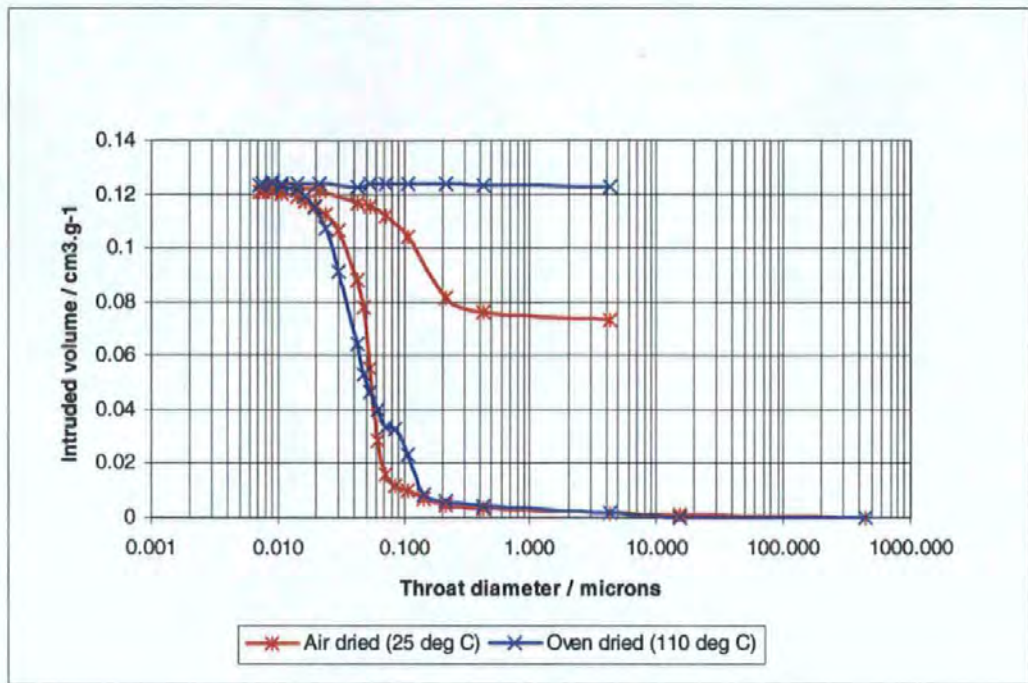
**Figure 26: Mercury porosimetry data for SPS with 17 pph latex**

The sample which had been air dried at ambient temperature had the largest characteristic throat size and the highest porosity. By drying this system at 110°C more shrinkage had occurred and both the porosity and the characteristic throat size were reduced. The extrusion data for the latex containing samples are also shown in Figure 26 and it is clear from these data that the use of heat has produced a structure which entraps mercury upon depressurisation of the porosimeter. This may be due to the presence of latex which has film-formed to produce "elastic" diaphragms within the interconnected pore network which can be penetrated by mercury during the pressurisation part of the cycle. However, upon depressurisation mercury cannot "manoeuvre" around these "partially reformed" diaphragms and mercury remains trapped within the pore structure of the sample. These hysteresis arguments have been discussed earlier (Section 4.4)
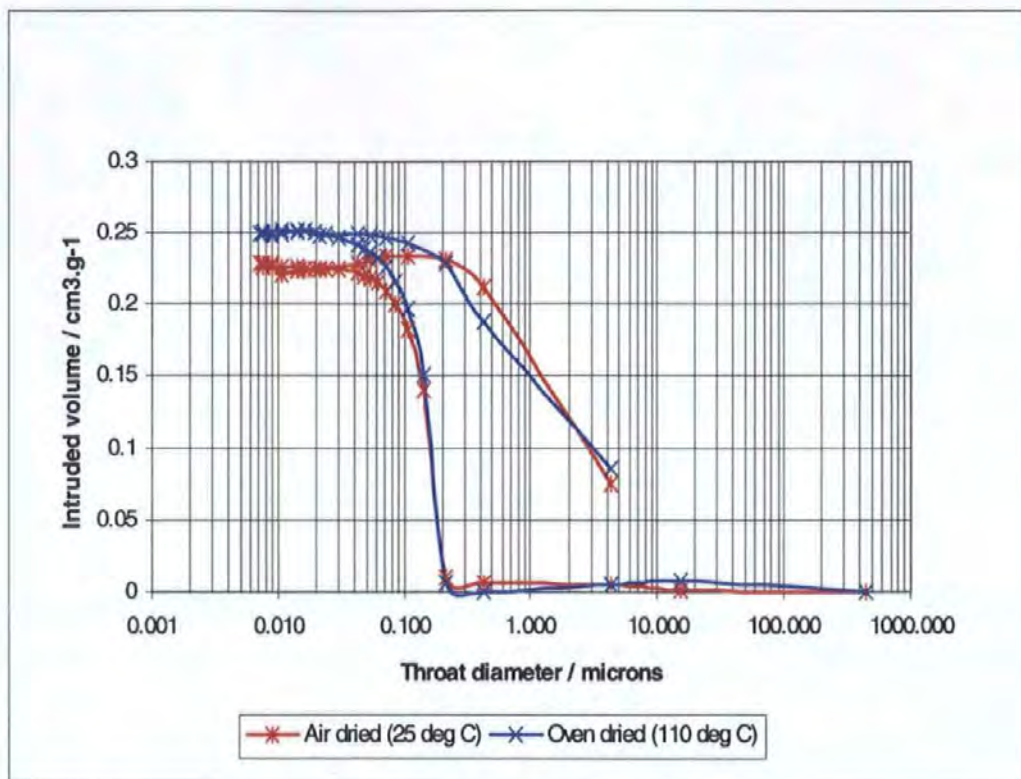
**Figure 27: Mercury porosimetry data for SPS with 5 pph starch**

The porosities of the starch-containing samples were larger than those for the samples that contained 17 pph latex. The characteristic throat size and porosity of the SPS / starch samples were slightly larger than SPS / latex, but in contrast to the samples containing latex, were unaffected by drying temperature (Figure 26). The samples which contained 5 pph starch did not entrap significant quantities of mercury upon depressurisation, Figure 26. This may be due to the lower level of binder and the fact that if the binder had formed diaphragms within the interconnected pore network, they may be inelastic, as starch films are brittle, and once penetrated, would not reform to hinder the extrusion of mercury.

The comparison between the latex containing samples and the starch containing samples highlights the packing properties of the latex spheres at room temperature and subsequent film formation associated with shrinkage at elevated temperatures. Starch is film-forming at all temperatures studied, and no significant progressive structural change is detected at

elevated temperature. The bulk moduli values indicate that the oven dried samples were more compressible than the air dried samples This is possibly due to the location of the binder films within the particle interfaces.

## 7.4    *Porosimetric measurements of paper samples*

### 7.4.1   Paper samples

A set of very simple commercially produced papers was also examined. Samples of paper containing a kaolin filler were calendered using a variety of different conditions (Chapter 2). The physical properties of the papers were measured using a range of conventional procedures as discussed in Chapter 3. The z-direction thicknesses (calipers) of the papers were measured using optical microscopy and image analysis and the air permeabilities of the papers were measured using a Gurley Permeability tester. Alignment of the kaolin particles within the sheet was assessed using X-ray diffraction and the pore structures of these papers were characterised using both mercury porosimetry and liquid porosimetry. A unique feature of this work is that for the first time it has been shown that two porosimetric techniques which measure overlapping pore size distributions may be combined to give a better indication of the total pore size distribution.

### 7.4.2   Physical properties of papers

An ESEM was used to produce images of the surface and section through each sample. A selection of these micrograph images are presented on the following pages. The uncalendered paper has more variable topography (is rougher) and has a more porous structure than the calendered papers. The supercalendered paper has a very smooth surface and its section is more dense than the sections of the soft calendered papers. This would be expected because the supercalendering conditions applied pressure to the sample for the

longest period of time. The appearance of the soft calendered sheets was intermediate between uncalendered sample and supercalendered samples, and the sheet that had been calendered at 400 m.min$^{-1}$ was less porous than the sheet calendered at 1800 m.min$^{-1}$ .
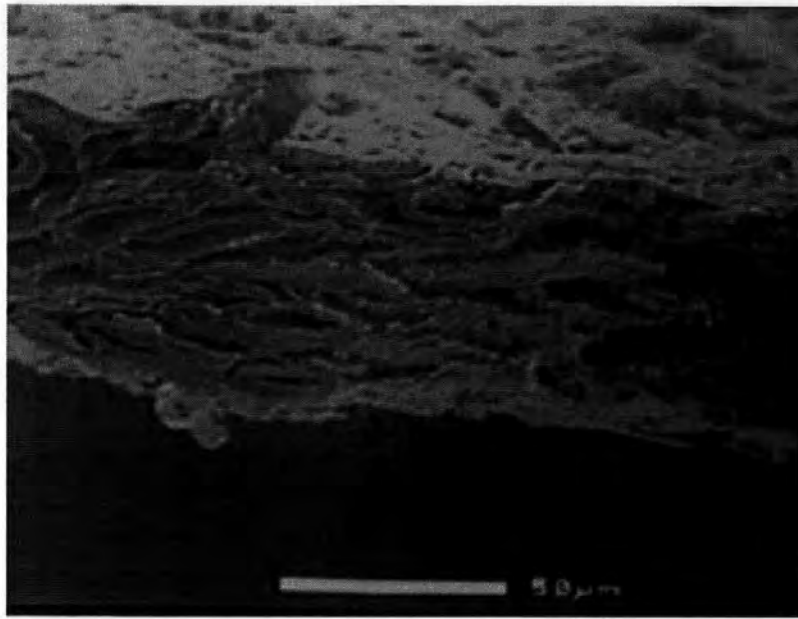
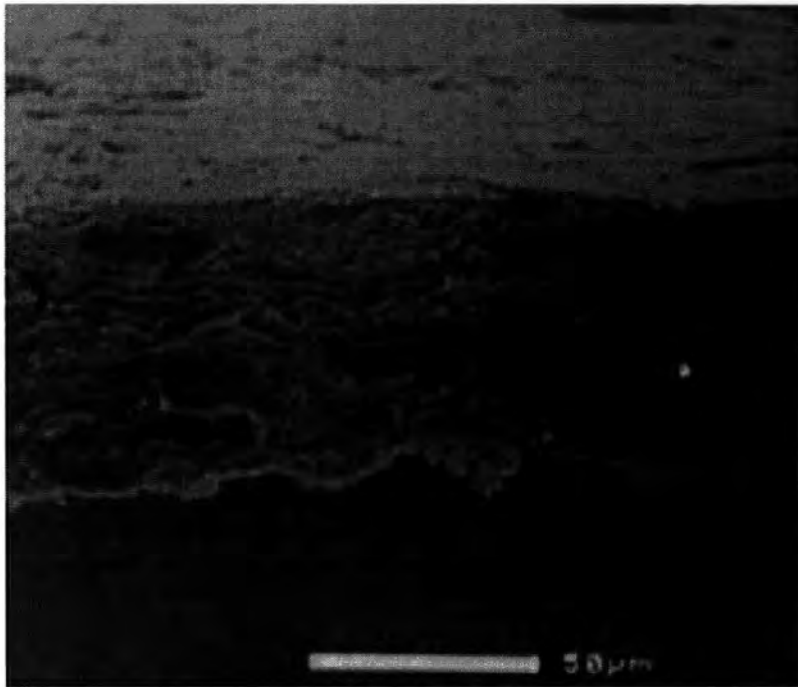Plate 11 : Uncalendered basepaper
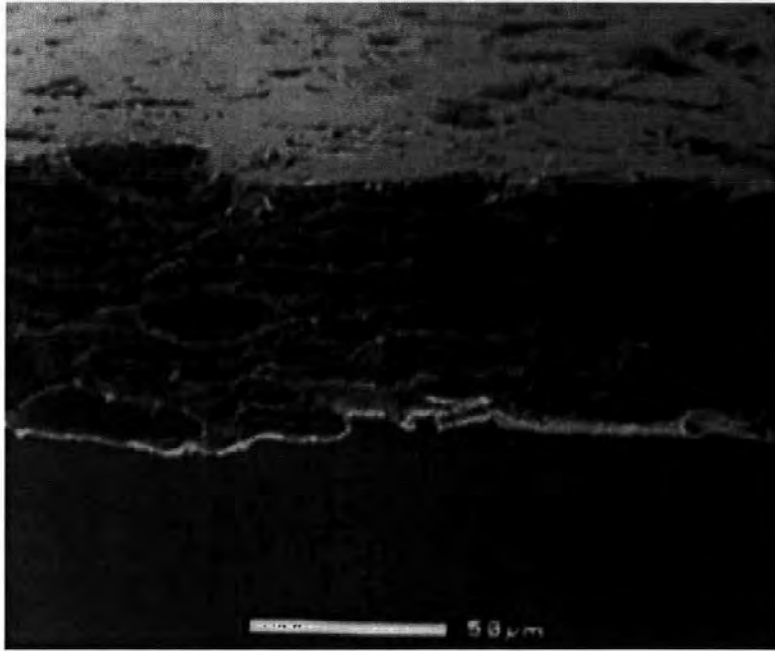


Plate 12: Supercalendered paper
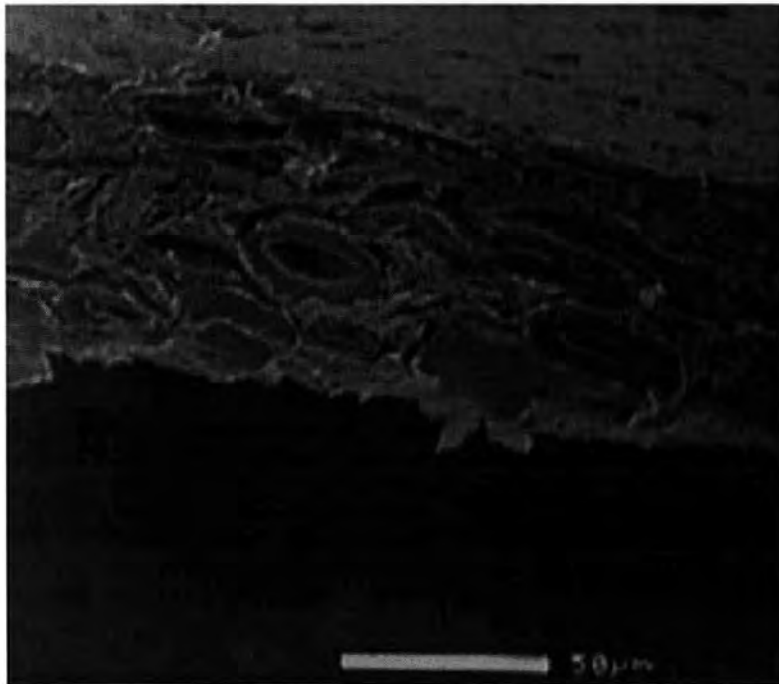
Plate 13: Soft calendered at 400m.min-1



Plate 14: Soft calendered at 1800 m. min-1

98

The physical dimensions of the papers expressed in terms of their mean calipers are listed in Table 5. The substance values of the sheets were determined by weighing known areas of the sheets. The respective densities and proportions of the solid materials (e.g. fibre and filler) are known. This information is sufficient to calculate the sheet porosities. As expected, the uncalendered basepaper sheet was the most porous and the sheets calendered after steam pretreatment had lower porosity than their equivalents that had been calendered without steam pretreatment. The conventional optical and printing properties of all the paper samples in this study were measured according to standard test procedures (TAPPI, Chapter 3) and the results are listed in Table 6.

Calendering the papers increased the sheet gloss and lowered the brightness and opacity. The improvement in sheet gloss is due to improved sheet smoothness. The decrease in sheet brightness is due to reduction in light scattering ability and increase in light absorption values. Supercalendering caused the paper to have the largest drop in brightness and had the lowest light scattering ability. The decrease in opacity is due to the papers being compressed to form thinner papers.

The XRD values indicated that the uncalendered sample had the lowest degree of particle orientation. Increasing the extent of calendering (by reducing the calender speed) improved the degree of particle orientation. Supercalendering generated the highest degree of particle alignment.

The Gurley Densometer (Section 3.1.4) was used to measure the time taken for 100 ml of air to pass through a specific cross-sectional area of the sheet. These values indicated that air permeability was very sensitive to the degree of calendering and the effect of steam pretreatment that the sheet had experienced; i.e. a high degree of calendering resulted in a

sheet of low permeability. It is possible to modify equation 1 to take into account the test cross-sectional area, the sample caliper and the time taken for 100 ml to flow through the sheet in order to convert these values into microDarcies (μD). These values are listed alongside the permeability air flow rate values in Table 5.

In general, the samples which had been steam pretreated (marked Y in Table 5) to increase their temperature and moisture content had superior paper and printing performance compared to samples which did not have any steam pretreatment (marked N in Table 5); i.e. higher sheet and print gloss, improved (lower) smoothness and lower permeability.

## Table 5: Physical dimensions of the papers

| | Uncalendered basepaper | Soft / 400 / Y | Soft / 400 / N | Soft / 800 / Y | Soft / 800 / N | Soft / 1800 / Y | Soft / 1800 / N | Super / 800 / Y | Super / 800 / N |
|---|---|---|---|---|---|---|---|---|---|
| Mean caliper / microns | 66.01 | 51.31 | 58.42 | 50.48 | 54.68 | 58.80 | 57.24 | 46.49 | 53.69 |
| Substance / gm-2 | 53.34 | 54.01 | 53.18 | 53.18 | 53.09 | 52.95 | 52.89 | 52.58 | 52.36 |
| Sheet density / g.cm-3 | 0.808 | 1.053 | 0.910 | 1.054 | 0.971 | 0.900 | 0.924 | 1.131 | 0.975 |
| Solid phase density / g.cm-3 | 1.723 | 1.723 | 1.723 | 1.723 | 1.723 | 1.723 | 1.723 | 1.723 | 1.723 |
| Sheet volume / cm3.g-1 | 1.238 | 0.950 | 1.099 | 0.949 | 1.030 | 1.111 | 1.082 | 0.884 | 1.025 |
| Solid phase volume of sheet / cm3.g-1 | 0.580 | 0.580 | 0.580 | 0.580 | 0.580 | 0.580 | 0.580 | 0.580 | 0.580 |
| Sheet Porosity / % | 53.103 | 38.906 | 47.173 | 38.857 | 43.654 | 47.742 | 46.370 | 34.362 | 43.402 |

## Table 6:  Measured properties of the paper samples

| Sample Reference | Gloss | Brightness | Opacity | Light scatter "S" / $cm^2.g^{-1}$ | Light absorption "k" / $cm^2.g^{-1}$ | Smoothness / $\mu m$ | XRD Degree of particle orientation | Print Gloss | Print Density | Gurley Permeability/ sec. / 100ml, microDarcies ($\mu D$) |
|---|---|---|---|---|---|---|---|---|---|---|
| Uncalendered | 4.1 | 70.1 | 94.0 | 696 | 26.4 | 5.87 | 3.79 | | | 60, 2357 |
| soft / 400 / Y | 34.3 | 67.7 | 92.9 | 597 | 27.5 | 1.31 | 1.37 | 57 | 1.86 | 308, 357 |
| soft / 400 / N | 28.8 | 68.0 | 93.2 | 618 | 28.5 | 1.43 | 1.36 | 55 | 1.83 | 240, 522 |
| soft / 800 / Y | 28.6 | 68.1 | 93.3 | 609 | 27.8 | 1.58 | 1.34 | 54 | 1.88 | 220, 492 |
| soft / 800 / N | 24.2 | 68.6 | 93.3 | 631 | 27.8 | 1.74 | 1.55 | 50 | 1.77 | 200, 587 |
| soft / 1800 / Y | 19.7 | 68.5 | 93.6 | 648 | 28.3 | 2.06 | 1.45 | 35 | 1.59 | 136, 927 |
| soft / 1800 / N | 14.7 | 68.3 | 93.9 | 660 | 28.3 | 2.30 | 1.62 | 31 | 1.72 | 122, 1005 |
| super / 800 / Y | 35.4 | 66.7 | 91.9 | 534 | 28.3 | 1.26 | 0.94 | 58 | 1.90 | 368, 271 |
| super / 800 / N | 25.8 | 68.3 | 93.0 | 611 | 28.1 | 1.53 | 1.18 | 47 | 1.76 | 276, 425 |

Key to sample references:  e.g. soft / 400 / Y means that the sheet had been soft nip calendered at 400 m.min$^{-1}$ with a steam shower before the calender nip

### 7.4.3 Mercury porosimetry of paper samples

A measured area (76 mm x 26mm) of each paper sample was subjected to mercury porosimetric analysis using the same parameters as specified for the consolidated pigment samples (Section 3.7). The mercury porosimetry curves for the papers are shown in Figure 28 and Figure 29, with characteristic properties shown in Table 7.

**Table 7: Mercury porosimetry data for the paper samples**

| Type of Sample | Characteristic Pressure, $P_{50}$ / MPa | Characteristic Diameter $d_{50}$ / $\mu$m | Porosity / % $\phi_{cal}$, $\phi'$, $\phi_{corr}$ | Compressibility $\psi_{ss}$ / $10^{-10}$ Pa$^{-1}$ | Bulk Modulus $M_{ss}$ / GPa |
|---|---|---|---|---|---|
| Uncalendered | 0.87 | 1.69 | 53.1, 64.1, 64.9 | 0.13 | 79.9 |
| soft / 400 / Y | 0.90 | 1.63 | 38.9, 45.0, 45.2 | 3.70 | 2.7 |
| soft / 400 / N | 0.88 | 1.68 | 47.1, 42.9, 44.1 | 1.63 | 6.1 |
| soft / 800 / Y | 1.03 | 1.43 | 38.9, 49.0, 49.1 | 4.24 | 2.3 |
| soft / 800 / N | 0.79 | 1.87 | 43.7, 48.6, 48.4 | 2.69 | 3.7 |
| soft / 1800 / Y | 1.10 | 1.34 | 47.7, 54.9, 52.2 | 1.72 | 3.8 |
| soft / 1800 / N | 0.95 | 1.55 | 46.3, 51.3, 52.4 | 3.20 | 3.1 |
| super / 800 / Y | 0.44 | 3.31 | 34.3, 43.7, 42.3 | 2.76 | 3.6 |
| super / 800 / N | 1.05 | 1.40 | 43.4, 44.5, 44.9 | 6.03 | 1.7 |

The mercury porosimetry curves cover a wide range of throat diameters extending over the range of 200 $\mu$m down to 0.007 $\mu$m. It was assumed, from the ESEM micrographs, that the pore volume attributed to throat diameters greater than 40$\mu$m resulted from sheet roughness (e.g. edge effects) rather than pore volume attributed to the bulk of the sheet. Hence the characteristic ($d_{50}$) diameters were calculated as the 50 % volume between the throat diameters of 40 $\mu$m to 0.007 $\mu$m. The mercury porosimetry data for the non steam pretreated sheets, Figure 28, shows that the uncalendred basepaper has the highest pore

volume in the 200 μm to 40 μm throat diameter region, i.e. the sheet surface is the roughest. This is in agreement with the Parker Printsurf results listed in Table 6. There is a step-wise decrease in the porosimetry curves for the soft calendered sheets, in line with the speed at which the sheets were calendered, i.e. the sheet calendered at 400 m.min^{-1} is less porous than the sheet calendered at 1800 m.min^{-1}. The porosimetry curve for the supercalendered sheet is almost coincident with the slowest soft calendered sheet. This indicates that without steam pretreatment it is possible to match the porous nature of the sheet by both calendering techniques. This finding has industrial significance due to the growing trend towards on-line soft calendering rather than off-line supercalendering. The calendered papers were more compressible than the uncalendered basepaper (Table 7).
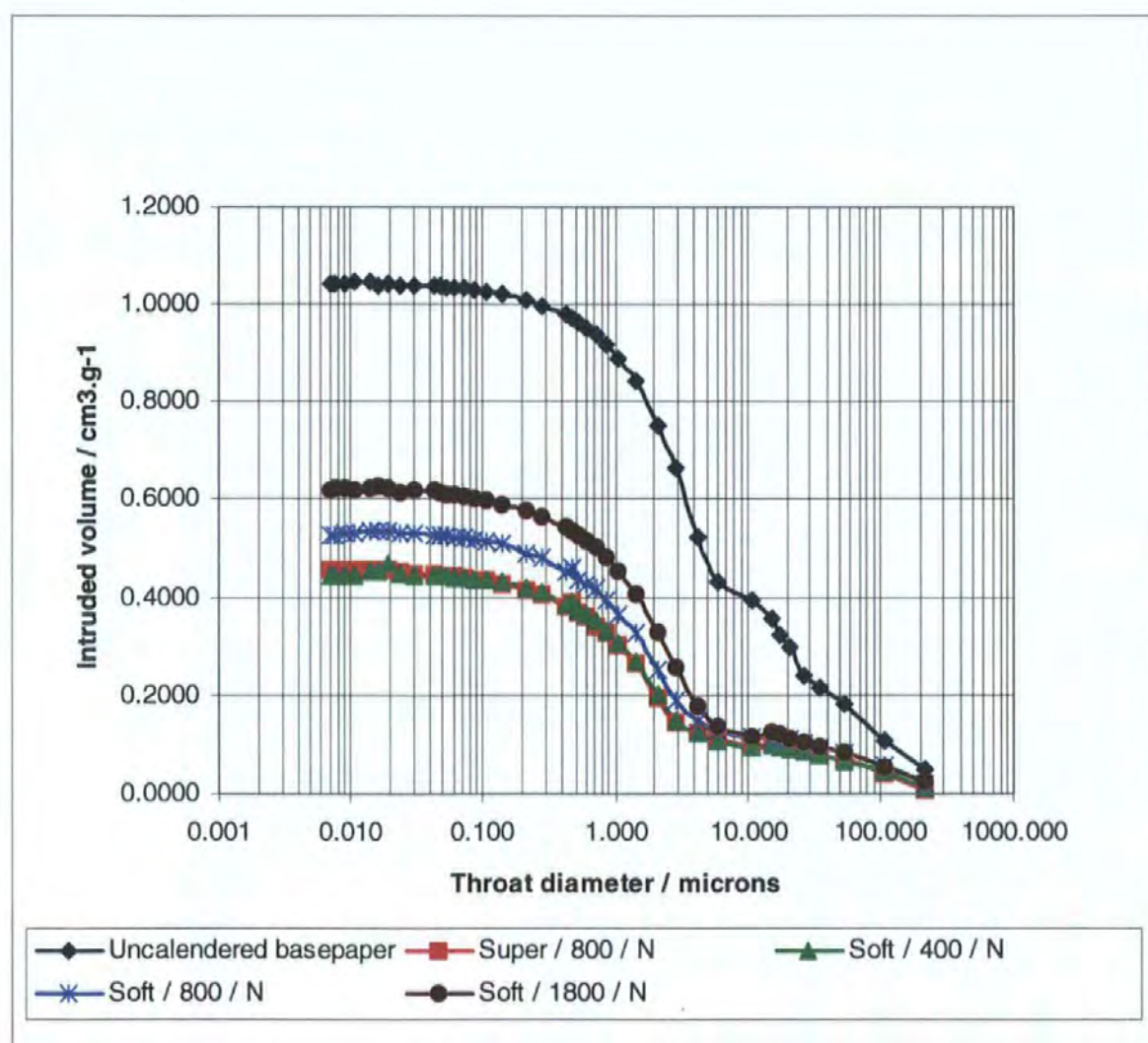


Figure 28: Mercury porosimetry of paper samples (without steam pretreatment)
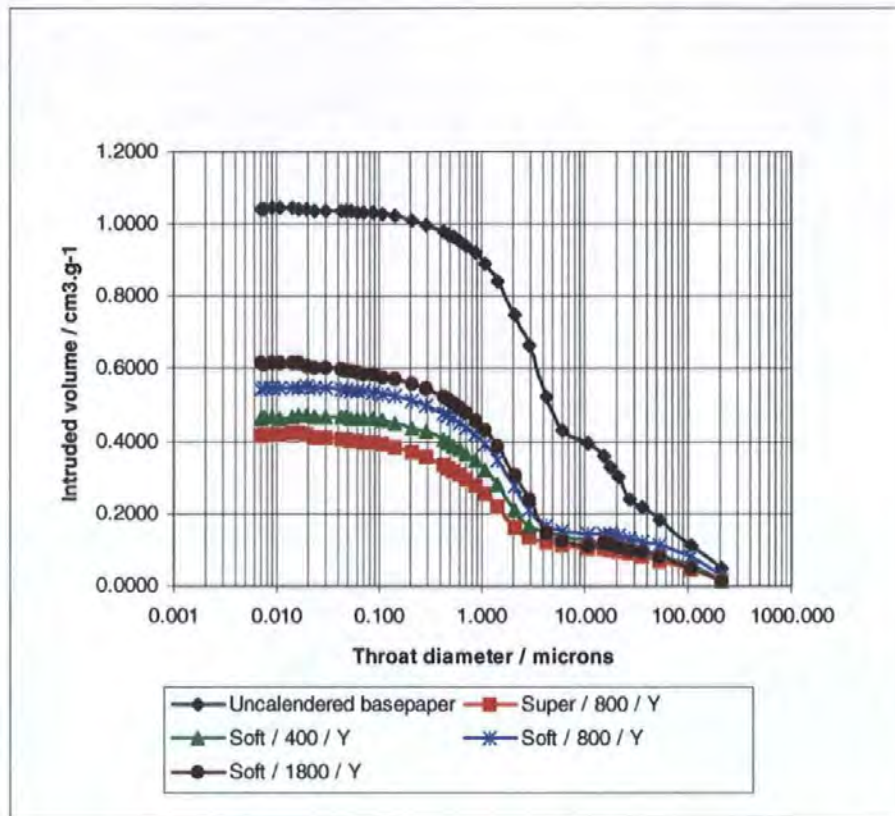
**Figure 29: Mercury porosimetry data for paper samples (with steam pretreatment)**

Figure 29 shows the mercury porosimetry data for the steam pretreated sheets, and there is a better distinction between the sheets calendered under different conditions. The steam pretreated calendered sheets had nominally lower porosity than their non steam pretreated equivalents. The use of steam pretreatment prior to supercalendering generated the most dense (least porous) sheet.

### 7.4.4 Liquid porosimetry of paper samples

The liquid porosimeter was used to measure the distributions of pore volume in the throat diameter region of 800 μm to 6 μm of the sheets used in this study. Figure 30 shows the liquid porosimetry curves for the sheets calendered without steam pretreatment. In line with the mercury porosimetry data, the uncalendered sheet was the most porous and there was a step-wise decrease in porosity as the calendering speed of the soft calender was reduced. The supercalendered sheet had the lowest porosity. The curves on the graph do

104

not reach zero volume because there is still some hexadecane probe liquid that has been retained in the porous structures of the sheets. The point of inflection that is present in the data for the uncalendered basepaper (throat diameter 30 µm to 40 µm) is reduced and shifted to a narrower throat diameter for the sheet that had been soft calendered at 1800 m.min$^{-1}$. This point of inflection is absent from the liquid porosimetry data of the more strongly calendered sheets because calendering has decreased the pore volumes of the sheets and shifted the distribution of throat diameters to smaller sizes.
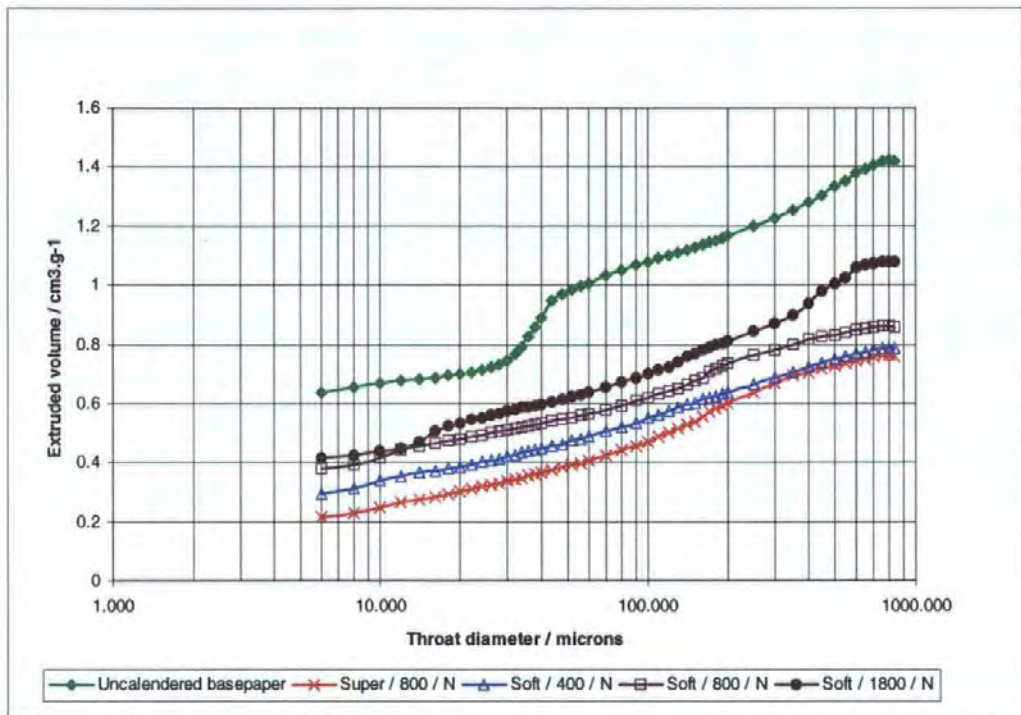


**Figure 30: Liquid porosimetry data for paper samples (without steam pretreatment)**
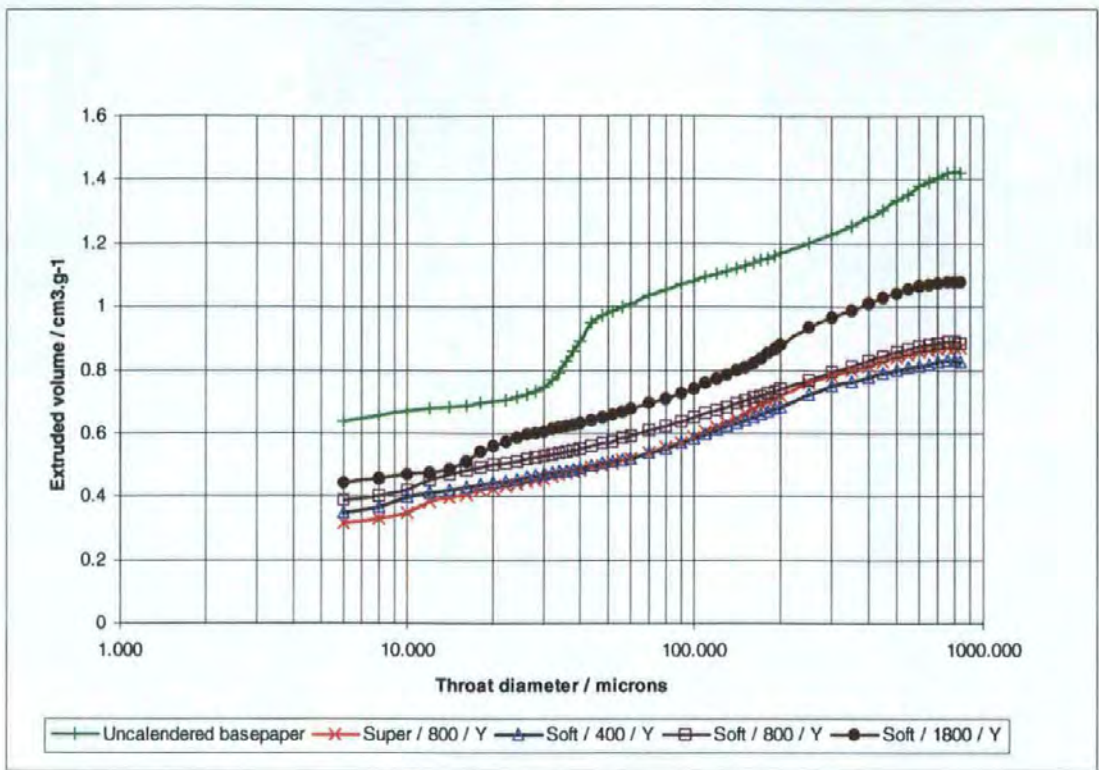
**Figure 31: Liquid porosimetry data for samples (with steam pretreatment)**

### 7.4.5 Combination of mercury porosimetry and liquid porosimetry data

The technique for combining these two types of porosimetry data has been described earlier in section 5.7. To illustrate this technique the data sets for sample, Soft / 400 / Y, were combined and the results are shown in Figure 32. By making this correction most of the pore volume associated with throat diameters greater than 40 microns can be considered to be an artefact of edge effects associated with surface features. This data was used for Pore-Cor simulation (Section 8.4).
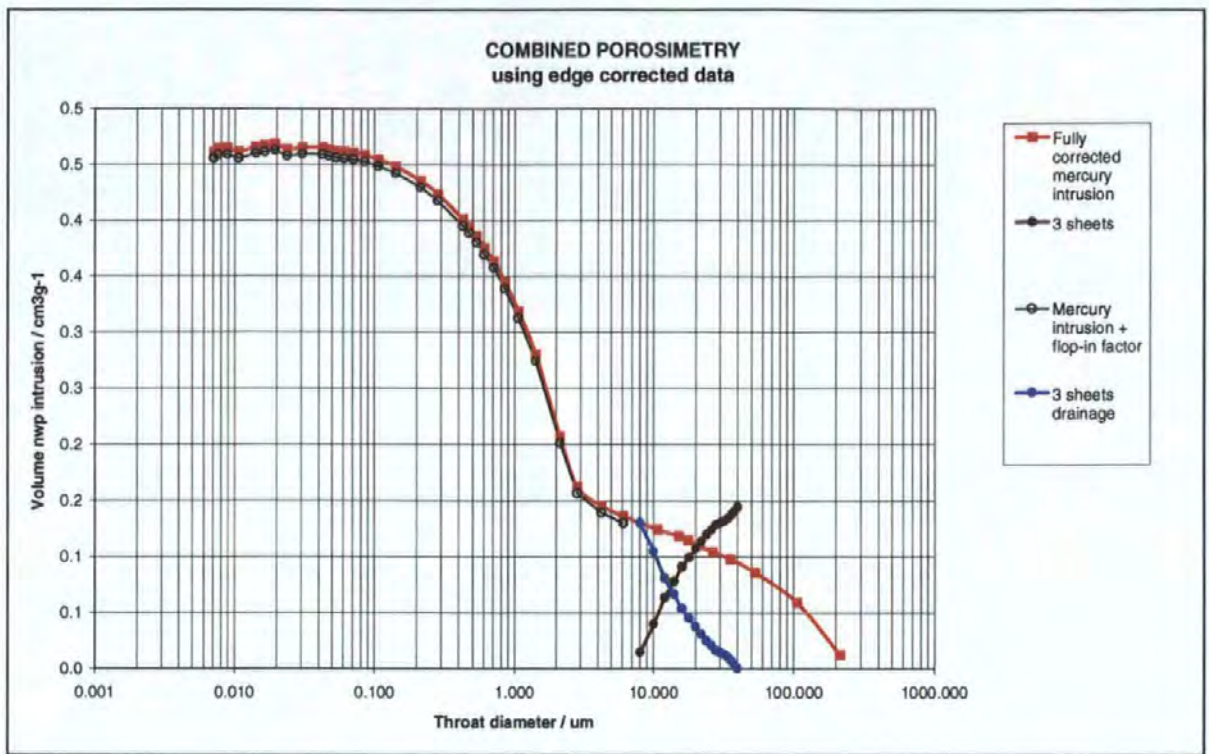
**Figure 32: Combined porosimetry curves for sample soft/400/y**

**Table 8: Summary of combination porosimetry**

| | All Pore Volume | Limited Pore Volume | Best fit pore volume data | |
|---|---|---|---|---|
| Density of solid phase: | 1.723 | 1.723 | 1.723 | g.cm-3 |
| Mercury intrusion, ignoring large pores: | 0.462 | 0.462 | 0.325 | cm3 g-1 |
| Hexadecane intrusion 6-40 um: | 0.490 | 0.281 | 0.073 | cm3 g-1 |
| Combined intrusion: | 0.952 | 0.743 | 0.398 | cm3 g-1 |
| Solid phase: | 0.580 | 0.580 | 0.580 | cm3 g-1 |
| Total vol: | 1.532 | 1.323 | 0.978 | cm3 g-1 |
| Total density: | 0.653 | 0.756 | 1.022 | g.cm-3 |
| Average caliper of a single sheet: | | 51.307 | 51.307 | microns |
| Density based on average caliper value: | | | 1.039 | g.cm-3 |
| Total porosity based on density measurements: | 0.621 | 0.561 | 0.441346 | |
| Porosity from Hg intrusion, ignoring large pores: | 44.299 | 44.299 | 35.912 | |
| Total porosity from Hg/hex ratio: | 0.91 | 0.71 | 0.439 | |

Table 8 summarises the calculation steps that were made in order to optimise the combination of porosimetry data. The porosity was found to be 91 % when all the pore volume measured by both porosimetry techniques was included. This is much higher than would be expected and is clearly heavily weighted by surface roughness features. By including only the pore volume attributed to pores less than 100 micron throat diameter, the

including only the pore volume attributed to pores less than 100 micron throat diameter, the porosity value was reduced to 71 %. Using a fitting technique, it was found by using the pore volume values attributed to throats less than 40 micron throat diameter a value of 43.9 % porosity was calculated. This is in good agreement with the value measured by mercury porosimetry in which the pore volume attributed to large pores were ignored.

# 8. VOID SPACE MODELLING RESULTS

## *8.1 Computer simulation results of plastic pigments.*

The corrected mercury intrusion data were simulated by the Pore-Cor computer program. The resulting simulated intrusion curves all matched the experimental curves closely. The liquid and air permeabilities of the simulated structures were calculated using the calculations described in Section 6.3. A summary of the calculated data for the plastic pigment samples is given in Table 9.

### Table 9: Simulated data for consolidated plastic pigment systems and calcite systems

| Sample Reference | Minimum throat diameter / μm | Maximum throat diameter / μm | Skew | Connectivity | Unit cell length / μm | Porosity / % $\phi_{exp}, \phi_{sim}$ | Permeability micro Darcies μD Liquid , Air ($N_2$) |
|---|---|---|---|---|---|---|---|
| HP91 | 0.04 | 1.0 | 0.47 | 3.3 | 11.05 | 32.9, 32.9 | 43.4, 159 |
| L2601 | 0.007 | 1.0 | 0.46 | 2.9 | 10.14 | 27.9, 27.9 | 0.85, 6.16 |
| L2301 | 0.007 | 0.427 | 0.84 | 2.7 | 4.46 | 23.2, 23.2 | 0.033, 0.73 |
| C90 | 0.007 | 0.213 | 0.54 | 2.9 | 2.43 | 26.2, 26.2 | 0.37, 6.38 |
| C60 | 0.007 | 0.427 | 0.09 | 2.8 | 4.74 | 28.8, 28.8 | 1.83, 15.5 |
| LX60 | 0.007 | 0.7 | 0.1 | 4.0 | 7.20 | 40.9, 40.9 | 33.3, 154 |
| C90 + S801 | 0.007 | 0.427 | 0.02 | 3.0 | 5.80 | 19.4, 19.4 | 1.55, 13.3 |
| C90 + 95L10 | 0.007 | 0.427 | 0.74 | 3.5 | 5.36 | 19.3, 19.3 | 1.02, 8.67 |
| C90 + DL950 | 0.007 | 0.427 | 0.67 | 3.3 | 5.11 | 21.3, 21.3 | 0.51, 5.72 |

### 8.1.1 Monosized spheres - Ropaque HP91

The inter-particle void space structure of Ropaque HP91 before the collapse of its polystyrene spheres has been simulated. The throat diameter and pore size distribution covers a range from 0.04 μm to 1.0 μm, Figure 33, the minimum throat diameter being

much larger than the minimum throat diameter of the other plastic pigment samples. The simulated permeability of the Ropaque sample is higher than any of the previous structures, at 43.4 µD for liquid and 159 µD for air, because of the larger minimum throat diameter, coupled with a skew towards larger sizes.
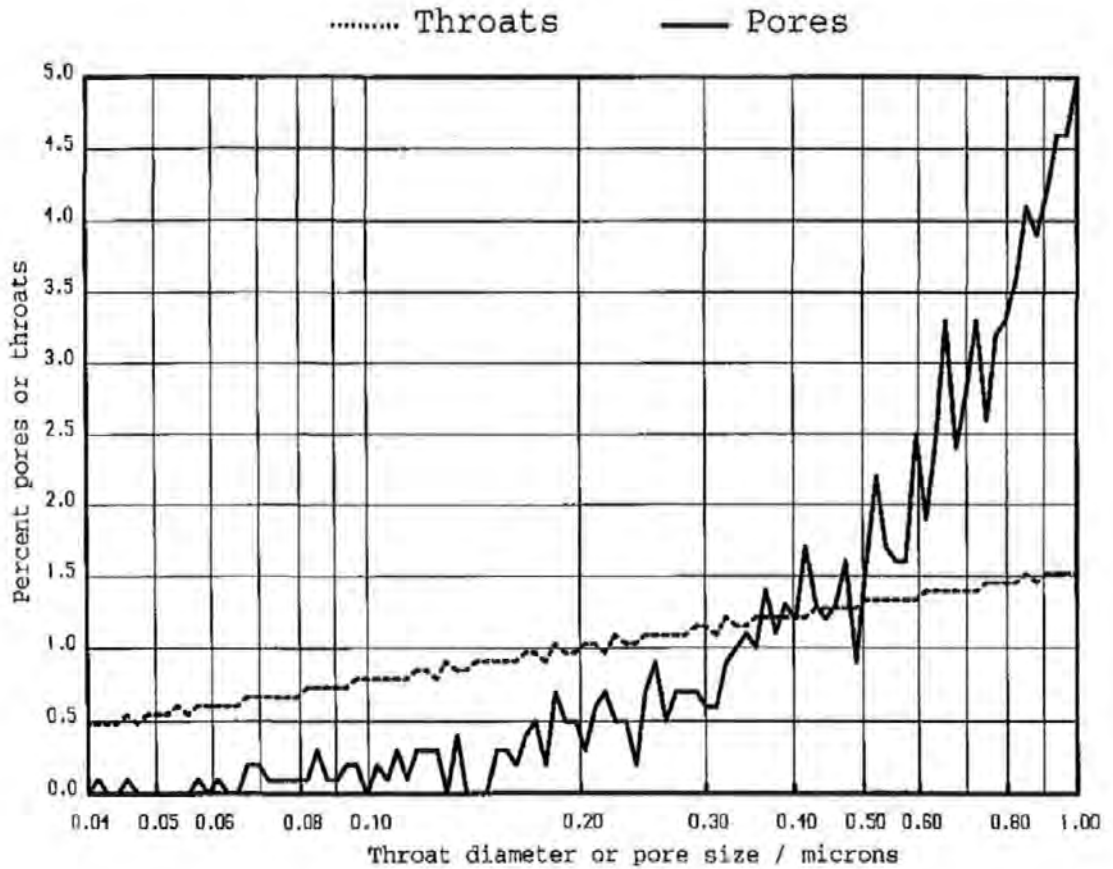


Figure 33: Pore and throat size distribution for Ropaque HP91

The 3D unit cell generated by this simulation is shown in Figure 34.
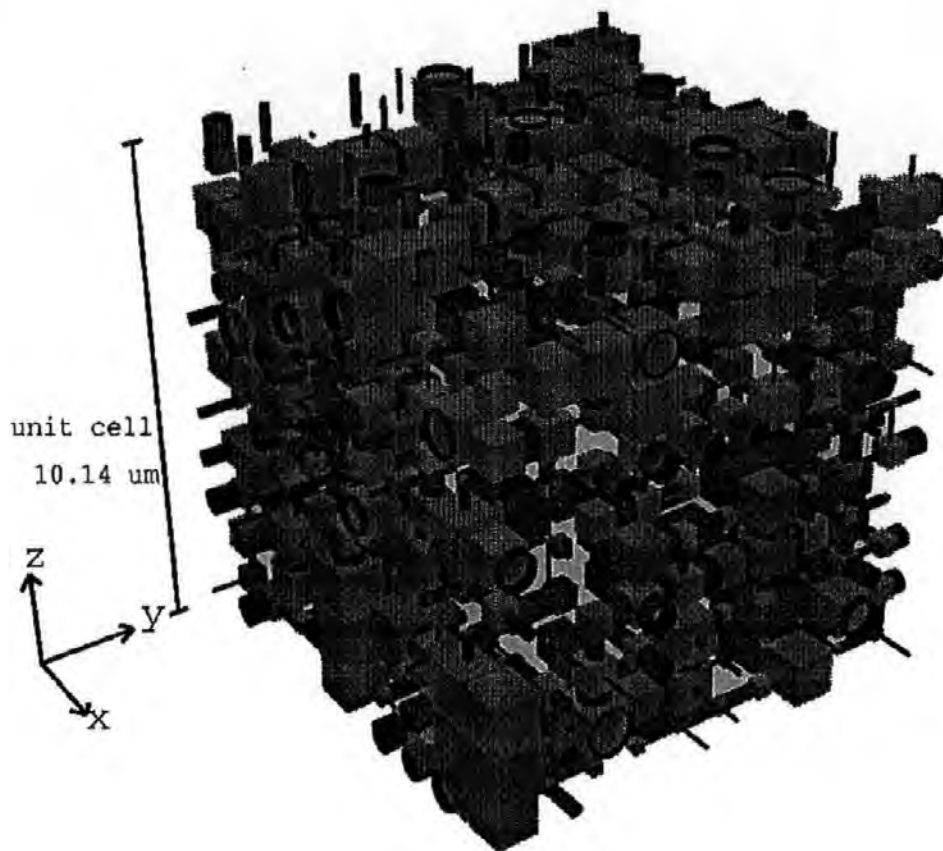
**Figure 34: Unit cell of HP91**

### 8.1.2 Plastic pigments with broad particle size distributions

The two solid plastic pigments have different size particles, as reflected in the modelling by the different throat diameter and pore size ranges, Figure 35 and Figure 36. The maximum simulated throat diameter for Lytron 2601 is twice the maximum simulated throat diameter for Lytron 2301, and the unit cell for Lytron 2601 is twice as large as that for Lytron 2301. Lytron 2601 has a simulated permeability of 0.850 μD compared to Lytron 2301 which has a simulated permeability of 0.033 μD. The differences between the throat diameter and pore size distributions, and between the simulated permeabilities of the two Lytron samples are in accord with the differences between their experimental particle sizes and porosities, Table 1.

111
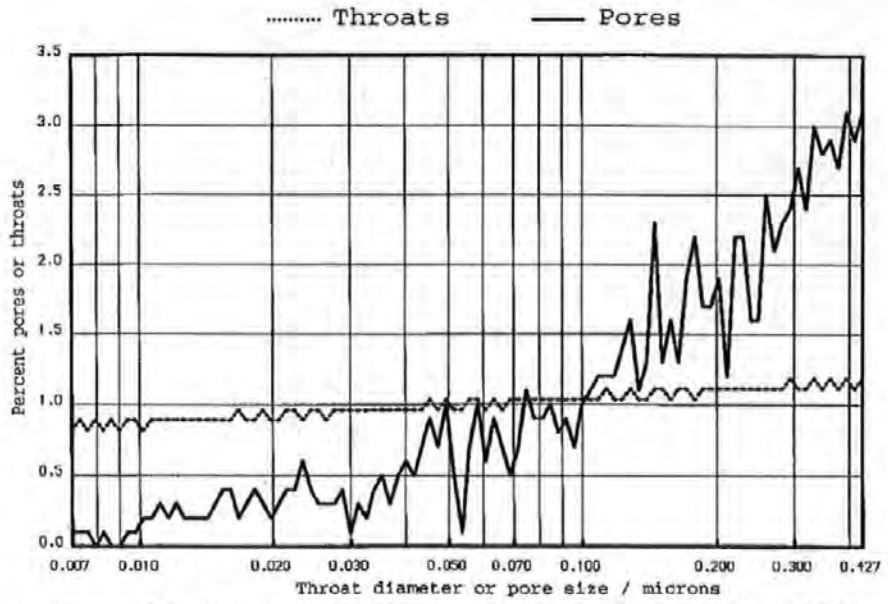
**Figure 35: Pore and throat size distribution for Lytron 2301**
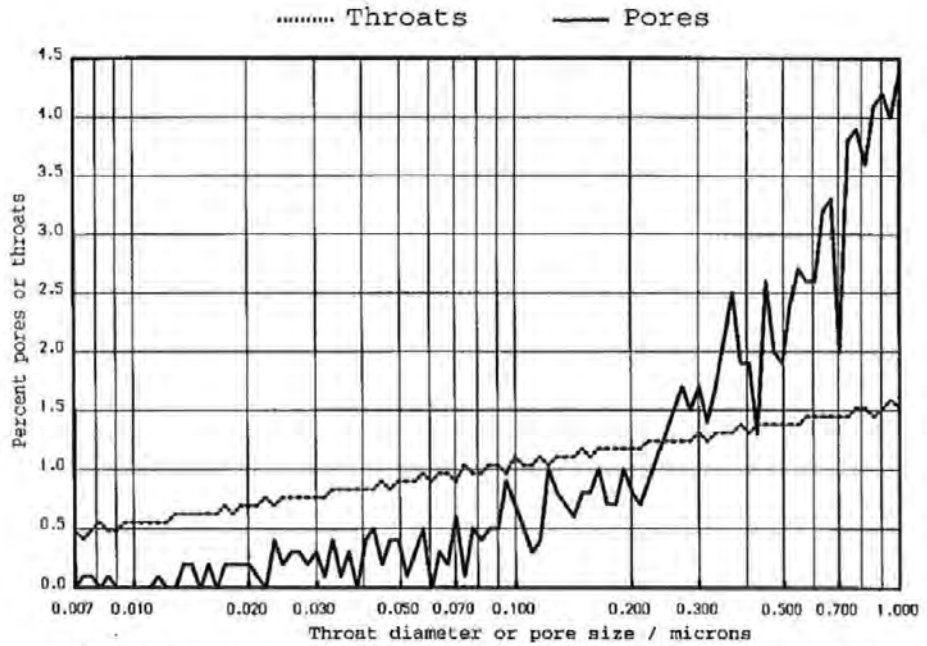


**Figure 36: Pore and throat size distribution of Lytron 2601**

The unit cell of Lytron 2601 is shown in Figure 37.
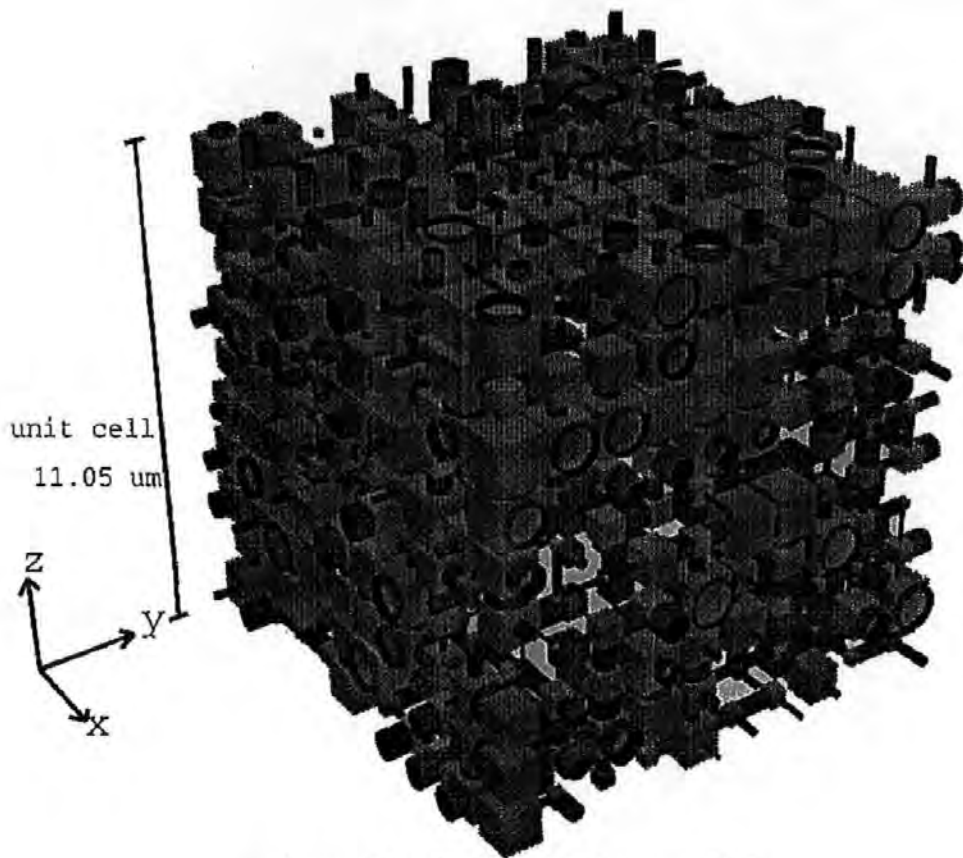
**Figure 37: Unit cell of Lytron 2601**

## 8.2 *Computer simulation of calcium carbonate systems*

### 8.2.1 Effects of particle size distribution

The pore and throat size distributions which generate the mercury intrusion curves for Carbital 90, Carbital 60 and LX 60 are summarised in Table 9. It can be seen that in this series, the percentages of pores and throats below 0.03 μm decrease, and the percentages of the large sizes increase (noting the different maximum sizes) Figures 38 - 40. This trend is in agreement with the relative sizes of the void spaces which would be expected between particles of sizes shown in Figure 3. Figure 41 is the unit cell of LX 60. Figure 42 and Figure 43 show the same size cube (7.20 μm) of the simulated void space structure of Carbital 90 and Carbital 60. The unit cell size varies for these samples as shown, and so these diagrams include more than one unit cell. As shown in Table 9, a higher connectivity (4.0) is required to simulate the steeper intrusion curve of LX 60. LX 60 also has a higher

porosity (note that all experimental and simulated porosities matched exactly). Overall, it can be seen that the simulated permeabilities increase by two orders of magnitude from Carbital 90 to LX 60, Table 9. Slip flow causes a 17-fold relative increase in permeability for Carbital 90, and an absolute increase of 6 µD. For the more permeable samples, the absolute increase caused by slip flow is greater, but the relative effect is smaller.
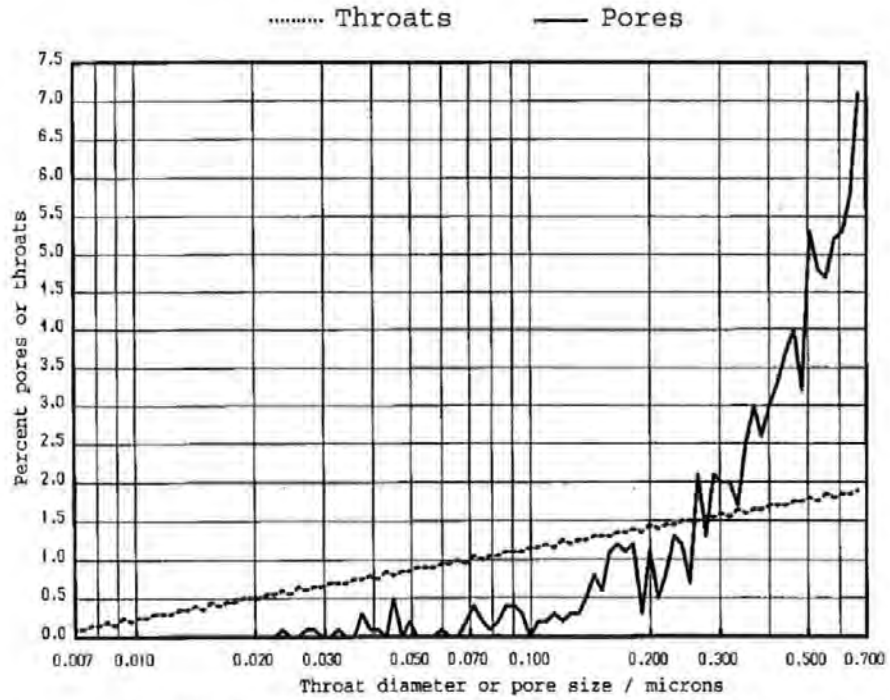


**Figure 38: Pore and throat distribution for LX60**
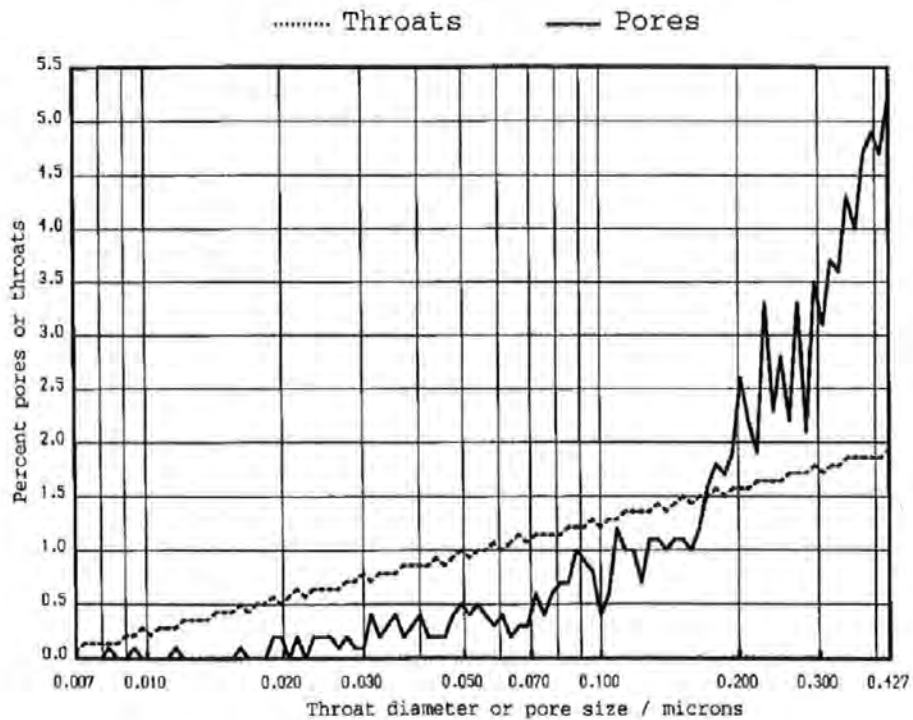


**Figure 39: Pore and throat distribution for C60**

114
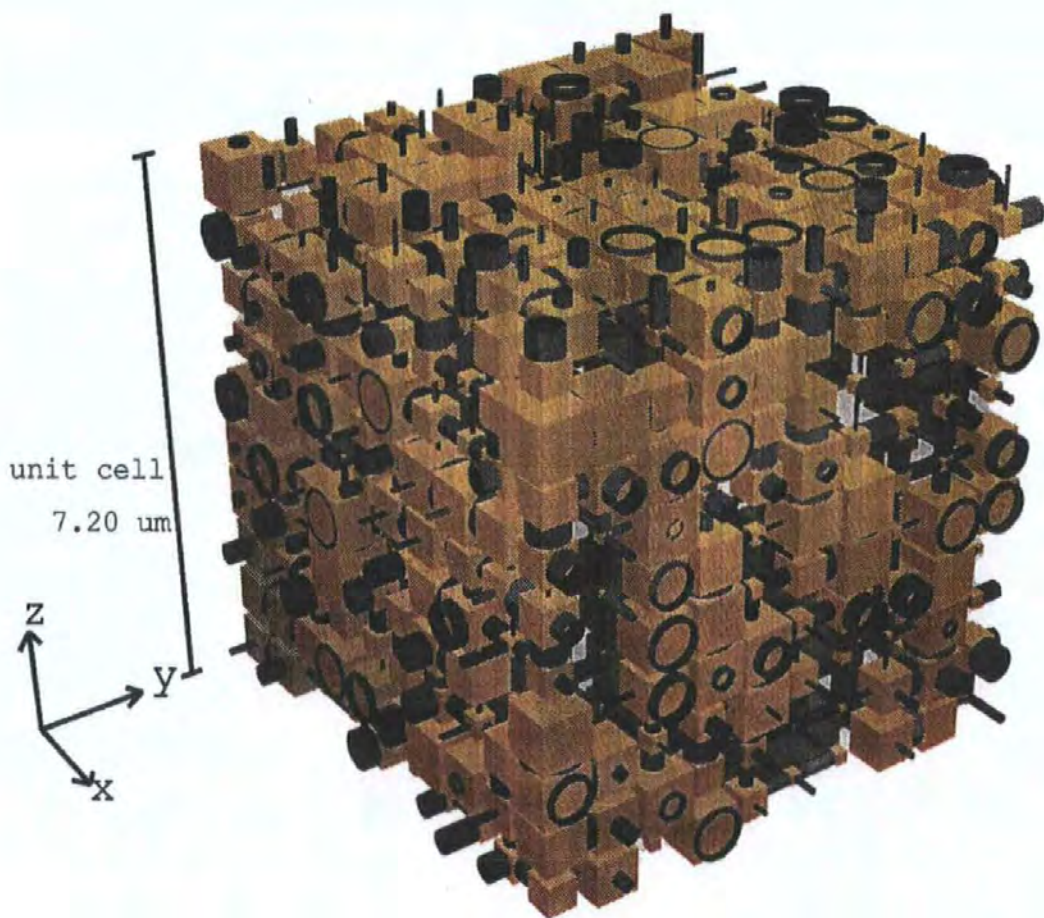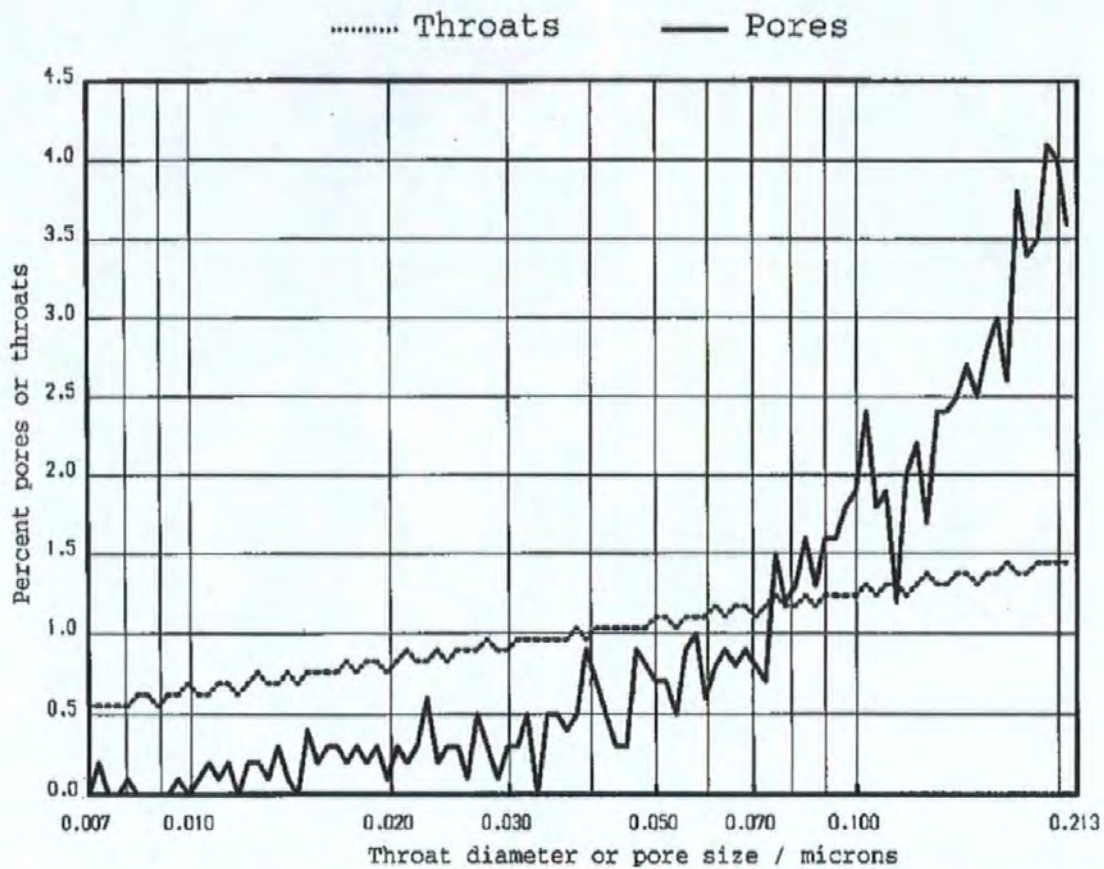
**Figure 40: Unit cell of LX 60**

unit cell
4.74 um

7.20 um
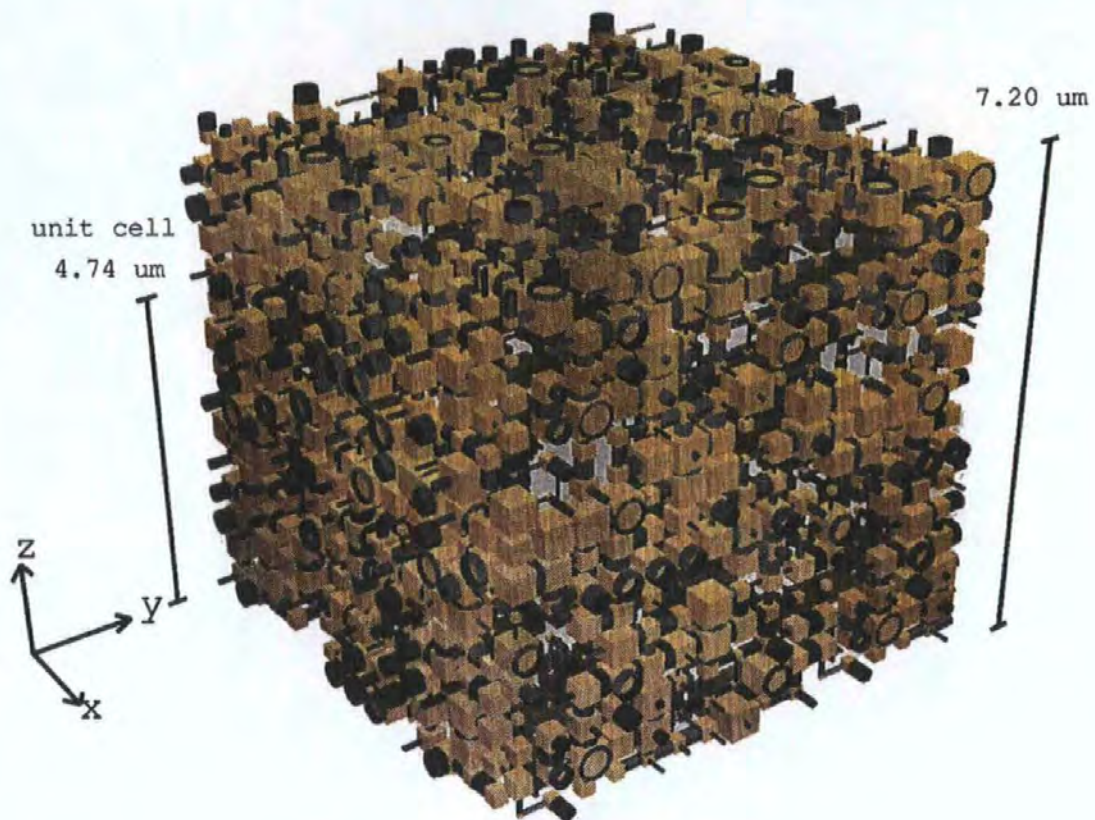
**Figure 41: Unit cell of Carbital 60**



unit cell
2.43 um

7.20 um
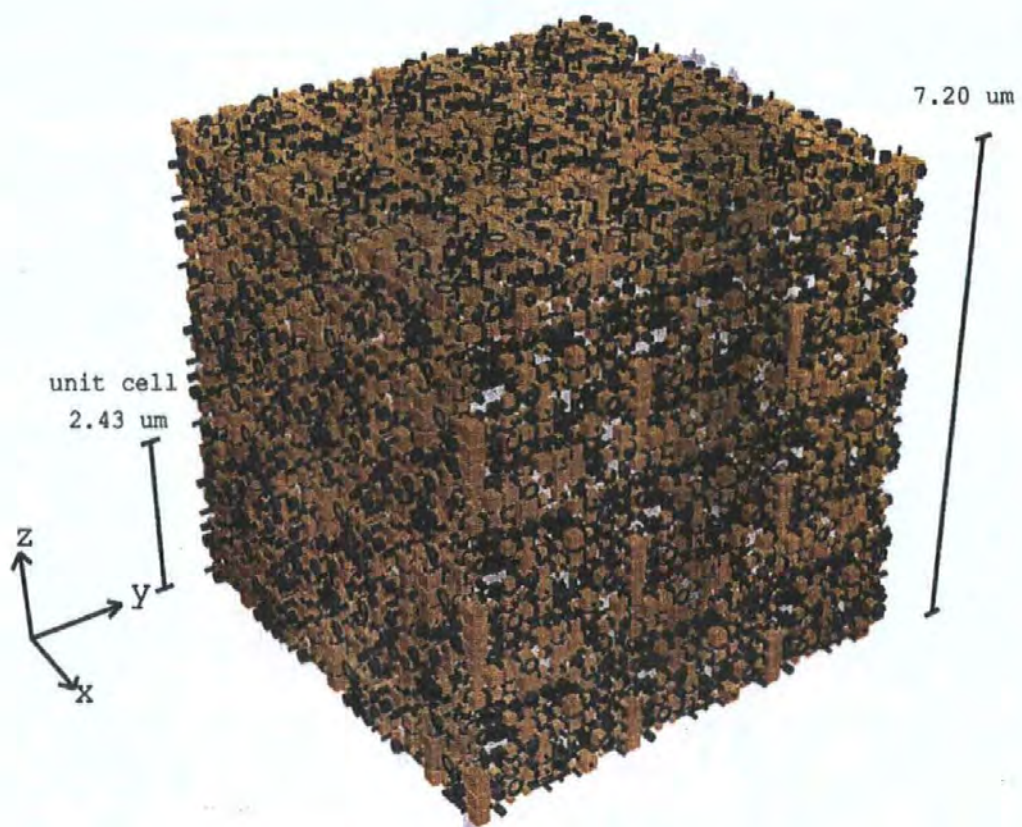
**Figure 42: Unit cell of Carbital 90**

116

### 8.2.2 Carbital 90 with added latex binder

The three coating colour samples have the throat diameter and pore size distributions summarised in Table 9, each covering the range 0.007 - 0.427 μm. The Carbital 90 + Acronal S801, has a lower skew and more large pores than the other two samples (Figure 43 c.f. Figure 44 and Figure 45). The porosities of the three samples are all around 20%, Table 9. The unit cell of the Carbital 90 + Acronal S801 is similar to that of Carbital 60, Table 9, although the unit cell sizes differ, Table 9. Carbital 90 + latex 95L10 has a unit cell similar to that of Carbital 90 + DL 950. There is a three-fold difference in the permeabilities of these three structures, which is small in comparison to the range of simulated permeabilies in the previous section.
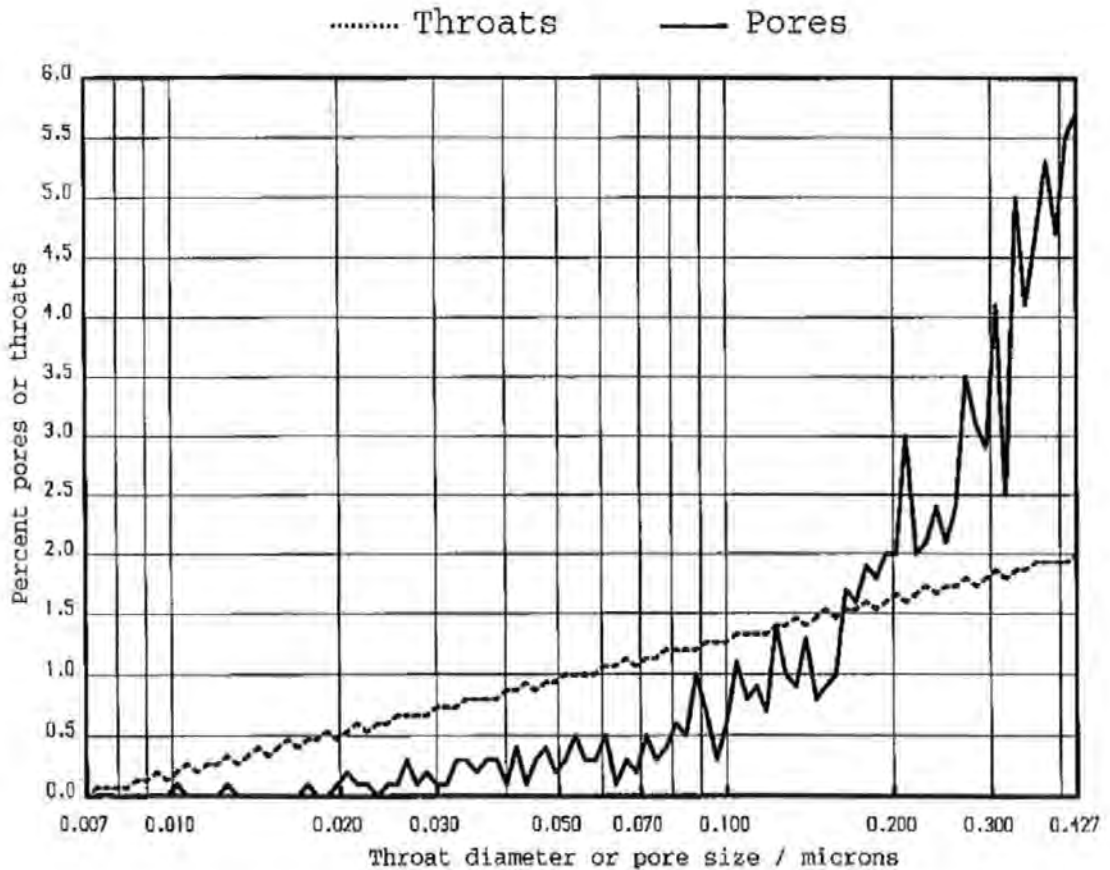


**Figure 43: Pore and throat size distribution for C90 with 12 pph A801**
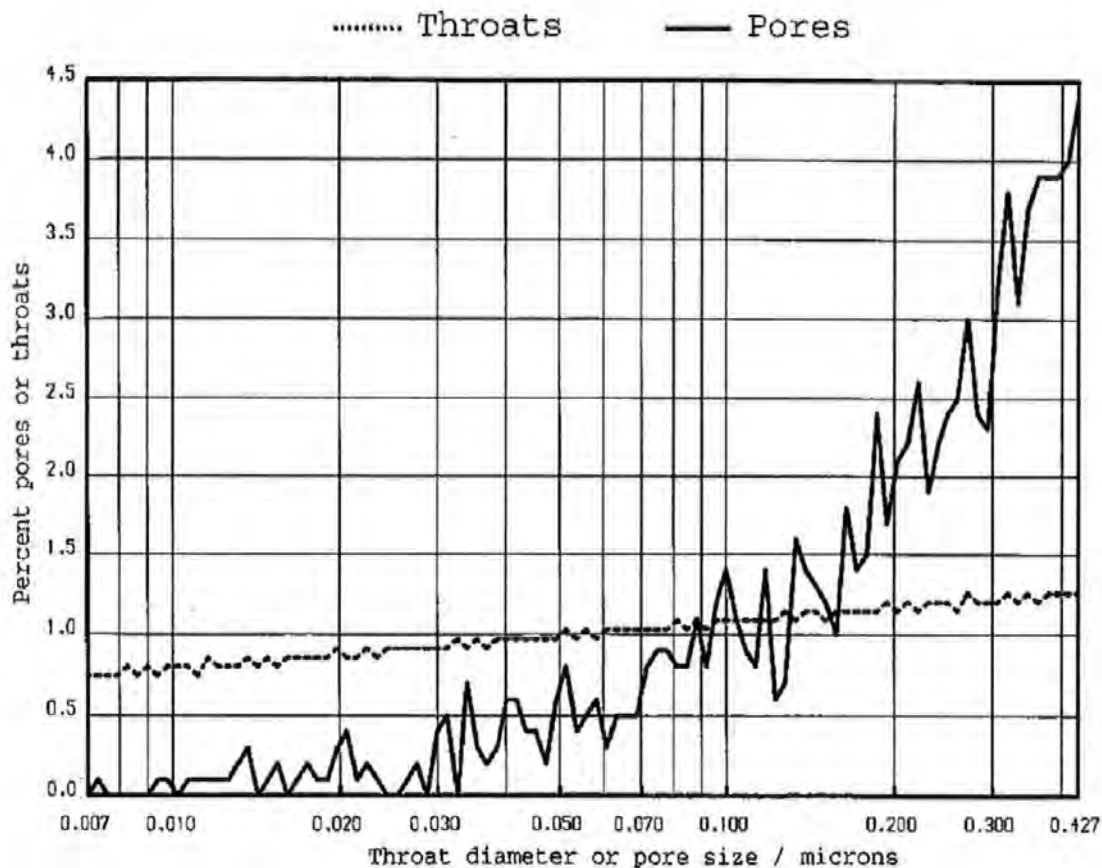
**Figure 44: Pore and throat size distribution for C90 with 12 pph 95L10 latex**
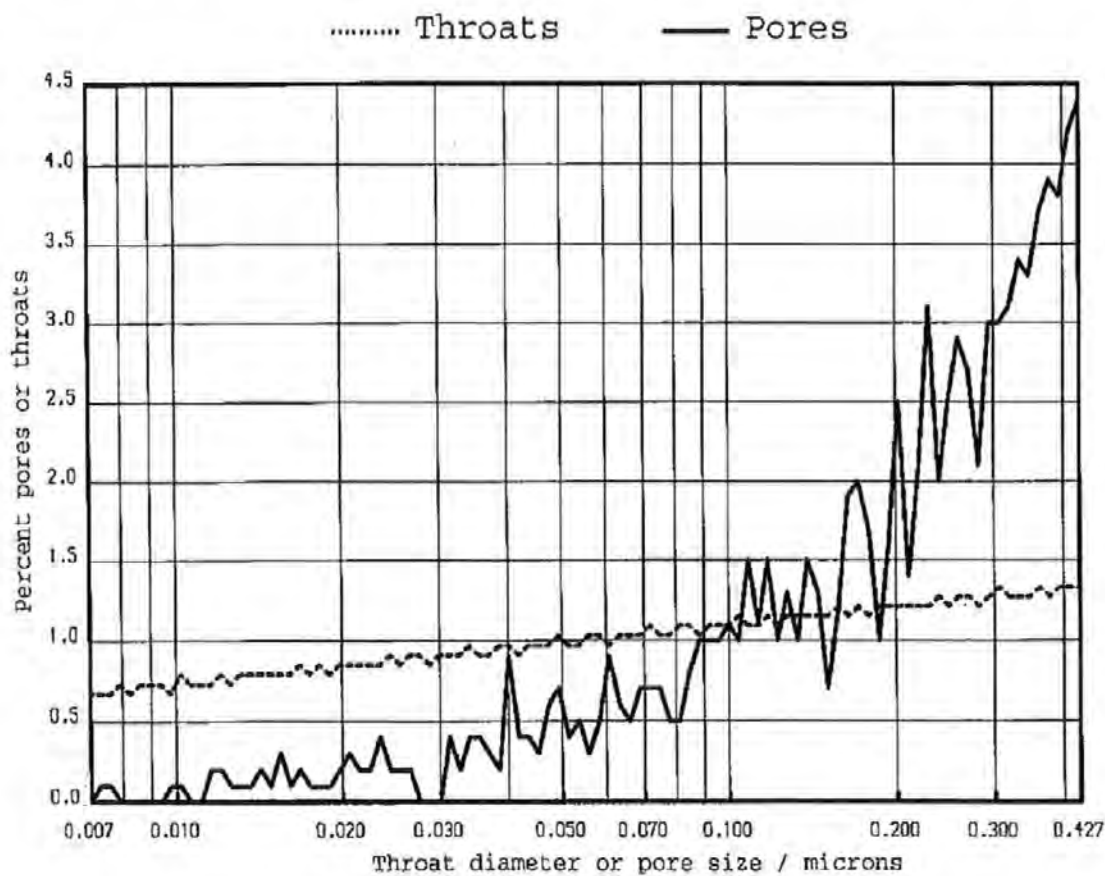


**Figure 45: Pore and throat size distribution of C90 with 12 pph DL950**

118

## 8.3    Computer simulation of kaolin systems

### 8.3.1    Alphafine and Centrifuged Alphafine systems

The pore and throat size distributions which generate the simulated mercury intrusion curves for Alphafine and Centrifuged Alphafine are summarised in Table 10.

**Table 10:  Simulated data for consolidated Alphafine systems**

| Sample Reference | Minimum throat diameter / $\mu m$ | Maximum throat diameter / $\mu m$ | Skew | Connectivity | Unit cell length / $\mu m$ | Porosity / % $\phi_{exp}, \phi_{sim}$ | Permeability micro Darcies $\mu D$ Liquid, Air $(N_2)$ |
|---|---|---|---|---|---|---|---|
| Alphafine | 0.007 | 0.213 | 0.82 | 2.9 | 2.13 | 36.0,  31.2 | 0.233, 4.58 |
| Centrifuged Alphafine | 0.007 | 0.213 | 0.15 | 2.8 | 2.13 | 40.5, 40.3 | 2.19, 29.20 |
| Alphafine 14 pph latex | 0.007 | 0.213 | 0.97 | 4.0 | 2.33 | 29.2, 29.2 | 0.731, 12.40 |
| Centrifuged Alphafine 14 pph latex | 0.007 | 0.427 | -0.17 | 2.9 | 4.75 | 31.4, 31.4 | 5.07, 34.5 |

Alphafine and Centrifuged Alphafine have similar connectivity, however the skew is smaller for Centrifuged Alphafine moving the simulation curve to larger pore sizes, Table 10, Figure 46.   This results in a ten fold increase in liquid permeability and a six fold increase in air permeability for Centrifuged Alphafine compared with Alphafine.

Addition of  14 pph latex to Alphafine and Centrifuged Alphafine  had a significant affect upon their respective pore structures (Chapter 7).  The latex addition to Alphafine resulted in an increase in the skew and connectivity, whereas the same addition of latex to Centrifuged Alphafine resulted in a negative skew without a significant change in

connectivity. The change in skew for the Centrifuged Alphafine results from the larger throat entry sizes for its experimental mercury intrusion curve, Figures 47 and 48.
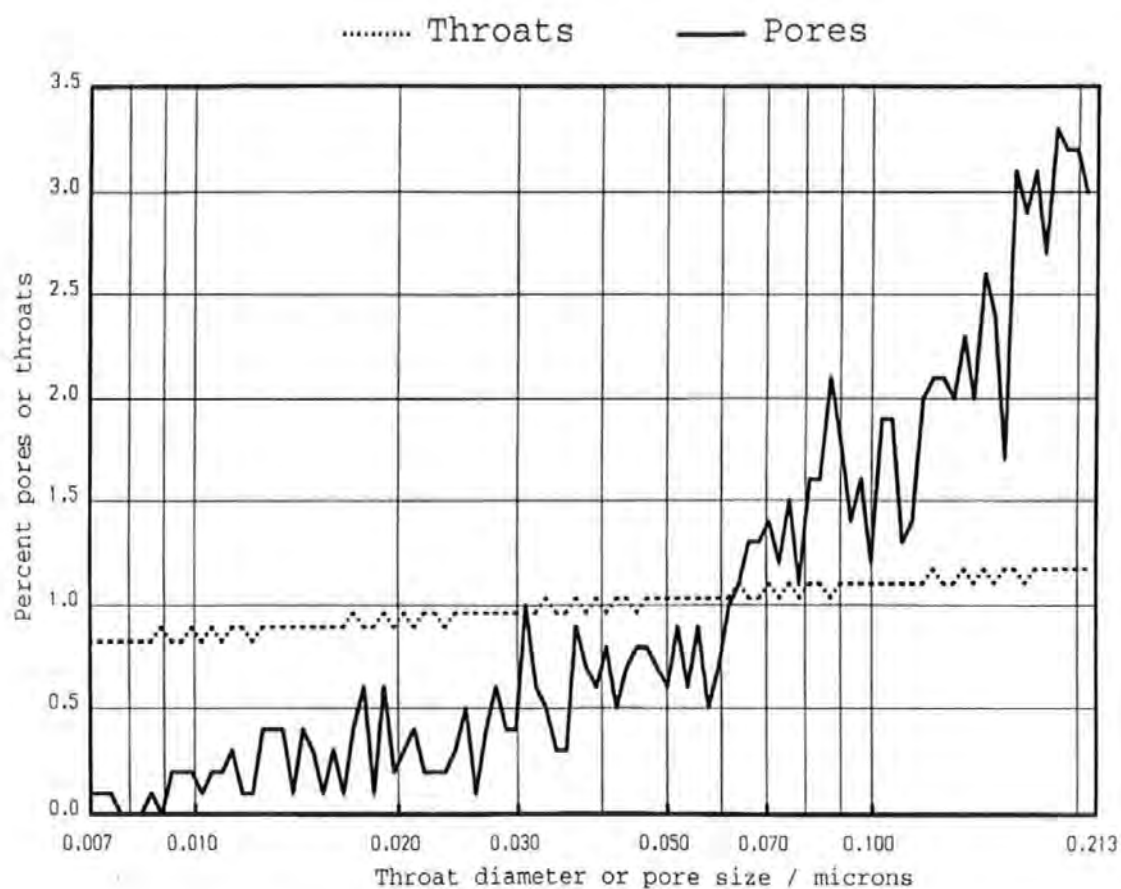


Figure 46: Pore and throat size distribution of Alphafine
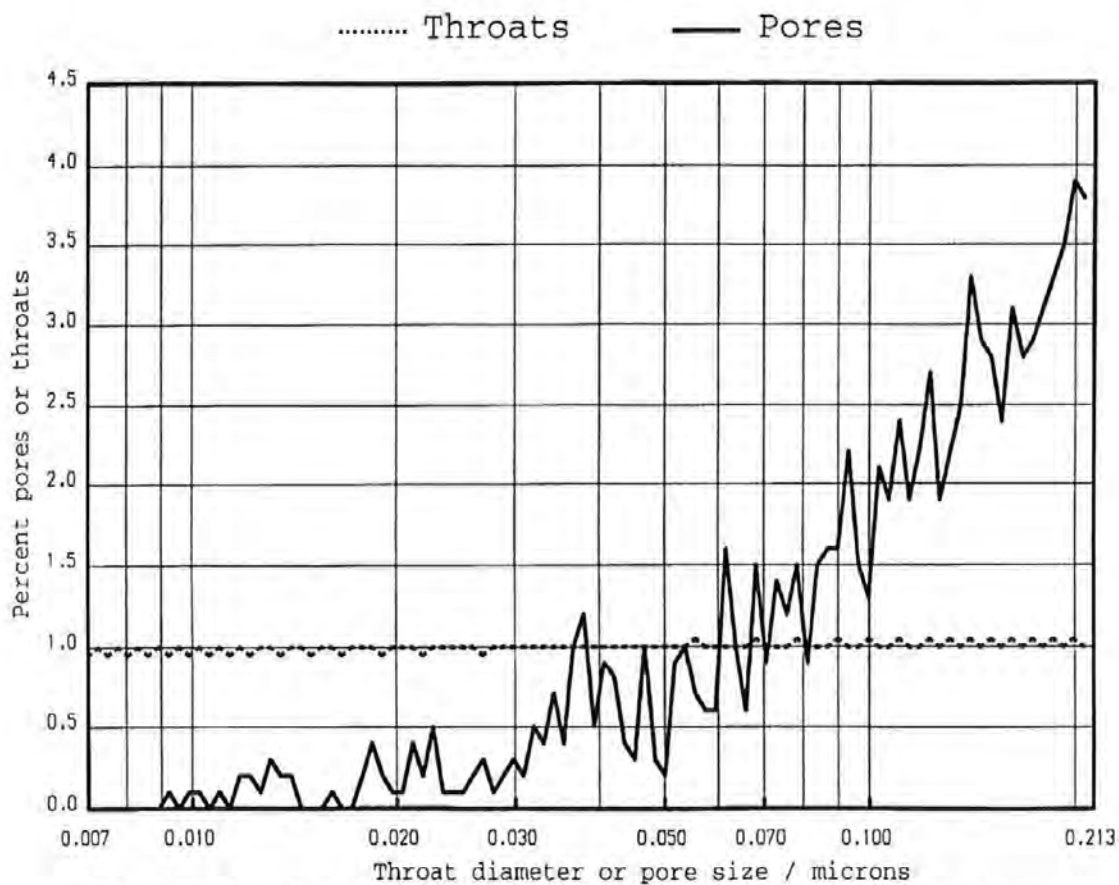
**Figure 47: Pore and throat size distribution for Alphafine with 14 pph latex**
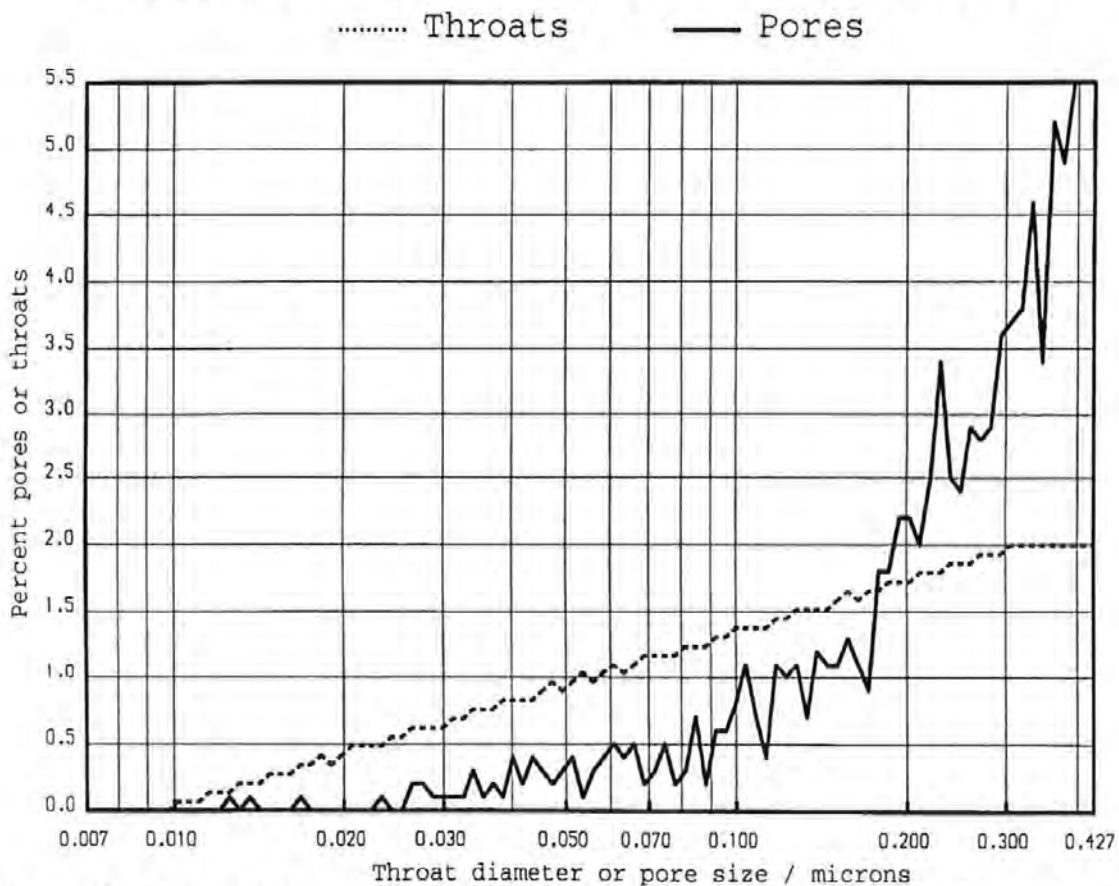


**Figure 48: Pore and throat size distribution for Centrifuged Alphafine with 14 pph latex**

The liquid and air permeabilities significantly increased for the structures that contained latex. This is probably due to the particle size of the latex acting as spacers during the consolidation process and film formation does not adversely affect these porous systems, Table 10.

These simulated property results are in agreement with the initial rise of the ink tack force data, i.e. Centrifuged Alphafine contains fewer ultrafine particles and therefore fewer micro - pores resulting in a negative skew towards larger pore sizes. The contradiction in this hypothesis is that the ink tack curves show faster decay for Alphafine systems than Centrifuged Alphafine systems even though the simulated data indicates that Alphafine is less permeable than Centrifuged Alphafine. This is further evidence to suggest that ink tack may not be considered as a simple function of sample porosity or permeability but also as a function of the complex surface chemistries of the ink, pigment systems.

## 8.3.2 Effects of formulation type and drying regime

The pore and throat size distributions which generated the simulated mercury intrusion curves for the samples of SPS with latex or starch are summarized in Table 11.

### Table 11: Simulated data for consolidated SPS systems

| Sample Reference | Minimum throat diameter / $\mu$m | Maximum throat diameter / $\mu$m | Skew | Connectivity | Unit cell length / $\mu$m | Porosity / % $\phi_{exp}$, $\phi_{sim}$ | Permeability micro Darcies $\mu$D Liquid, Air (N$_2$) |
|---|---|---|---|---|---|---|---|
| **SPS with latex** | | | | | | | |
| Air dried | 0.007 | 0.427 | 0.99 | 2.8 | 4.36 | 22.6, 22.6 | 0.0562, 1.6 |
| Oven dried | 0.007 | 0.213 | 0.98 | 3.1 | 2.56 | 19.4, 19.4 | 0.14, 2.9 |
| **SPS with starch** | | | | | | | |
| Air dried | 0.007 | 0.427 | 0.15 | 3.4 | 4.27 | 42.0, 42.0 | 8.72, 62.1 |
| Oven dried | 0.007 | 0.427 | -0.40 | 2.8 | 4.28 | 40.8, 40.8 | 10.1, 69.8 |
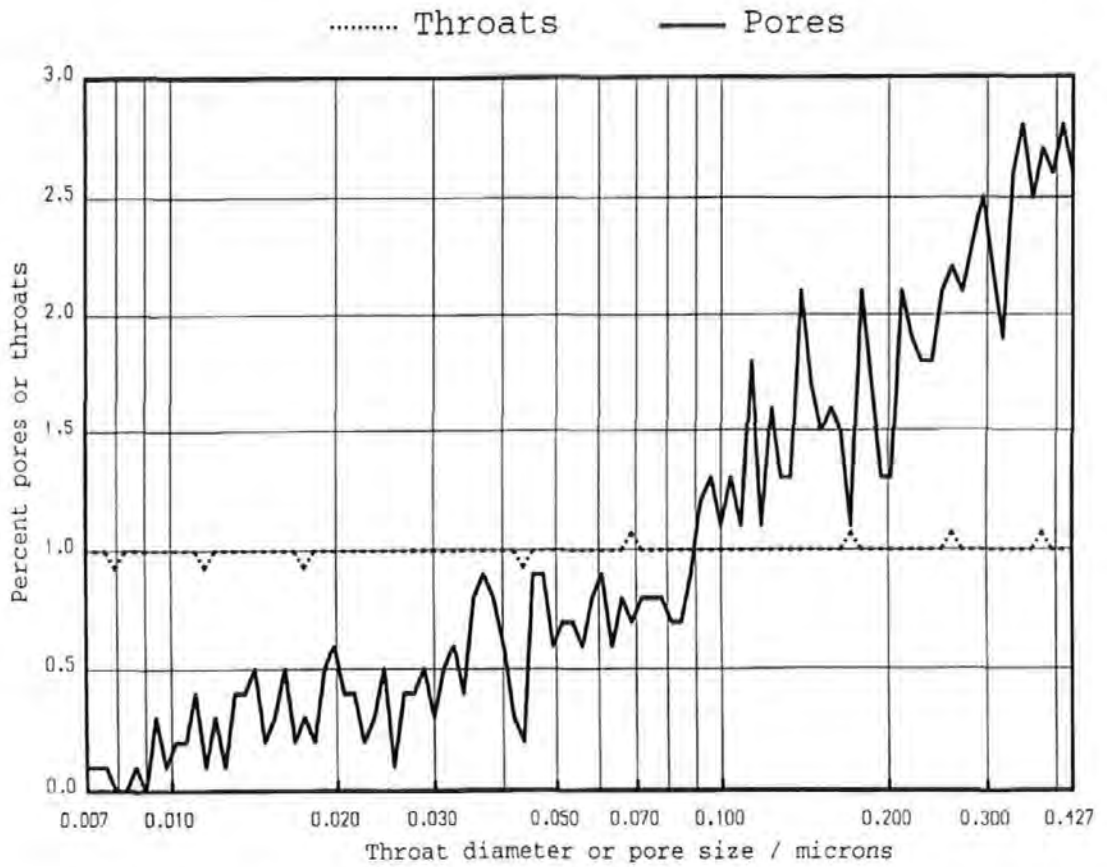
**Figure 49: Pore and throat size distribution for SPS with 17 pph latex (air dried)**
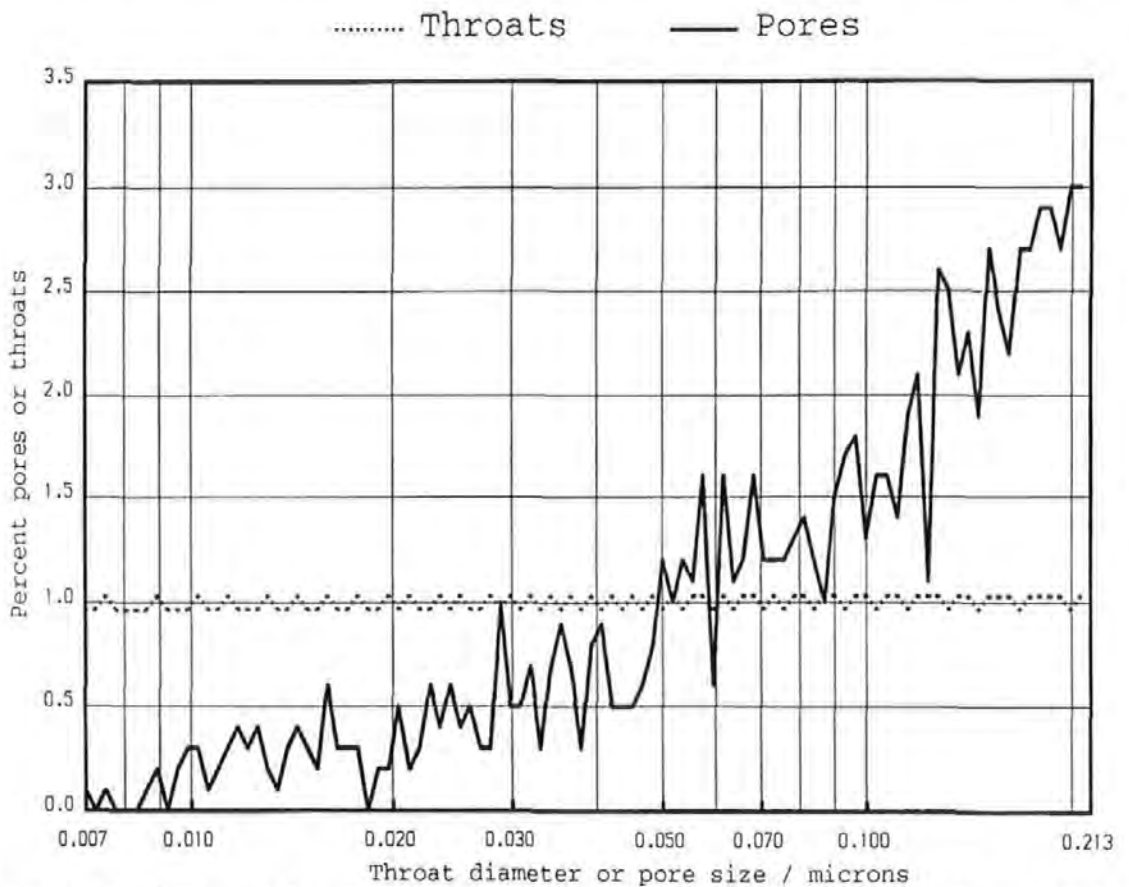


**Figure 50: Pore and throat size distribution for SPS with 17 pph latex (oven dried)**

123
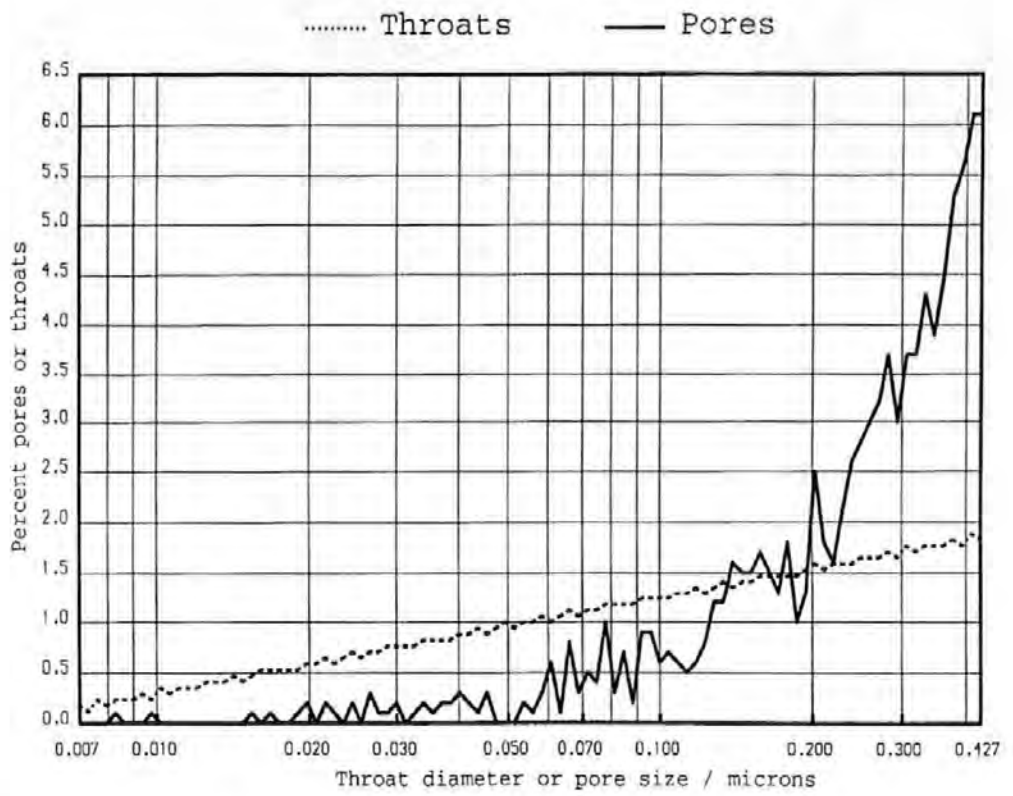
**Figure 51: Pore and throat size distribution for SPS with 5 pph starch (air dried)**
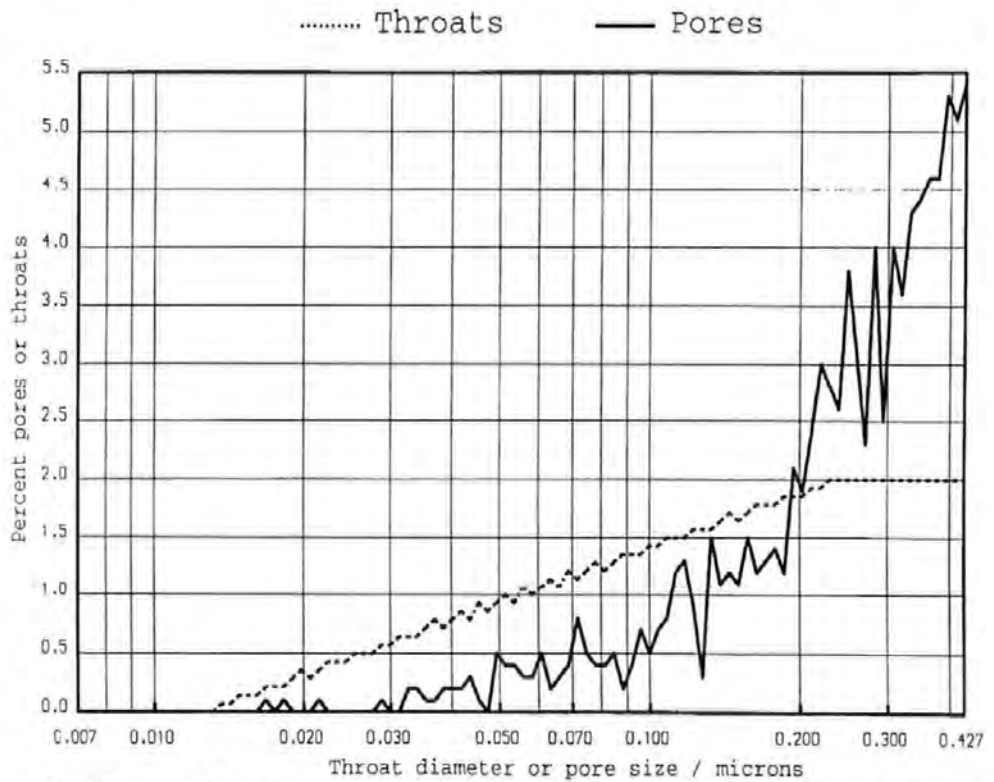


**Figure 52: Pore and throat size distribution for SPS with 5 pph latex (oven dried)**

The samples of SPS with latex had very similar values of skew, Figures 49 and 50 (Table 11). The sample dried at 110 °C had slightly higher connectivity giving rise to much higher (fifty fold) liquid permeability and roughly doubling the air permeability.

The SPS samples which contained starch had, as expected, lower skew values than the latex samples, Figures 51 and 52. However, in this case the sample dried under ambient conditions had higher connectivity than the sample dried at 110 °C. Despite the differences in drying regime both starch containing samples had very similar permeabilities and tortuosity values.

## 8.4    Simulated properties of paper systems

The pore and throat size distributions which generated the simulated mercury intrusion data are summarised in Table 12.

### Table 12:  Simulated data for paper systems

| Sample Reference | Minimum throat diameter / $\mu$m | Maximum throat diameter / $\mu$m | Skew | Connectivity | Unit cell length / $\mu$m | Porosity / % $\phi_{exp}, \phi_{sim}$ | Permeability micro Darcies $\mu$D Liquid , Air (N$_2$) |
|---|---|---|---|---|---|---|---|
| Soft / 400 / Y | 0.007 | 40 | 2.0 | 2.8 | 401 | 44 | 72.7, 90.1 |

The simulation of the combined porosimetry data is shown in Figure 53. This data generates a large skew value (e.g. 2), Figure 54, and a connectivity of 2.8. The simulation has generated liquid and air permeabilities that are 73 $\mu$D and 90 $\mu$D respecively. A permeability value of 357 $\mu$D was measured for this sample using a Gurley Permeability tester (Table 6). This value is approximately four times higher than the simulated value.

This difference may be attributed to assumptions made within the permeability simulation routine.
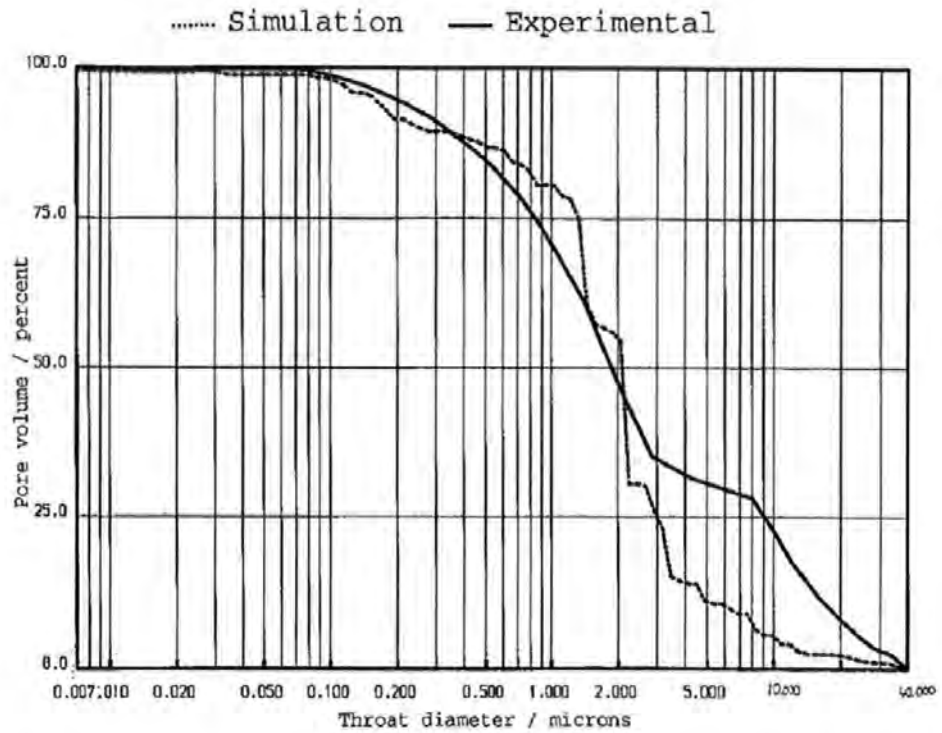


Figure 53: Simulation and combined porosimetry curves for calendered paper
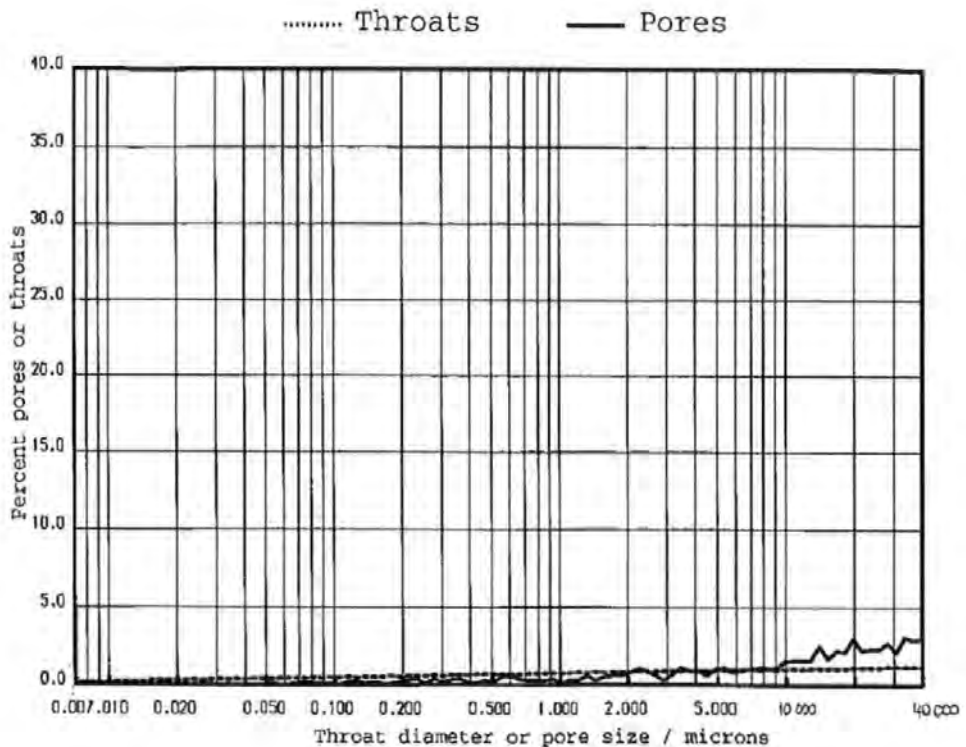


Figure 54: Pore and throat size distribution for calendered paper

## 9. CONCLUSIONS

Mercury porosimetry is a technique for the measurement of the porosities and pore size distributions of most porous media, but in the past, mercury porosimetry was rarely used for analysing the pore structure of uncoated and coated paper structures. The reasons for the limited application of this technique to paper based systems are simply that paper is very porous and very compressible. This means that the resulting porosimetry data contain information about the sample pore size that the mercury probes, as well as the surface roughness and compressibility of the paper systems. One may imagine that the results for a coated paper will be extremely complicated due to the high porosity of the base, the compressibility of the cellulose fibres and the relatively low porosity of the coating layer. In this work consolidated structures consisting of coating pigments were prepared on non-porous substrates and analysed by mercury porosimetry. Uncoated paper samples were also analysed by two separate types of porosimetry and it has been shown that it is possible to combine these data sets to more fully characterise the porous structure of paper.

A mercury porosimetry intrusion curve is typically sigmoid in shape and it has been traditionally assumed that a distribution of throat sizes (not distinguished from pore sizes) may be equated to the first derivative of the intrusion curve. This results in a distribution which has a peak at the point on the intrusion curve which has the highest gradient i.e. the point of inflection. The Washburn derived throat diameter at this point is often described as the characteristic throat diameter. However, the use of the first derivative is only valid for a porous solid which comprises a bundle of non-interconnecting capillary tubes, which

can be tortuous, but which have a constant diameter along their length. The micrographs presented in this thesis clearly show that this is not the case for a paper system.

These limitations were overcome and new techniques were discovered and applied to extend existing theory, to generate new calculations for the correction of data for real porous systems. Uniquely, this procedure has allowed the measurement of the bulk modulus of the continuous solid phase of a porous sample, by mercury porosimetry, thus revealing information about its microstructure, particle packing and interparticle bonding.

The corrected mercury intrusion curves have formed data sets for the Pore-Cor computer modelling package. The Pore-Cor model does not use the Washburn capillary bundle assumption, but as stated in Chapter 6, uses an invasion percolation algorithm. The advantage of this percolation algorithm is that it takes into account of the fact that a large pore may be "shielded" from mercury intrusion at the pressure predicted by the Washburn equation by small surrounding throats. The Pore-Cor computer model also takes into account the porosity and the connectivity of 3-dimensional void space networks. The computer model generates throat diameter and pore size distributions and a corresponding 3 dimensional unit cells for data that have been collected experimentally. It was also possible to calculate the air and liquid permeabilities of these simulated structures.

In this work mercury porosimetry was used to characterise the pore structure of a consolidated sample consisting of hollow plastic pigments. It was also shown that after the pores have been filled with mercury, the hollow plastic spheres collapse. The pressure at which the plastic spheres deform is defined by a second point of inflection on the mercury intrusion curve. Consolidated solid plastic pigments of different particle sizes were prepared and mercury porosimetry was successful used to show that increasing particle size

distribution shifts the pore size distribution to larger pore sizes and increased the overall porosity.

Calcium carbonate and kaolin are very important pigments in the paper coating industry. In this work it has been shown that, not only does particle size distribution of the calcium carbonate affect the pore size distribution of its consolidated structure, but that mercury porosimetry can be used to measure significant changes in bulk moduli that occur either by increasing the "fineness" of mineral particle size distribution (e.g. moving to finer particle size distribution correlates with increasing bulk modulus) or decreasing bulk modules by changing mineral type from marble to limestone.

Another important conclusion within this work is that incorporation of chemical additives (e.g. binders such as latex or starch) do have a significant affect upon the porosity and pore size distribution of a consolidated pigment (calcium carbonate or kaolin) coating. Mercury porosimetry shows extreme hysteresis for consolidated pigment/latex samples. This hysteresis results from the fact that upon intrusion of a non-wetting phase the throat radius controls the pressure at which the throat is intruded by mercury. However, mercury extrusion is governed by the pore size and if there is a large difference between the pore size and the throat size then the mercury will be unable to re-adjust its shape to extrude. When the mercury thread breaks, the remainder of the mercury is trapped within the porous network. The high degree of mercury entrapment, upon depressurisation of pigment/latex samples is surprising, but this behaviour may be explained in terms of an "elastic" diaphragm mechanism. It is suggested that any excess of latex in the pigment/latex system will concentrate at the pore:throat junction forming a latex film. This film is elastic and may serve to narrow the throat enough to cause mercury entrapment. This phenomenon was not observed for consolidated samples of kaolin/starch. This may

be due to the low addition level of starch in these samples compared to the level of latex in the kaolin/latex samples.

All of these consolidated pigment samples contain individual particles that are several orders of magnitude smaller than the consolidated sample that was analysed by mercury porosimetry. This ratio of particle size to sample size minimised "edge effects" due to sample roughness and this resulted in very steep pore size distributions for each of the pigment types. This is in accord with percolation theory and these data sets were successfully modelled using the Pore-Cor computer modelling program.

This situation is unfortunately not the case for uncoated paper samples. Paper consists of fibres that are probably only one or two orders of magnitude smaller than the cross-sectional dimension of the consolidated paper sheet. The structure of paper is also incredibly complicated being dependent upon fibre type, fibre size distribution and fibre orientation, as well as pigment filler type and filler distribution across the thickness of the paper sheet. As mentioned above, it has been uniquely possible to combine porosimetry data from a low pressure liquid (hexadecane, in this case) porosimeter, with those obtained from a mercury porosimeter. If structural information is sought, then water may not be used as a probe liquid in the liquid porosimeter because it causes the cellulose fibres to swell. However the information generated in this way can be very significant to a papermaker because it is a novel technique to measure the expansivity / stability of a paper sheet. Combination of the data from both types of porosimeter is an exiting development and enables edge effects to be removed from the data. The corrected data are similar to that expected from percolation theory.

This work has also enabled a clear set of trends in both basic paper properties and structural analysis to be quantified for a set of calendered papers. This information will be very useful to a papermaker and will advance the knowledge of uncoated and coated paper structure. The combined porosity data have also been modelled using Pore-Cor and the calculated simulated permeability matches within four orders of magnitude that measured for the calendered paper.

One of the most important properties of paper is its ability to accept a printed image. It was thought that the throat size distribution of a paper or coated paper determined the print quality. This work has indicated that printing properties are not only dependent upon the porous characteristics of the medium, but they must be influenced by the surface chemistry of the solid phase as well as the interconnectivity of the pore structure. It may be concluded that mercury porosimetry does reveal information about the porous nature of the bulk of the sample, but that this is not all the necessary information to fully characterise the printing and optical properties of papers. However, mercury porosimetry in conjunction with other specialised optical and adsorption techniques is a very valuable technique to assess the potential of new paper grades ands new printing technologies.

The methodology presented here has a wide applicability to other consolidated and compressible samples. This work has been a major advance in the knowledge of porous structures within the field of paper science.

# REFERENCES

Alince, B., Lepoutre, P., 1980a, *Journal of Colloid Interface Science*, **76**, 439-444.

Alince, B., Lepoutre, P., 1980b, *Journal of Colloid Interface Science*, **76**, 182-187.

Allen, T., 1981, *Particle Size Measurement*, third edition, 283-285.

Androutsopoulos, G.P., Mann, R., 1979, *Chemical Engineering Science*, **34**, 1203-1212.

Androutsopoulos, G.P., Mann, R., 1981, *Chemical Engineering Science*, **36**, 337-346.

Aspler, J.S., Lepoutre, P., 1991, *CPPA Symposium on Papercoating Fundamentals*, 77-98.

Bell, W.K., van Brakel, J., Heertjes, P.M., 1981, *Powder Technology*, **29**, 75-88.

Bery, Y.A., Loel, P.A., 1992, *Proceedings of International Printing & Graphic Arts Conference*, 53-73.

Blunt, M., King, P., 1990, *Physical Review A.*, **42**, 4780-4787.

Blunt, M., King, P., 1991, *Transport in Porous Media*, **6**, 407-433.

Bulletin, Mercury Penetration Porosimeter, Micromeritics Inst. Corp., Georgia.

Bunker, D.T., Conners, T.E., 1991, *Tappi Symposium on Papercoating Fundamentals*, 61-68.

Bragg, W.L., 1913, *Proceedings of the Royal Society*, London, A89, 248-262.

Brown, G.I., 1981, *Introduction to Inorganic Chemistry*, Longman Publishing.

Bryant, S.L., Mellor, D.W., Cade, C.A., 1993, *AIChE Journal*, **39**, 387-396.

Bryant, S., Mason, G., Mellor, D., 1996, *Journal of Colloid Interface Science*, **177**, 88-100.

Cebeci, O.Z., 1980, *Journal of Colloid Interface Science*, **78**, 383-389.

Chatzis, I., Dullien, F.A.L., 1985, *International Chemical Engineering*, **25**, 47-66.

Climpson, N. A., Taylor, J. H., 1976, *Tappi Journal*, **59**, 89-92.

Conner, W.C., Horowitz, J., 1988, *AIChE Symposium Series*, **84**, 29-34.

Conner, W.C., Blanco, C., Coyne, K., Neil, J., Mendioroz, S., Pajares, J., 1988, presented at the *C.O.P.S. Conference*, Elsevier, Amsterdam, 273-281.

Cook, R. A., Hover, K. C., 1993, *ACI Materials Journal*, Title no. 90-M16, March/April, 152-161.

Crotogino, R.H., 1982, *Tappi Journal*, **65**, 97-101.

Dawe, R.A., 1978, *Contemporary Physics*, **19**, 355-376.

Day, M., Parker, I.B., Bell, J., Fletcher, R., Duffie, J., 1991, presented at the *C.O.P.S II conference*, Elsevier, Amsterdam, 75-84.

Deer, Howie, Zussman., 1980. *Introduction. to Rock Forming Minerals,* Longman, 476-483.

Dunmore, J.M., Schols, R.S., 1974, *Society of Petroleum Engineers Journal,* October, 437-444.

Edington, J.W., 1990, *Monographs in Practical Electron Microscopy in Materials Science, Number 1, The Operation and Calibration of the Electron Microscope.*

Field, M., Merchant, M.E., 1945, *Journal of Applied Physics,* **20**, 741-745

Gane, P.A.C., Hooper, J.J., Baumeister, M., 1991, *Tappi Journal* **74**, 193-201.

Gane, P.A.C., Seyler, E.N., 1994, *Tappi Coating Conference Proceedings,* 243-260.

Gane, P.A.C., Hooper, J.J., Grunwald, A., 1995, *Tappi Coating Conference Proceedings,* 383-390.

Garboczi, E.J., 1991, *Powder Technology,* **67**, 121-125.

Gate, L.F., Lyne, W.H., *ECC International Research Report* 7102/10, (Confidential).

Gate, L.F., Windle, W., 1973, *Transactions of B.P.B.I.F. Symp. Fund. Props of Paper,* Cambridge, 438-461.

Gate, L.F., 1974, *Applied Optics,* **13**, 236-238.

Gavrilenko, P., Guegen, Y., 1989, *Geophysics Journal International,* **98**, 159-172.

German, R.M., 1989, *Particle Packing Characteristics,* MPIF, 93-119.

Good, R.J., Mikhail R.SH., 1981, *Powder Technology,* **29**, 53-62.

Haines, W.B., 1927, *Journal of Agricultural Science,* **17**, 264-290.

Hamlen, R.C., Scriven, L.E., 1991, *Tappi Coating Conference Proceedings,* 355-380.

Hampton, J.H.D., Savage, S.B., Drew, R.A.L., 1993, *Chemical Engineering Science,* **48**, 1601-1611.

Hilden, K.K., Sawley D., 1987, *Pulp and Paper Canada Journal,* **88**, 195-198.

Hirasaki,G.J., Morrow, N.R., 1990, editors, *Interfacial phenomena in Petroleum Recovery,* New York: Marcel Dekker, **3**, 77-99.

Ioanndis, M.A., Chatzis, I., 1993, *Journal of Colloid and Interface Science*, **161**, 278-291.

Ioanndis, M.A., Chatzis, I., Sudicky, E.A., 1993, *Water Resources Research*, **29**, 1777-1785.

Jerauld, G.R., Salter, S.J., 1990, *Transport in Porous Media*, **5**, 103-151.

Keller, S.F., 1992, *Tappi Coating Conference Proceedings*, May, 71-76.

Keller, S.F., 1994, *Journal of Pulp and Paper Science*, **20**, 33-37.

Kent, H.J, Lyne, M.B, 1989, *Nordic Pulp and Paper Research Journal*, **2**, 141-148.

Kent, H., Climpson, N., Gane, P., Coggon, L., and Hooper, J., 1986, *Tappi Coating Conference Proceedings*, 103-112

Kettle, J.P., Matthews, G.P., 1993, *TAPPI Advanced Coating Fundamentals Symposium*, 121-126.

Kettle, J.P., 1995, *PITA Coating Conference Proceedings*, 101-109.

Kloubek, J., 1981, *Powder Technology*, **29**, 63-73.

Kloubek, J., 1994, *Journal of Colloid and Interface Science*, **163**, 10-18.

Koplik, J., Lin, C., Vermette, M., 1990, *Journal of Applied Physics*, **56**, 3127-3131.

Kraske, D.J., 1960, *Tappi Journal*, **43**, 73-82.

Larrondo, L., St-Amour, S., 1992, *Tappi Coating Conference Proceedings*, 37-51.

Larrondo, L., St-Amour, S., 1995, *Tappi Coating Conference Proceedings* 79-93.

Lee, D.I., 1970, *Journal of Paint Technology*, **42**, 579-587.

Lee, J.A., Maskell, W.C., 1973, *Powder Technology*, **7**, 259-262.

Lepoutre, P., Rezanowich, A., 1977, *Tappi Journal*, **60**, 86-94.

Lepoutre, P., 1989, *Progress in Organic Coatings*, **17**, 89-106

Lenormand, R., Toubol, E., Zarcone, C., 1988, *Journal of Fluid Mechanics*, **189**, 165-180.

Lenormand, R., 1989, *Proceedings of the Royal Society* A**423**, 159-168.

Leskinen, A.M., 1987, *Tappi Journal*, **12**, 101-106.

Li, Y., Wardlaw, N.C., 1986, *Journal of Colloid and Interface*, **109**, 461-472.

Li, Y., Wardlaw, N.C., 1986, *Journal of Colloid and Interface Science*, **109**, 473-486.

Li, Y., Laidlaw, W.G., Wardlaw, N.C., 1986, *Advances in Colloid and Interfacial Science*, **26**, 1-68.

Li, Y., Wardlaw, N.C., 1990, *in "Interfacial Phenomena in Petroleum Recovery."* (N.R.Morrow, Ed.). **36,** 101-156, Marcel Dekker Inc.. New York and Basel.

Lymberopoulos, D.P., Payatakes, A.C., 1992, *Journal of Colloid and Interface Science,* **150,** 61-80.

Mark, R.E., 1984, *Handbook of Physical and Mechanical Testing of Paper and Paperboard* **2,** Chapter 16, 1-53.

Mason , G., 1971, *Journal of Colloid and Interface Science,* **35,** 279-287.

Mason, G., Morrow, N.R., Walsh, T., 1988, presented at the *C.O.P.S. Conference,* Elsevier, Amsterdam, 243-252.

Mason, G., Mellor, D.W., 1991, presented at the *C.O.P.S.II Conference,* Elsevier, Amsterdam, 41-50.

Mason, G., Mellor, D.W., 1994, *Journal of Colloid and Interface Science,* 130-141.

Matthews, G.P., Spearing, M.C., 1991, *Transport in Porous Media,* **6,** 71-90.

Matthews, G.P., Spearing, M.C., 1992, Marine Petroleum Geology, **9,** 146-154.

Matthews, G. P., Moss, A. K., Spearing, M. C., Voland, F. 1993, *Powder Technology,* **76,** 95-107.

Matthews, G. P., Moss, A. K., Ridgway, C. J., 1995a, *Powder Technology,* **83,** 61-77.

Matthews, G. P., Ridgway, C. J., Spearing, M. C., 1995b, *Journal of Colloid and Interface Science,* **171,** 8-27.

Miller, B., Tyomkin, I., 1986, *Textile Research Journal,* **56,** 35-41.

Miller, B., Tyomkin, I, 1994, *Journal of Colloid and Interface Science,* **162,** 163-170.

Millington, K.I., 1995, *PITA Coating Conference Proceedings,* 89-100

Nolan, G.T., Kavanagh, P.E., 1992, *Powder Technology,* **72,** 149-155.

Nolan, G.T., Kavanagh, P.E., 1993, *Powder Technology,* **76,** 309-316.

Nolan, G.T., Kavanagh, P.E., 1994, *Powder Technology,* **78,** 231-238.

Nolan, G.T., Kavanagh, P.E., 1995, *Powder Technology,* **84,** 199-205.

Pan, S.X., Davis, H.T., Scriven, L.E., 1995, *Tappi Coating Conference Proceedings,* 37-52

Parker, J.R., 1981, *Tappi Journal,* **64,** 56-58.

Payatakes, A.C., Tsakiroglou, C.D., 1992, *Journal of Colloid and Interface Science*, **146**, 479-494.

Payatakes, A.C, Constantinides, G.N. 1989, *Chemical Engineering Communication*, **81**, 55-81.

Payatakes, A.C, Tsakiroglou, C.D, 1990, *Journal of Colloid and Interface Science*, **137**, 315-345.

Peel, J., 1990, *Developments in Calendering Technology*, PIRA review publication.

Peel, J., 1993, *Transactions of the 10th Fundamental Research Symposium*, Oxford, September, 979-1054.

Portsmouth, R.L., Gladden, L.F., 1991, *Chemical Engineering Science*, **46**, 3023-3036.

Ranger, A.E.,1983, *Transactions of B.P.B.I.F. Symosium Fundamental Properties of Paper*, Cambridge, 685-734.

Ridgway, C.J., 1995, *PhD Dissertation*, University of Plymouth

Ritter, H.L., Drake, L.C., 1945, *Industrial Engineering Chemistry, Analytical Edition*, **17**, 783-786.

Robinson, J.V., 1975, *TAPPI Journal*, **58**, (10), 152-153.

Santkuyl, R.J., 1995, *Pulp and Paper Canada Journal*, **96**, 49-54.

Shaw, D.J., 1986, *"Introduction to colloid and surface chemistry"* 3rd Edition.

Sheehan, J.G., Scriven, L.E., 1991, *Tappi Coating Conference Proceedings*, 377-383.

Shinohara, K., 1990, *Crushing and Grinding, in Powder Technology Handbook*. K. Iinoya, K. Gotoh, K. Higashitani, editors. Marcel Dekker, Inc, New York. 481-501.

Smithwick, R.W., 1982, *Powder Technology*, **33**, 55-64

Spearing, M.C., Matthews, G.P., 1991, in D.G. Farmer and M. J. Rycroft (eds) in *"Computer Modelling in the Environmental Sciences"* IMA Conference series, Oxford University Press, Oxford.

Stanislawska, A., Lepoutre, P., 1995, *Tappi Coating Conference Proceedings*, 67-77

Tolman, R.C., 1949, *Journal of Chemical Physics*, **17**, 333-343.

van Brakel, J., 1975, *Powder Technology*, **11**, 205-236.

van Brakel, J., Modry, S., Svata, M., 1981, *Powder Technology*, **29**, 1-12

Wardlaw, N.C., Taylor, R.P., 1976, *Bulletin of Canadian Petroleum Geology*, **24**, 225-262

Wardlaw, N.C., Li, Y., Forbes, D., 1987, *Transport in Porous Media*, **2**, 597-614

Wardlaw, N.C., 1990, *in "North Sea Oil and Gas Reservoirs - II."* (Graham and Trotman, Eds).
229-243, Keynote Address 2.

Wardlaw, N. C., McKellar, M. 1981, *Powder Technology*, **29**, 127-143.

Warren, N., Nashner, R., 1976, *Theoretical Calculation of Compliances of a Porous Medium, in
The Physics and Chemistry of Minerals and Rocks.* R. G. J. Strens, editor. John Wiley &
Sons, London.New York.Sydney.Toronto, 197-216.

Washburn, E. W., 1921a, Proceedings of the National Academy of Science U.S.A., **7**, 115-116.

Washburn, E.W., 1921b, *The Physical Review*, **XVII**, (3), 273-283.

Watanabe, J., and Lepoutre, P., 1982, *Journal of Applied Polymer Science*, **27**, 4207-4219.

Whittaker, D.W., 1984, *OR on the micro*, Wiley, Chichester.

Yamazaki, H., Munakata, Y., 1993, *Transactions of the 10th Fundamental Research
Symposium*, Oxford, September, 913-934.

Yanuka, M., Dullien, F.A.L., Elrick, D.E., 1986, *Journal of Colloid and Interface Science*,
**112**, 24-41.

Zang ,Y-H., 1993, *Tappi Journal*, **76**, 97-103.

Zgrablich, G., Mendioroz, S., Daza, L., Pajares, J., Mayagoitia, V., Rojas, F., Conner, W.C., 1991,
*Langmuir*, **7**, 779-785.

# NOTATION

$A$         area of plane normal to flow

$C$         size of cubic pore

$d$         throat diameter

$dV/dt$         volumetric flow rate

$dV_{blank}$         total change in mercury volume during blank run

$dV_{Hgpen}$         increase in mercury volume due to compression of a volume of mercury which fills the empty penetrometer

$dV_{pen}$         increase in mercury volume due to penetrometer expansion

$dV_{Hg}$         increase in mercury volume due to compression of mercury during sample run

$dV_{Hgbulk}$         compression of mercury volume corresponding to sample bulk volume

$dV_{sample}$         increase in mercury volume caused by the compression of the sample

$dV_{ss}$         compression of continuous solid phase of sample

$dV_{su}$         compression of solid into unintruded void space

$h$         throat length

$k$         absolute permeability

$l_{cell}$         unit cell length

$m_{sample}$         mass of sample

$M_{ss}$         solid phase bulk modulus

$P$         applied pressure

$P_{50}$         pressure at which 50% pore volume is intruded

$P^z$         applied pressure at which accessible pore volume is fully intruded

$P^{max}$         maximum experimentally attainable applied pressure

$r$         radius

$t$         time

| $T_g$ | glass transition temperature |
| --- | --- |
| $V^1_{bulk}$ | bulk volume of sample at one atmosphere pressure |
| $V_{obs}$ | observed volume of mercury intruded |
| $V_{int}$ | volume intruded into sample |
| $V^1_{blank}$ | volume of mercury used in the blank experiment at one atmosphere pressure |
| $V^1_{pen}$ | volume of the penetrometer at one atmosphere pressure |
| $V^1_{Hg}$ | total volume of mercury in filled penetrometer (with sample) at one atmosphere pressure |
| $V^1_{Hgpen}$ | volume of mercury in filled penetrometer (no sample) at one atmosphere pressure |
| $V^1_{Hgbulk}$ | volume of mercury equal to the bulk volume of sample at one atmosphere pressure |
| $V^z_{ss}$ | volume of the continuous solid phase of the sample at zero void pressure |
| $V^1_{solid}$ | volume of solid at one atmosphere pressure calculated from composition and constituent densities |
| $w_{pigment}$ | relative weight of pigment in parts per hundred |
| $w_{binder}$ | relative weight of binder in parts per hundred |
| $x, y, z$ | Cartesian coordinates |

*Greek letters*

| $\beta$ | number of tubes in $z$ direction in a unit cell |
| --- | --- |
| $\gamma$ | mercury interfacial tension |
| $\lambda$ | mean free path length between molecular collisions in the fluid |
| $\mu$ | fluid viscosity |
| $\theta$ | mercury/solid/air contact angle |
| $\rho_{pigment}$ | density of pigment |
| $\rho_{binder}$ | density of binder |

$\phi^1$        porosity at one atmosphere pressure

$\phi_{uncorr}$        porosity uncorrected for compressibility

$\phi_{corr}$        corrected porosity

$\psi_{ss}$        solid phase compressibility

$\Omega$        network averaging operator

# APPENDIX 1

Acronal is a tradename of BASF, P.O. Box 4, Earl Road, Cheadle Hulme, Cheshire.

Dow Chemical Company, Lakeside House, Stockley Park, Uxbridge, Middlesex.

Gohsenol Products distributed by British Traders and Shippers Ltd.

Lytron is a tradename of Morton International Ltd., Speciality Chemicals Group, Greville House, Hibernia Road, Hounslow, Middlesex.

Revinex is a tradename of Doverstrand Ltd, Temple Fields, Harlow, Essex.

Ropaque is a tradename of Rohm & Haas Company, Lennig House, 2 Mason's Avenue, Croydon, Surrey.

# APPENDIX 2

The figure below is a schematic of the SEM used for this work (Jeol JSM - 840A). The main features of the microscope are an electrically heated tungsten filament, at a selected negative potential 20 kV, mounted on a ceramic insulator. The electrons emitted by the filament are accelerated to earth and are focussed via, a double condenser lens system with field limiting aperatures, onto the specimen. An image or diffraction pattern from the specimen is obtained on a fluorescent screen via a lens magnification system. Image contrast may be enhanced by the use of an objective aperature, and the area of diffraction may be selected by a selected area aperture. The image is focussed with the objective lens and magnification is controlled by the exitation of the intermediate and / or diffraction lens. The depth of field of the instrument is such that the top and bottom of the specimen are simultaneously in focus while its depth of focus enables the camera to capture the image.
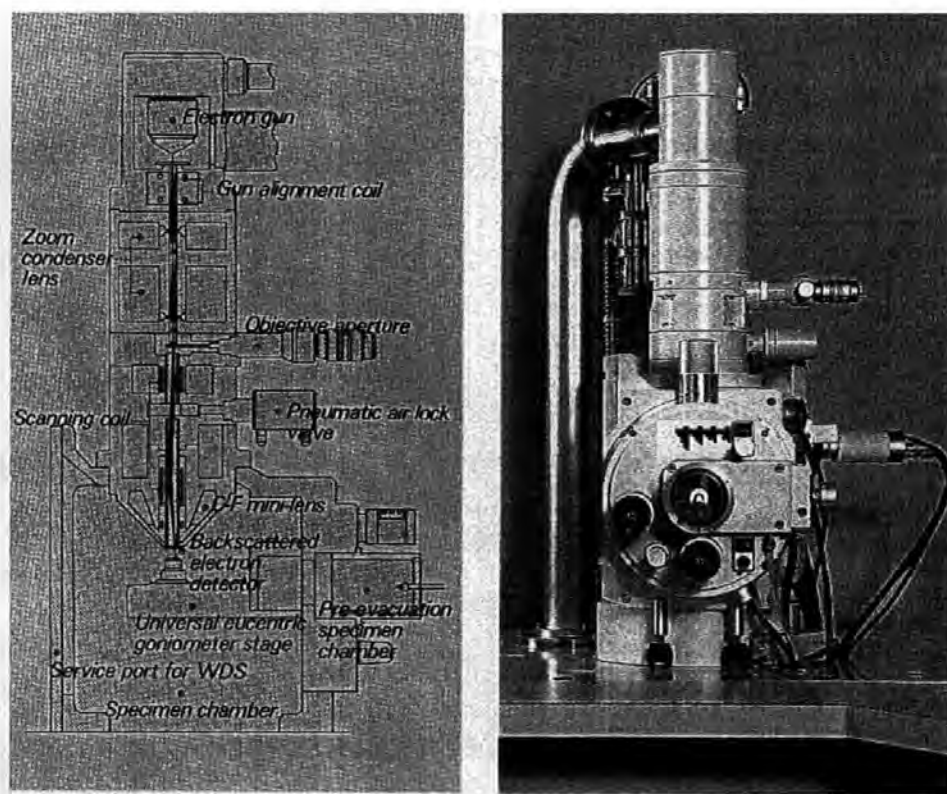


Figure 56: Scanning electron microscope

# APPENDIX 3

## X-Ray Powder Diffraction from a basepaper

Clay minerals consist of thin crystals which are themselves made up of ordered arrays of atoms arranged in a periodic or repetitive way. An incident beam of X-rays impinging on this array becomes scattered by the electrons distributed around the atoms. The intensity of the scattered X-rays depends on the electron density distribution associated with the atomic configuration and the direction of the scatter. Combinations of these geometrically scattered x-rays lead to a coherent interference/diffraction pattern depending on the relative phase of the scattered wavefronts, Bragg, (1913). The direction in which a diffraction maximum occurs is related to the size and shape of the repeating unit cell comprising the crystal structure. A diffraction or reflection plane within a crystal of unit cell dimensions {abc} is defined by the Miller indices (hkl). The spacing between the planes, $d_{hkl}$ , is related to the angle of diffraction, $\theta$, by

$$2 \sin \theta_{hkl} = \frac{\lambda}{d_{hkl}} \qquad (33)$$

for a given x-ray wavelength, $\lambda$.

Previous work by Kraske, (1960) developed the method of Field and Merchant, (1945) using "sample rocking" - a technique used widely for determining crystallite orientation of bulk structures such as machined metals, pre-stressed structures etc. The generalised approach of Kraske may be used to determine isometric crystal orientation as well as anisometric orientation and depends upon path length absorption of a given x-ray diffraction peak. The method described here differs from that of Kraske in that the anisometry, "plateyness", of kaolin particles provides an opportunity to study the effective

relative number of scattering units in the coating layer which contribute to given X-ray diffraction peaks. Without knowledge of the crystal structure factors, this method, unlike that of Kraske, cannot be used to describe an orientation angle quantitatively but does provide a more convenient means of evaluating comparative papers and paper coatings to determine relative degrees of orientation without the need for specialised sample mounting apparatus (Gane, (1995)).

Clays are characterised by intense first and second order basal reflections at d-spacings of $d_{001} \approx 7.1$ Å and $d_{020} \approx 3.57$ Å referring to crystal planes parallel to the ab and ac planes respectively, Figure 42.
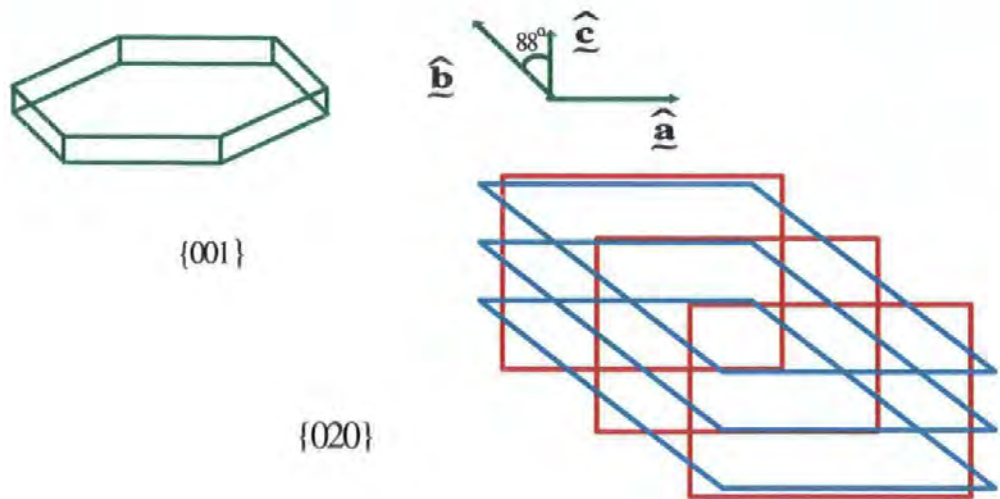


**Figure 57: Crystal plane structure of kaolin**

In the geometry of a reflection powder diffractometer, Figure 43, only kaolin platelets lying oriented parallel to the plane of the paper (i.e. parallel to the sample holder surface) will contribute to the intensity of the (001) peak. The (020) peak (second order reflection) is produced by diffraction from planes in the crystal which are almost perpendicular to the (001) planes (inclined at circa. 88°) and will only receive contribution to its intensity by particles imperfectly aligned with the plane of the paper. In principle, therefore, the ratio

particles imperfectly aligned with the plane of the paper. In principle, therefore, the ratio of the 020 to 001 peak intensities [I(020)/I(001)] is a relative measure of the ensemble average particle orientation of the pigment in the basepaper.
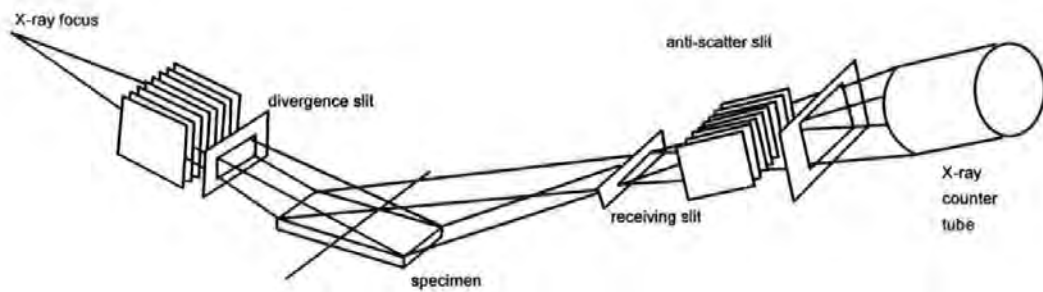


**Figure 58: Geometry of a powder reflection diffractometer**

# APPENDIX 4

## PUBLISHED PAPERS

*Computer modelling of the pore structure and permeability of pigmented coatings.*

Kettle, J.P., Matthews, G.P., Tappi Coating Fundamentals Conference 1993

Published in Conference Proceedings, 121-126

*Performance of LWC grade papers in a pilot - scale calendering study.*

Kettle, J.P., PITA Annual Coating Conference, Leicester, March 1995

Published in Conference Proceedings.

*Void space structure of compressible polymer spheres and consolidated calcium carbonate paper-coating formulations.*

Gane, P.A.C., Kettle, J.P., Matthews, G.P., Ridgway, C.J.

Published in Industrial Chemical and Engineering Research Journal, (35), 1753-1764, May, 1996.

# COMPUTER MODELLING OF THE PORE STRUCTURE AND PERMEABILITY OF PIGMENTED COATINGS

John P. Kettle
Assistant Scientist
ECC International Ltd
St Austell, PL24 2SQ

G.Peter Matthews
Principal Lecturer
University of Plymouth
Plymouth, PL4 8AA

## ABSTRACT

A network method is presented for the simulation of mercury intrusion and the calculation of the permeability of porous media. The method is specifically applied to different types of pigmented coating layers, but can be used for any porous medium. A network is derived in which the mercury intrusion curve and porosity agree with experiment. Combinations of the Darcy and Poiseuille equations of flow are used to generate terms expressing the flow capacity of each pore-throat-pore connection (arc). From the overall capacity of the network, calculated by means of a network analysis algorithm, is derived the permeability of each sample. The method is applied to fine ground calcium carbonate, both pure and with added latex binder, which have been coated onto an impermeable substrate and then removed. Its application to the study of fine coating clay samples is also discussed. Three-dimensional structure simulations are presented, and possible uses of the modelling method, for example in the study of the effects of calendering, are considered.

## INTRODUCTION

Paper coating technology has continued to advance rapidly over recent years. Blade coating machines are now capable of speeds that were impossible a decade ago. These advances are due not only to improved technology, but also to better understanding of the factors that influence the interactions between coating colour components and the effects that these have on rheology, water retention and runnability(1-4).

Paper is coated with pigment to improve its surface properties. The pigment particles cover a distribution of sizes and shapes. Their physical packing and interactions in the coating layer, both between particles and with coating formulation additives dictate the coating structure. The interaction between the resulting pores in the coating layer and printing inks is of great importance in determining the final print quality obtainable for a particular paper.

In this work we introduce a computer model of porous media. The model consists of an array of cubes and cylinders representing pores and throats. The program development has been based primarily on the study of permeability in sandstones, and has been successfully used to simulate some properties of outcrop samples (5). In the present study, a void space model is generated which accurately reproduces mercury intrusion measurements of paper coating pigments. The model is then used for the calculation of fluid permeability.

Our studies of coating structures have involved the preparation of pigmented coatings on aluminium which acts as an impermeable substrate. The coatings were air dried and were removed from the substrate as consolidated samples for the mercury porosimetry experiments. The pigments used were: (i) a fine coating grade calcium carbonate slurry, 90wt% < 2 micron (Carbital 90), and (ii) the same sample with 11pph of a non-thickening offset styrene-butadiene latex (Dow 950) added. The porosities of the two samples were measured as 29.5% and 34.2% respectively, using a mercury displacement technique. Both the samples are assumed isotropic. The use of the program for the simulation of an anisotropic (platey) English coating clay is also discussed.

## THE COMPUTER MODEL

The void space within a porous solid can be regarded as a network of void volumes (pores) connected by a network of smaller void channels (throats). In the terminology of Operational Research Network Analysis, the centre of each pore is a node, and pore-throat-pore links between the nodes are referred to as arcs. Thus the void space network comprises an array of nodes, connected by arcs along the line of each throat. We present such a simulation, using software which we have named PORE-COR (Pore-level properties Correlator), and use it to model the mercury intrusion curves and permeability of experimental samples of pigmented coatings.

**Figure 1** Unit cell of Carbital 90.
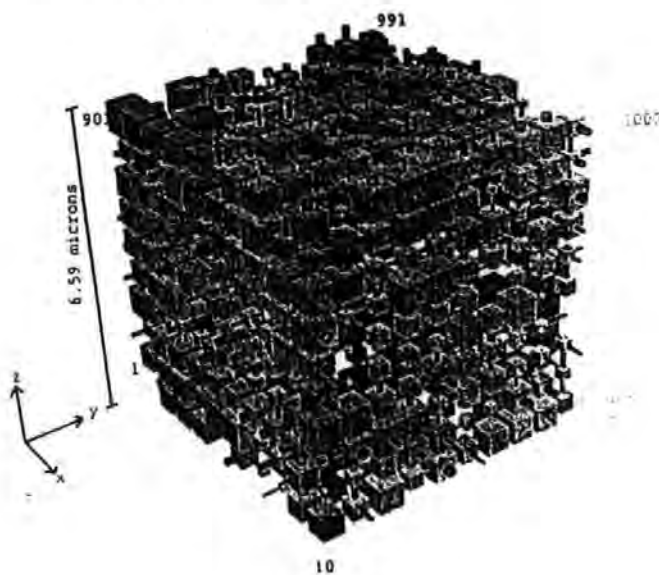
Our network comprises a three dimensional cubic unit cell containing 1000 nodes on a regular 10 x 10 x 10 matrix, Figure 1. The unit cell repeats infinitely in the x and y directions. In the z direction, both fluid intrusion and permeability apply to a single unit cell, although permeability would be the same for a repeated cell. Thus we are effectively modelling an infinite layer of thickness of 6.59 microns (or 7.42 microns for the sample with added latex). This corresponds to a coating of about 12 gsm (g m$^{-2}$).

The nodes are positioned using Cartesian coordinates x,y,z, although since the samples are assumed isotropic, the allocation of these axes is arbitrary. The void volume in the unit cell comprises up to 1000 cubic pores centred on the nodes. Connected to each pore are up to six cylindrical throats along the line of the arcs in the positive and negative x,y and z directions. We refer to the number of throats connected to a particular pore as the *pore co-ordination number*, and the arithmetic mean of this quantity over the whole unit cell as the *connectivity*. Individual pore coordination numbers may range from 0 to 6, while the connectivity of clay or calcium carbonate coatings was found to be approximately 3, as explained below.

An invasion percolation method is used to calculate the fraction of pore volume occupied at a series of increasing, static pressures in a mercury porosimetry simulation. In the absence of electron microscopic serial tomographic studies of pigment structures, which would reveal the relationship between pore and throat sizes, the pores are set equal to three times the diameter of the largest throat entering them. It has been shown in a previous work that this gives a pore:throat size correlation similar to limestone, but different from sandstone (5). The throat size distribution is adjusted manually to give a close fit to the experimental primary drainage mercury porosimetry curve, as represented by the larger arrows in Fig 2. Finally the row spacing of the matrix is set so that the porosity of the simulated network equals that of the experimental sample - increasing the pore row spacing lengthens the throats, increases the unit cell size, and reduces the porosity.

Using the same network, we also calculate the absolute permeability for an incompressible fluid. The calculation uses a combination of the Darcy and Poiseuille equations.

## CHARACTERISTICS AND SCOPE OF THE WORK

The network model which we present has three main characteristics: (i) it has a real geometry, (ii) the same network with precisely the same geometry is used to model properties, and (iii) no arbitrary parameters are invoked, and thus the model can be applied to any porous medium.

The first characteristic, the model's real pore space geometry, has been displayed above. The real, space-filling geometry of the network contrasts with other networks used for the simulation of porous media, which are mathematical arrays of nodes and arcs which often cannot be represented by a 3-D image. The second feature, the

wide range of properties which have been previously modelled with the different networks, is detailed in the box diagram, Fig. 2. Properties which have already been modelled are shown in the black shadowed boxes, together with references to previous publications. These publications have shown that the network reproduces the experimental mercury primary drainage curve (5), porosity (5,6), connectivity(6), pore:throat size correlation (5), tortuosity (6), and gaseous diffusion through a dry sample of sandstone (6), although not a saturated one. The surface area of the simulated void space is too smooth by two orders of magnitude, but can be easily roughened to match experiment (5). The model also has too high a fractal dimension (7).

**Figure 2** Scope and data flow of PORE-COR, showing references to previous work
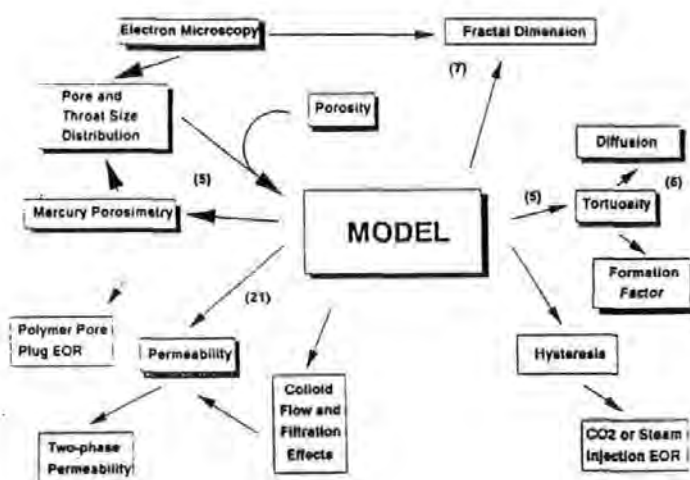


The present work involves the use of linear-logarithmic throat size distributions for the porosimetry simulation, and also the calculation of the permeability, shown grey shadowed in Fig. 2. The unshadowed boxes are the subject of tentative or unpublished work.

## MERCURY POROSIMETRY

### Discussion

The state of the art of mercury porosimetry in 1981 was reviewed by Van Brakel (8). In common with other users of this technique, we employ the Washburn (or Laplace) equation to relate mercury pressure to intruded throat size:

$$d = -\frac{4 \gamma \cos\theta}{P} \qquad (1)$$

where $\gamma$ is the interfacial tension between mercury and air (480 dynes cm$^{-1}$), P is the capillary pressure, and d is the throat diameter. $\theta$ is

the mercury contact angle, which is taken to be 140° pending precise measurement of this parameter. Van Brakel discusses the limitations in the use of this equation and the uncertainties in the values of γ and θ. However, to overcome these problems, the geometry of our network would have to be made excessively complicated to include, for example, the exact shape of the pore and throat connections (9,10), or a pseudo pore space model (11) would have to be used. Either approach would defeat the object of the present study, which is to generate a relatively simple pore-space network which can be used for the simulation of a wide range of properties.

The network presented here is the result of mapping the mercury intrusion curve of the pigmented coating onto a network of cubic pores and throats. When the percolation algorithm is applied to this network it then reproduces the original intrusion curve to a good approximation. Although the simulated network is neither a correct geometric representation of the actual porous "solid", nor a unique mapping from the intrusion curve, it nevertheless gives an insight into the nature of the solid, and can be used to generate other properties, including permeability. Clearly the mapping is to some extent arbitrary, in that it yields the artificially regular array of pores and throats of fixed geometry shown in Fig. 1. However the successful matching of this array to a range of properties produces an unique array within the constraints of the model. The properties which generate the array, shown with larger arrows at the top lefthand side of Fig. 2, are the sizes of the pores and throats and their coordination numbers, the mercury porosimetry primary drainage curve, and the porosity. Only when we have produced the pore and throat array, which is a representation of the true complexity of the medium, do we then average the pore properties in the form of a capacity term which is an explicit average over only the accessible pores and throats - i.e. it is an average which depends on the positional relationships within the network as well as the sizes of the void spaces themselves.

Garboczi (12) has pointed out that the two main limitations of an approach such as this are (i) that the tubes are all considered to be cylindrical, and (ii) that the mapping of the effective network derived from the mercury porosimetry curve is not necessarily the same as the real network. Calculations on specific shapes of pores have been carried out by Mason (13), who has also modelled the intrusion and extrusion of mercury in an array of packed spheres by using the Haines in-sphere approximation to model the void spaces between them (14). Conner (15) has used a range of rod- and plate-like structures to demonstrate that there is a relationship between shape of pores and throats, and the shapes of the intrusion and extrusion mercury hysteresis curves. Yanuka and co-workers have also used different void shapes, in the form of a three dimensional network of intersecting ellipsoids for their simulation of percolation processes (16). Kent and Lyne (17) have discussed the effect of the local geometry of the pore system in paper on fluid penetration. Payatakes and coworkers have used 20x20x20 and 30x30x2 networks (18,19) for the simulation of mercury intrusion and extrusion curves. They use an invasion percolation algorithm effectively the same as in this

work, but, like Kent and Lyne, include resistance effects due to pore shape (9). However, Garboczi (12) demonstrated mathematically that a range of pores and throats of different shapes and sizes could be successfully represented by a random network of interconnecting elliptical cylinders. The elliptical cylinders can range from circular cylinders (semi-minor axes equal) through to cracks (one semi-minor axis = 0). As will be demonstrated, we find that the mercury intrusion curve can be precisely mapped using solely throat size distribution, known pore/throat size correlation, and connectivity. Although shape is undoubtedly important, it can be subsumed within the even more important parameters of size and connectivity, the resulting sizes being functions of the true sizes and shapes of the void spaces (20).

The resulting simulated structure is thus a representation of the pore and throat sizes and shapes corresponding to non-wetting mercury intrusion as calculated by an invasion percolation algorithm. However, the properties of coatings are strongly dependent on the imbibition characteristics of wetting inks. These properties are likely to have a rather different shape dependence, which is outside the scope of this work.

## Results

Figure 3 shows the throat and pore size distribution for Carbital 90, which generates the mercury intrusion curve shown in Figure 4.

**Figure 3** Throat and pore size distribution for Carbital 90 , ------ throats, ——— pores



Throat diameter or pore size / microns
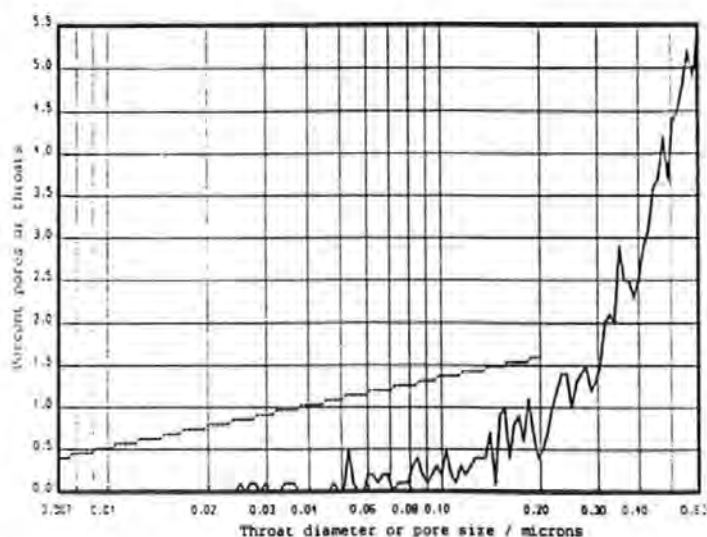
**Figure 4** Mercury intrusion curve for Carbital 90,
———— experimental, -------- simulation
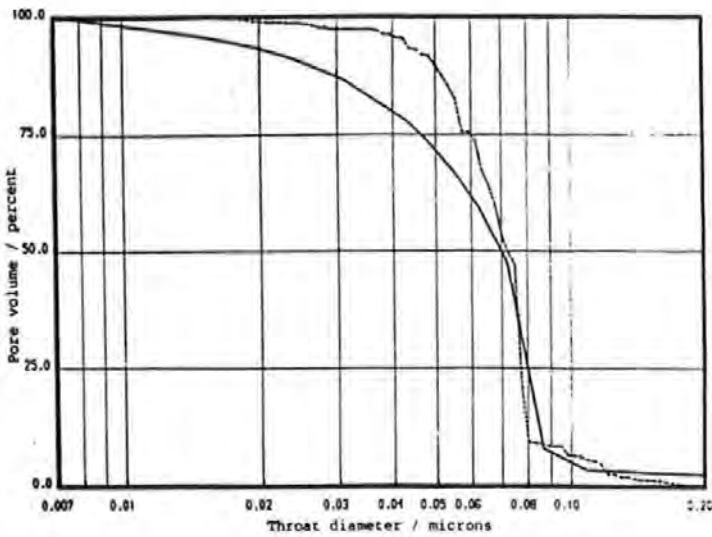


Figures 5 and 6 are the corresponding results for Carbital 90 with 11 pph of Dow 950 latex added. The simulated unit cell for Carbital 90 plus latex is shown in Figure 7 - note the increased unit cell size.

**Figure 5** Throat and pore size distribution for Carbital 90 with added latex    -------- throats, ———— pores



breakthrough pressure of 147.1 atm abs (2162 psia), when the mercury has penetrated down through all accessible pores and throats of $9.864 \times 10^{-2}$ microns (98.64 nm) or greater.

It should be noted that the throat size distributions, Figures 3 and 5, bear no relation to the derivative of the corresponding mercury intrusion curves, Figures 4 and 6, as is often assumed in the literature.

**Figure 6** Mercury intrusion curves for Carbital 90 plus added latex.  ———— experimental, -------- simulation
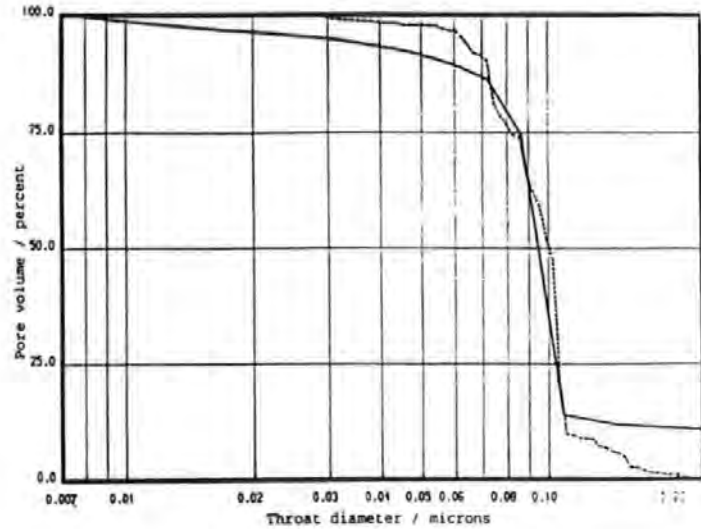


The shape at the point of inflexion is also determined by the connectivity. The correct shape at the point of inflexion is generated by a connectivity of 3.5. Higher connectivities give a steeper shoulder above the point of inflexion due to the greater suddenness with which the mercury invades the network near the breakthrough pressure. Also, breakthrough occurs at a lower pressure (higher throat diameter) because of the increased number of routes available through the network.

Also in this figure is shown in black the extent of the mercury intrusion of the outer layers of the unit cell at the mercury

**Figure 7** Unit cell of Carbital 90 plus 11ph latex. Extent of mercury intrusion at breakthrough pressure shown in black.
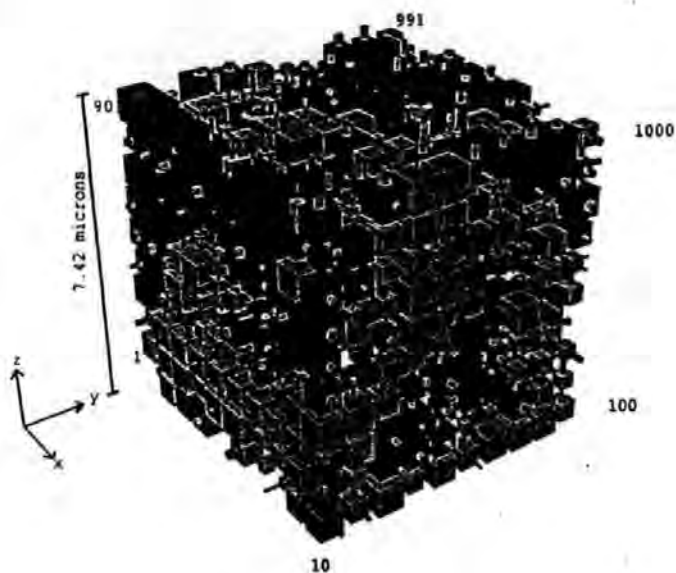


## PERMEABILITY CALCULATIONS

### Discussion

A long standing problem in the study of porous media has been the question of how to calculate the permeability of a solid from a knowledge of the geometry of the void space within it. The absolute permeability k of a porous solid is traditionally defined in terms of Darcy's law. With reference to a cell of the solid of unit volume, this may be written:

$$\left(\frac{dV}{dt}\right)_{cell} = -\frac{k\, A_{cell}\, \delta P_{cell}}{\eta\, l_{cell}} \qquad (2)$$

where $(dV/dt)_{cell}$ is the volumetric flow rate across the cell, $\eta$ is the shear viscosity of the fluid, $\delta P_{cell}/l_{cell}$ is the (negative) pressure gradient across the length $l_{cell}$ of the cell in the direction of flow, and $A_{cell}$ is the cross-sectional area.

An incompressible fluid flowing through a tube takes up a parabolic velocity profile, with maximum flow rate down the centre of the tube. If the flow at the walls is assumed to be zero, integration over the velocity profile yields the Poiseuille equation:

$$\left(\frac{dV}{dt}\right)_{tube} = -\frac{\pi r^4_{tube}\, \delta P_{tube}}{8\eta\, l_{tube}} \qquad (3)$$

$(dV/dt)_{tube}$ is the volume flow rate, $r_{tube}$ the radius of the tube and $\delta P_{tube}/l_{tube}$ is the pressure gradient across the tube.

Combining equations 2 and 3:

$$k = \frac{\pi}{8}\, \Omega\left(\frac{r^4_{tube}}{l_{tube}}\right)_{cell}\, \frac{l_{cell}}{A_{cell}} \qquad (4)$$

A network analysis approach to this problem supplies the term $\Omega(r^4_{tube}/l_{tube})$ as the maximal flow capacity through the network of pores and throats. The term $r^4_{tube}/l_{tube}$ is modified to take into account the flow capacity through individual pore-throat-pore arcs. $\Omega$ is an averaging operator over all the arc capacities in the unit cell (21). There is an overall conservation of flow, so that the entire volume of fluid entering the top of the unit cell (Fig. 1) emerges at the bottom, with no build up through the network. However, the unit cell infinitely repeats in all horizontal (x and y) directions, and fluid can pass out sideways from one unit cell to the next. Conservation is maintained by an identical volume flowing in at the opposite face of the cell. The value obtained as the maximal flow is an average of the capacity values over only the channels found to carry flow. Corrections to the terms can also be made to allow for the slip flow of gases (21), known in geological circles as the Hagenbach correction. In this work, however, the fluid is taken to be an incompressible liquid with a negligible mean free path distance between molecular collisions relative to the size of the pores and throats.

### Results

The absolute permeability of the Carbital 90 was calculated as 2.65 µD (2.65 x 10⁻⁶ Darcies), and that of the Carbital 90 plus latex as 10.3 µD. The increase in permeabiity on adding latex is due to the latex disrupting the structure during drying (22), as also demonstrated by the increase in porosity from 29.5% to 34.2%.

### FUTURE WORK

Work has begun on the simulation of the structure of SPS, a relatively fine English clay comprising oblate spheroid particles with an average aspect ratio of approximately 25. Not only does the modelling of this substance require the z dimension of the unit cell to be reduced relative to the x and y dimensions by a factor of 25, but also involves the calculation of the relative connectivities in the z direction relative to the x and y directions. Simulations of the packing of oblate spheroids are currently under way to determine this.

It is intended that the modelling procedure described in this work be used for the study of the change in structure and permeability during calendering, by a similar z axis scaling procedure.

### CONCLUDING REMARKS

We have presented a method for the simulation of mercury intrusion curves into paper coating pigments. We have also shown how the resulting structure can be used for the calculation of the fluid

permeability of the sample, which will be of relevance to the understanding of dewatering phenomena during coating and assist in the control of bulk porosity for end processing of coated paper. The method is being extended to platey samples and to the study of the changes of structure of pigment coatings during calendering.

## ACKNOWLEDGMENTS

## REFERENCES

1. P.A.C.Gane, P.M.McGenity, P.Watters *Tappi 1992 Coating Conference Proceedings* 117-132

2. P.M.McGenity, P.A.C.Gane, J.C.Husband, M.S.Engley *Tappi 1992 Coating Conference Proceedings* 133-145.

3. J.C.Husband, J.M.Adams, *Paper coating and Chemistry Symposium* Stockholm 1992

4. L.E.Larrondo, P.Lepoutre, *Tappi 1990 Coating Conference* 43-50

5. M.Spearing, G.P.Matthews, *Trans. in Porous Media* 6: 71-90, 1991

6. G.P.Matthews, M.C.Spearing, *Marine and Petroleum Geology*, 9, (1992) 146.

7. M.C.Spearing, G.P.Matthews, in *"Computer Modelling in the Environmental Sciences"*, ed. D.G.Farmer and M.J.Rycroft. IMA Conference Series, Oxford University Press, Oxford, 1991.

8. J. Van Brakel, S. Modry, M.Svata, *Powder Technol.*, 29, (1981)

9. C.D.Tsakiroglou and A.C.Payatakes, *J.Colloid Interface Sci.*, 137, (1990) 315.

10. R.J.Good, R.Sh.Mikhail, *Powder Technology*, 29, (1981), 53.

11. J.Van Brakel, *Powder Technol.*, 11, (1975) 205.

12. E.J. Garboczi, *Powder Tech.* (Nos 2) Aug. (1991) 121-125

13. G.Mason, N.R.Morrow, T.Walsh, *Characterisation of Porous Solids*, 243, Elsevier, Amsterdam, 1988.

14. G.Mason, D.W.Mellor, *Characterisation of Porous Solids II*, 41, Elsevier, Amsterdam, 1991.

15. W.C.Conner, C.Blanco, K.Coyne, J.Neil, S.Mendioroz, J.Pajares. *Characterisation of Porous Solids*, Elsevier, Amsterdam, 1988.

16. M.Yanuka, F.A.L.Dullien, D.E.Elrick, *J.Colloid Interface Sci.*, 112,(1986) 24.

17. H.J.Kent, M.B.Lyne, *Nordic Pulp and Paper Research Journal* 2: (1989) 141.

18. C.D.Tsakiroglou, A.C.Payatakes, *J.Colloid Interface Sci.*, 146, (1992) 479.

19. G.N.Constantinides, A.C.Payatakes, *Chem. Eng. Comm.*, 81, (1989) 55.

20. O.Z.Cebeci, *J.Colloid Interface Sci.*, 78, (1980) 383.

21. Matthews, G.P., A.K.Moss, M.C.Spearing, F.Voland, *Powder Technology*, submitted for publication (1992).

22. Groves R., *Paper coating and Chemistry Symposium* Stockholm 1992

PAPER INDUSTRY TECHNICAL ASSOCIATION



# 1995

# PITA COATING CONFERENCE

# COATING FOR PROFITABLE PERFORMANCE

Organised by the PITA Coating Working Group

Conference Proceedings

14-15 March 1995

# PERFORMANCE OF LWC GRADE PAPERS
## IN A PILOT - SCALE CALENDERING STUDY

**John Kettle**
**ECC International R & D**

## Abstract

The quality of a finished coated sheet is dependent upon many factors during the production process. Most, but not all, paper grades are calendered with the main objective of producing a smoother, more glossy surface for printing. Many paper mills are interested in producing grades that are equivalent to highly supercalendered grades of paper using modern soft nip calenders as on-machine or off-machine units.

The focus of this study was to characterise how paper quality may be modified by altering the coating colour formulation and the calendering conditions. Two commercially available pigments were selected for this study, SPS, an English coating clay, and Carbital 90, a fine ground marble. Both pigments were pilot-coated in a latex / cmc formulation and a latex / starch formulation onto an lwc base to produce coatings of 10 $gm^{-2}$ coatweight. The papers were calendered using a pilot-scale soft nip calender and a supercalender. The conventional paper properties were measured and more specialised techniques such as surface profilometry (Paperscape and Walsh analysis), cross-section profilometry, and ink tack development were used to characterise qualities of these sheets prepared under different calendering conditions.

## Introduction

Calendering or "finishing" is the final, but necessary, step in the production of coated paper grades. There are two types of calenders that are generally used for LWC production: a conventional supercalender or a modern soft calender. Each type offers particular advantages to papermakers who are faced with the very real demands of ever increasing coater speeds and high print quality.

In a calendering process, the coated web is subjected to pressure and temperature and undergoes a thermo-mechanical transformation. During calendering, the web may respond in

three different ways. Firstly, the web responds as an elastic medium. Then, at higher compressive loads it exhibits "plastic" behaviour and flows in the direction of the applied stress. Finally, the paper has a "memory or history" of what it has previously experienced and some fibre relaxation can occur [1]. Sheet properties such as brightness, opacity and, of course, gloss, smoothness, and print quality are modified by calendering. The extent of this modification depends upon the calendering conditions selected [2].

Soft calendering at high roll temperatures and nip pressures has been investigated for the last thirty years. Brecht et al, in 1968 and 1971 [3,4] reported some effects of high temperature calendering. Subsequent work focused on understanding the nature of paper compression during calendering. Crotogino [5] improved the paper industry's understanding of these phenomena in a series of classic papers on the concept of temperature gradient calendering. Vreeland et al [6,7] applied Fourier's Law to develop the Substrata Thermal Moulding process, in which the glass transition temperature $(T_g)$ of the web material was reached at a depth of approximately $8\mu m$ into the web i.e. typically near the coating-base interface. Most recently, Keller [8] has investigated the effects of nip pressure, nip dwell time and roll temperature on coated paper properties.

Although calendering affects the nature and uniformity of the coating layer, "calenderability" is not only limited by the machinery available to the paper maker but also by such properties as the formation of the base, and the composition and method of application of the coating. This study illustrates how differences in quality may be generated by the off-line use of either a soft calender or a supercalender and how the type of pigment and the chosen formulation can also generate differences in quality.


**Application and Calendering details**

ECC International's Technicentre at Lixhe in Belgium was used to prepare the coated sheets and to calender the coated paper. A 38 gm$^{-2}$ basepaper was supplied by Kymmene Caledonian for this work. The pigments, Carbital 90 and SPS, were formulated with either latex / cmc or latex / starch. The coating colours were applied using a trailing blade application at 1000 m.min$^{-1}$ and the colour solids were optimised to avoid dilatant behaviour. The coating colour details are summarised in Table 1 and it is not surprising that the starch containing colours were coated at lower solids than the colours that contained cmc. Coatings of nominally 10 gm$^{-2}$ per side were obtained for each colour and were dried to a target final sheet moisture of 5.5 wt%.

**Table 1    Coating colour formulations**

|  | SPS LATEX / CMC | SPS LATEX / STARCH | CARBITAL 90 LATEX / CMC | CARBITAL 90 LATEX / STARCH |
|---|---|---|---|---|
| FORMULATION |  |  |  |  |
| DOW 950 / pph | 11 | 8 | 11 | 8 |
| FINNFIX 5 / pph | 1 | 0 | 1 | 0 |
| PENFORD GUM 280 / pph | 0 | 8 | 0 | 8 |
| SOLIDS / wt.% | 58.5 | 56.9 | 65.2 | 58.3 |
| MACHINE SPEED / m.min-1 | 1000 | 1000 | 1000 | 1000 |

A Kleinewefers supercalender and a Kleinewefers soft compact calender were used off-line to calender the coated papers. The calender details are summarised in Table 2 and a schematic layout of the calenders is shown in Figure 1. The calendering conditions employed for the samples reported in this work were selected to illustrate the different qualities that could be achieved by the two different calendering regimes.

**Table 2    Pilot calender operating conditions.**

| KLEINEWEFERS | SUPERCALENDER | SOFT CALENDER |
|---|---|---|
| MACHINE SPEED / m.min-1 | 800 | 1000 |
| REVERSE NIP POSITION | 6/7 |  |
| NUMBER OF NIPS | 11 | 2 |
| LINEAR LOAD / kN.m-1 | 340 | 300 |
| TEMPERATURE / °C | 100 | 150 |
| ROLL COVERS | FIBERUN GB | ELAPLAST |
| HARDNESS / ShoreD | 86-87 | 92 |

3

**Figure 1**      Schematic diagram of the pilot calenders.



KLEINEWEFERS SUPERCALENDER

BOWL NUMBER

12
11
10
9
8
7
6
5
4
3
2
1

KLEINEWEFERS SOFT COMPACT CALENDER
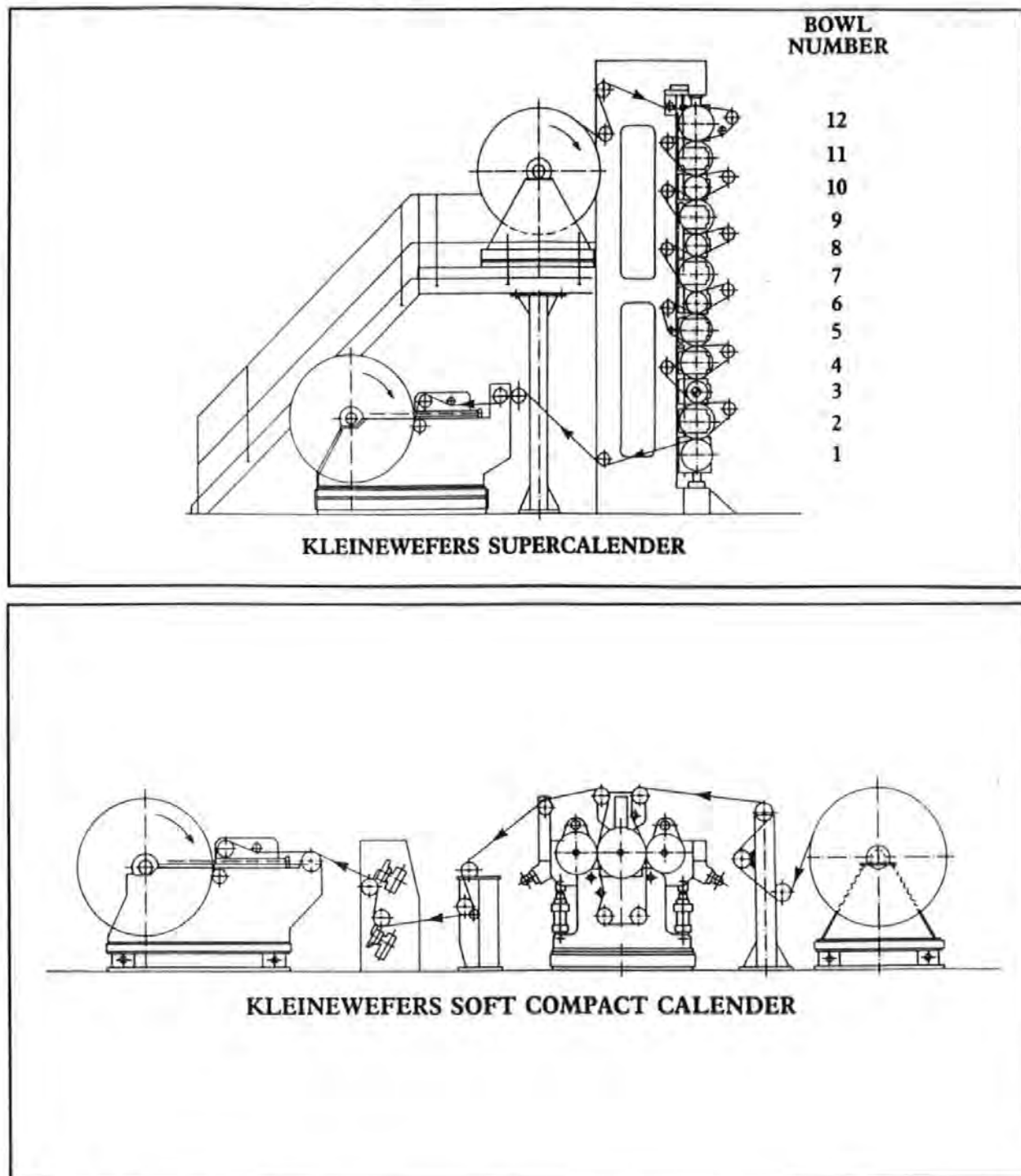
## Results - Paper properties.

A range of papers were produced during the pilot calendering trial and the results reported here provide only a "snap-shot" of the choices available. The papers selected for this study had been calendered using the most severe conditions possible available on each calender. The supercalendered sheets were calendered more severely in this study than the soft calendered

sheets and it followed that the sheet gloss of the supercalendered sheets was higher [Figure 2]. It is also clear from Figure 2 that the sheet gloss of the Carbital 90 coatings is lower than the sheet gloss of the SPS coatings and that the latex/starch coatings had lower sheet gloss than the latex/cmc coatings.

**Figure 2**

**Gloss variation against calender type.**
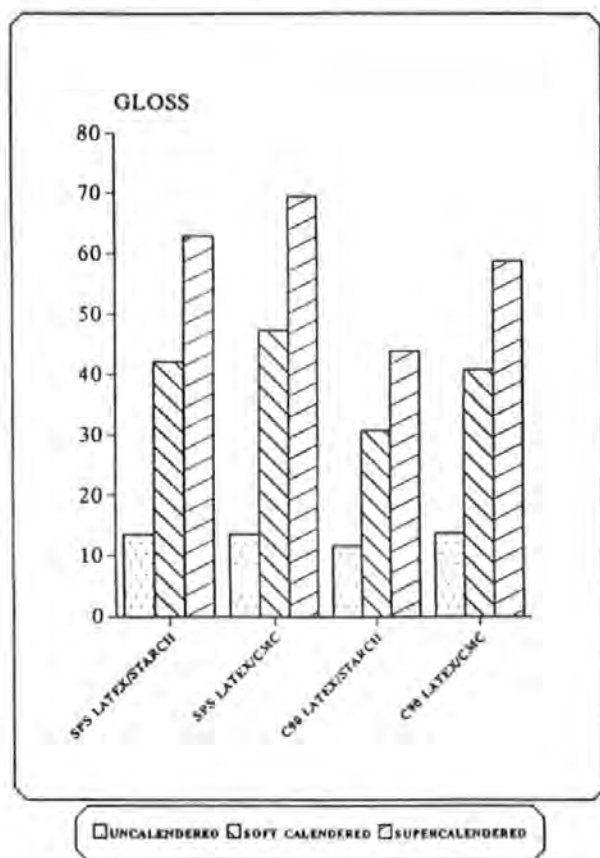
**Figure 3**

**Parker Roughness variation against calender type.**
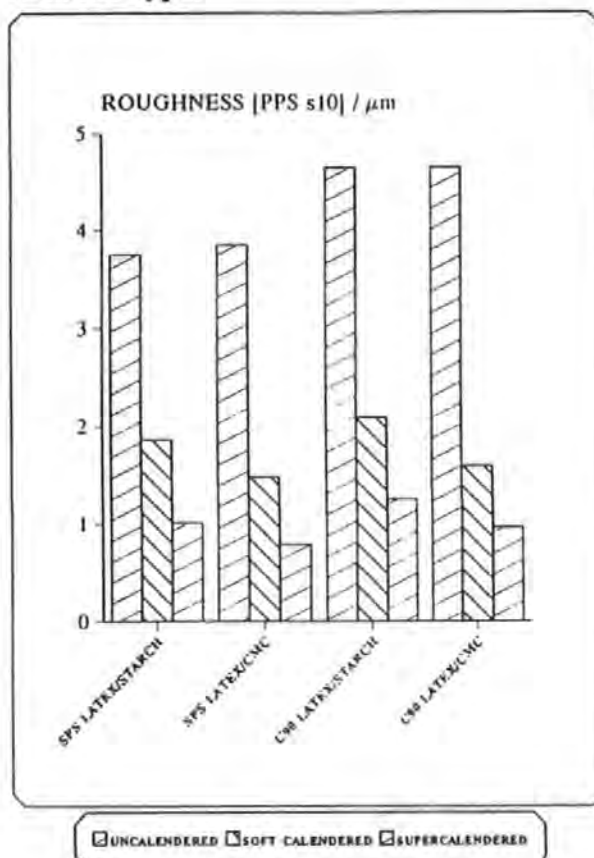




The sheet roughness was assessed, firstly by the conventional Parker Printsurf technique [9]. The results are shown in Figure 3 and indicate clearly that the uncalendered sheets were rougher than the calendered sheets. The soft calendered sheets were nominally rougher than the sheets that had been supercalendered and the latex/starch-containing coatings were rougher than the latex/cmc-containing coatings. It was also observed that the Carbital 90 coatings were rougher than the clay coatings.

An alternative proven technique for assessing sheet roughness is stylus profilometry. This technique uses a modified TALYSTEP instrument which maps the surface roughness [10]. In order to quantify the information, a Walsh transform technique is employed which resolves the jumble of peaks and troughs into a series of component waveforms [11]. To simplify

5

matters further, a single measure of roughness rather than a distribution of amplitudes may be achieved by calculating spectral moments by summing amplitudes and wavenumbers. A good description of the roughness characteristics which control sheet gloss is provided by $\mu_2$, the second order moment, generally at a span length of $128\mu$m. A plot of $\mu_2$ against sheet gloss is shown in Figure 4 (latex/cmc formulation) and Figure 5 (latex/starch formulation). Similar trends were observed for both types of formulation; the Carbital 90 coatings were marginally rougher than the SPS coatings in the uncalendered and soft calendered states. However, after supercalendering the SPS coating was marginally rougher than the Carbital 90 coating despite achieving higher gloss.

**Figure 4**
**$\mu_2$ Roughness at $128\mu$m span length variation against calender type.**
**Latex / cmc coatings**
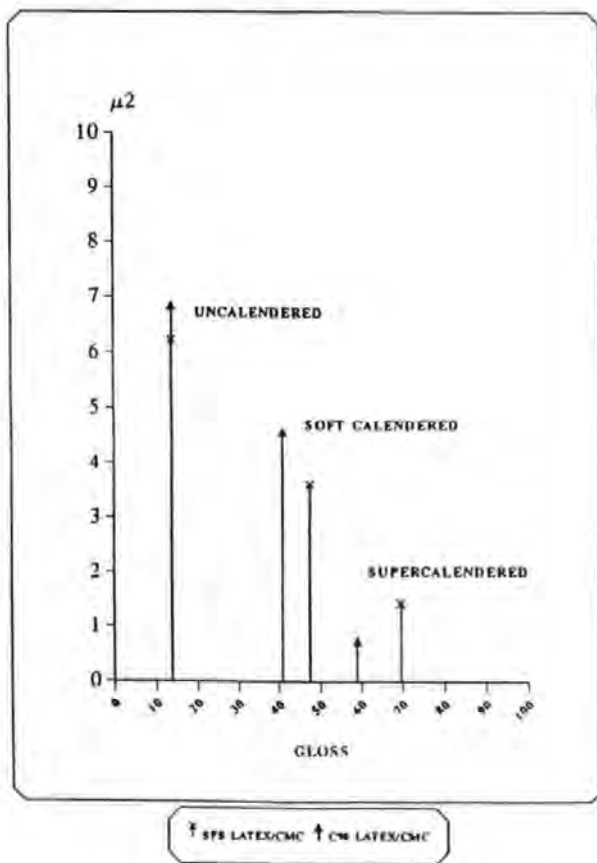
**Figure 5**
**$\mu_2$ Roughness at $128\mu$m span length variation against calender type.**
**Latex / starch coatings**
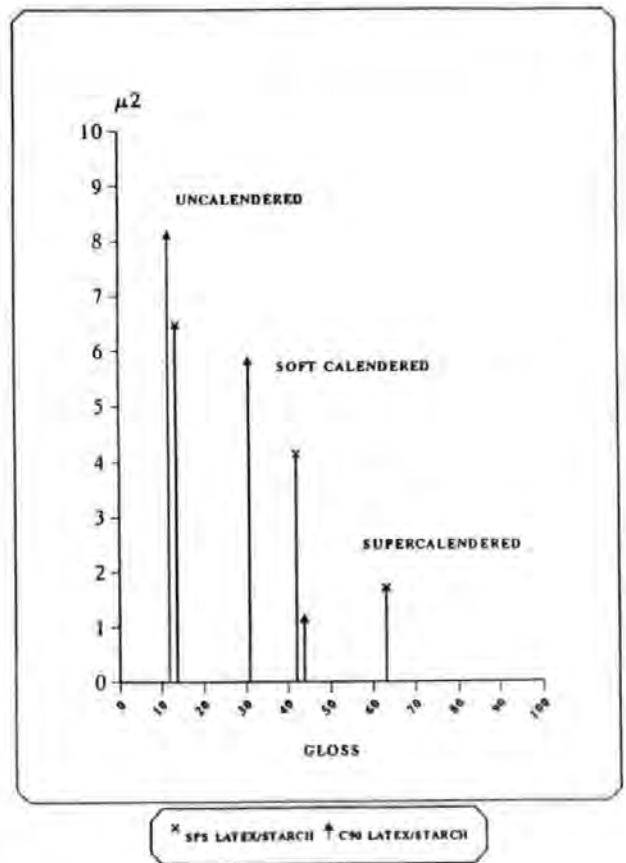




It was expected that the Carbital 90 coatings would maintain a brightness advantage over the SPS coatings. This was found to be true, as shown in Figure 6, and it was also observed that the Carbital 90 maintained a brightness advantage after supercalendering. It was also found that the latex/starch formulation suffered a small loss in brightness compared to the latex/cmc formulations. The trends of opacity change with calendering are not as clear as those for

6

brightness. In the uncalendered form, the SPS coatings had higher opacity than the Carbital 90 coatings with the starch-containing formulations generating lower opacity than the cmc-containing coatings. It is also clear that the soft calender maintained more opacity than the supercalender.

**Figure 6**
**Brightness variation**
**against calender type.**
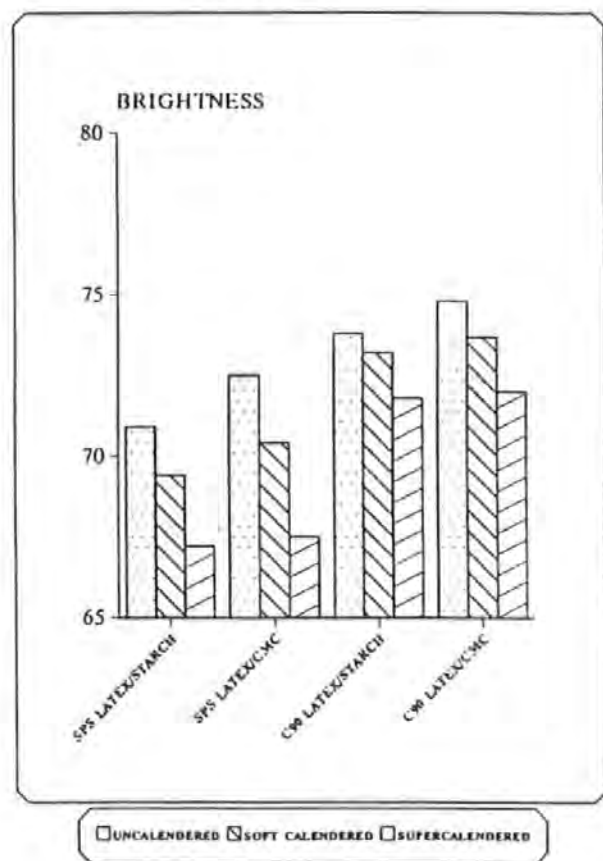
**Figure 7**
**Opacity variation**
**against calender type.**
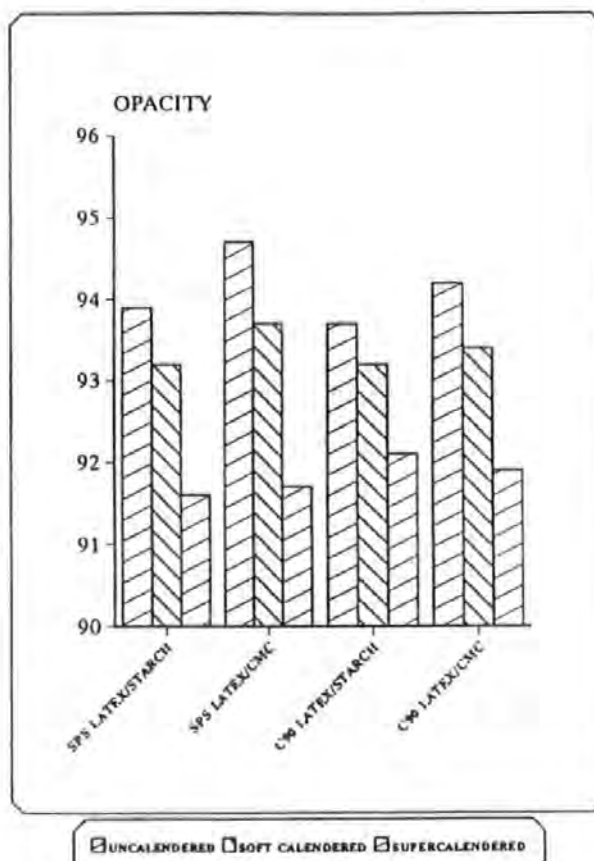


In summary, there are bigger changes in gloss, roughness, brightness and opacity for coatings of SPS than for coatings of Carbital 90. This may be because SPS coatings have a more compressible structure than Carbital 90 coatings.

**Results - Printing properties.**

The print quality of the sheets were assessed in our print laboratory. The print gloss and print density of the sheets were measured using both dry and litho conditions. The print gloss results are shown in Figure 8 and Figure 9. The supercalendered papers had higher print gloss than the soft calendered papers. The Carbital 90 coatings had lower print gloss than the SPS

7

coatings and the coatings that contained starch had lower gloss than the coatings which contained cmc. Obviously, the litho print gloss values are lower than the dry print gloss values due to water interference. The dry print density values of the sheets are very similar as shown in Figure 10. However, the extent of water interference is clearly shown in Figure 11. The coatings that contained starch had very poor litho print density and had inferior quality compared to the coatings that contained cmc. The differences in print quality result from differences in coating pore structure and coating wettability by the ink in the presence of the water in the litho test.

**Figure 8**
**Dry print gloss variation against calender type.**
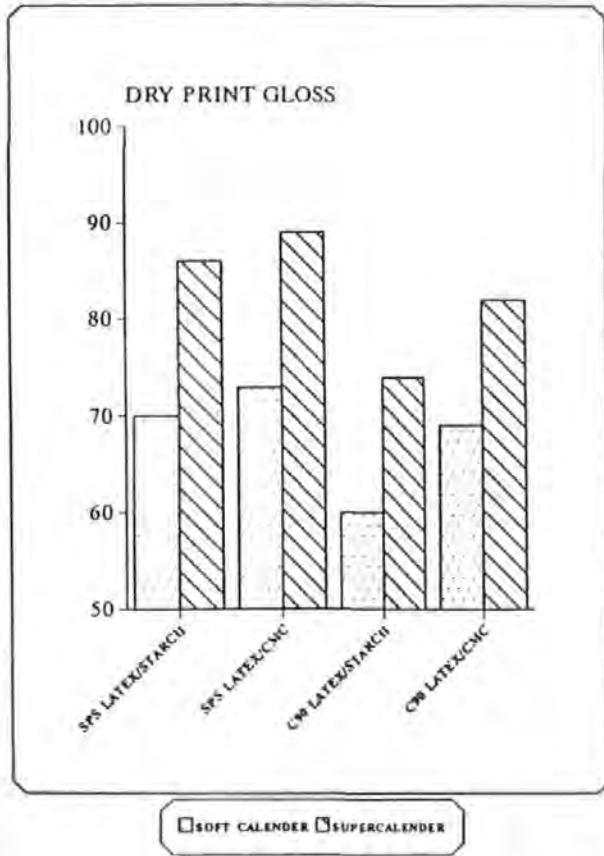
**Figure 9**
**Litho print gloss variation against calender type.**



DRY PRINT GLOSS

☐SOFT CALENDER ☐SUPERCALENDER



LITHO PRINT GLOSS

☐SOFT CALENDERED ☐SUPERCALENDERED
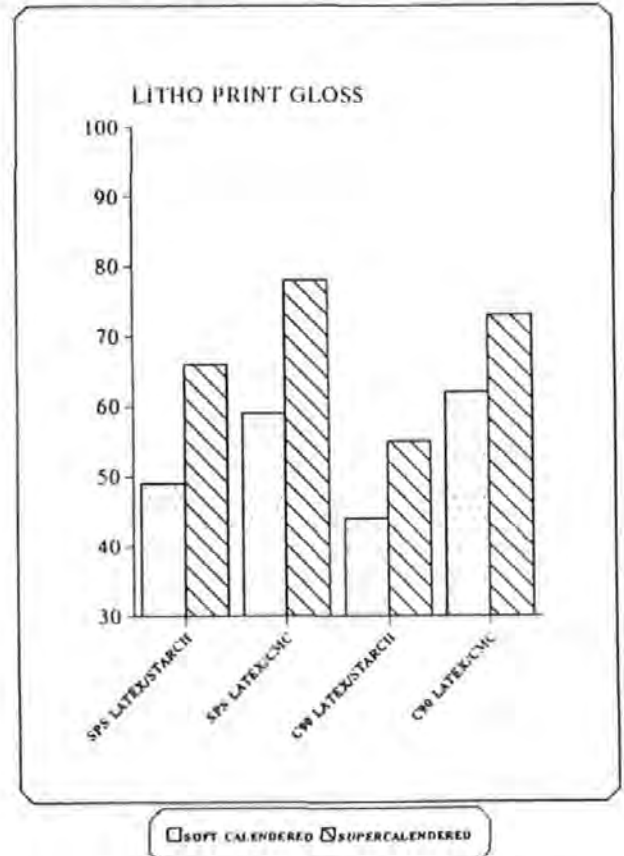
The ECC "Ink Tack Force Development Tester" was used to monitor the development of tackiness of offset inks on coated paper [Figures 10 and 11]. A complete description of this instrument and the interpretation of results are given in reference 12. Imbibition of the fluid phase of the ink controls the cohesive force within the ink layer. In Figure 10 and 11 it can be seen that the latex / cmc coatings produce different results from the latex / starch-containing coatings. The initial rate of ink tack force development is related to the coating structure i.e. its micro-porosity. In each set of comparisons the supercalendered coatings had more

micro-porosity than the soft calendered coatings. However, the most striking difference is the lack of micro-porosity of the latex / starch-containing coatings. This difference is most noticeable for the SPS coatings. This is in very good agreement with the poor litho print densities of the starch containing coatings.

There is a plateau in the observed force for the smooth microporous coatings used in this study. The plateau is defined by the surface adhesion properties of the ink / coating interface. The drying of the ink at longer time scales is observed as a decrease in affinity of the ink surface for the printing disc. The time taken for this decay to occur is considered to be a measure of the "total" available pore volume for the uptake of ink fluid.

**Figure 8a**
**Dry print density variation against calender type.**



**Figure 9a**
**Litho print density variation against calender type.**

**Figure 10**

**Ink tack force development - Carbital 90**



Max. Separation Force / mN vs Time / Seconds

CARBITAL 90
■ SUPER - LATEX/CMC    ○ SOFT - LATEX / CMC
▲ SOFT - LATEX / STARCH    ▼ SUPER - LATEX / STARCH
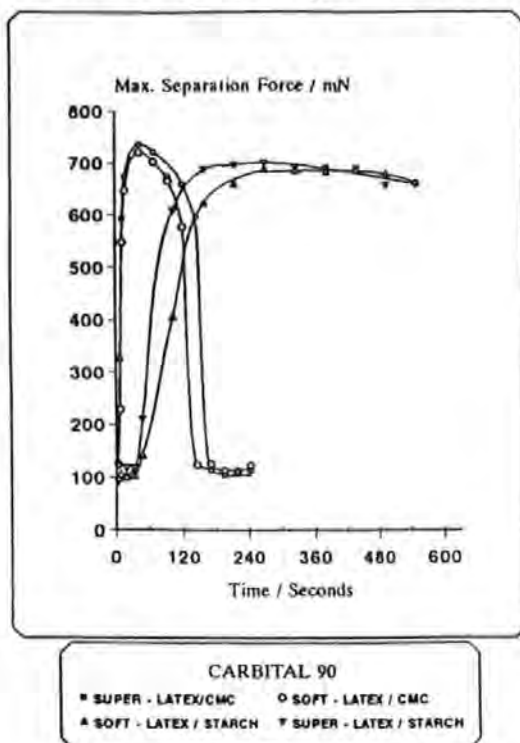
**Figure 11**

**Ink tack force development - SPS**



Max. Separation Force / mN vs Time / Seconds

SPS
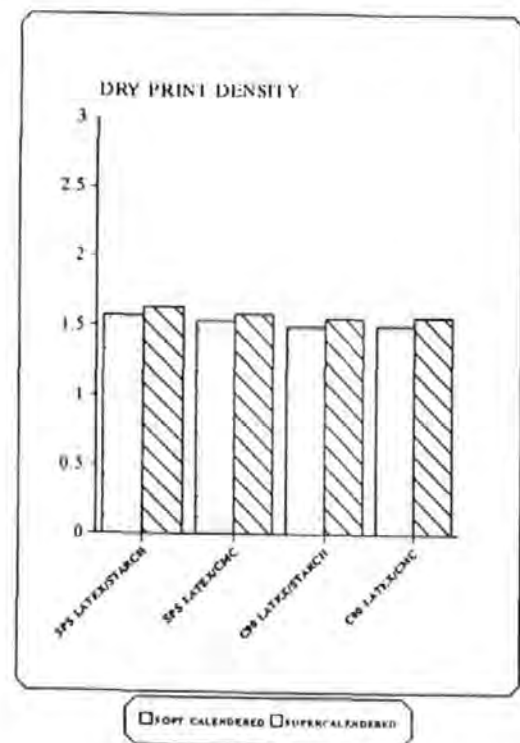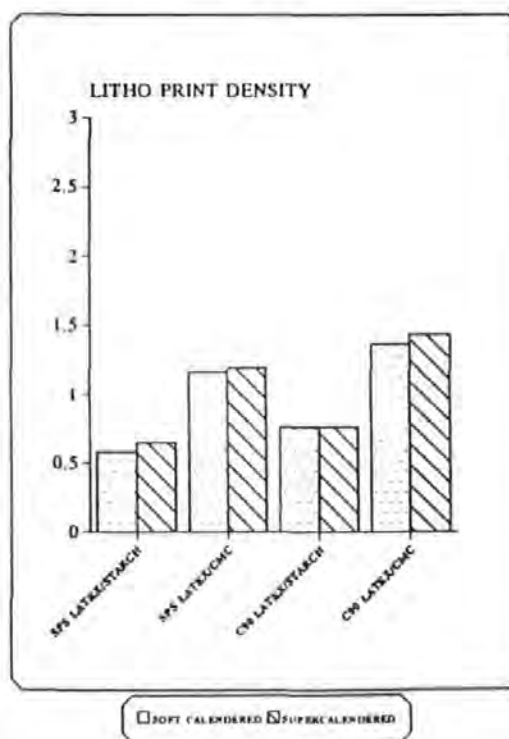▼ SUPER - LATEX / CMC    ■ SOFT - LATEX / CMC
▲ SOFT - LATEX / STARCH    ‡ SUPER - LATEX / STARCH
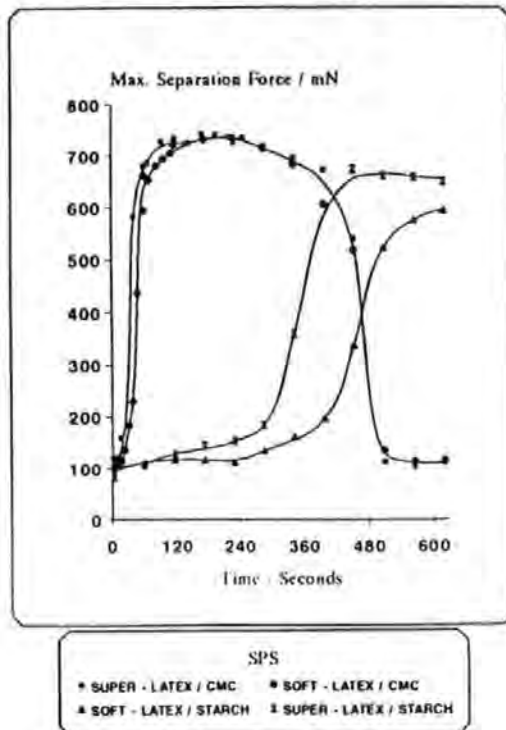
**Results - Cross section analysis.**

The cross-section profiles of coating layers and underlying base paper were measured. A full description of the technique is given in reference 13. An illustration of the effect that calendering has upon the z-direction profile is shown in Figure 12. The supercalendered sheet has a smoother profile than the soft calendered sheet and it is also clear that both types of calendering have significantly altered the coating and base profiles. It is possible to calculate the $\mu_2$ values for these profiles. The $\mu_2$ values (at $128\mu m$ span length) for the coating surface profiles are shown in Figure 13. The uncalendered papers have the roughest surface profiles and the profiles of the soft calendered paper surface are rougher than the profiles of the supercalendered paper. It can be seen in Figure 14 that the surface profiles, in terms of $\mu_2$ values (at $128\mu m$ span length) are determined by the much rougher base / coating interface profiles. The uncalendered coatings that contained starch had rougher base / coating profiles than the cmc-containing coatings due to their solids contents and applied tube pressures used to apply the coating colours. The ranking of the base / coating interface profiles of the Carbital 90 coated sheets does not change. However, the supercalender produces marginally smoother profiles than the soft calender. The difference between the profiles of the SPS coatings are minimised by calendering and the profiles are smoother than those for the Carbital 90 coatings. This is a further indication that the SPS coating can compress more easily than the Carbital 90 coating. The surface profile of Carbital 90 with latex / cmc is rougher than

10

# Figure 12

# Embedded cross section profiles

# Coated base



# Soft calendered coated base



# Supercalendered coated base

## Figure 13

$\mu_2$ Roughness at 128$\mu$m span length of coating surface profile.



$\mu2$ of coating surface profile

UNCALENDERED  SOFT CALENDERED  SUPERCALENDERED
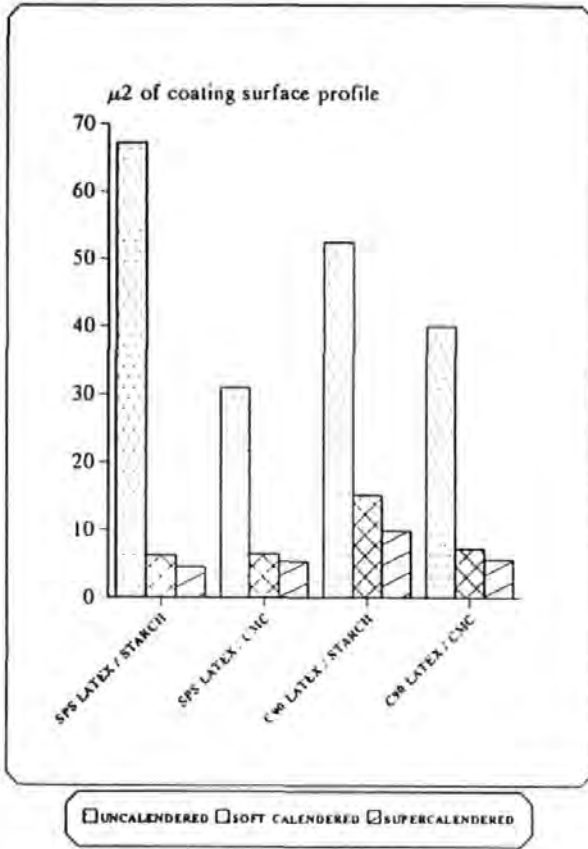
## Figure 14

$\mu_2$ Roughness at 128$\mu$m span length of base / coating interface profile.



$\mu2$ of coating / base interface profile

UNCALENDERED  SOFT CALENDERED  SUPERCALENDERED

12
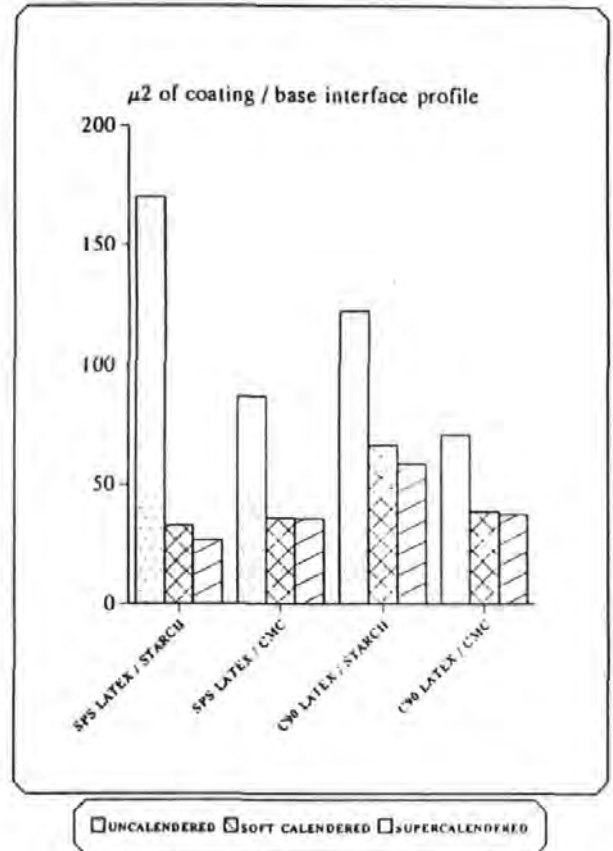
## Conclusions.

The physical and printing properties of coated sheets can be modified by calendering. A pilot-scale supercalender and a soft compact calender have been used to illustrate how these modifications may be produced. Coating colours based on idealised pigments, a clay (platey) and a calcium carbonate (blocky) were formulated and used to generate differing coating structures. The sheet properties have been assessed using conventional and advanced analytical techniques.

Calendering caused bigger changes in gloss, roughness, brightness and opacity for coatings of SPS than for coatings of Carbital 90. This may be because SPS coatings have a more compressible structure than Carbital 90 coatings. It was also observed that coatings of Carbital 90 in a latex / cmc formulation were enhanced more by calendering than the same pigment in a latex / starch formulation due to the smoother base / coating interface profile. It is clear that the coating / base interface profile significantly affects the coating surface profile prior to, and after calendering.

Calenders represent a large investment for paper mills, and their usage has to be optimised within the constraints of the paper mill. To optimise calendered paper quality it is important to appreciate a fundamental finding of this study. Irrespective of the calender type / desired paper grade, it is still vitally important to produce a good quality base and to appreciate the significance of a well formulated colour that best suits the type of coater used.

13

**References**

1. R. Rounsley
   Tappi Journal (1) 105 - 109 (1991)

2. J.T. Brown, J.J. Latimer
   Tappi Coating Conference Proceedings 77-90 (1992)

3. W. Brecht and G. Muller
   Tappi Journal 51 (2) 61A - 66A (1968)

4. W.Brecht, H.L.Baumgarten, and S. Zikovic
   Das Papier 25 (7) 366 - 379 (1971)

5. R.H. Crotogino
   Tappi Journal 65 (10) 97-101 (1983)

6. J.H. Vreeland, E.R. Ellis and K.B. Jewett
   Tappi Journal 71 (11) 139-145 (1989)

7. J.H. Vreeland, E.R. Ellis and K.B. Jewett
   Tappi Journal 71 (12) 201-206 (1989)

8. S.F. Keller
   Tappi Coating Conference Proceedings 71-76 (1992)

9. J.R. Parker
   Tappi Journal 54 (6) 943-949 (1971)

10. H.J. Kent, N.A. Climpson, P.A.C. Gane, L. Coggon, and J.J. Hooper
    Tappi Journal 69 (5) 78-83 (1986)

11. E.H. Smith, W.M. Walmsley
    Wear 57 : 157 (1979)

12. P.A.C. Gane, E.N. Seyler, and A. Swan
    Tappi Coating Conference Proceedings 243-260 (1994)

13. P.A.C. Gane, J.J.Hooper, and M. Baumeister
    Tappi Journal 74 (9) 193-201 (1991)

# Void Space Structure of Compressible Polymer Spheres and Consolidated Calcium Carbonate Paper-Coating Formulations

Patrick A. Gane,[†] John P. Kettle,[‡] G. Peter Matthews,* and Cathy J. Ridgway

*Department of Environmental Sciences, University of Plymouth, PL4 8AA Devon, U.K.*

A methodology is presented for the study of the void space structure of consolidated calcium carbonate paper-coating formulations and compressible polymer spheres, using mercury porosimetry. Two limitations of mercury porosimetry are addressed: first, that the shrinkage of compressible samples causes an apparent increase in void volume, and, second, that large void spaces shielded by smaller ones are not intruded until anomalously high applied pressures of mercury are reached. The first limitation is overcome by means of a new correction procedure which, uniquely, also allows the measurement of the bulk modulus of the continuous solid phase of a porous sample. Shielding effects are taken into account by means of our software package known as Pore-Cor, which generates a three-dimensional structure which has both a mercury intrusion curve and porosity in close agreement with experiment. The simulated permeabilities provide realistic and useful values, which cannot be measured experimentally.

## 1. Introduction

Paper is formed on a fine screen from an aqueous suspension of wood fibers (pulp) and fillers known as *mineral pigments*. The mineral pigments are usually made from high-brightness calcite (ground marble or limestone) or china clay (kaolin) which has undergone various grinding and separation processes. To improve gloss, shade, opacity, and printing characteristics, paper is often coated with a *coating color*. The coating color is an aqueous dispersion which contains mineral pigments similar to those used as filler, although with a finer particle size distribution, together with around 10% by weight of adhesive known as *binder*, frequently in the form of synthetic latex particles, and possibly a small quantity of synthetic *plastic pigment* in the form of polystyrene spheres to increase gloss and/or opacity. Although not considered here, additives may also be present to enhance binding and/or induce a loose form of association known as flocculation, which affects the structure on drying.

The drying of clay–latex coatings has been studied by Watanabe and Lepoutre (1982). In the first phase of the process, water evaporates or is drawn from a dispersion in which clay and latex particles can move freely. At the first critical concentration, free motion ceases and a bulky and deformable three-dimensional network forms. The wet coating then shrinks under the increasing capillary forces until, at the second critical concentration, all structural changes stop. From this time on, capillaries empty until drying is completed. Thus, the dried coating is not a continuous film, but a porous structure of pigment particles bound together at their points of contact. The particle diameters of the mineral pigments in the coating range from around 0.01 to 10 $\mu$m ($10^{-8}$–$10^{-5}$ m), and the synthetic pigments, and latex particles prior to film formation, are in the 0.1–1 $\mu$m diameter range. The voids within the dried paper coating are therefore in a similar size range. The structure, size, and interconnectivity of these voids affect both the optical properties of the paper (Alince and Lepoutre, 1980a; Climpson and Taylor, 1976; Lep-

outre and Rezanowich, 1977) and the way in which ink sets on the paper during the very short time period allowed in modern high-speed printing presses (Gane and Seyler, 1994). The void structure of the surface has been studied directly by profilometry of the surface and electron microscopy of vertical sections through resin-embedded samples (Kent *et al.*,1986). Other studies have involved the measurement of the change in reflectance of an imbibed ink drop with time (Larrondo and St-Amour, 1992; Ranger, 1976). Hamlen and Scriven (1991) have developed regular and irregular pore models of fiber sheets and use them in the study of the variation of permeability on compression.

In this work we describe the use of mercury porosimetry for the characterization of the pore structure of paper coatings, i.e., the measurement of the volume of mercury injected and withdrawn from a sample at a range of increasing and then decreasing applied pressures. Mercury porosimetry has been little used for the study of paper coatings, and in this work we overcome two limitations of the method. The first is that some of our samples are compressible. The compressibility may be related to calcium carbonate particle inter- and/or intracompaction, the compression of the latex binder, or, in the case of the synthetic pigments, the compression or collapse of the polystyrene spheres. A new method for compensating for these effects is presented, which also gives a measure of the compressibility or bulk modulus of the sample. The second limitation is that the traditional interpretation of mercury porosimetry measurements is based on a bundle of tortuous capillary tubes (Yamazaki and Munakata, 1993) and does not allow for the fact that small void spaces, or *throats*, can shield larger void spaces, *pores*, from injection by mercury within a three-dimensional interconnected network. In the present study, we interpret the measurements by means of a computer modeling package we have developed called "Pore-Cor" (pore-level properties correlator) which does take shielding effects into account. Pore-Cor has previously been used in the study of mercury intrusion (Spearing and Matthews, 1991), mercury intrusion hysteresis (Matthews *et al.*, 1995b), permeability (Matthews *et al.*, 1993; Matthews *et al.*, 1995a), and gas diffusion (Matthews and Spearing, 1992) in homogeneous and banded outcrop and reservoir sandstones and in paper coatings (Kettle and

---

**Table 1. Sample Details**

| type of sample | commercial name | sample characteristics | sample wt/g | characteristic pressure $P_{50}$/MPa | porosity $\phi^1$, $\phi_{uncorr}$, $\phi_{corr}$/% | compressibility $\psi_{ss}$/$10^{-10}$ Pa$^{-1}$ | bulk modulus $M_{ss}$/GPa |
|---|---|---|---|---|---|---|---|
| dried slurry; finely ground calcium carbonate | Carbital 90 | 90% by weight < 2 μm | 1.2777 | 23 | 26.2, 28.4, 26.1 | 0 | ∞ |
| | Carbital 60 | 60% by weight < 2 μm | 1.6972 | 11 | 28.8, 29.3, 28.7 | 0.51 | 20 |
| | LX 60 | 60% by weight < 2 μm, steeper distribution | 1.5738 | 5 | 40.9, 42.0, 39.7 | 2.4 | 4.1 |
| dried coating color; Carbital 90 with added latex binder | Carbital 90 + 12 pph Acronal S801 | styrene–acrylic latex; $T_g$ = 26–44 °C | 0.7690 | 13 | 19.4, 24.9, 22.5 | 0 | ∞ |
| | Carbital 90 + 12 pph Revinex 95L10 | styrene–butadiene latex; $T_g$ = 5 °C | 0.6757 | 16 | 19.3, 22.7, 19.2 | 0.48 | 21 |
| | Carbital 90 + 12 pph DL 950 | Styrene-butadiene latex; $T_g$ = 8 °C | 0.7539 | 15 | 21.3, 25.2, 20.5 | 0.72 | 14 |
| plastic pigment | Lytron 2601 | solid polydisperse polystyrene spheres, av. diam. = 0.612 μm; for gloss | 0.352 | 9 | 27.9, 32.5, 30.0 | 0.87 | 12 |
| | Lytron 2301 | solid polydisperse polystyrene spheres, av. diam. = 0.316 μm; for gloss | 0.3552 | 35 | 23.2, 30.7, 25.1 | 1.4 | 6.9 |
| | Ropaque HP91 | hollow spheres, mean diam. = 1.012 μm; for gloss & opacity | 0.1159 | 5 | 32.9, 41.1, 40.1 | 6.4 | 1.6 |

Matthews, 1993). The model is a simplified yet versatile representation of the void space structure of a porous medium, the advantages and limitations of which have been discussed in detail elsewhere (Matthews *et al.*, 1993).

**1.1. Description of Samples.** The calcium carbonate samples used in this study were produced by ECC plc Europe and have the trade names Carbital 90, Carbital 60, and LX 60 (Table 1). Carbital 90 is a fine paper coating grade of calcium carbonate made from ground marble which has 90% by weight of its particles finer than 2 μm. In Carbital 60, 60% of the particles are finer than 2 μm. LX 60 is made from limestone and has 60% finer than 2 μm but has also been engineered to have fewer fine particles than a conventional carbonate pigment; i.e., it has a steeper particle size distribution. Figure 1 shows the different particle size distributions for these three calcium carbonates, as measured by a Micromeritics sedigraph.

A study has also been made of Carbital 90 mixed with 12 parts per hundred (pph) by weight, relative to 100 parts of dry pigment, of three different latex binders. The first was an Acronal styrene–acrylic copolymer latex (S801), with a glass transition temperature $T_g$ in the range 26–44 °C, and a pH of 8–8.5. The second binder was a Revinex styrene–butadiene latex (95L10), with a $T_g$ around 5 °C. The third, DL 950, was a carboxylated styrene–butadiene copolymer, with a $T_g$ of 8 °C and pH of 5.5. (Acronal is a trade name of BASF, P.O. Box 4, Earl Road, Cheadle Hulme, Cheshire, U.K.; Revinex is a trade name of Doverstrand Ltd., Temple Fields, Harlow, Essex, U.K.; and DL 950 is manufactured by the Dow Chemical Co., Lakeside House, Stockley Park, Uxbridge, Middlesex, U.K.)

Three different synthetic pigments were also studied. Two pigments, designed to enhance gloss, comprise aqueous dispersions of solid spheres made from styrene copolymer: Lytron 2301, which has a quoted mean particle diameter of 0.3 μm, and Lytron 2601, with a
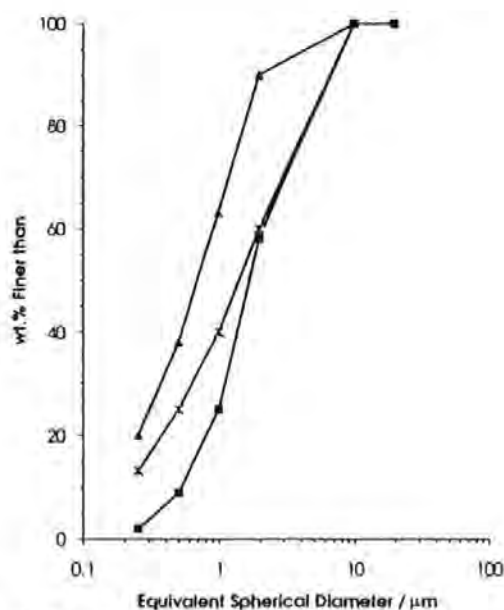


**Figure 1.** Particle size distribution of dispersed calcium carbonates: (▲) Carbital 90; (*) Carbital 60; (■) LX 60.

quoted mean particle diameter of 0.6 μm. The pH of these pigments are in the range of 8.7–9.3, and they have a $T_g$ of greater than 60 °C. The third, Ropaque HP91, developed to impart both gloss and opacity to paper coatings, in aqueous suspension comprises water-filled styrene–acrylic copolymer spheres which dehydrate to form a dry, consolidated coating of hollow spheres with a quoted mean diameter of 1 μm. The glass transition temperature of Ropaque HP91 is quoted as being greater than 95 °C, its pH of suspension as 9.5, wet density as 1.03 g cm$^{-3}$, and dry density as 0.55 g cm$^{-3}$. (Lytron is a trade name of Morton International Ltd., Speciality Chemicals Group, Greville House, Hibernia Road, Hounslow, Middlesex, U.K.; Ropaque is a

**Plate 1.** Electron micrograph of Lytron 2301, showing a 1 $\mu$m scale bar.

trade name of Rohm & Haas Co., Lennig House, 2 Mason's Avenue, Croydon, Surrey, U.K.)

The mean diameters of these three plastic pigments were measured as 0.32, 0.61, and 1.01 $\mu$m, respectively, by photon correlation spectroscopy. Electron microscopy revealed particles in the range 0.15–0.65 $\mu$m for Lytron 2301 (Plate 1), and 0.25–0.75 $\mu$m for Lytron 2601, the latter skewed toward the larger sizes in agreement with the 0.6 $\mu$m average. The electron micrograph of Ropaque HP91 confirmed that it was essentially monosized, with a few particles of diameter 0.95 $\mu$m and a few of 1.1 $\mu$m.

For simplicity, all the samples in this study were homogeneous lumps of dried coating material. Although such lumps are never encountered in paper making, their study provides a basis for understanding the properties of paper coating constituents; Alince and Lepoutre, for example, have studied the porosity and opacity of clay coated onto a transparent polyester film (1980a) and of a coating made solely from plastic pigments (1980b). We have examined typical lump samples by electron microscopy, which shows the expected void size range and film-forming characteristics.

## 2. Mercury Porosimetry

**2.1. Basic Principles.** A mercury porosimetry experiment entails the evacuation of a porous sample to remove trapped gases, after which the sample is surrounded with mercury. The amount of mercury displaced by the sample allows calculation of the sample's bulk volume, $V_{bulk}$. Pressure is then applied to the mercury so that it intrudes into the sample through pores connected to the external surface.

Washburn (1921) proposed that mercury injection into a porous material could be used to measure pore size distributions. As is normal in this field, the Washburn (or Laplace) equation is used in the present work to relate throat size to mercury pressure:

$$d = -\frac{4\gamma \cos\theta}{P} \tag{1}$$

where $\gamma$ is the interfacial tension at the mercury surface (0.48 N m$^{-1}$), $P$ the applied pressure, $\theta$ the contact angle, and $d$ the throat diameter. In the absence of experimental measurements of relevant contact angles, $\theta$ is given the typical mercury/sandstone/air contact angle of 140° throughout this work, although estimates of this angle vary (Matthews et al., 1995b). With these values of $\gamma$ and $\theta$, eq 1 predicts that mercury will intrude voids

of diameter 0.0072 $\mu$m or greater at the upper experimental pressure limit of 207 MPa.

van Brakel (1981) also discussed the uncertainties in the values of $\gamma$ and $\theta$, and the limitations in the use of the Washburn equation (1). However, to overcome these uncertainties entirely, the simulated void space network used in Pore-Cor would need to have an extremely complicated geometry. Such intricacy would defeat the object of this present study, which is to create a relatively simple pore-space network which can be used for the simulation of a wide range of pore-level properties of consolidated pigmented coatings. The Washburn equation (1) is not used until section 4, and therefore the $\gamma$ and $\theta$ uncertainties do not affect the measurement of bulk moduli in section 3.

**2.2. Correction Terms for Incompressible Samples.** Various corrections must be applied to mercury porosimetry measurements to obtain a true measure of the increase of intruded volume with pressure. The approach which we describe in this section and section 2.3 is an extension of that described by Cook and Hover (1993) for concrete.

The intruded mercury volume reading, $V_{obs}$, observed during a mercury porosimetry experiment not only is a measure of the volume of intrusion into the sample, $V_{int}$, but also contains significant volumes corresponding to the expansion of the porosimeter chamber or *penetrometer*, $\delta V_{pen}$, and the compression of the mercury $\delta V_{Hg}$:

$$V_{obs} = V_{int} + \delta V_{pen} + \delta V_{Hg} \tag{2}$$

(Any term such as the mercury compression, $\delta V_{Hg}$, or sample compression in section 2.3, which makes a positive contribution to the observed volume, $V_{obs}$, is given a positive numerical value. $\delta$ denotes a small correction to a larger term.) The mercury also expands because of heat transfer from the pressurizing fluid (oil), but we assume that this effect is the same for the sample experiment as for the blank experiment, described below, and therefore that the resultant effect is zero.

A *blank* experiment is one carried out under the same temperature and pressure conditions, but with no sample in the penetrometer. The volume, $V^1_{blank}$, of mercury used in the blank experiment is equal to the volume of the penetrometer, $V^1_{pen}$, both at 1 atm pressure:

$$V^1_{blank} = V^1_{pen} \tag{3}$$

(Superscripts are used to denote the value of a particular variable at a specified pressure.)

The change in the blank volume reading, $\delta V_{blank}$, is taken as zero at the lowest experimentally attainable applied pressure $P$. Increases in $\delta V_{blank}$ with pressure are caused by the compression, $\delta V_{Hgpen}$, of the volume of mercury needed to fill the empty penetrometer and increases in the available volume, $\delta V_{pen}$, of the penetrometer due to expansion of the glass chamber:

$$\delta V_{blank} = \delta V_{Hgpen} + \delta V_{pen} \tag{4}$$

When a sample is mounted in the penetrometer, it displaces a volume of mercury, $V^1_{Hgbulk}$, equal to the sample bulk volume, $V^1_{bulk}$, at 1 atm pressure. The penetrometer is loaded with mercury to the same calibration mark as for the blank experiment, and thus the total volume of mercury, $V^1_{Hg}$, now used in the experiment is

$$V^l{}_{Hg} = V^l{}_{Hgpen} - V^l{}_{Hgbulk} \qquad (5)$$

The same relationship holds for the mercury expansion:

$$\delta V_{Hg} = \delta V_{Hgpen} - \delta V_{Hgbulk} \qquad (6)$$

Equations 2, 4, and 6 can be combined to yield:

$$V_{obs} = V_{int} + \delta V_{blank} - \delta V_{Hgbulk} \qquad (7)$$

The compression, $\delta V_{Hgbulk}$, of the additional mercury volume in the blank experiment can be related to its volume, $V^l{}_{bulk}$, at atmospheric pressure by use of a form of the Tait equation (Cook and Hover, 1993), which gives an experimentally derived expression for the compression of mercury, equivalent to a mercury compressibility of $0.40 \times 10^{-10}$ Pa$^{-1}$:

$$\delta V_{Hgbulk} = 0.175(V^l{}_{bulk}) \log(1 + P/1820) \qquad (8)$$

in which $P$ is in MPa (1820 MPa = 264 000 psi). (Note that eq 8 has the wrong asymptote as $P \rightarrow \infty$ but is correct for the smaller pressure changes, and hence small relative compressions, considered here.)

The working equation for incompressible samples may, therefore, be derived from eqs 7 and 8:

$$V_{int} = V_{obs} - \delta V_{blank} + 0.175(V^l{}_{bulk}) \log(1 + P/1820) \qquad (9)$$

**2.3. Corrections for Compressible Samples.** Mercury at a high applied pressure not only will intrude a porous compressible sample but also will cause it to compress by an amount $\delta V_{sample}$. Compression effects typically become important above pressures of 40 MPa (at which pressure mercury penetrates throats with diameters down to 0.04 $\mu$m) and cause an increase in the apparent intruded volume. For compressible samples, eq 7 becomes:

$$V_{obs} = V_{int} + \delta V_{blank} - \delta V_{Hgbulk} + \delta V_{sample} \qquad (10)$$

where $\delta V_{sample}$ is the (positive) increase in observed mercury volume caused by the compression of the sample.

The compressibility $\psi_{ss}$ of a homogeneous, continuous solid sample may be expressed in terms of its bulk modulus $M_{ss}$:

$$M_{ss} = \frac{1}{\psi_{ss}} = dP / \left( \frac{-dV_{ss}}{V_{ss}} \right) \qquad (11)$$

(For an incompressible sample, $\psi_{ss}$ is zero, and $M_{ss}$ is infinite.) However, the compression of a porous sample by intruding mercury is more complicated. If the mercury entirely surrounds the continuous solid phase, it will compress it according to eq 11. This type of compression will occur above a pressure $P^z$ (the *zero void pressure*) at which all the accessible void space has been intruded by mercury, up to the maximum experimentally attainable applied pressure $P^{max}$, provided that no other changes in the sample are induced. Increasing the applied mercury pressure $P$ above $P^z$ causes the continuous solid phase of the porous sample to compress from volume $V_{ss}{}^z$ to a volume $V_{ss}{}^z - \delta V_{ss}$ and the apparent volume of mercury intruded to increase by an amount $\delta V_{ss}$. Integrating eq 11 to find $\delta V_{ss}$:

$$\int_{P^z}^{P} dP = M_{ss} \int_{V_{ss}{}^z}^{V_{ss}{}^z - \delta V_{ss}} \frac{dV_{ss}}{V_{ss}} \qquad (12)$$

and thus

$$\delta V_{ss} = V_{ss}{}^z \left( 1 - \exp\left[ \frac{(P^z - P)}{M_{ss}} \right] \right) \qquad (13)$$

The zero void pressure $P^z$ may be identified from experimental curves as the point above which the corrected intrusion curve continues to indicate an increase in intruded mercury volume, but the extrusion curve, measured during subsequent pressure decrease, is identical to the intrusion curve. The coincidence of the two curves indicates an absence of mercury trapping and, therefore, demonstrates that the only cause of the corrected mercury volume increase, $\delta V_{sample}$, is compression of the continuous solid phase of the sample. (Incompressible samples show no increase in mercury volume above $P^z$.) Thus,

$$\text{for } P > P^z \qquad \delta V_{sample} = \delta V_{ss} \quad \text{and} \quad dV_{int}/dP = 0 \qquad (14)$$

However, at applied mercury pressures below $P^z$, there are unintruded voids in the sample, and the sample can undergo an additional type of compression, $\delta V_{su}$, because of compression into this void space (Warren and Nashner, 1976). Both this compression into the void space and the compression of the solid phase contribute to the increase, $\delta V_{sample}$, in the observed intruded volume of mercury, and the effects are impossible to distinguish as they proceed:

$$\text{for } P < P^z \qquad \delta V_{sample} = \delta V_{ss} + \delta V_{su} \qquad (15)$$

Thus, we are compelled to assume that the compression of the solid into unintruded void space, $\delta V_{su}$ (eq 15), is negligible, an approximation which is also implicit in the work of Cook and Hover (1993).

The maximum compressions of the samples in the present work are mostly less than 1% of the sample bulk volume, rising to 6% for the most compressible sample. For these small relative compressions, the compression may be related to the volume, $V^l{}_{ss}$, of the solid phase at atmospheric pressure $P^l$ to an approximation much better than the experimental uncertainty. Thus, eq 12 becomes:

$$\int_{P^l}^{P} dP \approx M_{ss} \int_{V_{ss}{}^l}^{V_{ss}{}^l - \delta V_{ss}} \frac{dV_{ss}}{V_{ss}} \qquad (16)$$

Also at 1 atmosphere pressure the solid-state volume is, to a similarly good approximation, calculable from the bulk volume and the porosity $\phi$:

$$V^l{}_{ss} = V^l{}_{bulk}(1 - \phi^l) \qquad (17)$$

Applying these approximations to eq 13:

$$\delta V_{sample} = V^l{}_{bulk}(1 - \phi^l) \left( 1 - \exp\left[ \frac{(P^l - P)}{M_{ss}} \right] \right) \qquad (18)$$

The working equation for compressible samples is then derived from eqs 8, 10, and 18:

$$V_{int} = V_{obs} - \delta V_{blank} + [0.175(V^l{}_{bulk}) \log(1 + P/1820)] - V^l{}_{bulk}(1 - \phi^l) \left( 1 - \exp\left[ \frac{(P^l - P)}{M_{ss}} \right] \right) \qquad (19)$$

$\phi^1$ can be determined as described in section 2.5. Thus, all the terms on the right-hand side of eq 19 can be measured, except for $M_{ss}$ which can be found by constraining eq 19 to obey eq 14.

**2.4. Correction Terms for Samples with Unintrudable Compressible Space.** In this work, we measure and interpret the mercury porosimetry curves of two types of samples containing unintrudable compressible space. The first type are samples which are microcrystalline—i.e., the particles contain mosaics of crystals in close proximity to each other, with imperfections and discontinuities between the crystals which are much too small to be intruded by mercury but which, nevertheless, contribute to the compressibility of the sample (Deer *et al.*, 1992). If the sample is ground to produce finer particles, the grinding causes cleavages at these microcrystal boundaries. The smaller particles thus contain relatively fewer microcrystal boundaries and are less compressible (Shinohara, 1990).

The second type of unintrudable compressible space occurs in the centers of the hollow plastic spheres of the Ropaque pigment. At a sufficently high applied mercury pressure, which is above $P^z$, the spheres collapse irreversibly.

**2.5. Measurement of Porosity.** If no correction is made for the compressibility of a sample, its porosity $\phi$ appears to increase with pressure because more mercury is intruded than expected. Conversely, if a proper correction has been made for compressibility, the corrected porosities at 1 atm pressure and at elevated pressure should be the same, and their similarity can be used as a verification of the correction procedure.

At atmospheric pressure

$$\phi^1 = (V^1_{bulk} - V^1_{solid})/V^1_{bulk} \quad (20)$$

where $V^1_{solid}$ is the volume of the solid phase at 1 atm pressure, calculated from the known composition and densities of the sample constituents by means of a simple relationship which for a coating color is:

$$V^1_{solid} = \frac{M_{sample}}{(w_{pigment} + w_{binder})}\left(\frac{w_{pigment}}{\varrho_{pigment}} + \frac{w_{binder}}{\varrho_{binder}}\right) \quad (21)$$

where $m_{sample}$ is the mass of the sample, $w$ the weights of pigment and binder, and $\rho$ the densities. As mentioned previously, in the present work the weights are measured on a parts per hundred of pigment scale, i.e., $w_{binder}$ relates to $w_{pigment} = 100$.

At higher pressures, the porosity, $\phi_{uncorr}$, uncorrected for compressibility would be

$$\phi_{uncorr} = (V_{int} + \delta V_{sample})/(V_{int} + \delta V_{sample} + V_{solid}) \quad (22)$$

whereas the corrected porosity is simply

$$\phi_{corr} = V_{int}/(V_{int} + V_{solid}) \quad (23)$$

## 3. Porosimetry Results and Discussion

**3.1. Experimental Conditions.** The mercury porosimetry experiments reported in this study were measured using a Micromeritics 9320 porosimeter, which has an upper pressure limit of 207 MPa (30 000 psi). In order to obtain results of sufficient accuracy for the present work, it was necessary to impose two important restrictions on the operating conditions of this instrument, which are also relevant when using other porosimeters. First, it was found that, if the mercury

pressure was increased too quickly, equilibrium was not achieved at each step. As a consequence, when the applied pressure was decreased from its maximum value to measure the hysteresis curve, the intruded volume initially continued to increase. To avoid this, the applied pressure had to be held for at least 1 min at each pressure setting. Therefore, to be certain of complete equilibrium, the porosimeter was, in fact, held at each applied pressure for 4 min before measuring the intruded volume and changing the pressure.

Second, it was found that the expansion characteristics of the glass porosimeters could change between runs and, therefore, that it was impossible to provide a totally reliable value of the blank volume $\delta V_{blank}$ appertaining to a particular experimental run. Lee and Maskell (1973) reported problems with blank runs on a Micromeritics 903-1 porosimeter and overcame them by means of a consideration of the precise geometry of the penetrometer and the subsequent matching of empirical factors to experiment. In our experiments, sufficient accuracy was obtained by using sample weights large enough such that $\delta V_{blank}$ was less than 10% of $V_{int}$ at the highest applied pressure and by remeasuring $\delta V_{blank}$ for a particular penetrometer every few runs.

**3.2. Calcium Carbonate Lump Samples.** The calcium carbonate samples Carbital 90, Carbital 60, and LX 60 were supplied in a fully dispersed slurry form at 75% solids by weight. Each slurry was stirred to ensure that it was homogeneous. Approximately 5−10 g of each slurry was coated onto aluminum foil and dried at room temperature in order to form a consolidated slab of pigmented coating. Approximately 1 g of each consolidated sample was cleaved from the slab to produce a lump that was the full depth of the dried slab, which was then placed in the penetrometer.

The mercury intrusion and extrusion curves for these samples are shown in Figure 2. The graphs are expressed as an apparent volume of mercury intruded against applied mercury pressure $P$. The volume axis is in absolute units, and the total volume intruded is, therefore, dependent on the mass of a sample and its porosity, shown in Table 1. As can be seen, as the pressure increases, there is a sudden increase in pore volume intrusion. The characteristic intrusion pressures $P_{50}$ at which 50% of the void volume of each is intruded are shown in Table 1. ($P_{50}$ is insensitive to the exact measure of 100% pore volume intruded.) It can be seen in the table and in Figure 2 that $P_{50}$ decreases in the order C90, C60, and LX 60, in agreement with the coarsening of the particle size distribution in this series.

The graphs in Figure 2 show the observed intrusion $V_{obs}$ (■) and extrusion (□), which are then corrected for penetrometer expansion and mercury compression (eq 9), to give the volume $V_{int}$ for intrusion (◆) and extrusion (◇). For Carbital 90, the corrected extrusion curve diverges from the intrusion curve immediately after the applied pressure is reduced. Carbital 90 is, therefore, assumed to be incompressible, according to the criteria discussed previously, as indicated by the values for $\psi_{ss}$ and $M_{ss}$ in Table 1. (The simulated intrusion curves (○) shown in this and subsequent figures are discussed in section 5.)

Also shown in Table 1 are the Carbital 90 porosity at 1 atm $\phi^1$ (eq 20), and the uncorrected and corrected porosities $\phi_{uncorr}$ and $\phi_{corr}$ (eqs 22 and 23), determined at the maximum applied pressure. The values are 26.2%, 28.4%, and 26.1%, and the close agreement
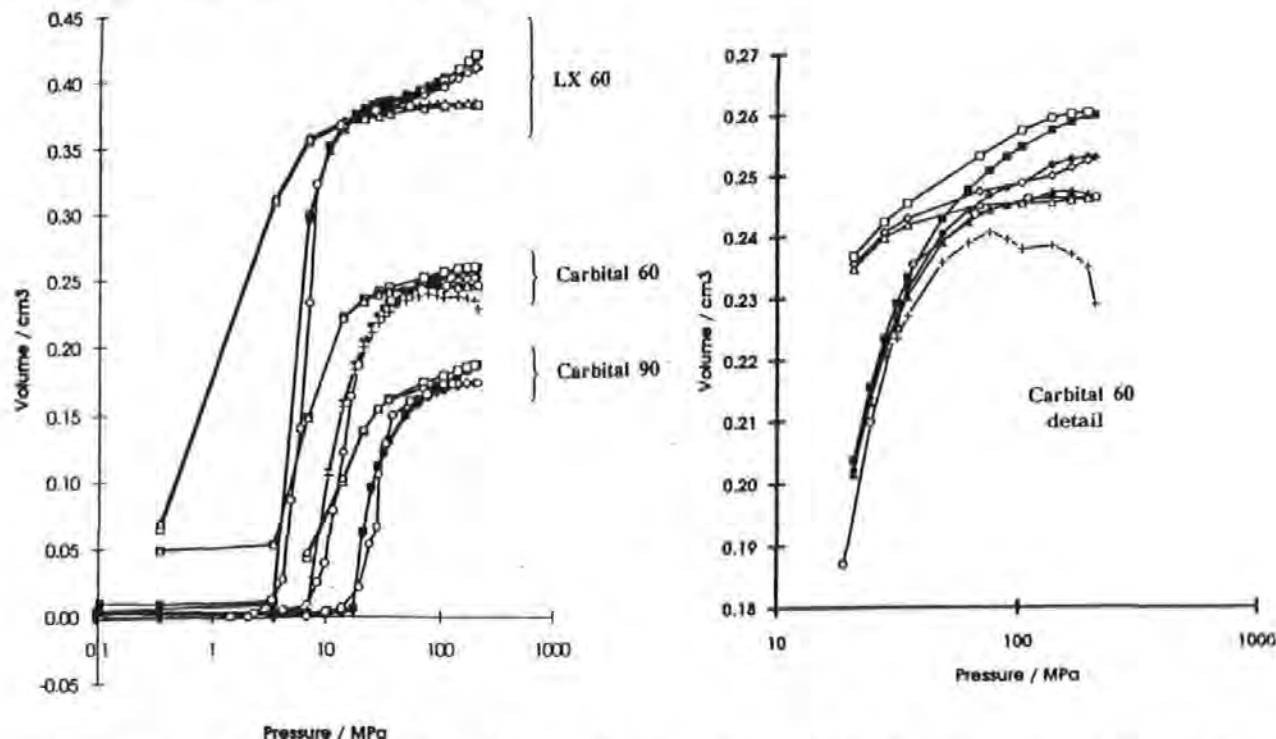
**Figure 2.** Mercury intrusion and extrusion curves for Carbital 90, Carbital 60, and LX 60. Key for Figures 2–7: (■) observed intrusion; (□) observed extrusion; (♦) corrected for Hg and chamber intrusion; (◇) corrected for Hg and chamber extrusion; (▲) fully corrected intrusion; (△) fully corrected extrusion; (○) simulated intrusion; (+) overcorrected intrusion.

between $\phi^1$ and $\phi_{corr}$ brought about by application of the correction terms provides an independent validation of the correction procedure.

The corrected extrusion curve for Carbital 60 coincides with the intrusion curve, to within experimental uncertainty, at pressures above a $P^z$ value of around 130 MPa (Figure 2). Also, both of the coincident curves increase with pressure above $P^z$. Thus, Carbital 60 is compressible, and the intrusion and extrusion curves may be solved according to eqs 14 and 19 to give a solid-phase compressibility $\psi_{ss}$ of $0.51 \times 10^{-10}$ Pa$^{-1}$ and a solid-phase bulk modulus $M_{ss}$ of 20 GPa ($2 \times 10^{10}$ N m$^{-2}$) (Table 1). Correction of the intrusion and extrusion curves for compressibility via eq 19 gives the fully corrected intrusion (▲) and extrusion (△) curves which also satisfy eq 14. Also shown in Figure 2 is the effect of overcorrecting the intrusion curve (+) by using a compressibility of $2 \times 10^{-10}$ Pa$^{-1}$ (bulk modulus = 5 GPa). The obvious resulting error gives a visual measure of the sensitivity of the method in measuring compressibility.

The corresponding results for LX 60 are also shown in Figure 2 and listed in Table 1. For both Carbital 60 and LX 60, the $\phi_{corr}$ values include the correction for compressibility, and their similarity with the $\phi^1$ values confirms the derived compressibilities and bulk moduli.

We refer to samples in the present study which have an infinite solid-phase bulk modulus as incompressible, those with a bulk modulus between 10 and 100 GPa as medium compressible, and those with a bulk modulus less than 10 GPa as very compressible. It can be seen from Table 1 that Carbital 90 is incompressible, Carbital 60 is medium compressible, and LX 60 is very compressible. Calcite in its crystalline form might be expected to be incompressible. However, as discussed previously in section 2.4, mineral samples are seldom formed from single macrocrystals, and the medium compressibility of Carbital 60 may be attributable to compression at microcrystalline boundaries within an internal mosaic structure. It is more compressible than solid glass, which typically has a bulk modulus of around 40 GPa (Cook and Hover, 1993). LX 60, by contrast, is made from limestone, and its high compressibility can be attributed to its formation from the remains of marine organisms together with a significant organic content.

**3.3. Carbital 90 Samples with Added Latex Binder.** The effects on Carbital 90 of adding 12 parts per hundred by weight of three different latex binders have also been investigated. The preparation of the coating color involved pouring the Carbital 90 slurry, at 75% solids by weight, into a high-speed mixer, adding 12 parts per hundred by weight of the latex, and adjusting to pH 9 with sodium hydroxide. The color was then passed through a 53 $\mu$m screen, coated onto aluminum, and oven dried at 100 °C. Since this temperature is much higher than any of the glass transition temperatures, it might be expected that the latex would film-form after the coating color reaches the first critical concentration, and we have confirmed this by electron microscopy.

The mercury intrusion and extrusion curves of the coating colors can be seen in Figures 3–5. As can be seen, the characteristic intrusion pressures $P_{50}$ are similar for these three samples. The porosities $\phi^1$ are all around 20%, and once again the corrections improve the agreement between the high-pressure porosity and that at 1 atm. The major difference between the samples is that the Carbital 90/Acronal S801 coating color is incompressible, as indicated by its horizontal intrusion curve at high pressure (Figure 3). In contrast, the coating colors containing the latices 95L10 and DL 950 are medium compressible. A possible explanation of this is that the compressibility of the latter two samples is caused by the latex forming interstices with high surface to volume ratio between the calcite grain contact points as the coating color passes through the first critical concentration, whereas the Acronal S801
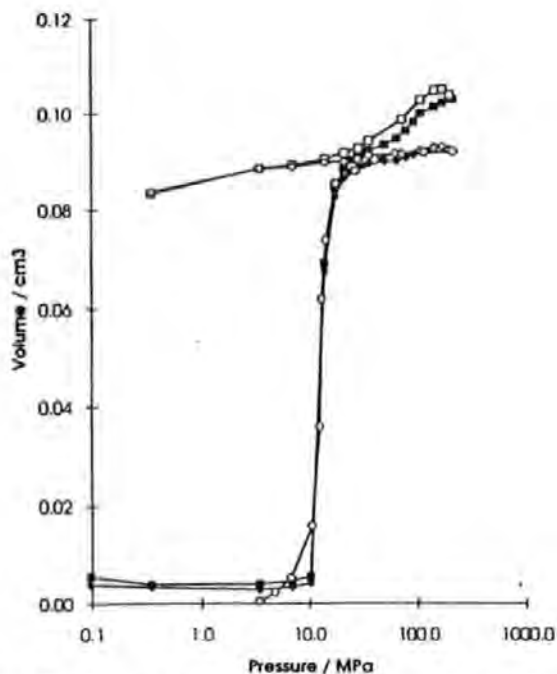
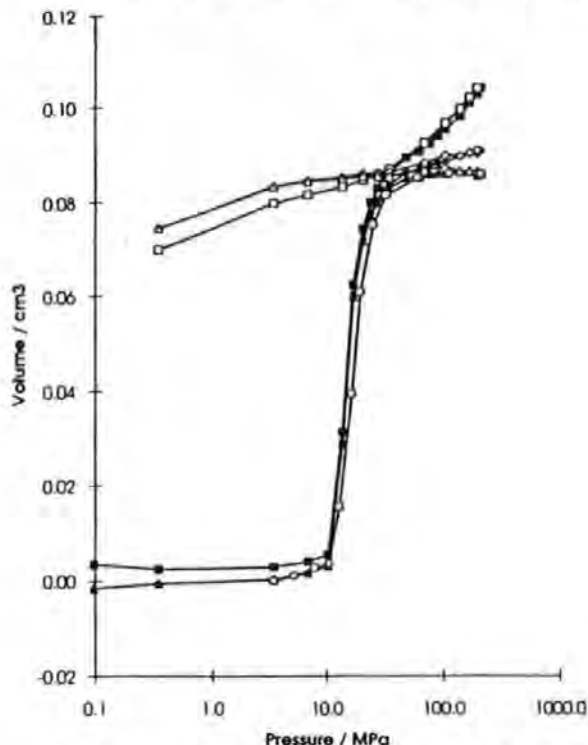**Figure 3.** Mercury intrusion and extrusion curves for Carbital 90 + Acronal S801.



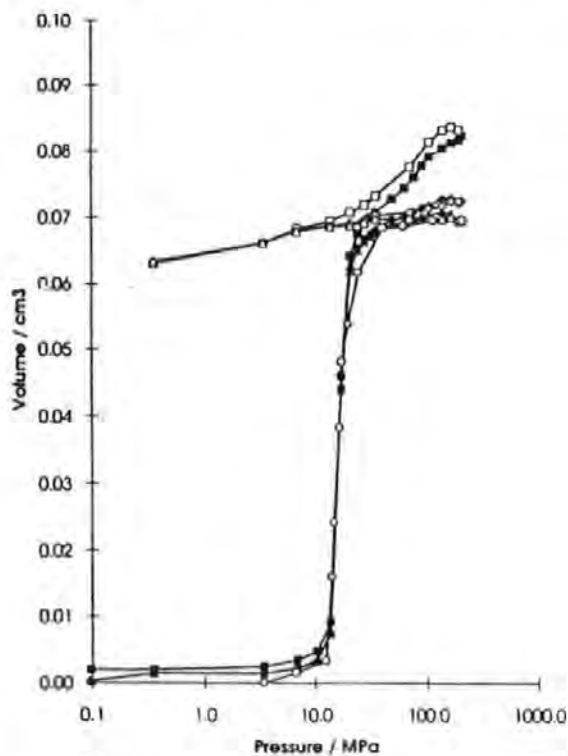**Figure 4.** Mercury intrusion and extrusion curves for Carbital 90 + latex 95L10.



**Figure 5.** Mercury intrusion and extrusion curves for Carbital 90 + DL 950.



**Figure 6.** Mercury intrusion and extrusion curves for Lytron 2601 and Lytron 2301.

with a higher $T_g$ does not do this. However, this cannot be proved from our electron micrographs, because the latex films mask the grain contact points.

**3.4. Plastic Pigments.** As described previously, the plastic pigments studied were Lytron 2601 (solid spheres, mean diameter 0.612 μm), Lytron 2301 (solid, 0.316 μm), and Ropaque HP91 (hollow, 1.012 μm). Ten gram samples of emulsions of the pigments were left to air dry in a desiccator for 48 h. Approximately 0.2 g of the consolidated samples was used for mercury porosimetry.

The porosimetry results for the Lytron products are shown in Figure 6 and Table 1. The characteristic intrusion pressures $P_{50}$ for Lytron 2601 and Lytron 2301
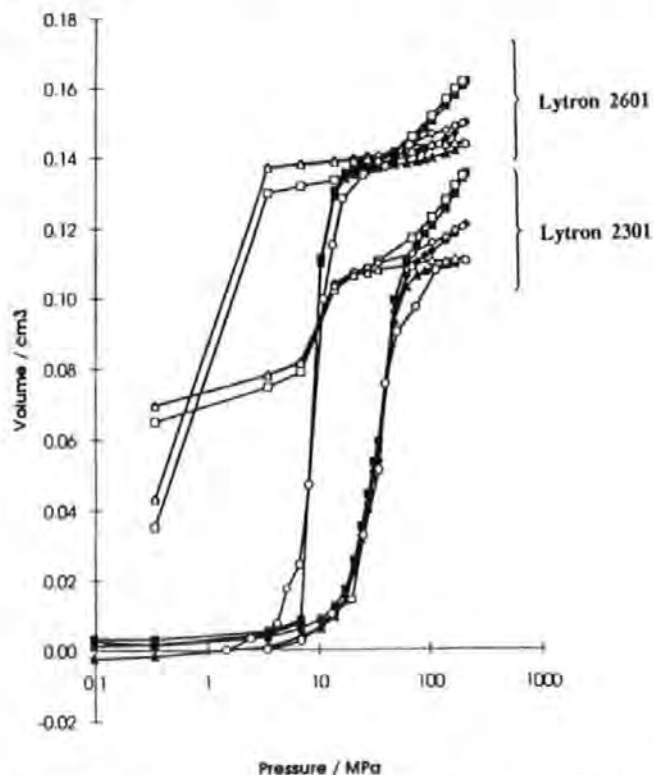
are 9 and 35 MPa, respectively. The smaller particle size (and compressibility) of the Lytron 2301 affects the first critical concentration (Watanbe and Lepoutre, 1982) and leads to a structure in which there are smaller void spaces.

The intrusion and extrusion curves for the Ropaque HP91 pigment are shown in Figure 7. The intrusion curve has two points of inflection, at 5 and 41 MPa. The first results from intrusion of the spaces between the
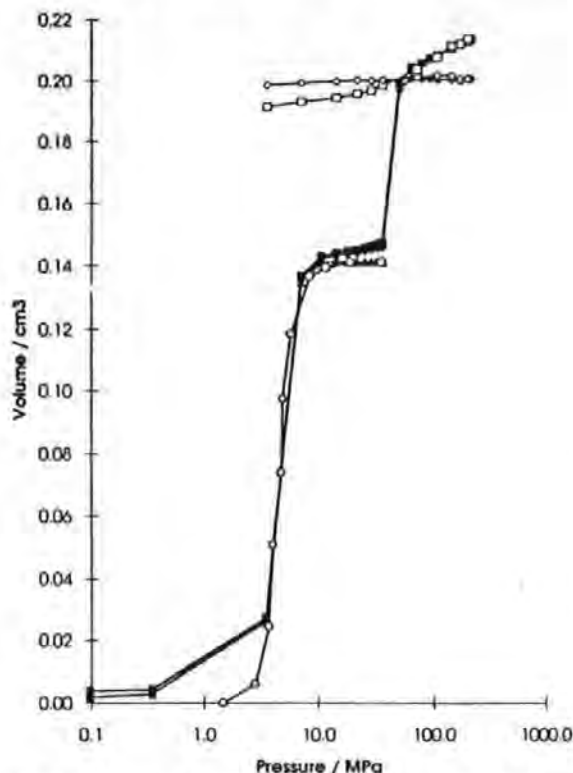
**Figure 7.** Mercury intrusion and extrusion curves for Ropaque HP91.

spheres and the second from the compression of the hollow spheres themselves. As can be seen, the extrusion curve is nearly horizontal, demonstrating that the high-pressure compression of the hollow spheres is irreversible, which we therefore refer to as collapse.

The porosities of the Lytron pigments (Table 1) again tend to validate the correction terms. However, there is a discrepancy between the Ropaque HP91 porosity values of $\phi^1_{atm} = 32.9\%$ and $\phi_{corr} = 40.1\%$. The most likely explanation is that the effective dry density is 0.65 g cm$^{-3}$ rather than 0.55 g cm$^{-3}$ as quoted, which would change the porosity values to 43.2% and 44.1%, respectively, via eqs 18, 19, and 21.

The solid-phase bulk moduli of the plastic pigments decrease in the order Lytron 2601, Lytron 2301, and Ropaque HP91, corresponding to an increase in compressibility from medium to very compressible (Table 1). Thus, the agglomeration of smaller Lytron spheres is rather more compressible than that containing the larger spheres, and, as expected, the agglomeration of hollow spheres is much more compressible than that of the solid spheres. By comparison, the bulk modulus of solid nylon is around 5.3 GPa, similar to Lytron 2301 (Cook and Hover, 1993).

## 4. Void Space Computer Model

**4.1. Construction of the Void Space Model.** The void space within a porous coating layer may be regarded as an array of pores connected by throats. We simulate the void space with a network of *nodes* positioned at the center of each pore, connected by *arcs* along the line of each throat. The complete network comprises a series of identical three-dimensional unit cells, repeating indefinitely in each Cartesian direction $x$, $y$, and $z$.

Each unit cell contains 1000 nodes in a $10 \times 10 \times 10$ array equally spaced in the Cartesian coordinates. The void volume in the unit cell consists of up to 1000 cubic

pores centered on the nodes. Each pore is connected to a maximum of six cylindrical throats which lie along the line of the arcs in the positive and negative $x$, $y$, and $z$ directions. The number of throats connected to a particular pore is referred to as the *coordination number*, and the arithmetic mean of this quantity over the whole unit cell is referred to as the *connectivity*. The two outermost layers of a typical unit cell (LX 60) are shown in Figure 8. It can be seen that, in this case, the cell is a cube of length $l_{cell} = 7.20 \ \mu$m. For the calculation of the intrusion and extrusion of a nonwetting fluid, and permeability to a wetting fluid, the fluid is applied at the top face ($z = l_{cell}$) in the $-z$ direction, or withdrawn in the $+z$ direction, for each repeating unit cell. Thus, intrusion and permeability both apply to an infinite sheet of thickness $l_{cell}$, although, in practice, the permeability is the same as it would be for an infinite lump of the modeled substance.

We define the term *skew* as being the percentage of throats of the smallest of the 100 diameters in a simulated log/linear size distribution. In Figure 9, the skew is set to 1.00%, i.e., 1.00% of the throats have the smallest diameter, 0.007 $\mu$m. As there are 100 different diameters, it follows that there are 1.00% of all other diameters, to the nearest integral number of throats. Hence, we term this an *unskewed* distribution. The connectivity of the distribution is 3.5; i.e., there are on average 3.5 throats per pore. As there are always 1000 nodes in the unit cell and each throat connects to two nodes, the number of throats in this instance is 1750. Hence, there are, to the nearest integer, 17 or 18 throats set at each of the 100 diameters, which explains the oscillation of the throat size distribution in Figure 9.

The 1750 throats are randomly positioned within the unit cell. A pore is then assigned to each node that has at least one throat connected to it, the pore being of a size equal to the diameter of the largest throat reaching that node. The random positioning of the throats introduces a degree of randomness into the pore sizes, as shown. This pore size/throat size correlation is typical of natural (unground) sandstone but not natural limestone (Wardlaw and McKellar, 1981; Spearing and Matthews, 1991). However, gaining such information from paper coatings is much more complicated and has yet to be attempted.

The distribution can also be skewed. Figure 10, for example, shows a distribution with a skew of 0.54% (and connectivity 2.9), which is that for Carbital 90.

Mercury intrusion is simulated by means of an invasion percolation algorithm which calculates the fraction of pore volume occupied at a series of increasing, static mercury pressures. The throat size distribution and the skew are adjusted iteratively until a close fit to the experimental primary drainage mercury porosimetry curve is attained (Matthews et al., 1995b). Finally, the row spacing of the matrix is set so that the porosity of the simulated network equals that of the experimental sample. Increasing the pore row spacing lengthens the throats, increases the unit cell size, and hence reduces the porosity.

The tortuosity of the unit cell may be simulated by means of a three-dimensional random walk through the cell, with statistical weighting to simulate the path of an ionic particle. If the Pore-Cor unit cell is adjusted to mimic cubic close packing, its tortuosity agrees with theoretical values calculated by other workers (Spearing and Matthews, 1991).
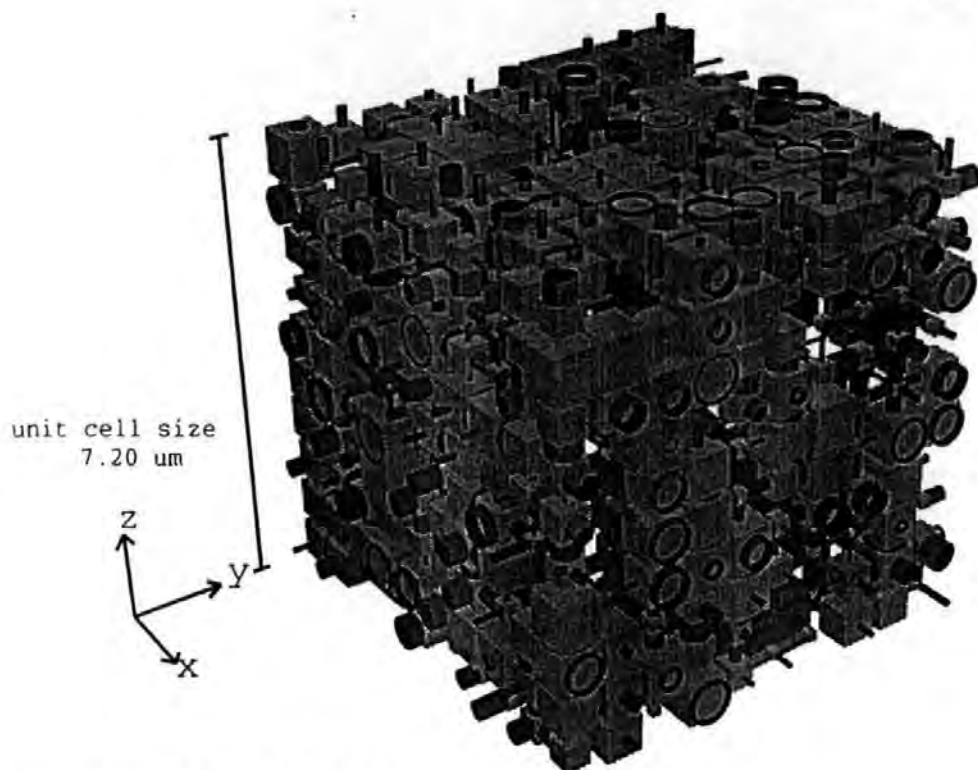
unit cell size
7.20 um

z

y

x

**Figure 8.** Two outermost layers of the unit cell of LX 60.



PORE and THROAT SIZE DISTRIBUTION

........ Throats        ——— Pores

**Figure 9.** Unskewed throat diameter and pore size distribution.



PORE and THROAT SIZE DISTRIBUTION
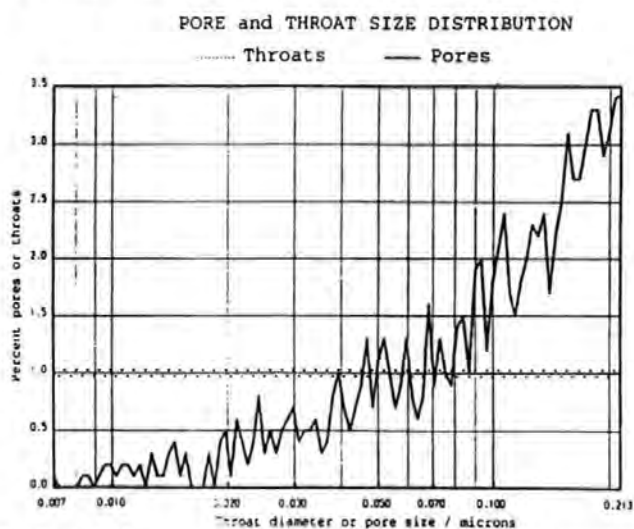
........ Throats        ——— Pores

**Figure 10.** Carbital 90 throat diameter and pore size distribution.

The question remains as to whether the resulting unit cell structure is a unique representation of the experimental properties of the sample or whether other unit cells would provide an equally good fit. The uniqueness of the unit cell can be judged by inspection of plots of how the deviation between simulation and experiment varies as the modeling parameters are varied (Matthews et al., 1995b) and the effect of varying the seed of the pseudo random number generator which determines the positioning of the throats, and hence the adjacent pores (Matthews et al., 1995a).

**4.2. Calculation of Permeability.** Permeabilities are calculated for both liquid and air at 1 atm pressure, by a method described previously (Matthews et al., 1993, 1995a). It is assumed that, in a liquid, there is a negligible mean free path length between intermolecular collisions in the fluid phase and that the mean free path length in air is the same as that of nitrogen, i.e., 0.0698 $\mu$m. Permeability is very dependent on con-
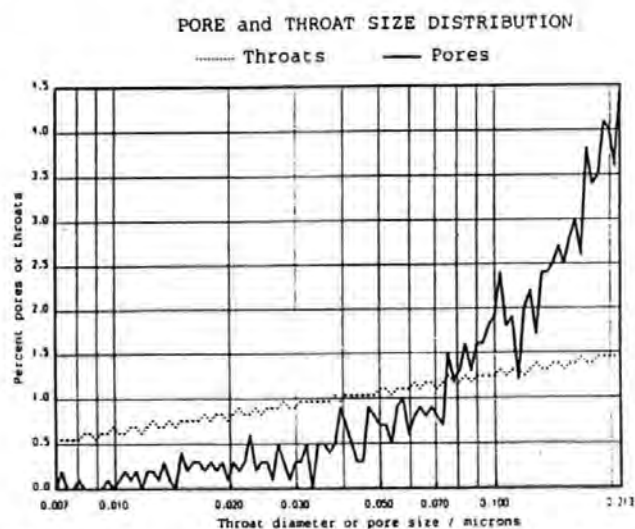
nectivity and correlation effects, which are not well characterized for the reasons described previously. The permeability calculations are therefore the best available with the current state of knowledge but should be used for ranking the samples rather than as absolute values. The permeability units are microDarcies, where 1 $\mu$D = 9.87 $\times$ 10$^{-19}$ m$^2$.

**5. Void Space Modeling Results**

The corrected intrusion data have been simulated by the Pore-Cor computer program. The resulting simulated intrusion curves (⊙) all match the corrected experimental curves closely, as can be seen in Figures 2–7.

**5.1. Fine Ground Calcium Carbonates.** The pore and throat size distributions which generate the mercury intrusion curves for Carbital 90, Carbital 60, and LX 60 are summarized in Table 2. It can be seen that, in this series, the percentages of pores and throats below

**Table 2. Simulation Results**

| type of sample | commercial name | min. throat diam./µm | max. throat diam./µm | skew | connectivity | unit cell length $l_{cell}$/µm | porosity $\phi$/% | permeability/µD (liquid, air) |
|---|---|---|---|---|---|---|---|---|
| dried slurry of finely ground calcium carbonate | Carbital 90 | 0.007 | 0.213 | 0.54 | 2.9 | 2.43 | 26.2 | 0.37, 6.38 |
| | Carbital 60 | 0.007 | 0.427 | 0.09 | 2.8 | 4.74 | 28.8 | 1.83, 15.5 |
| | LX 60 | 0.007 | 0.7 | 0.10 | 4.0 | 7.20 | 40.9 | 33.3, 154 |
| dried coating color; Carbital 90 with added latex binder | Carbital 90 + Acronal S801 | 0.007 | 0.427 | 0.02 | 3.0 | 5.80 | 19.4 | 1.55, 13.3 |
| | Carbital 90 + latex 95L10 | 0.007 | 0.427 | 0.74 | 3.5 | 5.36 | 19.3 | 1.02. 8.67 |
| | Carbital 90 + DL 950 | 0.007 | 0.427 | 0.67 | 3.3 | 5.11 | 21.3 | 0.51, 5.72 |
| plastic pigment | Lytron 2601 | 0.007 | 1.0 | 0.46 | 2.9 | 10.14 | 27.9 | 0.85, 6.16 |
| | Lytron 2301 | 0.007 | 0.427 | 0.84 | 2.7 | 4.46 | 23.2 | 0.033, 0.73 |
| | Ropaque HP91 | 0.04 | 1.0 | 0.47 | 3.3 | 11.05 | 32.9 | 43.4, 159 |



unit cell size
2.43 um
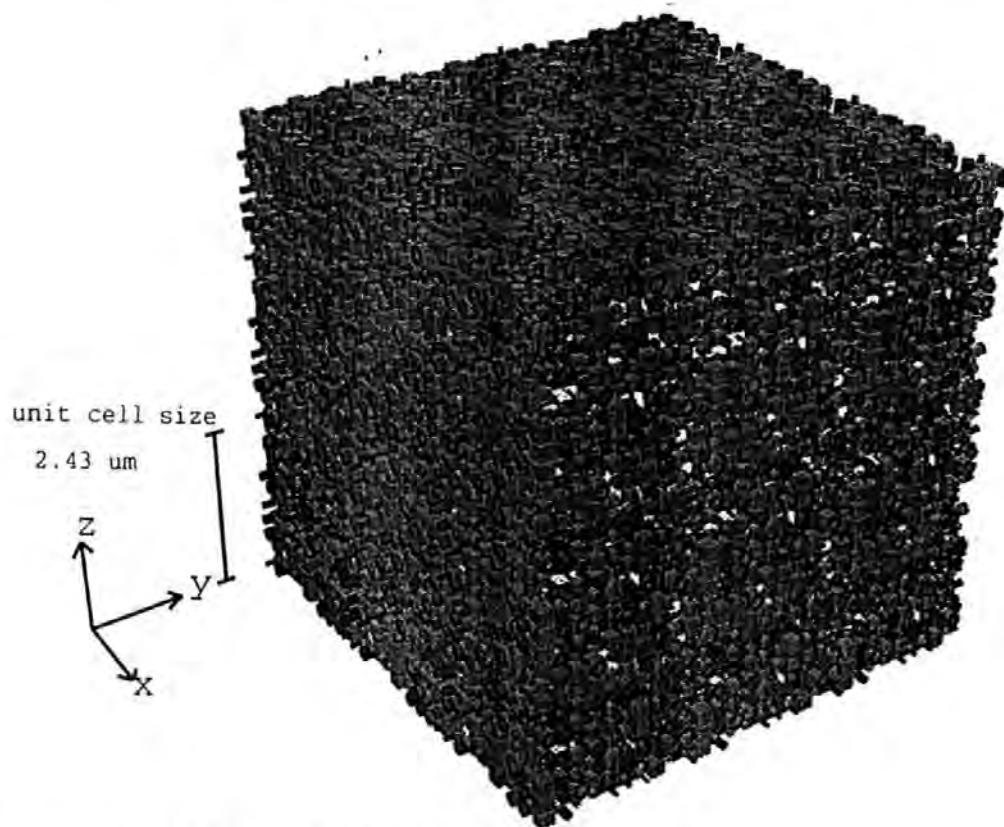
**Figure 11.** Two outermost layers of the unit cell of Carbital 90.

0.03 µm decrease and the percentages of the large sizes increase (noting the different maximum sizes). This trend is in agreement with the relative sizes of the void spaces which would be expected between particles of sizes shown in Figure 1. Figure 8, shown previously, is the unit cell of LX 60. Figures 11 and 12 show the same size cube (7.20 µm) of the simulated void space structure of Carbital 90 and Carbital 60. The unit cell size varies for these samples as shown, and so these diagrams include more than one unit cell. As shown in Table 2, a higher connectivity (4.0) is required to simulate the steeper intrusion curve of LX 60. LX 60 also has a higher porosity (all experimental and simulated porosities match exactly). Overall, it can be seen that the simulated permeabilities increase by 2 orders of magnitude from Carbital 90 to LX 60 (Table 2). Slip flow causes a 17-fold relative increase in permeability for Carbital 90 and an absolute increase of 6 µD. For the more permeable samples, the absolute increase

caused by slip flow is greater but the relative effect is smaller.

**5.2. Carbital 90 with Added Latex Binder.** The three coating color samples have the throat diameter and pore size distributions shown in Table 2, each covering the range 0.007–0.427 µm. The Carbital 90 + Acronal S801 has a lower skew and more large pores than the other two samples. The porosities of the three samples are all around 20% (Table 2). The unit cell of the Carbital 90 + Acronal S801 is similar to that of Carbital 60 (Figure 12), although the unit cell sizes differ (Table 2). Carbital 90 + latex 95L10 has a unit cell similar to that of Carbital 90 + DL 950. There is a 3-fold difference in the permeabilities of these three structures, which is small in comparison to the range of simulated permeabilities in the previous section.

**5.3. Plastic Pigments.** The two solid plastic pigments have different size particles, as reflected in the modeling by the different throat diameter and pore size
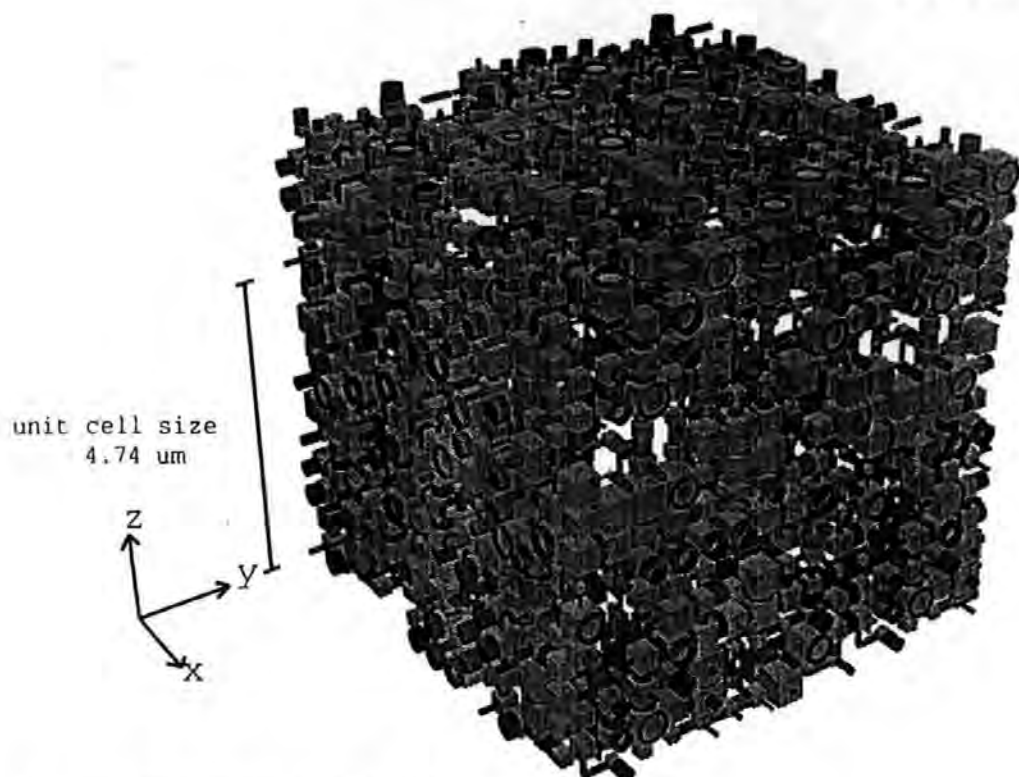
**Figure 12.** Two outermost layers of the unit cell of Carbital 60.

ranges. The maximum simulated throat diameter for Lytron 2601 is twice the maximum simulated throat diameter for Lytron 2301, and the unit cell for Lytron 2601 is twice as large as that for Lytron 2301. Lytron 2601 has a simulated permeability of 0.850 $\mu$D compared to Lytron 2301 which has a simulated permeability of 0.033 $\mu$D. The differences between the throat diameter and pore size distributions and between the simulated permeabilities of the two Lytron samples are in accord with the differences between their experimental particle sizes and porosities (Table 1).

The interparticle void space structure of Ropaque HP91 before the collapse of its polystyrene spheres has been simulated. The throat diameter and pore size distribution covers a range from 0.04 to 1.0 $\mu$m, the minimum throat diameter being much larger than the minimum throat diameter of the other samples. The simulated permeability of the Ropaque sample is higher than any of the previous structures, at 43.4 $\mu$D for liquid and 159 $\mu$D for air, because of the larger minimum throat diameter, coupled with a skew toward larger sizes.

## 6. Conclusions

This study has shown how mercury porosimetry can be used to measure the bulk moduli of the compressible solid phase of porous samples, thus revealing information about their microstructure, packing, and interparticle bonding. The corrected mercury intrusion curves have formed a data set for our computer modeling package Pore-Cor, which takes into account porosity, connectivity, and shielding effects in three-dimensional void space networks. The computer model generates throat diameter and pore size distributions, and corresponding three-dimensional unit cells. The void space structure determines properties such as ink setting characteristics and opacity, and its improved determination is therefore of importance to the paper-making

and printing industries. The modeling package also simulates permeabilities which cannot be measured experimentally. The methodology presented here has wide applicability to other consolidated and compressible samples.

## Nomenclature

$d$ = throat diameter

$\delta V_{blank}$ = total change in mercury volume during a blank run

$\delta V_{Hgpen}$ = increase in mercury volume due to compression of a volume of mercury which fills the empty penetrometer

$\delta V_{pen}$ = increase in mercury volume due to penetrometer expansion

$\delta V_{Hg}$ = increase in mercury volume due to compression of mercury during a sample run

$\delta V_{Hgbulk}$ = compression of mercury volume corresponding to sample bulk volume

$\delta V_{sample}$ = increase in mercury volume caused by the compression of the sample

$\delta V_{ss}$ = compression of the continuous solid phase of the sample

$\delta V_{su}$ = compression of the solid into unintruded void space

$l_{cell}$ = unit cell length

$m_{sample}$ = mass of sample

$M_{ss}$ = solid-phase bulk modulus

$P$ = applied pressure

$P_{50}$ = pressure at which 50% pore volume is intruded

$P^z$ = applied pressure at which accessible pore volume is fully intruded

$P^{max}$ = maximum experimentally attainable applied pressure

$T_g$ = glass transition temperature

$V^1_{bulk}$ = bulk volume of the sample at 1 atmosphere pressure

$V_{obs}$ = observed volume of mercury intruded

$V_{int}$ = volume intruded into the sample

$V^1_{blank}$ = volume of mercury used in the blank experiment at 1 atm pressure

$V^1_{pen}$ = volume of the penetrometer at 1 atm pressure

$V^1_{Hg}$ = total volume of mercury in a filled penetrometer (with sample) at 1 atm pressure

$V^1_{Hgpen}$ = volume of mercury in a filled penetrometer (no sample) at 1 atm pressure

$V^1_{Hgbulk}$ = volume of mercury equal to the bulk volume of the sample at 1 atm pressure

$V^z_{ss}$ = volume of the continuous solid phase of the sample at zero void pressure

$V^1_{solid}$ = volume of the solid at 1 atm pressure calculated from composition and constituent densities

$w_{pigment}$ = relative weight of pigment in parts per hundred

$w_{binder}$ = relative weight of binder in parts per hundred

$x, y, z$ = Cartesian coordinates

*Greek Letters*

$\gamma$ = mercury interfacial tension

$\theta$ = mercury/solid/air contact angle

$\rho_{pigment}$ = density of pigment

$\rho_{binder}$ = density of binder

$\phi^1$ = porosity at 1 atm pressure

$\phi_{uncorr}$ = porosity uncorrected for compressibility

$\phi_{corr}$ = corrected porosity

$\psi_{ss}$ = solid-phase compressibility

$\Omega$ = network averaging operator

## Literature Cited

Alince, B.; Lepoutre, P. Porosity and Optical Properties of Clay Coatings. *J. Colloid and Interface Sci.* **1980a**, *76*, 439–444.

Alince, B.; Lepoutre, P. Light Scattering of Coatings Formed from Polystyrene Pigment Particles. *J. Colloid Interface Sci.* **1980b**, *76*, 182–187.

Climpson, N. A.; Taylor, J. H. Pore Size Distributions and Optical Scattering Coefficients of Clay Structures. *Tappi J.* **1976**, *59*, 89–92.

Cook, R. A.; Hover, K. C. Mercury Porosimetry of Cement-Based Materials and Associated Correction Factors. *ACI Mater. J.* **1993**, March/April, 152–161.

Deer, W. A.; Howie, R. A.; Zussman, J. *Introduction to Rock Forming Minerals*, 2nd ed.; Longman: 1992.

Gane, P. A. C.; Seyler, E. N. *Tappi Coat. Conf. Proc.* **1994**, 243–250.

Hamlen, R. C.; Scriven, L. E. *Tappi Coat. Conf. Proc.* **1991**, 355–191.

Kent, H.; Climpson, N.; Gane, P.; Coggon, L.; Hooper, J. *Tappi Coat. Conf. Proc.* **1986**, 103–112.

Kettle, J. P.; Matthews, G. P. *Adv. Coat. Fundam. Symp.*: Atlanta, **1993**, 121–126.

Larrondo, L.; St-Amour, S. *Tappi Coat. Conf. Proc.* **1992**, 37–51.

Lee, J. A.; Maskell, W. C. Correction factors involved in mercury porosimetry. *Powder Technol.* **1973**, *7*, 259–262.

Lepoutre, P.; Rezanowich, A. Optical Properties and Structure of Clay–Latex Coatings. *Tappi J.* **1977**, *60*, 86–91.

Matthews, G. P.; Spearing, M. C. Measurement and Modelling of Diffusion, Porosity and Other Pore Level Characteristics of Sandstones. *Mar. Pet. Geol.* **1992**, *9*, 146–154.

Matthews, G. P.; Moss, A. K.; Spearing, M. C.; Voland, F. Network Calculation of Mercury Intrusion and Absolute Permeability in Sandstone and Other Porous Media. *Powder Technol.* **1993**, *76*, 95–107.

Matthews, G. P.; Moss, A. K.; Ridgway, C. J. The Effects of Correlated Networks on Mercury Intrusion Simulations and Permeabilities of Sandstone and Other Porous Media. *Powder Technol.* **1995a**, *83*, 61–77.

Matthews, G. P.; Ridgway, C. J.; Spearing, M. C. Void Space Modelling of Mercury Intrusion Hysteresis in Sandstone, Paper Coating and Other Porous Media. *J. Colloid Interface Sci.* **1995b**, *171*, 8–27.

Ranger, A. E. *Fundam. Prop. Pap. Relat. Its Uses Trans. Symp.* **1976**, 685–737.

Shinohara, K. *Powder Technology Handbook*; Iinoya, K., Gotoh, K., Higashitani, K., Eds; Marcel Dekker, Inc.: New York, 1990; pp 481–501.

Spearing, M. C.; Matthews, G. P. Modelling Characteristic Properties of Sandstones. *Transp. Porous Media* **1991**, *6*, 71–90.

van Brakel, J.; Modry, S.; Svata, M. Mercury Porosimetry: State of the Art. *Powder Technol.* **1981**, *29*, 1–12.

Wardlaw, N. C.; McKellar, M. Mercury Porosimetry and the Interpretation of Pore Geometry in Sedimentary Rocks and Artificial Models. *Powder Technol.* **1981**, *29*, 127–143.

Warren, N.; Nashner, R. *The Physics and Chemistry of Minerals and Rocks*; Strens, R. G. J., Ed; John Wiley & Sons: London, 1976; pp 197–216.

Washburn, E. W. *Proc. the Natl. Acad. Sci. U.S.A.* **1921**, *7*, 115–116.

Watanabe, J.; Lepoutre, P. A Mechanism for the Consolidation of the Structure of Clay–Latex Coatings. *J. Appl. Polym.Sci.* **1982**, *27*, 4207–4219.

Yamazaki, H.; Munakata, Y. *Oxford Fundam. Res. Symp. Proc.* **1993**, 913–934.